

# Important Notice

This copy may be used only for the purposes of research and private study, and any use of the copy for a purpose other than research or private study may require the authorization of the copyright owner of the work in question. Responsibility regarding questions of copyright that may arise in the use of this copy is assumed by the recipient.

# Seismic Migration/Inversion for Transversely Isotropic Elastic Media

by

David W.S. Eaton

Ph.D. Thesis  
The University of Calgary  
Department of Geology and Geophysics  
December, 1991



*Consortium for Research in Elastic Wave Exploration Seismology*

THE UNIVERSITY OF CALGARY

SEISMIC MIGRATION/INVERSION  
FOR  
TRANSVERSELY ISOTROPIC ELASTIC MEDIA

by

David W.S. Eaton

A THESIS

SUBMITTED TO THE FACULTY OF GRADUATE STUDIES  
IN PARTIAL FULFILLMENT OF THE REQUIREMENTS FOR THE  
DEGREE OF  
DOCTOR OF PHILOSOPHY

DEPARTMENT OF GEOLOGY AND GEOPHYSICS

CALGARY, ALBERTA

DECEMBER, 1991

© David W.S. Eaton 1991



# SEISMIC MIGRATION/INVERSION FOR TRANSVERSELY ISOTROPIC ELASTIC MEDIA

*David W.S. Eaton*

*The University of Calgary, 1991*

## ABSTRACT

Classical seismic imaging techniques assume an acoustic isotropic medium. In this thesis, new methods are developed for isotropic and/or transversely isotropic (TI) elastic media. These new assumptions facilitate the analysis of both mode-converted waves and anisotropic parameters within the earth.

Processing mode-converted seismic data requires special binning techniques, because the lateral position of the conversion point varies with depth. Previously published algorithms for approximate common-conversion-point (CCP) trace sorting are unsuitable for imaging multiple depth zones, and are sometimes prone to periodic binning artifacts. In this thesis, a depth-variant CCP mapping technique is used to overcome these difficulties. The mapping algorithm produces unmigrated  $P$ - $SV$  stacked images that are directly comparable to common-midpoint (CMP) stacked sections obtained from conventional ( $P$ - $P$ ) seismic data. An example of single-depth trace sorting for a strongly anisotropic material with a vertical infinite-fold symmetry axis illustrates that, unlike isotropic media, conversion-point shift toward the source is possible for  $qP$ - $qSV$  arrivals.

The latter half of this thesis deals with migration and inversion of seismic data based on a least-squares ray-Born formalism. The following assumptions are employed to simplify the problem: the orientation of the infinite-fold anisotropic symmetry axis is known, and coplanar with the sources and receivers; the medium and acquisition geometry are two-dimensional; based on prior information, an accurate and smooth (ray-

valid) reference model can be defined; coherent noise has been removed from the data. At least six parameters are required to characterize an elastic medium with TI symmetry. Here, for convenience, the model-parameter set is chosen to be  $qP$  and  $qS$  velocities, density, and the three Thomsen anisotropy parameters.

In order to implement the migration/inversion strategy, robust and efficient methods for computing high-frequency background Green's functions are required. For this purpose, an existing methodology for finite-difference traveltimes and amplitude computation for isotropic media is adapted for use with TI media. The traveltimes technique tracks seismic wavefronts by solving the sixth-order anisotropic eikonal equation on a hexagonal mesh. Differentiation of the computed traveltimes field yields estimates of the slowness and polarization vectors. The initial ray parameters are determined by perturbing the source location on the grid, and are then used to estimate the  $2\frac{1}{2}$ -dimensional geometrical-spreading function. In numerical tests using a Sun Sparcstation 2, accurate traveltimes were computed at a rate of about 50 per CPU second. However, the computed amplitudes contain small oscillatory artifacts.

The migration/inversion problem is posed as a least-squares optimization, which is solved by an iterative algorithm consisting of three steps: filtered backprojection (migration) of the current data residual, application of an approximate inverse-Hessian matrix to yield parameter perturbation estimates, and re-scattering from the new model to update the data-residual vector. Application of this procedure to synthetic crosswell data demonstrates that Thomsen's  $\epsilon$  parameter can be resolved as well as, or better than, any of the isotropic parameters. Migration/inversion of a ray-traced dataset produced erroneous estimates of density and anisotropic parameters, but illustrates that superior imaging of slope discontinuities in the subsurface is possible when all elastic wave types (i.e.,  $qP$ - $qP$ ,  $qP$ - $qSV$ ,  $qSV$ - $qSV$ , etc.) are used.

## ACKNOWLEDGEMENTS

I would like to thank my thesis supervisor, Rob Stewart, who has fostered a dynamic and open research environment. His quick insight and ability to look at problems from several different angles were always a source of inspiration. He has also taught me perseverance! My understanding of anisotropy (and my awareness of how not to boldly split infinitives) has benefitted tremendously from working with Jim Brown. I have also learned a lot about stacking charts and elastic processing in general through collaboration with Don Lawton. In addition, suggestions and comments by Wafik Beydoun and Peter Cary were very helpful, and came at critical times in my research.

My fellow graduate students and the staff of CREWES have been a constant source of help, ideas, good conversation and, not the least, companionship during late-night work sessions. In particular, I have shared moments of revelation with Robin Slotboom and Don Easley that turned out to be very significant points. Whatever skills that I have acquired as computer programmer have been picked up from working with Malcolm Bertram and Henry Bland.

My greatest thanks go to my wife, Pam, who has endured years of financial insecurity, stress, long work hours and periods of time when I have been with her in body but not necessarily in mind, only to watch me go off to another conference for a week! She has always been there when I needed her. Our two children have never known any lifestyle but the student-family lifestyle, and are in for a shock. A moment that I am sure to remember always occurred one night while I was putting Jaclyn to bed, when out of the blue she issued the teary-eyed plea, "Daddy.. I hope you finish your thesis soon!". Nobody could have put it better!

**To Dad, the scientist who has always inspired me.**

# TABLE OF CONTENTS

<b>APPROVAL PAGE</b>	<b>ii</b>
<b>ABSTRACT</b>	<b>iii</b>
<b>ACKNOWLEDGEMENTS</b>	<b>v</b>
<b>TABLE OF CONTENTS</b>	<b>vii</b>
<b>LIST OF TABLES</b>	<b>x</b>
<b>LIST OF FIGURES</b>	<b>xi</b>
<b>1 Introduction</b>	<b>1</b>
1.1 Statement of the problem	1
1.1.1 Acquisition geometry	2
1.1.2 Assumptions	2
1.2 Review of transverse isotropy	6
1.2.1 Intrinsic anisotropy	9
1.2.2 Periodic-thin layering	10
1.2.3 Fractured media	14
1.3 Summary	16
<b>2 Background Theory</b>	<b>18</b>
2.1 Introduction	18
2.2 Wave propagation in a homogeneous anisotropic medium	18
2.2.1 Plane-wave solutions: Slowness and wave surfaces	20
2.2.2 The approximate elastodynamic Green's tensor	24
2.3 Ray method	28
2.4 The ray-Born approximation	32
2.4.1 Stationary-phase correction for out-of-plane scattering	42
2.5 Least-squares inversion	44
2.6 Summary	45
<b>3 Converted-wave binning techniques</b>	<b>47</b>
3.1 Introduction	47
3.2 Raypath geometry for converted waves: Isotropic case	48
3.3 Review of common-conversion-point trace-sorting techniques	54
3.4 <i>P-SV</i> stacking charts and binning periodicity	61
3.5 Depth-variant CCP mapping	65
3.5.1 Description of the algorithm	65
3.5.2 Examples	67
3.7 Anisotropic CCP trace sorting	70

3.8	Summary	77
<b>4</b>	<b>Finite-difference calculation of ray-Green's functions</b>	<b>78</b>
4.1	Introduction	78
4.2	Traveltime calculation	84
4.2.1	Description of the algorithm	84
4.2.2	Examples	89
4.3	Calculation of eigenvectors	97
4.3.1	Description of the algorithm	98
4.3.2	Examples	99
4.4	Initial-slowness calculation	99
4.4.1	Description of the algorithm	101
4.4.2	Example	103
4.5	Out-of-plane spreading function	103
4.5.1	Description of the algorithm	105
4.5.2	Example	106
4.6	Estimation of seismic amplitudes	106
4.6.1	Description of the algorithm	107
4.6.2	Examples	109
4.7	Concluding remarks	113
<b>5</b>	<b>Least-squares migration/inversion</b>	<b>116</b>
5.1	Introduction	116
5.2	Description of the algorithm	118
5.2.1	Overview	118
5.2.2	Filtered backprojection of the data residual	120
5.2.3	The approximate Hessian	128
5.2.4	Computing the step size	129
5.3	Examples	131
5.3.1	Surface-data examples	131
5.3.2	Crosswell examples for an isotropic background model	139
5.3.3	Crosswell examples for an anisotropic background	145
5.3.4	Crosswell examples for a complex geological model	145
5.3.5	Migration/inversion using a non-Born dataset	150
5.4	Conclusions	154
<b>6</b>	<b>Conclusions</b>	<b>159</b>
6.1	Thesis summary	159
6.2	Future work	160
	<b>References</b>	<b>163</b>

## Appendices

<b>A</b>	<b>Elastic-scattering radiation patterns</b> .....	<b>173</b>
A.1	Stiffness components and vector constraints .....	173
A.2	The scattering vector .....	174
<b>B</b>	<b>Time-shifted hyperbolic moveout for converted waves</b> .....	<b>175</b>
B.1	Derivation of the formula .....	175
B.2	Comparison with other formulas .....	177
<b>C</b>	<b>The eikonal equation as a sixth-order polynomial</b> .....	<b>179</b>
C.1	Derivation .....	179

## LIST OF TABLES

2.1	Convention for indicial conversion between elastic stiffness notations . . . . .	19
2.2	Incident and scattered wave types for diffraction patterns . . . . .	36
3.1	Acquisition geometry for synthetic dataset . . . . .	57
3.2	Empirical velocity function used to NMO correct the anisotropic dataset . . . .	74
4.1	Summary of models used to test the finite-difference algorithms . . . . .	80
4.2	Parameters for model 4.3 . . . . .	81
5.1	Summary of models used to test the migration/inversion algorithm . . . . .	132
5.2	Summary of integrated M/I perturbation values, models 5.1a and 5.1b . . . . .	138
5.3	Summary of integrated M/I perturbation values, models 5.2 and 5.3 . . . . .	144

## LIST OF FIGURES

1.1 Schematic illustration of VSP, surface and crosswell acquisition geometries . . .	3
1.2 Canonical models for transverse isotropy in sedimentary rocks . . . . .	7
1.3 Graph of $\delta$ vs. $\epsilon$ and $\gamma$ vs. $\epsilon$ for intrinsic anisotropy in sedimentary rocks . . .	11
1.4 $P$ -wave velocities for Upper Cretaceous sediments . . . . .	14
2.1 Geometrical relationship between phase velocity and group velocity . . . . .	23
2.2 Slowness surface and wave surface for the Greenhorn shale . . . . .	25
2.3 Normalized amplitude surface for the Greenhorn shale . . . . .	28
2.4 Elementary ray tube . . . . .	32
2.5 Rayleigh scattering for isotropic parameters . . . . .	37
2.6 Rayleigh scattering for anisotropic parameters, vertical axis of symmetry . . . .	38
2.7 Rayleigh scattering for anisotropic parameters, 45° axis of symmetry . . . . .	39
2.8 Rayleigh scattering for anisotropic parameters, horizontal axis of symmetry . .	40
2.9 Isotropic/anisotropic comparison of radiation patterns . . . . .	42
3.1 Converted-wave raypath geometry in a horizontally stratified medium . . . . .	49
3.2 $P$ -wave and estimated $S$ -wave layer velocities, for a well at 4-22-53-12W5 . .	54
3.3 Location map showing position of seismic line and well location . . . . .	55
3.4 Map view of synthetic survey, showing shot numbers . . . . .	57
3.5 Shot record 6 from the synthetic dataset . . . . .	57
3.6 Stacked data gathered using the asymptotic approximation . . . . .	58
3.7 Stacked data gathered using the straight-ray approximation ( $z = 500$ m) . . . .	59
3.8 Stacked data gathered using the straight-ray approximation ( $z = 2000$ m) . . . .	60
3.9 $P$ - $SV$ stacking chart . . . . .	63
3.10 Asymptotic binning, $\Delta r = 30$ m . . . . .	66
3.11 Stacked data generated using $P$ - $SV$ mapping technique . . . . .	69
3.12 Normalization array corresponding to mapped data shown in Fig 3.11 . . . . .	70
3.13 Portion of stacked $P$ - $SV$ data from line CC-SW-02 . . . . .	71
3.14 Graph of conversion-point offset versus source-receiver offset . . . . .	74
3.15 Shot record 6 from the anisotropic dataset . . . . .	74
3.16 Anisotropic data gathered for a target depth of 1000 m . . . . .	75
3.17 Asymptotic gathering applied to anisotropic dataset . . . . .	76
4.1 Configuration for model 4.4 . . . . .	81
4.2 Layer configuration for model 4.5 . . . . .	82
4.3 Grey-scale plots of the medium parameters for model 4.5 . . . . .	83
4.4 Hexagonal mesh used for finite-difference calculations . . . . .	85
4.5 Plot of $f(p_3) = \xi_j p_3^j$ for the Greenhorn shale ( $p_1 = p_2 = 0$ ) . . . . .	88
4.6 Algorithm for finite-difference traveltimes calculation . . . . .	89
4.7 Finite-difference $P$ -wave traveltimes for model 4.1 . . . . .	90
4.8 Finite-difference traveltimes computed for model 4.2 . . . . .	91
4.9 Finite-difference traveltimes error for model 4.2 . . . . .	92

4.10	Finite-difference traveltimes for model 4.3	94
4.11	Ray-traced and finite-difference traveltimes at top of model 4.3	95
4.12	Finite-difference $qP$ traveltimes for model 4.4	96
4.13	Finite-difference $qP$ traveltimes for model 4.5	98
4.14	Angular difference between the eigenvector and the analytic solution	100
4.15	$qP$ polarization direction with respect to the $x_3$ -axis for model 4.5	101
4.16	Sketch of the raypaths joining four closely spaced source points to $P$	102
4.17	$qP$ initial phase angle for model 4.5	104
4.18	$qP$ out-of-plane spreading factor ( $\tau_{22}$ ) for model 4.5	106
4.19	Method for calculating $\Delta\gamma_1$	108
4.20	Normalized amplitudes computed for model 4.1	110
4.21	Normalized amplitudes computed for model 4.2	111
4.22	Theoretical amplitude function (normalized) for model 4.2	112
4.23	Normalized amplitudes computed for model 4.3	114
4.24	Normalized amplitudes computed for model 4.5	114
5.1	Flow chart for MITI program	119
5.2	Sketch of elastic-migration isochron curves	122
5.3	Elastic-migration impulse response, vertical source and receiver	124
5.4	Elastic-migration impulse response, horizontal source and receiver	125
5.5	Elastic-migration impulse response, vertical source and horizontal receiver	126
5.6	Elastic-migration impulse response, transverse source and receiver	127
5.7	Model geometry used for the first three examples	133
5.8	Input and rescattered data for model 5.1a	135
5.9	Results of migration/inversion for model 5.1a	136
5.10	Results of migration/inversion for model 5.1b	137
5.11	Input and rescattered data for model 5.2a	140
5.12	Results of migration/inversion for model 5.2a	141
5.13	Results of migration/inversion for model 5.2b	142
5.14	Results of migration/inversion for model 5.2c	143
5.15	Results of migration/inversion for model 5.3	146
5.16	Acquisition geometry for model 5.4	147
5.17	Input and rescattered data for model 5.4	148
5.18	Migration/inversion results for model 5.4	149
5.19	Migration/inversion results for density after 1, 2 and 10 iterations	151
5.20	Graph of data-residual energy as a function of iteration for model 5.4	152
5.21	Geological model and acquisition geometry for model 5.5	153
5.22	Input and rescattered data for model 5.5	155
5.23	Migration/inversion results for model 5.5	156
5.24	Schematic illustration of interface segments for model 5.5	157
B.1	Comparison of moveout formulas for converted waves	178

# Chapter 1

## Introduction

### 1.1 Statement of the problem

Seismic migration and inversion are closely related processes for obtaining images of the subsurface. Underlying principles and methods vary, but in essence both techniques attempt to quantify the task of inferring petrophysical and structural parameters from seismic data. Historically, the term inversion has been applied to the problem of estimating intrinsic properties that characterize a physical system (Tarantola, 1987), whereas the term migration has been reserved for imaging of the structural configuration of geologic discontinuities (Stolt and Benson, 1986). In both cases, however, the mathematical link between observed data and the final image is the same: a set of equations of motion that are derived from a constitutive model for the earth.

When a constitutive model is chosen such that properties of the earth at any point are directionally dependent, it is said to be anisotropic. On a microscopic scale, virtually all of the constituent minerals in the earth's crust have crystal structures that are anisotropic (Musgrave, 1970). Anisotropy on a macroscopic scale can be caused by preferred orientation of these minerals, as well as periodic-thin layering and stress-aligned fracturing (Crampin et al., 1984). Fundamental differences exist between wave propagation in an anisotropic and an isotropic solid (Duff, 1960; Crampin, 1981). Previous studies of seismic imaging in anisotropic media (Meadows, 1985; Geoltrain and Cohen, 1989; Uren et al., 1990; Tura, 1990) have stressed the importance of accounting for anisotropic wave-propagation effects, but have dealt primarily with special cases, such

as elliptical anisotropy or plane layering.

This thesis deals with seismic imaging and inversion in the presence of transverse isotropy, a widely applicable form of anisotropy. The problem can be stated as follows: based on observations of the scattered wavefield (i.e., that part of the observed seismic wavefield that has undergone single reflection or diffraction from geologic discontinuities), coupled with a number of assumptions given below, what is the distribution and nature of elastic heterogeneities within some region of interest? The main objectives of this study are to develop practical imaging techniques for this type of medium and to assess the relative resolution of the various elastic parameters that are characteristic of transverse isotropy. A linearized inverse-scattering approach is used to achieve these goals. This strategy represents a natural synthesis of ray, Born, and general-inverse theories, and establishes an effective framework for continued study of this problem.

### **1.1.1 Acquisition geometry**

Fig. 1.1 illustrates basic geometrical features of the seismic-reflection method, showing surface recording, vertical-seismic profiling (VSP) and crosswell acquisition geometries. In the ideal case, all three of these methods are used in conjunction to maximize the angular coverage of the zone of interest. This situation is rare, however, and more often only one type of survey is available at a given location. In this study, the sources and receivers are confined to the  $x$ - $z$  plane, although in practice, 3-D surface acquisition and non-coplanar crosswell surveys are not uncommon. Because of strong near-surface heterogeneities, recordings at the surface are typically noisier, contain lower frequencies, and have less reliable amplitude information than borehole recordings.

### **1.1.2 Assumptions**

Several assumptions, such as the far-field, high-frequency and small-perturbation

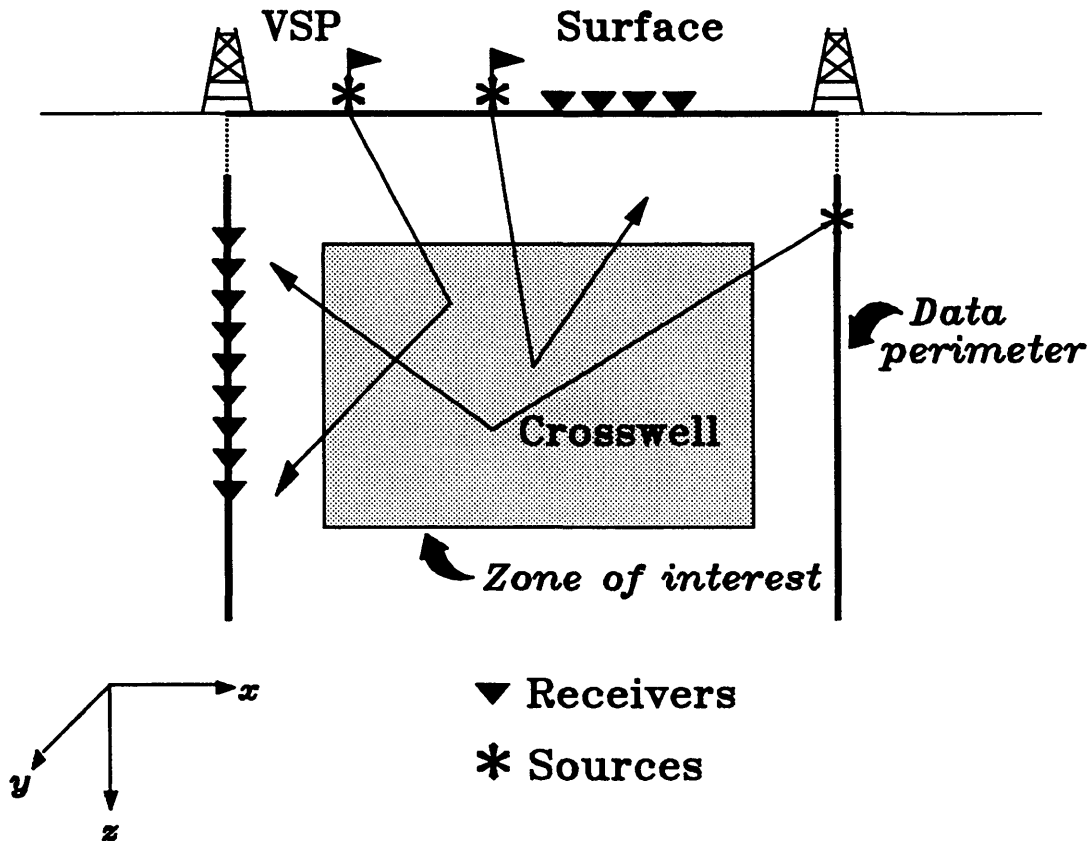


**Fig. 1.1.** Schematic illustration of VSP, surface and crosswell acquisition geometries (not all sources and receivers are shown). Raypaths indicate scattering of the seismic wavefield from localized elastic heterogeneities within the zone of interest.

assumptions, are incorporated directly in the ray-Born modeling formalism, and will be discussed in chapter 2. The following additional assumptions are employed here in order to simplify the problem:

- 1) the medium is transversely isotropic (TI); the direction of the symmetry axis is assumed to be known, and to be coplanar with the sources and receivers;
- 2) the medium and recording geometry are two-dimensional; medium parameters are independent of the  $y$  coordinate;

3) using prior information, it is possible to define elastic parameters for a reference medium that are smoothly varying, and are a close approximation to the true earth parameters;

4) preprocessing of the data has removed any part of the recorded signal that is not accounted for in the modeling procedure, such as surface waves or multiple reflections.

The first assumption asserts the layered nature of sedimentary rocks, since transverse isotropy is the most natural symmetry system for laminated or fractured materials (Backus, 1962; Hudson, 1981; Helbig, 1984). The additional degrees of freedom provided by the adoption of the TI model are likely to provide valuable new information, and to yield improved imaging potential in exploration applications, particularly those involving shear waves. This conjecture is supported by mounting theoretical and empirical evidence (Robertson and Corrigan, 1983; Melia and Carlson, 1984; Helbig, 1984; Crampin, 1985; 1987; Winterstein, 1986; Thomsen, 1986; Byun et al., 1989; Gibson and Toksöz, 1990; Lynn and Thomsen, 1990; Winterstein and Paulsson, 1990; Zamora and Poirier, 1990; Byun and Corrigan, 1990; Carcione et al., 1991). Although in some cases even less degenerate symmetry classes, such as orthorhombic or monoclinic, may be appropriate (Winterstein and Meadows, 1990), there is a strong motivation to determine the simplest elastic symmetry system that can adequately explain observed phenomena.

It is also considered to be reasonable to assume that the orientation of the symmetry axis is known. For the various causal mechanisms for transverse isotropy in sedimentary rocks, discussed below, the direction of the symmetry axis with respect to geologic dip and/or the regional stress field is well defined (either parallel or perpendicular). Hence, the prior information necessary to define a background model

should also be sufficient to ascertain the anisotropic orientation. Attempting to solve for the direction of the symmetry axis in the inversion has been found to complicate the procedure significantly.

The second assumption stems from the dimensionally constrained nature of the observations. Inferences regarding a three-dimensional earth made using a two-dimensional experiment can be facilitated by making some assumption about how geologic parameters vary in the offline ( $y$ ) direction (Fig. 1.1). The simplest assumption is that parameters are constant. Because the model is then two-dimensional (only two coordinates are required to characterize a point) and wave propagation is inherently three-dimensional, this scenario has sometimes been referred to as *2½-dimensional* (see Bleistein, 1986).

The third assumption is justified when additional sources of information, such as well control, geologic models, tomographic and velocity inversion, etc., limit the range of acceptable parameter values. In an exploration setting, this is normally the case. Thus, the inversion algorithm seeks to resolve small-scale (relative to the dominant seismic wavelength) perturbations to elastic parameters about a smooth, prior background model, rather than the entire wavelength spectrum of the absolute medium parameters. This strategy is in accord with the widely held view that the spectral resolution of seismic data is limited to two bands, and that the inversion for the short-wavelength components is nearly linear (Jananne et al., 1989; Claerbout, 1985). This assumption also leads directly to the distorted-wave Born approximation (Newton, 1966), which accounts for single scattering of seismic waves from weak elastic perturbations. Because multiple scattering, surface waves, tube waves etc. are not accounted for, they must be removed from the data by preprocessing prior to the migration/inversion step. As with any

inversion scheme, coherent energy not accounted for by the forward model produces inversion artifacts.

## 1.2 Review of transverse isotropy

Transverse isotropy is one of eight anisotropic symmetry systems in seismology (Winterstein, 1990). The characteristic symmetry elements are a single, infinite-fold axis of symmetry oriented perpendicular to an infinite set of 2-fold axes of symmetry, where an  $n$ -fold symmetry axis is defined to be a direction about which a rotation of  $2\pi/n$  radians produces a solid that is indistinguishable from the material prior to rotation (Winterstein, 1990). Throughout this thesis, the term *symmetry axis* is used as a synonym for the infinite-fold axis of symmetry in a TI medium. Wavefront properties in a TI solid depend only on the angle between the direction of propagation and the symmetry axis. Because of its suitability for modeling layered or fractured media, TI symmetry has been studied extensively in the seismic literature (see Helbig, 1981; Crampin, 1986).

Three generally accepted (canonical) models for transverse isotropy in sedimentary rocks are considered here, and discussed in Crampin et al. (1984). *Intrinsic* anisotropy (Fig. 1.2a) is most commonly manifested in shales, and is attributed to parallel alignment of platy mineral grains during deposition. The anisotropic behaviour is, for the purposes of seismology, independent of wavelength. Hence this is the only form of transverse isotropy that can be studied directly using laboratory rock samples. *Periodic-thin-layering* (PTL) anisotropy (Fig. 1.2b) refers to a succession of thin layers (thickness  $\ll$  dominant wavelength) with alternating properties. In the asymptotic limit, this type of composite material can be replaced by an equivalent homogeneous, TI medium with its axis of symmetry perpendicular to bedding (Backus, 1962). Finally, an originally

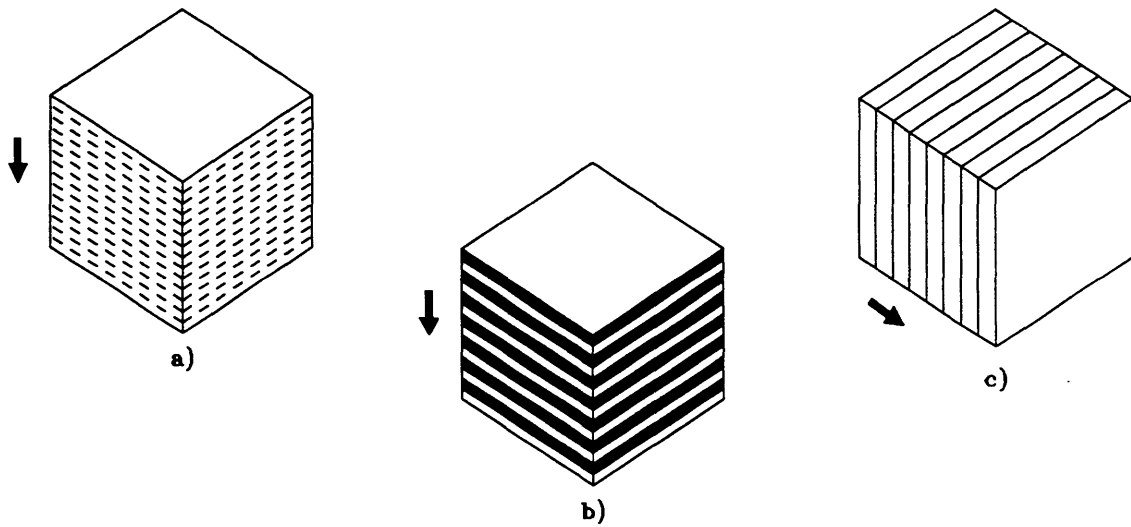


**Fig. 1.2.** Canonical models for transverse isotropy in sedimentary rocks. a) Intrinsic anisotropy; b) Periodic-thin layering; c) Fracturing (extensive-dilatancy anisotropy). Arrows show the direction of the infinite-fold axis of symmetry for each case.

---

isotropic solid containing parallel fractures also exhibits TI symmetry (Hudson, 1981; Crampin, 1981). *Extensive-dilatancy* anisotropy is a term sometimes used for anisotropy caused by stress-aligned, fluid-filled fractures (Crampin, 1987).

The stress-strain relationships for a TI solid can be described using a  $6 \times 6$  matrix of elastic stiffnesses (Musgrave, 1970). Referred to a co-ordinate system with the  $z$ -axis aligned with the symmetry axis, this matrix has the form:

$$\begin{bmatrix} C_{11} & C_{12} & C_{13} & 0 & 0 & 0 \\ C_{12} & C_{11} & C_{13} & 0 & 0 & 0 \\ C_{13} & C_{13} & C_{33} & 0 & 0 & 0 \\ 0 & 0 & 0 & C_{44} & 0 & 0 \\ 0 & 0 & 0 & 0 & C_{44} & 0 \\ 0 & 0 & 0 & 0 & 0 & C_{66} \end{bmatrix}, \quad (1.1)$$

where  $C_{12} = C_{11} - 2C_{66}$ . The most obvious (although not necessarily the best) parameterization for a TI medium makes use of the five independent stiffnesses and density, plus the orientation of the symmetry axis, if necessary. Equivalent parameterizations may suffice to characterize a medium, and it is often preferable to work with parameters that have a more intuitive foundation. The reference set of parameters in this study consists of  $P$ - and  $S$ -wave velocity in the direction of the symmetry axis, Thomsen's (1986) anisotropy parameters, and density. Defined in terms of the elastic stiffnesses, the first five parameters may be written (Thomsen, 1986):

$$\begin{aligned} \alpha &\equiv (C_{33}\rho^{-1})^{1/2}, \\ \beta &\equiv (C_{44}\rho^{-1})^{1/2}, \\ \gamma &\equiv \frac{C_{66} - C_{44}}{2C_{44}}, \\ \delta &\equiv \frac{(C_{13} + C_{44})^2 - (C_{33} - C_{44})^2}{2C_{33}(C_{33} - C_{44})}, \end{aligned} \quad (1.2)$$

and

$$\epsilon \equiv \frac{C_{11} - C_{33}}{2C_{33}} .$$

Note that for an isotropic medium, the parameters  $\alpha$  and  $\beta$  defined above are simply the  $P$ - and  $S$ -wave velocity, respectively; for an anisotropic medium,  $\alpha$  and  $\beta$  refer specifically to the compressional and shear-wave phase velocity in the direction of the symmetry axis. The dimensionless parameters  $\gamma$ ,  $\delta$  and  $\epsilon$  have also been defined in a physically meaningful way. In the limit of weak anisotropy,  $\epsilon$  and  $\gamma$  represent the factors normally associated with  $qP$ - and  $SH$ -wave anisotropy (i.e., the fractional difference between the fast and slow velocities). The remaining factor,  $\delta$ , governs the behaviour of  $qP$  and  $qSV$  wavefields for directions of propagation that are oblique with respect to the symmetry axis. The notation  $qP$  and  $qSV$  ( $q$  for quasi) is used here to emphasize the impure polarization of compressional and  $SV$  waves in a TI medium. However, the polarization of  $SH$  waves in a TI medium is identical to that in an isotropic medium (Thomsen, 1986). Therefore, the notation  $qSH$  is not used in this context.

The properties of the three canonical models are now considered in more detail in order to seek criteria that could be used to distinguish between them based on estimates of the seismic parameters, and to investigate the relationships between seismic and physical parameters. In addition, possible interdependence between parameters will be examined in an effort to further constrain seismic inversion results. The validity of the elliptical approximation (Helbig, 1983), in which  $qP$  wavefronts are assumed to be ellipsoids of revolution, will also be addressed for each of the three models.

### 1.2.1 Intrinsic anisotropy

To date, mathematical models to predict the intrinsic anisotropic properties of sedimentary rocks based on mineralogy, lithology or stratigraphic setting, etc., have not

been fully developed. Thus, empirical data provide the only available constraints. Several years ago, Thomsen (1986) compiled results of laboratory studies available at that time. In this study he showed that the condition for elliptical anisotropy is expressed by the equality  $\delta = \epsilon$ . Fig. 1.3a shows a graph of  $\delta$  vs.  $\epsilon$  from this data compilation (see also Fig. 4 in Thomsen, 1986), and clearly indicates that this condition is rarely met in nature, based on the data Thomsen collected.

Fig. 1.3b compares another pair of anisotropic parameters ( $\gamma$  vs.  $\epsilon$ ) using this dataset. A reasonably good linear relation between  $\gamma$  and  $\epsilon$  appears to exist, for both sandstone and shale lithologies. The equation of the best-fit line (by least-squares regression) is

$$\gamma = 1.5346\epsilon - 0.0277 \quad . \quad (1.3)$$

The implications of this relationship for seismic modeling and inversion are similar to Gardner's relation (Gardner et al., 1974) between  $P$ -wave velocity and density. When insufficient information is available to estimate one of  $\gamma$  or  $\epsilon$  directly, a reasonable value could be obtained using (1.3). It may also be advantageous to apply equation (1.3) as an additional constraint for seismic inversion, provided that the mechanism is known to be intrinsic anisotropy.

### 1.2.2 Periodic-thin layering

PTL anisotropy is a term that is applicable to stratified media with layers that are much thinner than the dominant seismic wavelength. Extensive theory concerning the nature of the equivalent homogeneous, TI medium has been developed for such a scenario (Postma, 1955; Krey and Helbig, 1956; Backus, 1962). Since this is a long-wavelength phenomenon, the effects of PTL anisotropy are primarily relevant here for the calculation of background Green's tensors.

Backus (1962) gave formulae for computing the effective elastic constants for a

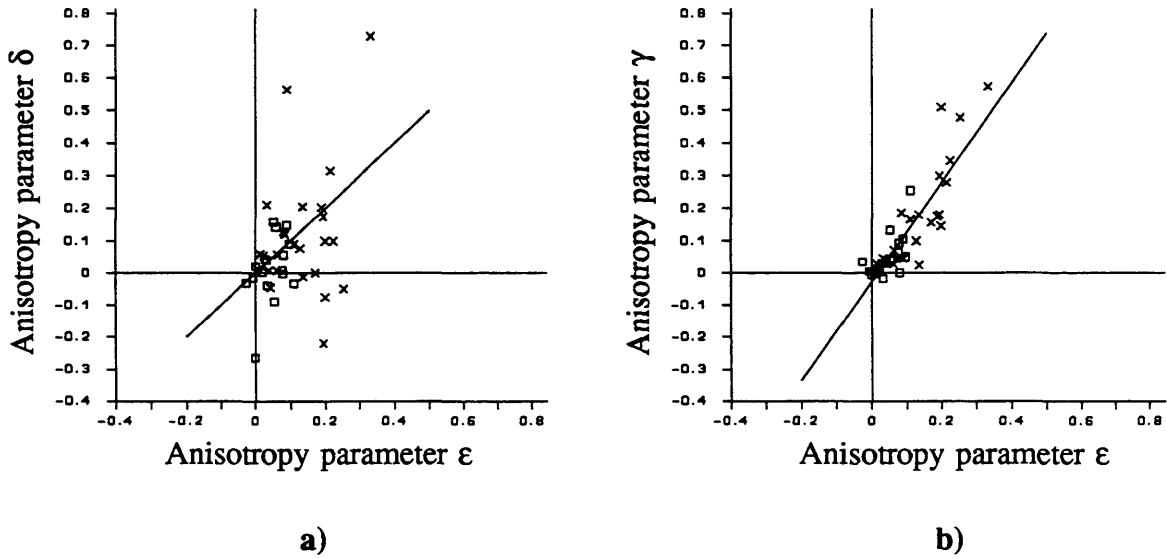


**Fig. 1.3.** a) Graph of  $\delta$  vs.  $\epsilon$  for intrinsic anisotropy in sedimentary rocks (modified from Thomsen, 1986). Squares represent sandstones and crosses indicate shales. The line represents the ellipticity condition ( $\delta = \epsilon$ ). b) Graph of  $\gamma$  vs.  $\epsilon$ , from the same set of data. Here, the line shows the  $l_2$  best-fit line through the data points, given by  $\gamma = 1.5346\epsilon - 0.0277$ .

TI-equivalent medium, where each of the thin layers in the stratified model is transversely isotropic or isotropic. In terms of stiffnesses, these formulae may be written

$$\begin{aligned}
 \bar{C}_{11} &= \langle C_{11}^{(i)} - (C_{13}^{(i)})^2 (C_{33}^{(i)})^{-1} \rangle + \langle (C_{33}^{(i)})^{-1} \rangle^{-1} \langle C_{13}^{(i)} (C_{33}^{(i)})^{-1} \rangle^2, \\
 \bar{C}_{33} &= \langle (C_{33}^{(i)})^{-1} \rangle^{-1}, \\
 \bar{C}_{13} &= \langle (C_{33}^{(i)})^{-1} \rangle^{-1} \langle C_{13}^{(i)} (C_{33}^{(i)})^{-1} \rangle^2, \\
 \bar{C}_{44} &= \langle (C_{44}^{(i)})^{-1} \rangle^{-1},
 \end{aligned} \tag{1.4}$$

and

$$\bar{C}_{66} = \langle C_{66}^{(i)} \rangle .$$

In these expressions, the overbar signifies the values that are associated with the equivalent medium, and  $C_{jk}^{(i)}$  is the  $jk$ th stiffness of the  $i$ th layer. The symbol  $\langle \rangle$  denotes a weighted averaging, so that, for a sequence of  $N$  layers,

$$\langle C_{66}^{(i)} \rangle = \frac{\sum_{i=1}^N h_i C_{66}^{(i)}}{\sum_{i=1}^N h_i} , \quad (1.5)$$

where  $h_i$  is the thickness of the  $i$ th layer. Levin (1979) specialized these formulae to the case where each layer is isotropic, and expressed them in terms of  $P$ - and  $S$ -wave velocities and density, rather than stiffnesses. Here these formulae are recast in terms of the three anisotropic parameters, giving

$$\bar{\gamma} = \frac{\langle \rho\beta^2 \rangle - \langle (\rho\beta^2)^{-1} \rangle^{-1}}{2\langle (\rho\beta^2)^{-1} \rangle^{-1}} , \quad (1.6)$$

$$\bar{\delta} = \frac{[\langle 1 - 2\frac{\beta^2}{\alpha^2} \rangle \langle (\rho\alpha^2)^{-1} \rangle^{-1} + \langle (\rho\beta^2)^{-1} \rangle^{-1}]^2 - [\langle (\rho\alpha^2)^{-1} \rangle^{-1} - \langle (\rho\beta^2)^{-1} \rangle^{-1}]^2}{2\langle (\rho\alpha^2)^{-1} \rangle^{-1} [\langle (\rho\alpha^2)^{-1} \rangle^{-1} - \langle (\rho\beta^2)^{-1} \rangle^{-1}]} ,$$

and

$$\bar{\epsilon} = \frac{[\langle 4\rho\beta^2(1 - \frac{\beta^2}{\alpha^2}) \rangle + \langle 1 - (2\frac{\beta^2}{\alpha^2}) \rangle^2] \langle (\rho\alpha^2)^{-1} \rangle^{-1}}{2\langle (\rho\alpha^2)^{-1} \rangle^{-1}} ,$$

for a sequence of isotropic layers with  $P$ - and  $S$ -wave interval velocities of  $\alpha$  and  $\beta$ , and density  $\rho$  (the  $(i)$  superscript has been dropped for clarity). Some order-of-magnitude insight can be gained by doing a sample calculation for these quantities using actual layer velocities. Sonic-log  $P$ -wave velocities (Fig. 1.4a) from a well in central Alberta (Mobil Cynthian 4-22-53-12W5) have been used for this purpose. The interval considered extends from 907 m to 1174 m depth, and represents the Upper Cretaceous Belly River Formation, a sequence of fine- to medium-grained sandstones interbedded with mudstones, siltstones and shales (Iwuagwu and Lerbekmo, 1982). Shear-wave velocities for this interval were computed using an estimated  $\alpha/\beta$  ratio of 1.93, based on correlation of nearby  $P$ - $P$  and  $P$ - $SV$  surface seismic data (Harrison, 1989). Under the further assumption that density is given by Gardner's relation (Gardner et al., 1974), the values calculated by applying equations (1.6) to the point-by-point parameters illustrated in Fig. 1.4 are:

$$\begin{aligned}\bar{\gamma} &= 0.025 \quad ; \\ \bar{\delta} &= -0.005 \quad ; \\ \bar{\epsilon} &= 0.015 \quad .\end{aligned}$$

Although the magnitudes of these anisotropic parameters are small, several important observations can be made. First, computational savings are possible for this medium, at least for kinematic modeling, when an equivalent homogeneous TI medium is used; instead of storing parameters for each individual layer, only 5 parameters are required to characterize the response of the entire sequence. Secondly, it is evident that elliptical anisotropy is not well suited for the medium considered here, since  $\delta \neq \epsilon$ . Moreover, it is straightforward to show that when PTL anisotropy is due to a sequence of thin

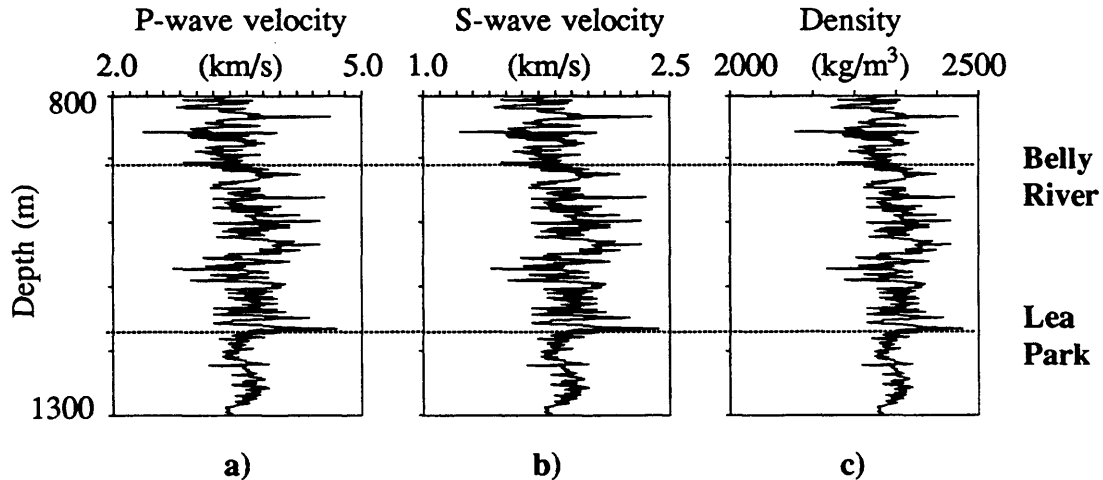


**Fig. 1.4.** a) *P*-wave velocities for Upper Cretaceous sediments, from sonic log at 4-22-53-12W5. Analysis zone is the Belly River Formation (907 m - 1174 m). b) *S*-wave velocities, derived from a) using  $\alpha/\beta = 1.93$ . c) Densities, derived from a) using Gardner's relation (Gardner et al., 1974).

isotropic layers, elliptical anisotropy can occur only for unrealistically large values of  $\alpha/\beta$ .

### 1.2.3 Fractured media

Anisotropy due to the presence of steeply dipping subsurface joints and microfractures is particularly relevant to both reservoir characterization and seismic monitoring of enhanced-oil-recovery operations. In some oil and gas fields, primary recovery is possible only because of the presence of fractures; elsewhere, the migration of injected fluids is controlled by fracturing (Babcock, 1978).

As in PTL anisotropy, the calculation of effective elastic constants for a cracked elastic solid involves averaging over a scale length that is large compared to the fracture dimensions. Formulae for effective elastic stiffnesses in a cracked solid have been derived by Garbin and Knopoff (1975) and Hudson (1981). An isotropic material

permeated with circular, infinitely thin, fluid-filled microfractures normal to the  $z$  axis will be considered here (steeply dipping fractures can be described by performing the appropriate rotation to the stiffness tensor). In this case, the only stiffness parameter that is affected by the fracturing is  $C_{44}$  (Hudson, 1981). Denoting the crack radius as  $a$  and the crack density as  $\nu$ , the perturbation is given to first order in  $(\nu a^3)$  by Hudson (1981) as

$$\Delta C_{44} = -\frac{32}{3}(\nu a^3)\mu \left( \frac{\lambda + 2\mu}{3\lambda + 4\mu} \right) , \quad (1.7)$$

where  $\lambda$  and  $\mu$  are the background Lamé parameters. Thus, from equations (1.2) and (1.7) and using the fact that velocities for the unfractured material are given by  $\rho\alpha^2 = \lambda + 2\mu$  and  $\rho\beta^2 = \mu$ , the effective anisotropy parameters are

$$\begin{aligned} \gamma &= \frac{\nu a^3 \zeta}{2(1 - \nu a^3 \zeta)} \approx \frac{\nu a^3 \zeta}{2} , \\ \delta &= -2 \frac{\beta^2}{\alpha^2} \frac{(\alpha^2 - \beta^2) \nu a^3 \zeta}{\alpha^2 - \beta^2 (1 - \nu a^3 \zeta)} \approx -2 \frac{\beta^2}{\alpha^2} \nu a^3 \zeta , \end{aligned} \quad (1.8)$$

and

$$\varepsilon = 0 ,$$

with

$$\zeta \equiv \frac{32}{3} \left( \frac{\alpha^2}{3\alpha^2 - 2\beta^2} \right) . \quad (1.9)$$

Note that in this case, the elliptical approximation is impossible, since  $\varepsilon = 0$  while  $\delta$  is strictly less than zero.

Again it is worthwhile to use actual numbers in these expressions to develop a

feel for their magnitude in sedimentary rocks. Babcock (1975) has presented measured parameters for fracturing in the McMurray Formation, located in northeastern Alberta. The mean length of fractures parallel to the outcrop face, taken here to be the diameter under the assumption of circular fractures, is given as 0.57 m. The mean spacing between fractures is 0.17 m. Assuming a spacing of 1 m between fractures in the strike direction leads to an estimate of  $5.9 \text{ m}^{-3}$  for the fracture density. This set of parameters gives  $\nu\alpha^3 \approx 0.109 \ll 1$ . Using  $\alpha = 3000 \text{ m/s}$  and  $\beta = 1500 \text{ m/s}$ , the values of  $\gamma$  and  $\delta$  from (1.7) are:

$$\begin{aligned}\gamma &= 0.43 \quad ; \\ \delta &= -0.20 \quad .\end{aligned}$$

These parameters imply a much greater degree of anisotropy for quasi-shear waves than  $qP$  waves. For example, the minimum  $qP$ -wave phase velocity occurs at a phase angle of  $45^\circ$  with respect to the fractures, and differs by 4.3% from the maximum, whereas the minimum  $SH$  phase velocity (perpendicular to fracturing) is 36% smaller than the maximum  $SH$  phase velocity (parallel to fracturing).

### 1.3 Summary

Based on a number of simplifying assumptions (e.g., two-dimensional medium, adequate suppression of coherent noise, etc.) and a suitable choice of reference medium, the goal of this study is to estimate the nature and distribution of localized elastic perturbations, relative to a smooth prior background model. The anisotropic symmetry system is assumed to be transverse isotropy, and for convenience, the anisotropic parameters  $\gamma$ ,  $\delta$  and  $\epsilon$  suggested by Thomsen (1986) have been adopted, rather than actual stiffness components. The use of different recording geometries, such as surface

and crosswell, is also considered.

Transverse isotropy in sedimentary rocks is classified according to a set of three canonical models. Long-wavelength averaging of medium properties plays a central role in two of these models (PTL anisotropy and fracturing). Each mechanism for anisotropy appears to be well separated from the others in parameter space. For example, PTL anisotropy resulting from a sequence of isotropic layers for which  $\alpha/\beta = 2.0$  leads to the condition  $\delta = 0$ , while fluid-filled fracturing, to first order in  $(\nu\alpha^3)$  leads to the condition  $\varepsilon = 0$ . There is ample evidence that the elliptical approximation is unsuitable for modeling any of the three forms of anisotropy considered here, and should not be used.

# Chapter 2

## Background Theory

### 2.1 Introduction

The intent of this chapter is to present a concise overview of the mathematical principles underlying the migration/inversion (M/I) method. These principles are derived from theoretical investigations of anisotropic-elastic wave propagation, the ray and Born approximations and generalized least-squares inversion. By grouping this material together and using a consistent set of notation, mathematical similarities between these different theories are emphasized, and the discussion in subsequent chapters is free to focus on more practical aspects of the procedure. Where possible, results are expressed in general anisotropic form, and later are specialized to conform with the particular assumptions used here (transversely isotropic and 2½-dimensional).

### 2.2 Elastic wave propagation in a homogeneous anisotropic medium

My starting point is the law of conservation of linear momentum, or Newton's second law, which may be written as

$$\sigma_{ij,j} - \rho \ddot{u}_i = f_i \quad . \quad (2.1)$$

In this equation,  $\sigma_{ij}(\mathbf{x})$  is the stress field,  $\rho(\mathbf{x})$  is density,  $\ddot{u}_i(\mathbf{x},t)$  is the second time derivative of the particle displacement vector,  $\mathbf{u}$ , and  $\mathbf{f}(\mathbf{x},t)$  is the body force per unit volume. For an elastic solid, stress is related to strain,  $\varepsilon_{ij}$ , by Hooke's law,

$$\sigma_{ij} = c_{ijkl} \epsilon_{kl} \quad , \quad (2.2)$$

where  $c_{ijkl}(\mathbf{x})$  is the stiffness tensor. Symmetry of  $\sigma_{ij}$  and  $\epsilon_{kl}$ , along with energy considerations, reduces the maximum number of independent components of the stiffness tensor from 81 to 21. For a TI solid, symmetry conditions further reduce this number to five, and for the isotropic case, only two elastic moduli are required. Because of this high degree of symmetry, an alternative matrix notation for the stiffness tensor is often used (see equation (1.1)). The relationship between matrix and tensor elements is summarized in Table 2.1. While the tensor notation is more compact for mathematical formulae, the matrix notation is also very useful.

Substituting (2.2) into (2.1) and using the definition for strain,  $\epsilon_{kl} = (u_{k,l} + u_{l,k})/2$ , leads to the elastic equations of motion,

$$(c_{ijkl} u_{k,l})_{,j} - \rho \ddot{u}_i = f_i \quad . \quad (2.3)$$

Many of the derivations that follow are simpler in the frequency domain. Fourier transforming (2.3) into the frequency domain gives

$$(c_{ijkl} \bar{u}_{k,l})_{,j} + \rho \omega^2 \bar{u}_i = \bar{f}_i \quad , \quad (2.4)$$

where

$$\bar{u}_i(\mathbf{x}, \omega) = \int_{-\infty}^{\infty} u_i(\mathbf{x}, t) e^{-i\omega t} dt \quad . \quad (2.5)$$

<i>ij</i> or <i>kl</i>	11	22	33	32 or 23	31 or 13	12 or 21
<i>I</i> or <i>J</i>	1	2	3	4	5	6

**Table 2.1.** Convention for indicial conversion between tensor notation,  $c_{ijkl}$ , and matrix notation,  $C_{IJ}$ , for elastic stiffnesses.

For notational convenience, the  $\sim$  superscript is omitted below, where the context is unambiguous. For a homogeneous medium, spatial derivatives of the stiffness tensor vanish, and the equations of motion become

$$c_{ijkl}u_{k,lj} + \rho\omega^2u_i = f_i \quad . \quad (2.6)$$

### 2.2.1 Plane-wave solutions: Slowness and wave surfaces

Valuable insight about the geometrical properties of elastic waves in anisotropic solids can be gained by studying a number of surfaces in slowness and velocity space. The definitions for these surfaces follow naturally from plane-wave solutions to equation (2.6). I therefore consider particle displacements of the form

$$u_k(\mathbf{x}, \omega) = Ag_k e^{i\omega(\mathbf{p}\cdot\mathbf{x})} \quad , \quad (2.7)$$

where  $A$  is a scalar amplitude and  $\mathbf{g}$  is a unit polarization vector. The slowness vector,  $\mathbf{p}$ , points in the direction of the wavefront normal,  $\mathbf{n}$ , and has a magnitude of  $1/v_p$ , where  $v_p$  is the phase velocity (the ratio of frequency to wavenumber,  $\omega/k$ ). Substituting (2.7) into the equations of motion, (2.6), leads to the set of equations

$$[c_{ijkl}p_j p_l - \rho\delta_{ik}]g_k = 0 \quad , \quad (2.8)$$

or, alternatively,

$$[c_{ijkl}n_j n_l - \rho v_p^2 \delta_{ik}]g_k = 0 \quad . \quad (2.9)$$

The latter are known as the Kelvin-Christoffel equations (Musgrave, 1970), and require, for a non-trivial solution, that

$$\det|c_{ijkl}n_j n_l - \rho v_p^2 \delta_{ik}| = 0 \quad . \quad (2.10)$$

The roles of  $\rho v_p^2$  and  $\mathbf{g}$  are evident from the form of the Kelvin-Christoffel

equation;  $(\rho v_p^2)$  are the eigenvalues of the matrix  $\Gamma_{ik} \equiv c_{ijkl}n_jn_l$ , and the  $\mathbf{g}$ 's are the corresponding eigenvectors (Crampin, 1981). Allowing  $\mathbf{n}$  to vary over the unit sphere and solving for phase velocity generates a sixth-order surface of 3 sheets, called the *normal* surface (Auld, 1973). Similarly, the function

$$S(\mathbf{p}) = \det|c_{ijkl}p_jp_l - \rho\delta_{ik}| = 0 \quad , \quad (2.11)$$

defines another surface of fundamental importance, known as the *slowness* surface (Synge, 1957). Intersections of different sheets of the slowness surface occur when two of the eigenvalues of  $\Gamma_{ik}$  are equal. These points on the slowness surface are called singularities (Duff, 1960). In general, the geometrical properties of the slowness surface, coupled with the distribution and nature of singularities, determines the behaviour of body waves in an anisotropic solid (Musgrave, 1970; Crampin, 1981).

It is not necessary to solve equation (2.10) to evaluate phase velocity in a TI medium. Explicit formulae for *qP*, *qSV* and *SH* waves in terms of the reference parameters used here are given by Thomsen (1986):

$$\begin{aligned} v_p^2(\theta) &= \alpha^2[1 + \epsilon \sin^2\theta + D(\theta)]; \quad (qP \text{ waves}) \\ v_p^2 &= \beta^2[1 + \frac{\alpha^2}{\beta^2}\epsilon \sin^2\theta - \frac{\alpha^2}{\beta^2}D(\theta)]; \quad (qSV \text{ waves}) \quad , \quad (2.12) \\ v_p^2 &= \beta^2[1 + 2\gamma \sin^2\theta], \quad (SH \text{ waves}) \end{aligned}$$

where  $\theta$  is phase angle with respect to the symmetry axis, and the term  $D$  is defined as

$$D \equiv \frac{1}{2} \left(1 - \frac{\beta^2}{\alpha^2}\right) \left\{ \left[ 1 + \frac{4\delta^*}{(1-\beta^2/\alpha^2)^2} \sin^2\theta \cos^2\theta + \frac{4(1-\beta^2/\alpha^2 + \epsilon)\epsilon}{(1-\beta^2/\alpha^2)^2} \sin^4\theta \right]^{1/2} - 1 \right\}, \quad (2.13)$$

and  $\delta^* \equiv (1 - \beta^2/\alpha^2)(2\delta - \epsilon)$ .

A quantity that has more direct physical significance than either phase velocity or slowness is the group velocity,

$$v_g = v \equiv \frac{\partial\omega}{\partial k}, \quad (2.14)$$

which determines the rate of energy transport. Unless noted otherwise, the symbol  $v$  is used below to denote group velocity rather than phase velocity. In an anisotropic medium, the group velocity defines another surface, called the *wave surface*, which represents the envelope at 1 s of plane waves that pass through the origin at time zero (Musgrave, 1970) (Fig. 2.1). In terms of the slowness surface,  $S(\mathbf{p})$ , the group velocity may be written (Synge, 1957),

$$v_i = \frac{\partial S / \partial p_i}{p_j (\partial S / \partial p_j)}. \quad (2.15)$$

However, a more convenient expression for computational purposes is given by Kendall and Thompson (1989),

$$v_i = \frac{c_{ijkl} p_l D_{jk}}{\rho D_{qq}}, \quad (2.16)$$

where  $D_{jk}$  is a cofactor of  $[c_{ijkl} p_i p_l / \rho - \delta_{jk}]$ .

The slowness and wave surfaces are linked by an important geometrical relationship, known as the principle of duality (Duff, 1960; Musgrave, 1970). For a given

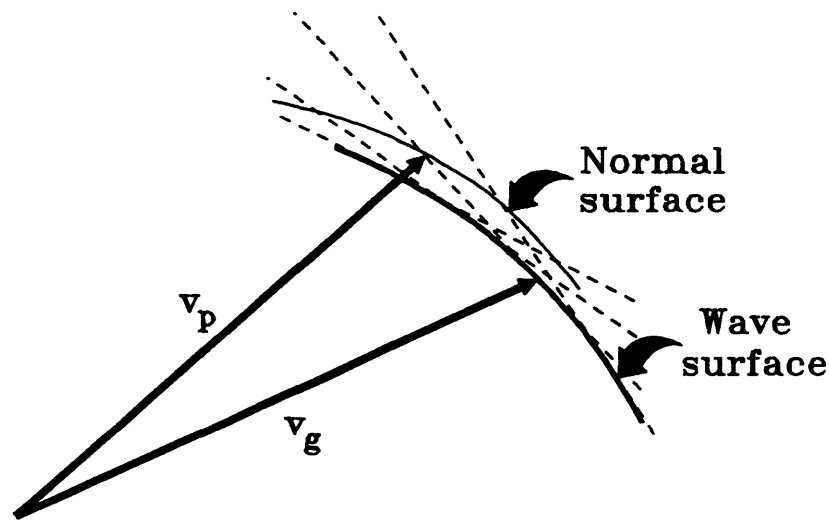


**Fig. 2.1.** Geometrical relationship between phase velocity,  $v_p$ , and group velocity,  $v_g$ . The wave surface is the envelope of plane waves associated with the normal surface, each passing through the origin at time zero (Musgrave, 1970).

---

slowness, the group velocity  $v(\mathbf{p})$  is normal to the slowness surface. Likewise, for a given direction of propagation, the slowness vector is normal to the wave surface. Based on this principle, it can be deduced that parabolic points (inflection points in two dimensions) on the slowness surface map to cusps on the wave surface. Furthermore, it can be shown that the maximum number of distinct body-wave arrivals from a point dislocation in an anisotropic solid is 75, compared to 2 for the isotropic case. Fortunately, the anisotropy associated with most TI sedimentary rocks is weak (Thomsen, 1986), and the total number of arrivals is likely to be much fewer than 75.

Many of the complexities associated with anisotropy are illustrated by the slowness and wave surfaces for the Greenhorn shale, an intrinsically anisotropic rock of

Cretaceous age located in the Williston basin. Parameters for this rock, based on ultrasonic measurements made at large confining pressure (Jones and Wang, 1981) are:

$$\begin{array}{lll} \alpha = 3377 \text{ m/s} & \beta = 1490 \text{ m/s} & \rho = 2420 \text{ kg/m}^3 \\ \gamma = 0.510 & \delta = -0.075 & \varepsilon = 0.2 \end{array}$$

The three anisotropy parameters for the Greenhorn shale are larger in magnitude than most other sedimentary rocks (Thomsen, 1986). Throughout the remainder of this thesis, this material is used as a reference medium for testing algorithms under conditions of extreme anisotropy.

Vertical cross-sections through the slowness and wave surfaces for the Greenhorn shale are shown in Figure 2.2. Because the  $qSV$  slowness sheet contains parabolic points (e.g.,  $A$  and  $B$  in Fig. 2.2), cusps and triplications are evident in the corresponding wave sheet. The  $SH$  wavefront has the simplest shape of the three, since  $SH$  wavefronts are always elliptical in a TI medium (Thomsen, 1986).

### 2.2.2 The approximate elastodynamic Green's tensor

The elastodynamic Green's tensor for a homogeneous, anisotropic medium satisfies the relation

$$c_{ijkl}G_{mk,lj} + \rho\omega^2G_{mi} = -\delta_{mi}\delta(\mathbf{x}-\mathbf{s}) \quad , \quad (2.17)$$

where  $G_{mk}(\mathbf{s},\mathbf{x},\omega)$  represents the  $k$ -component of particle displacement at  $\mathbf{x}$  due to a point force in the  $m$ -direction at  $\mathbf{s}$ , occurring at time zero. Buchwald (1959) and Ben-Menahem and Sena (1990) have derived an asymptotic expression for  $G_{mk}$  as the product  $(\omega r)$  tends to infinity:

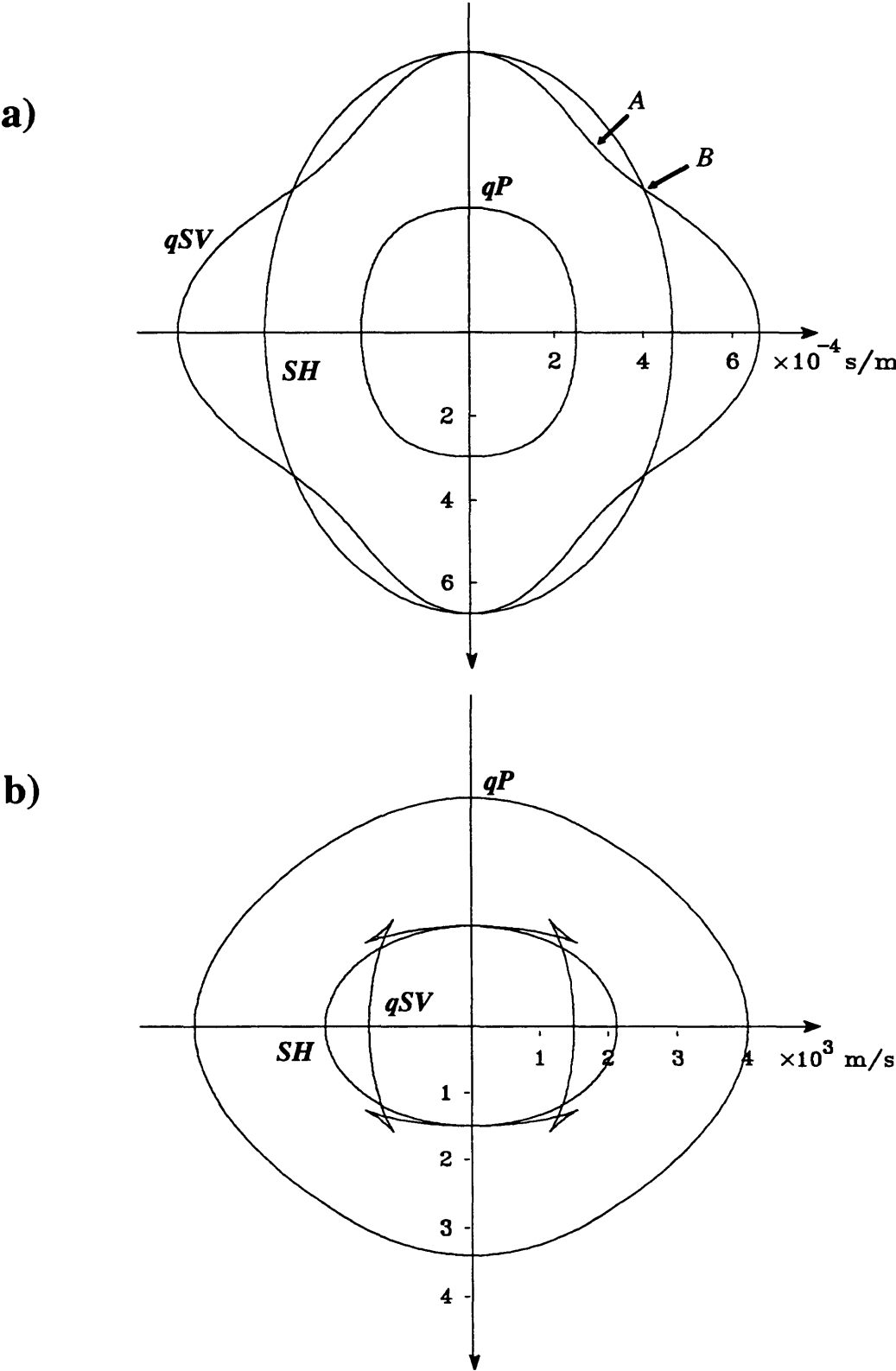


Fig. 2.2. Slowness surface (a) and wave surface (b) for the Greenhorn shale.

$$G_{mk}(\mathbf{x}, \mathbf{y}, \omega) = \sum_{i=1}^N \frac{g_m(\mathbf{p}) g_k(\mathbf{p}) e^{i\omega(\mathbf{p} \cdot \mathbf{r})}}{4\pi\rho v r K^{1/2}} \quad (K \neq 0) \quad (2.18)$$

In this expression,  $\mathbf{r} = (\mathbf{x} - \mathbf{y})$ ,  $r = |\mathbf{r}|$ ,  $\mathbf{g}(\mathbf{p})$  is a unit eigenvector of  $\Gamma_{ik}$  and the summation is over the set of all points  $\mathbf{p}$  on the slowness surface where the surface normal is parallel to  $\mathbf{r}$ .  $K(\mathbf{p})$  is the Gaussian curvature of the slowness surface, defined to be the reciprocal of the product of the principle radii of curvature at any point on the surface (Graustein, 1962). Buchwald (1959) gives the formula

$$K = \frac{\sum_{ijk} [S_k^2 (S_{ii} S_{jj} - S_{ij}^2) + 2S_i S_j (S_{ik} S_{jk} - S_{ij} S_{kk})]}{(S_1^2 + S_2^2 + S_3^2)^2}, \quad (2.19)$$

where  $S_j = \partial S / \partial p_j$  and the summation is cyclical with respect to  $i$ ,  $j$  and  $k$ .  $K$  has dimensions of velocity squared, and in the isotropic limit  $K \rightarrow v^2$ . Thus, for the isotropic case equation (2.18) reduces to the well known far-field isotropic Green's tensor (Aki and Richards, 1980), which may be written

$$G_{mk}(\mathbf{x}, \mathbf{y}, \omega) = \sum_{\Omega=1}^3 \frac{g_m(\mathbf{p}) g_k(\mathbf{p}) e^{i\omega r/v}}{4\pi\rho v^2 r}, \quad (2.20)$$

where the index  $\Omega$  signifies the three wave types ( $P$ ,  $SV$  and  $SH$ ), and the dependence on  $\Omega$  for  $\mathbf{g}$  and  $v$  is understood.

The asymptotic expression for  $G_{mk}$  in equation (2.18) is valid for  $K > 0$  and  $K < 0$ . Points on the slowness surface that satisfy the first condition are said to be elliptical, and represent the normal case of a convex surface. Points on the slowness surface where  $K < 0$  are called hyperbolic (e.g., between  $A$  and  $B$  in Fig. 2.2a). This occurs where the two principle radii of curvature point in opposing directions. The waveform on the

corresponding portions of the wavefront is the Hilbert transform of the source waveform (Singh and Chapman, 1988). For both the elliptical and hyperbolic cases, amplitude decay is proportional to  $r^{-1}$ .

Two well known geometrical conditions cause the approximation in (2.18) to fail, and are mentioned here briefly, for completeness. The first exception occurs when the Gaussian curvature vanishes, at *parabolic* points on the slowness surface. The corresponding points on the wave surface form cuspidal edges. The second condition occurs when the set of points for the summation in (2.18) is infinite, i.e. a plane is tangent to the slowness surface along a closed curve. The corresponding single point on the wave surface is called a conical point. This is known to occur for some minerals with hexagonal symmetry, such as apatite and zinc (Musgrave, 1970), but has not been reported for sedimentary rocks. Buchwald (1959) showed that the rate of amplitude decay on the wavefront at cuspidal edges and conical points is  $r^{-5/6}$  and  $r^{-1/2}$ , respectively.

In order to visualize the dependence of amplitude on direction, it is convenient to define an amplitude surface, given by

$$A(l) = [4\pi\rho v^2(l)K(l)^{1/2}]^{-1} \quad , \quad (2.21)$$

representing the amplitude function (with dimensions of  $\text{mN}^{-1}$ ) on the wavefront at a time of 1 s, where  $(l_1, l_2, l_3)$  are the direction cosines of  $\mathbf{v}_g$ . Figure 2.3 shows this surface for the Greenhorn shale, after normalization such that  $A = 1$  on the  $qP$  wavefront travelling in the direction  $(0, 0, 1)$ . For the isotropic case, this surface would be composed of two spherical sheets, with a ratio between the  $S$  amplitude and  $P$  amplitude equal to  $(\alpha/\beta)^3$ . In this case, the  $SH$  amplitude sheet is approximately spherical, but the  $qP$  and  $qSV$

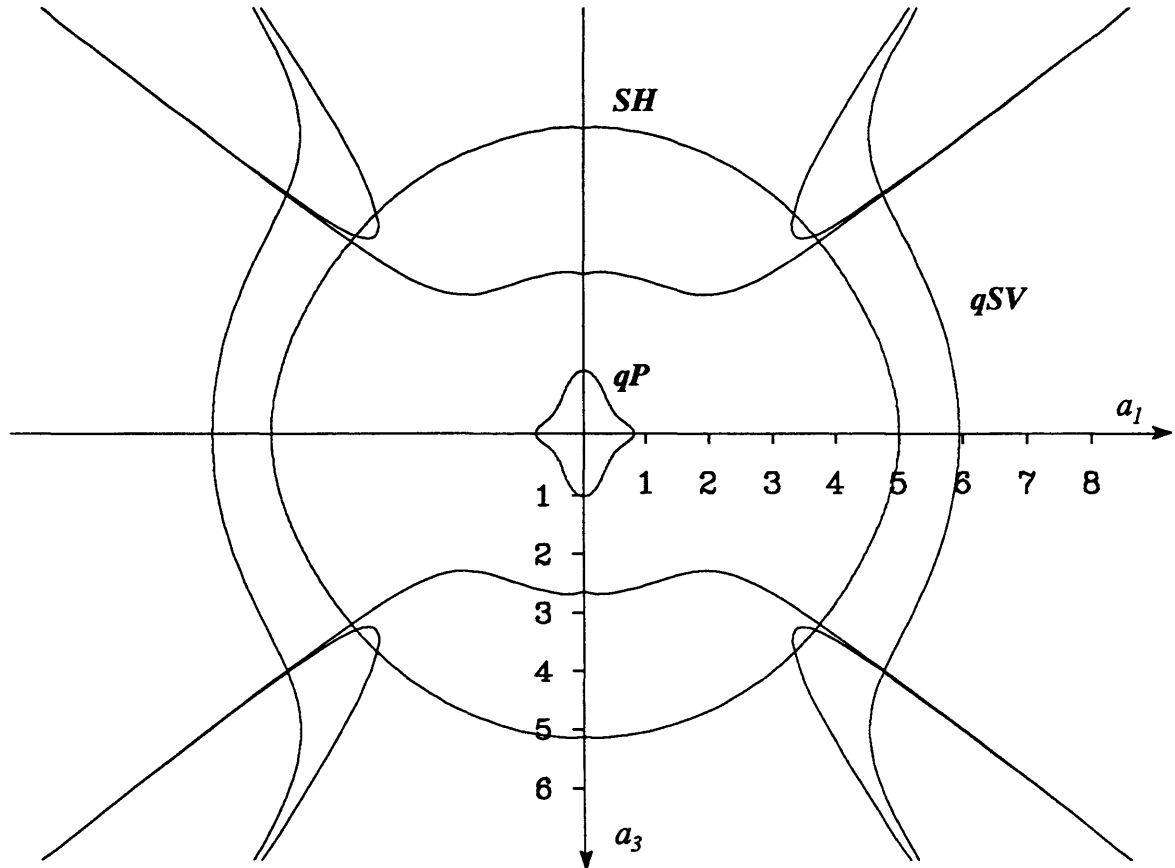


Fig. 2.3. Normalized amplitude surface for the Greenhorn shale.

amplitude sheets indicate a significant directional dependence. In particular, the failure of equation (2.18) at the cusps on the wavefront is obvious. This shortcoming is analogous to amplitude singularities along caustics in isotropic ray theory (Červený et al., 1977).

### 2.3 Ray method

I will now consider the more realistic case of a medium that is not homogeneous. The ray method seeks to find an approximate solution to the equations of motion (2.3),

subject to certain validity conditions: medium parameters must vary slowly compared to the dominant seismic wavelength, and the radius of curvature of interfaces must also be large (Ben-Menahem and Beydoun, 1985). This technique is an extension of the WKBJ method for ordinary differential equations (Bleistein, 1984), and is used in this thesis for the computation of approximate background Green's functions. The derivation of the basic ray equations is reviewed briefly below.

The application of the ray method to anisotropic media was first described (outside the Soviet Union) by Červený (1972). A trial solution in the form of an asymptotic ray series is assumed:

$$u_k(\mathbf{x}, t) = \sum_{n=0}^{\infty} U_k^{(n)} f_n(t - \tau(\mathbf{x})) \quad , \quad (2.22)$$

where the functions  $f_n(\psi)$  are chosen so that

$$\partial f_{n+1}(\psi) / \partial \psi = f_n(\psi) \quad . \quad (2.23)$$

The function  $\tau(\mathbf{x})$  is the travelt ime function, or the time for a given type of wave to pass from source to receiver. Equation (2.23) implies that the order of the discontinuity on a wavefront ( $t = \tau$ ) of each succeeding  $f_n$  is less than the preceding one.

Substituting (2.22) into (2.3) leads to a recurrent series of equations of the form

$$\mathbf{N}(\mathbf{U}^{(n)}) - \mathbf{M}(\mathbf{U}^{(n-1)}) + \mathbf{L}(\mathbf{U}^{(n-2)}) = 0 \quad n = 0, 1, 2, \dots \quad (2.24)$$

with  $\mathbf{U}^{(-1)} = \mathbf{U}^{(-2)} = 0$  (Červený, 1972; Červený et al., 1977). The vector operators  $\mathbf{N}$ ,  $\mathbf{M}$  and  $\mathbf{L}$  are given by

$$\begin{aligned}
N_i(\mathbf{U}^{(n)}) &= \rho^{-1} c_{ijkl} p_j p_l U_k^{(n)} - U_i^{(n)} \quad , \\
M_i(\mathbf{U}^{(n)}) &= \rho^{-1} c_{ijkl} p_j U_{k,l}^{(n)} + (c_{ijkl} p_l U_k^{(n)})_{,j} \quad , \\
L_i(\mathbf{U}^{(n)}) &= \rho^{-1} (c_{ijkl} U_{k,l}^{(n)})_{,j} \quad .
\end{aligned} \tag{2.25}$$

Setting  $n = 0$  in (2.25) gives the first equation in the series,

$$[c_{ijkl} p_j p_l - \rho \delta_{ik}] U_k^{(0)} = 0 \quad , \tag{2.26}$$

which is equivalent to equation (2.8). For a nontrivial solution to equation (2.26),

$$\det |c_{ijkl} p_j p_l - \rho \delta_{ik}| = 0 \quad . \tag{2.27}$$

Since  $p_j = \partial\tau/\partial x_j$ , equation (2.27) can be considered as a nonlinear partial-differential equation governing the traveltime function,  $\tau$ . It is sometimes referred to by the geometrical optics term, *eikonal* equation, stemming from the Greek word *eikon* for image.

Červený (1972) showed that the higher-order principle-component amplitude terms satisfy:

$$2A_{,i}^{(n)} v_i + \rho^{-1} A^{(n)} (\rho v_{i,i}) = (\mathbf{L}(\mathbf{U}^{(n-1)}) - \mathbf{M}(\mathbf{W}^{(n)})) \cdot \mathbf{g} \quad , \tag{2.28}$$

where  $\mathbf{g}$  is an eigenvector of  $\Gamma_{ik}$  and

$$A^{(n)} \equiv \mathbf{U}^{(n)} \cdot \mathbf{g} \quad . \tag{2.29}$$

In seismology, it is customary to consider only the leading-order term in the ray expansion (Červený et al., 1977). Noting that for  $n = 0$  the right side in (2.28) vanishes, the (first) transport equation may be written

$$2A_{,i}^0 v_i + \rho^{-1} A^0 (\rho v_i)_{,i} = 0 \quad . \quad (2.30)$$

Insight regarding the nature of functions that satisfy equation (2.30) is provided by the concept of an *elementary ray tube*. In three dimensions, a ray tube is bounded by three rays (Fig. 2.4) with initial parameters  $(\gamma_1, \gamma_2)$ ,  $(\gamma_1 + \delta\gamma_2)$  and  $(\gamma_1, \gamma_2 + \delta\gamma_2)$ , where  $\gamma_1$  and  $\gamma_2$  are any two parameters that uniquely specify the direction of the ray at the source position. In the zeroth-order approximation, the energy flux through the walls of the ray tube is zero (Červený, 1972; Červený et al., 1977; Bleistein, 1984). Conservation of energy then requires that the ratio between the amplitude terms  $A_1$  and  $A_2$  at traveltimes  $\tau_1$  and  $\tau_2$  be given by

$$\frac{A_2}{A_1} = \left[ \frac{\rho_1 v_p^{(1)} \delta S_1}{\rho_2 v_p^{(2)} \delta S_2} \right]^{1/2} \quad (2.31)$$

where  $\delta S$  is the area of intersection of the ray tube with the wavefront, and  $v_p^{(j)}$  is the local phase velocity at time  $\tau_j$  (Fig. 2.4). In the ray-theoretical literature, this relation is often expressed using the ray Jacobian,  $J$ , rather than the area,  $\delta S$ .  $J$  is defined by the vector cross product:

$$J = \left| \frac{\partial \mathbf{x}}{\partial \gamma_1} \times \frac{\partial \mathbf{x}}{\partial \gamma_2} \right| \quad , \quad (2.32)$$

where the derivatives are evaluated at constant  $\tau$ .

Combining the first term in equation (2.22) with the solutions of the eikonal and transport equations, (2.27) and (2.30), the zeroth-order ray solution to equation (2.17) is given by the superposition of terms of the form

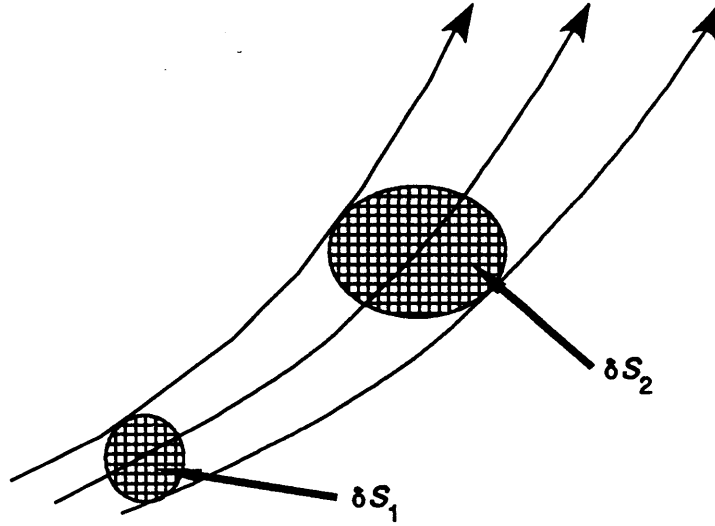


**Fig. 2.4.** Elementary ray tube bounded by three rays with initial parameters  $(\gamma_1, \gamma_2)$ ,  $(\gamma_1 + \delta\gamma_1, \gamma_2)$  and  $(\gamma_1, \gamma_2 + \delta\gamma_2)$ . In the zeroth-order ray approximation, energy flux through the walls of the ray tube is zero.

---


$$A^0 \mathbf{g} f_0(t - \tau) \quad . \quad (2.33)$$

Commonly, the frequency-domain ansatz  $f_n = e^{i\omega\tau}(i\omega)^{-n}$  is used, in which case each term in the zeroth-order solution has the form

$$A^0 \mathbf{g} e^{i\omega\tau} \quad . \quad (2.34)$$

## 2.4 The ray-Born approximation

The ray method is suitable for modeling high-frequency body-wave arrivals in a slowly varying medium; however, it does not account for diffractions and elastic scattering from localized heterogeneities. For this purpose, it is useful to combine the ray method with the Born approximation.

Following Beylkin and Burridge (1990), the first step in the derivation of the ray-Born approximation is to write the stiffnesses, density and Green's function as the sum of two parts,

$$\begin{aligned} c_{ijkl} &= c_{ijkl}^0 + \Delta c_{ijkl} \quad , \\ \rho &= \rho^0 + \Delta\rho \quad , \end{aligned} \quad (2.35)$$

and

$$G_{mk} = G_{mk}^0 + U_{mk} \quad , \quad (2.36)$$

such that  $G_{mk}^0(\mathbf{s}, \mathbf{x}, \omega)$  satisfies the background equations

$$(c_{ijkl}^0 G_{mk,l}^0)_{,j} + \rho^0 \omega^2 G_{mi}^0 = -\delta_{mi} \delta(\mathbf{x} - \mathbf{s}) \quad . \quad (2.37)$$

$U_{mk}$ , the difference between the exact Green's function and the reference Green's function, is often referred to as the *scattered wavefield*. Substituting (2.32) and (2.33) into the equations of motion (2.17) and making the assumption that, to a first approximation,  $G_{mk}(\mathbf{s}, \mathbf{x}, \omega) \approx G_{mk}^0(\mathbf{s}, \mathbf{x}, \omega)$ , the scattered wavefield may be written:

$$\begin{aligned} U_{mn}(\mathbf{s}, \mathbf{r}, \omega) \approx \int_D [\Delta\rho \omega^2 \tilde{G}_{mi}^0(\mathbf{s}, \mathbf{x}, \omega) \hat{G}_{ni}^0(\mathbf{x}, \mathbf{r}, \omega) + \\ \Delta c_{ijkl} \tilde{G}_{mk,l}^0(\mathbf{s}, \mathbf{x}, \omega) \hat{G}_{ni,j}^0(\mathbf{x}, \mathbf{r}, \omega)] dx \quad . \end{aligned} \quad (2.38)$$

where  $\Delta\rho = \Delta c_{ijkl} = 0$  outside of the domain  $D$ . The tilde ( $\sim$ ) and caret ( $\hat{\phantom{x}}$ ) superscripts are used to distinguish quantities associated with the incident and scattered background Green's tensors. Equation (2.38) is the Born, or single-scattering, approximation for a general elastic medium, and is valid for  $|\Delta c_{ijkl}/c_{ijkl}| \ll 1$  and  $|\Delta\rho/\rho| \ll 1$  (i.e., small perturbations). Physically, elastic waves propagate through the background (unperturbed) medium, and diffract independently from each point in  $D$ ;  $U_{mn}$  is the superposition of

all such scattered arrivals. The interaction of the wavefield with each point in  $D$  is equivalent to the *Rayleigh* mode of scattering, where elastic waves are diffracted from a spherical heterogeneity whose radius is much smaller than the dominant seismic wavelength, and whose properties differ only slightly from the background material (Newton, 1966; Wu and Aki, 1985).

Next, I consider the approximate Green's tensors given in equations (2.18) and (2.34). For each wave type (or ray code),  $\Omega$ , one can associate a term of the form

$$G_{mk}^{\Omega}(\mathbf{s}, \mathbf{x}, \omega) \approx A g_m(\mathbf{s}) g_k(\mathbf{x}) e^{i\omega\tau} \quad . \quad (2.39)$$

The leading singular terms of the spatial derivatives of the Green's tensor may be written

$$G_{mk,l}^{\Omega} \approx i\omega\tau_{,l} A(\mathbf{s}, \mathbf{x}) g_m(\mathbf{s}) g_k(\mathbf{x}) e^{i\omega\tau} \quad . \quad (2.40)$$

Combining (2.38), (2.39) and (2.40), the ray-Born representation for the scattered wavefield is obtained (Beylkin and Burridge, 1990):

$$U_{mn}^{\Omega}(\mathbf{s}, \mathbf{r}, \omega) \approx \omega^2 g_m(\mathbf{s}) g_n(\mathbf{r}) \int_D [\Delta\rho\delta_{ik} + \Delta c_{ijkl} \bar{p}_l \hat{p}_j] A \bar{g}_k \hat{g}_i e^{i\omega\tau} dx \quad , \quad (2.41)$$

where

$$A = \bar{A} \hat{A} \quad ,$$

and

$$(2.42)$$

$$\tau = \bar{\tau} + \hat{\tau} \quad .$$

The term  $[\Delta\rho\delta_{ik} + \Delta c_{ijkl} \bar{p}_l \hat{p}_j] \bar{g}_k \hat{g}_i$  represents the elastic scattering radiation patterns, and can be simplified for the case of a TI medium. In Appendix A, it is shown that this term may be written as  $\mathbf{s} \Delta \mathbf{m}^0$ , where  $\Delta \mathbf{m}^0 = \Delta(C_{11}, C_{33}, C_{13}, C_{44}, C_{66}, \rho)^T$  is the model-parameter vector in terms of stiffnesses. The scattering vector,  $\mathbf{s}$ , may be written

$$\mathbf{s} = ( \hat{p}_1 \bar{p}_1 \hat{g}_1 \bar{g}_1, \hat{p}_3 \bar{p}_3 \hat{g}_3 \bar{g}_3, \hat{p}_1 \bar{p}_3 \hat{g}_1 \bar{g}_3 + \hat{p}_3 \bar{p}_1 \hat{g}_3 \bar{g}_1, \hat{p}_1 \bar{p}_1 \hat{g}_3 \bar{g}_3 + \hat{p}_3 \bar{p}_3 \hat{g}_1 \bar{g}_1 + \hat{p}_1 \bar{p}_3 \hat{g}_3 \bar{g}_1 + \hat{p}_3 \bar{p}_1 \hat{g}_1 \bar{g}_3, 0, -\hat{g}_q \bar{g}_q )^T, \quad (2.43)$$

for  $qP$  and  $qSV$  waves, and

$$\mathbf{s} = (0, 0, 0, \hat{p}_3 \bar{p}_3, \hat{p}_1 \bar{p}_1, -1)^T, \quad (2.44)$$

for  $SH$  waves. These formulae apply also to the isotropic case, but can be simplified since  $\mathbf{g}$  is always either parallel or perpendicular to  $\mathbf{p}$  (see Beylkin and Burridge, 1990).

For a different parameterization, one can write the scattering term as  $\mathbf{sL}\Delta\mathbf{m}$ , where  $\Delta\mathbf{m}$  is the new model parameter vector and  $L_{ij} \equiv [\partial m_i^0 / \partial m_j]$ . For the reference parameterization of this study, the matrix  $\mathbf{L}$  may be written

$$\mathbf{L} = \begin{bmatrix} 2\rho\alpha(2\varepsilon+1) & 0 & 0 & 0 & 2\rho\alpha^2 & \alpha^2(2\varepsilon+1) \\ 2\rho\alpha & 0 & 0 & 0 & 0 & \alpha^2 \\ \zeta_1 & \zeta_2 & 0 & \xi 2\rho^2\alpha^2(\alpha^2-\beta^2) & 0 & \zeta_3 \\ 0 & 2\rho\beta & 0 & 0 & 0 & \beta^2 \\ 0 & 2\rho\beta(2\gamma+1) & 2\rho\beta^2 & 0 & 0 & \beta^2(2\gamma+1) \\ 0 & 0 & 0 & 0 & 0 & 1 \end{bmatrix} \quad (2.45)$$

where:

$$\begin{aligned} \zeta_1 &= \xi(8\rho^2\alpha^3\delta - 4\rho^2\beta^2\alpha\delta + 4\rho^2\alpha(\alpha^2 - \beta^2)) ; \\ \zeta_2 &= -\xi(4\rho^2\alpha^2\beta\delta + 4\rho^2\beta(\alpha^2 - \beta^2)) ; \\ \zeta_3 &= \xi[4\rho\alpha^2\delta(\alpha^2 - \beta^2) + 2\rho(\alpha^2 - \beta^2)] - \beta^2 ; \\ \xi &= [2\rho^2\alpha^2(\alpha^2 - \beta^2)\delta + \rho^2(\alpha^2 - \beta^2)^2]^{1/2} . \end{aligned} \quad (2.46)$$

The parameters in (2.45) and (2.46) refer to the background medium; hence, for an isotropic background,  $\gamma$ ,  $\delta$  and  $\varepsilon$  are all zero.

Elastic scattering radiation patterns for a homogeneous, isotropic reference medium have been computed using equations (2.43) - (2.46), and are shown in Figs. 2.5 to 2.8. The plots are organized so that for each parameter there are nine scattering patterns, corresponding to incident and scattered wave types given in Table 2.2. The same format was used by Tarantola (1986). The incident wavefield propagates in the positive  $x_3$ -direction (downwards), and the amplitude of the scattered wavefield is plotted using polar coordinates in the  $x_1$ - $x_2$  plane. The direction of first particle displacement for the scattered waves is indicated by arrows. Each parameter has a unique scattering pattern; it is the differences between these patterns that enables the inversion algorithm to distinguish between different types of scatterers (Tarantola, 1986).

Figure 2.5 shows scattering from isotropic perturbations,  $\Delta\alpha$ ,  $\Delta\beta$  and  $\Delta\rho$ . These plots are essentially the same as Fig. 4 of Tarantola (1986). Parameter perturbations do not affect all wave types. For example, changes to the  $P$ -wave velocity have no effect

$P-P$ ↓	→ $SV-P$	$SH-P$ ⊙
$P-SV$ ↓	→ $SV-SV$	$SH-SV$ ⊙
$P-SH$ ↓	→ $SV-SH$	$SH-SH$ ⊙

**Table 2.2.** Wave types corresponding to the diffraction patterns shown in Figs. 2.5 to 2.8. The incident wave propagates vertically downwards; arrows indicate the corresponding sense of the first particle motion. The first and last wave types in each pair denote the incident and scattered wave types, respectively.

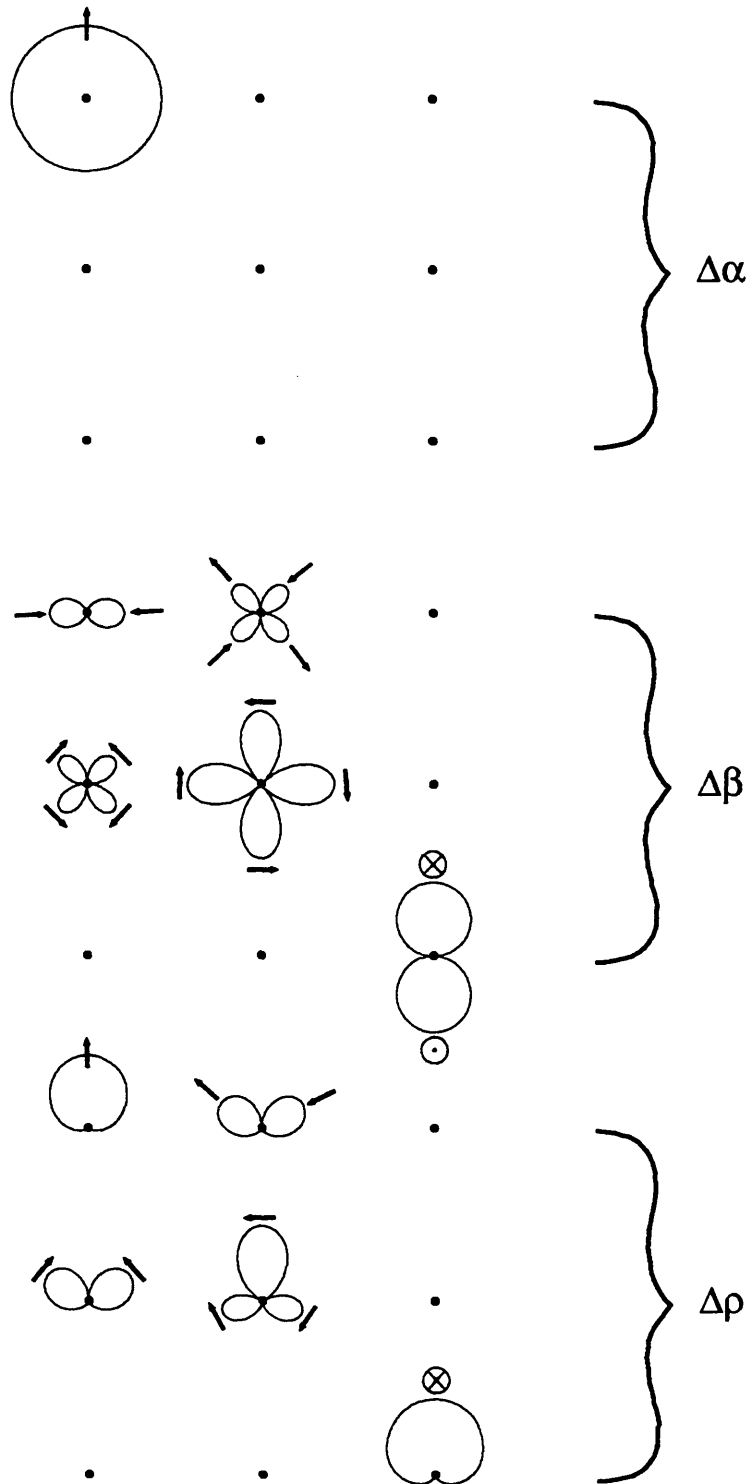


**Fig. 2.5.** Rayleigh scattering patterns in the  $x_1$ - $x_3$  plane for perturbations to isotropic parameters. Incident and scattered wave types are discussed in Table 2.2. Arrows indicate sense of first motion for the scattered wave.

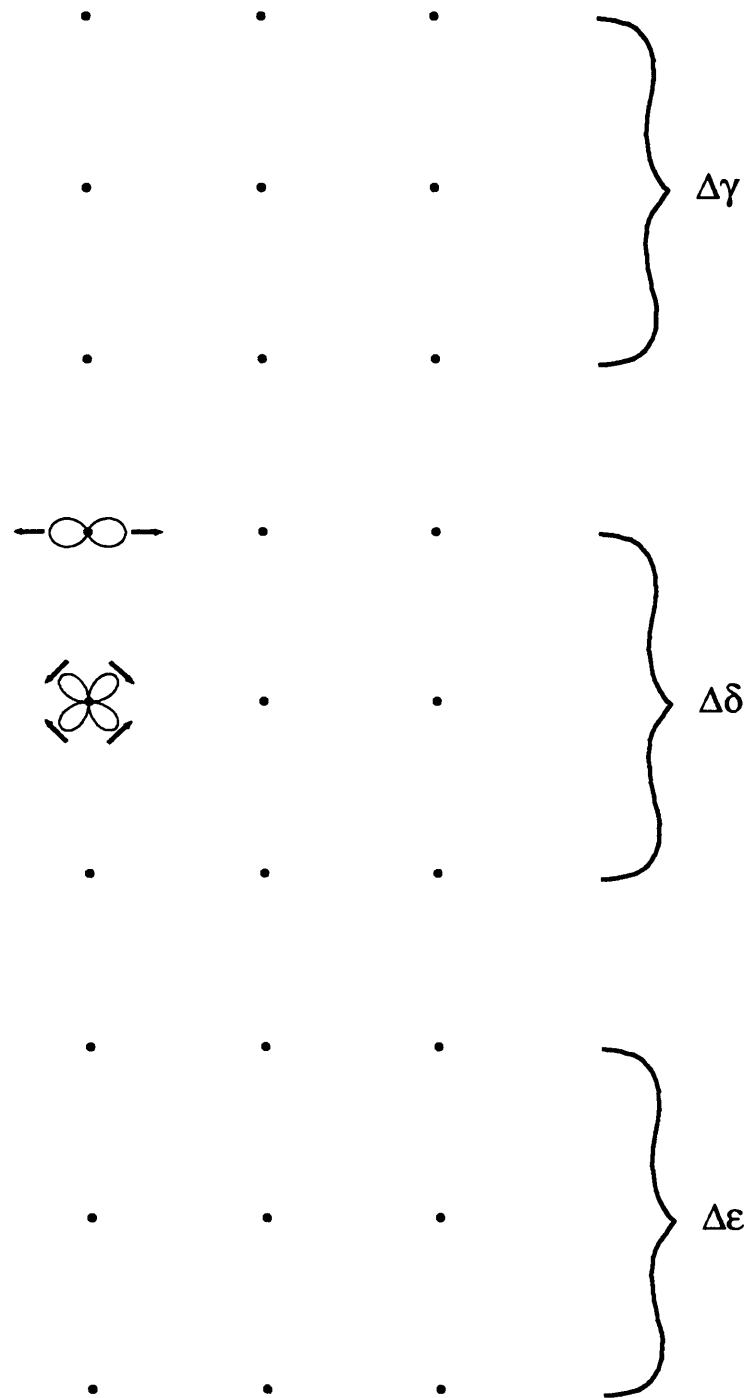


**Fig. 2.6.** Rayleigh scattering patterns in the  $x_1$ - $x_3$  plane for perturbations to anisotropic parameters, with a vertical symmetry axis. Wave types follow the same scheme as in Fig. 2.5 and arrows show sense of first motion for the scattered wave.

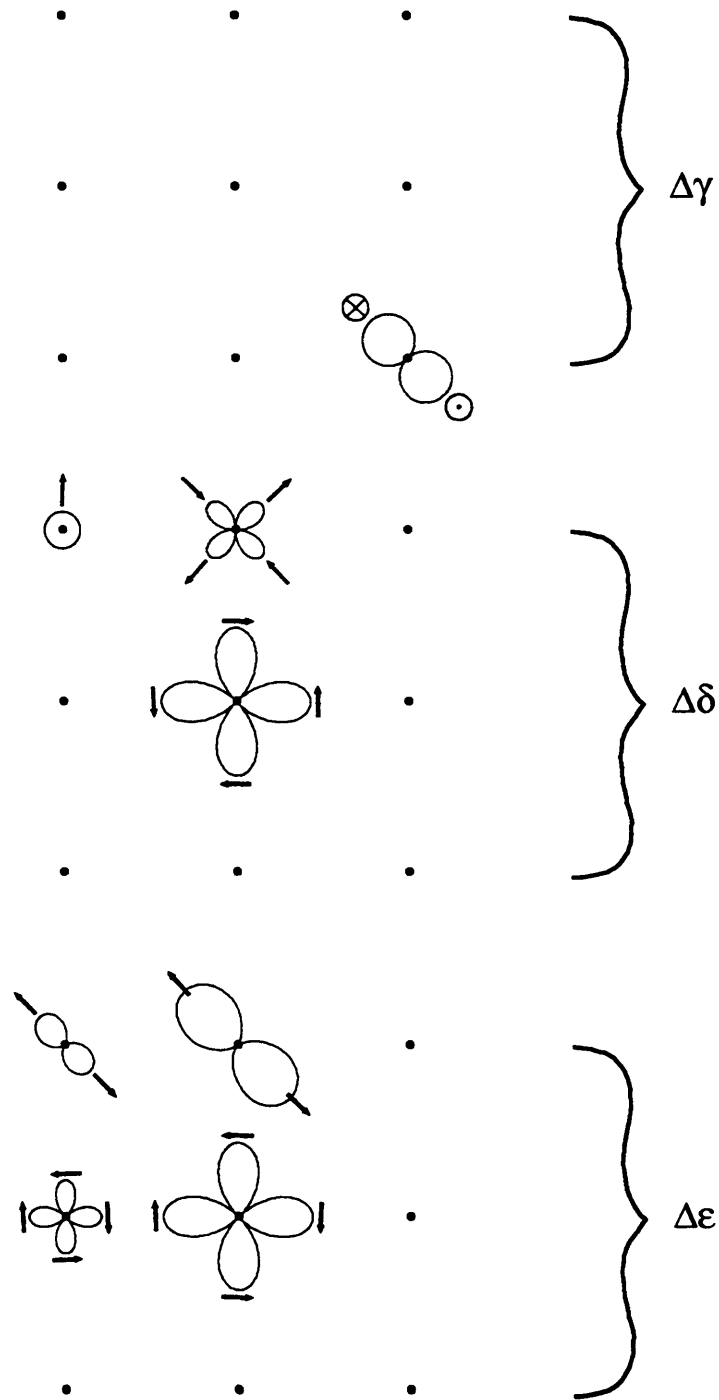


**Fig. 2.7.** Rayleigh scattering patterns in the  $x_1$ - $x_3$  plane for perturbations to anisotropic parameters, with a symmetry axis inclined at  $45^\circ$ . Wave types follow the same scheme as in Fig. 2.5, and arrows show sense of first motion for the scattered wave.

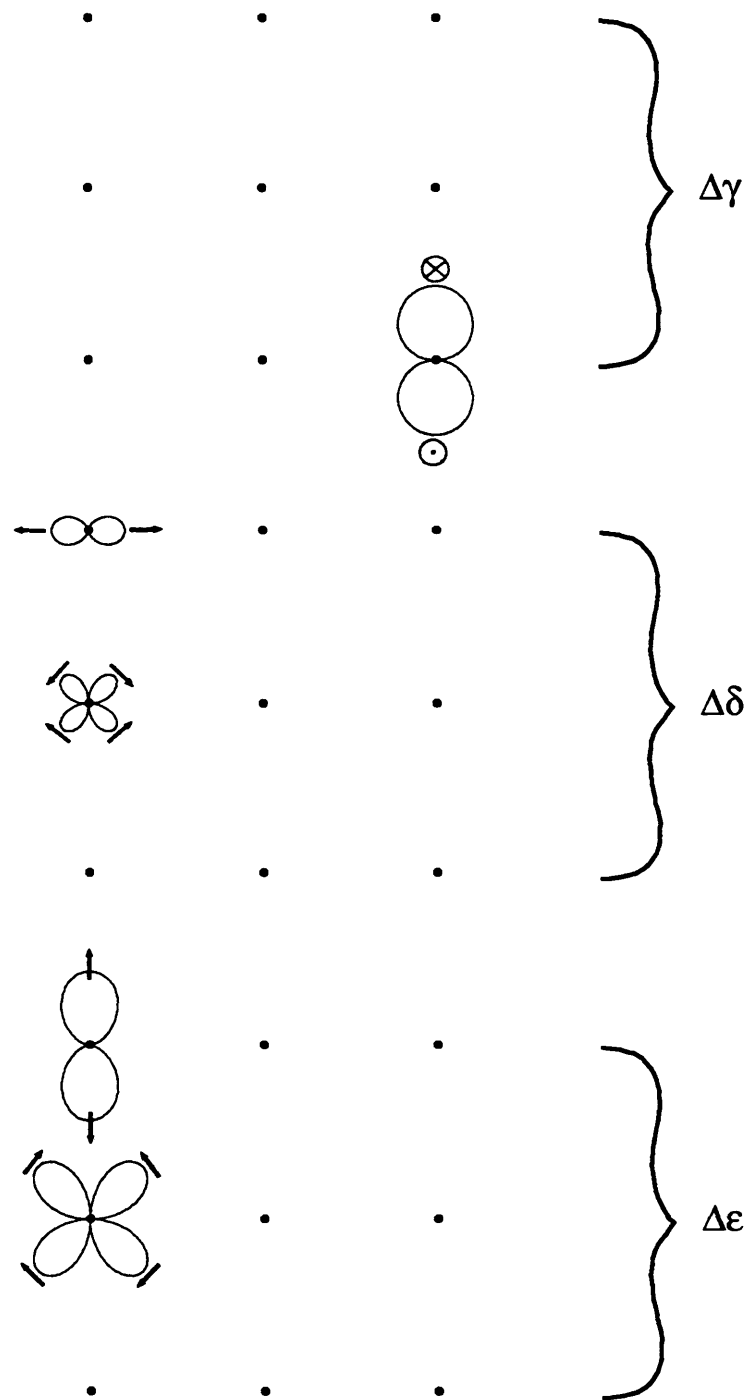


**Fig. 2.8.** Rayleigh scattering patterns in the  $x_1$ - $x_3$  plane for perturbations to anisotropic parameters, for a horizontal symmetry axis. Wave types follow the same scheme as in Fig. 2.5, and arrows show sense of first motion for the scattered wave.

on shear-wave or converted-wave scattering. For near normal-incidence recording using  $P$  waves only, it is difficult to distinguish between scattering from a density perturbation and scattering from a  $P$ -wave velocity perturbation. This ambiguity leads to parameter coupling in the inversion problem (Beydoun et al., 1989).

Unlike the parameters  $\alpha$ ,  $\beta$  and  $\rho$ , scattering from the anisotropic parameters is sensitive to the orientation of the symmetry axis. To illustrate this, Fig. 2.6 shows scattering from perturbations to  $\gamma$ ,  $\delta$  and  $\epsilon$ , where the axis of symmetry is vertical, and Figs. 2.7 and 2.8 show the same radiation patterns, for an axis of symmetry inclined at angles of  $45^\circ$  and  $90^\circ$ , respectively. Note that the same diffraction patterns would be produced by keeping the symmetry direction fixed and varying the incidence angle. In Fig. 2.6, there is only scattering from the  $\delta$  parameter. Maximum scattering occurs for a symmetry-axis direction of  $45^\circ$ . Note also that it is possible to have  $qP$ - $qSV$  or  $qSV$ - $qP$  backscattering at zero offset, due to a perturbation to the  $\epsilon$  parameter (see Fig. 2.7).

For the isotropic case, changes to the parameters of the reference medium only scale the diffraction patterns. However, for anisotropic media the precise shape of the Rayleigh scattering patterns depends on the parameters of the background. To illustrate this point, Fig. 2.9 shows vertical-incidence diffraction patterns for  $qP$ - $qP$  scattering due to a small perturbation to the parameter  $\alpha$ , for three different reference media. The density and vertical phase velocities are the same in all three cases, and the symmetry axis is taken to be vertical. In Fig. 2.9a, the reference medium is isotropic; in Fig. 2.9c, the reference medium has the parameters of the Greenhorn shale (p. 23); in Fig. 2.9b, the magnitude of the anisotropy parameters ( $\gamma$ ,  $\delta$  and  $\epsilon$ ) for the Greenhorn shale have been divided by two. As the level of anisotropy increases (from left to right), the scattering pattern deviates more from circular. Similar effects have been observed for scattering due to perturbations to other elastic parameters.

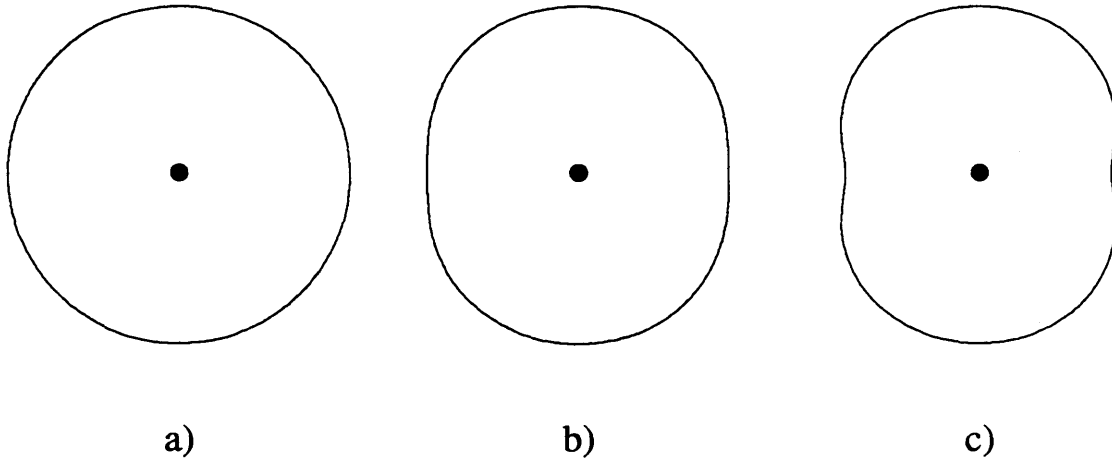


**Fig. 2.9.** a) Circular amplitude radiation pattern in the  $x_1$ - $x_3$  plane for Rayleigh scattering from a perturbation to the parameter  $\alpha$ . The background medium is isotropic, with parameters  $\alpha = 3377$  m/s,  $\beta = 1490$  m/s and  $\rho = 2420$  kg/m<sup>3</sup>. The incident wavefield propagates vertically downwards. b) Same as a), but the background medium is moderately anisotropic and has a vertical symmetry axis.  $\alpha$ ,  $\beta$  and  $\rho$  are the same as in a), but in this case  $\gamma = 0.255$ ,  $\delta = -0.0375$  and  $\epsilon = 0.1$ . These are 50% of the magnitudes of the anisotropic parameters for the Greenhorn shale. The scattering pattern is no longer exactly circular. c) Same as b), but the background medium is strongly anisotropic and has the same parameters as the Greenhorn shale ( $\gamma = 0.51$ ,  $\delta = -0.075$ ,  $\epsilon = 0.2$ ). The deviation of the scattering pattern from circular is now more evident.

---

#### 2.4.1 Stationary-phase correction for out-of-plane scattering

The assumptions made about the symmetry of the medium (section 1.1.3) make it possible to correct analytically for out-of-plane scattering effects. This permits calculations to be performed more economically, in two dimensions rather than three. I begin by rewriting (2.38) to make the  $x_2$  dependence explicit:

$$U_{mn}^{\Omega}(\mathbf{s}, \mathbf{r}, \omega) \approx \omega^2 g_m(\mathbf{s}) g_n(\mathbf{r}) \int_{x_1}^{x_2} \int_{y_1}^{y_2} \int_{z_1}^{z_2} [\Delta \rho \delta_{ik} + \Delta c_{ijkl} \bar{p}_l \hat{p}_j] A \bar{g}_k \hat{g}_i e^{i\omega \tau} dx_1 dx_2 dx_3 \quad . \quad (2.47)$$

For  $(\omega\tau)$  large, the stationary-phase approximation (Bender and Orszag, 1978) can be used to obtain:

$$U_{mn}^{\Omega}(\mathbf{s}, \mathbf{r}, \omega) \approx \omega^{3/2} e^{i\pi/4} g_m(\mathbf{s}) g_n(\mathbf{r}) \int_A [\Delta \rho \delta_{ik} + \Delta c_{ijkl} \bar{p}_l \hat{p}_j] (\tau_{,22})^{-1/2} A \bar{g}_k \hat{g}_i e^{i\omega \tau} dx \quad , \quad (2.48)$$

where  $A$  is the area of intersection of the  $x_1$ - $x_3$  plane with the domain  $D$ , and  $\tau_{,22}$  is evaluated at  $x_2 = 0$ . The scattering integral has thus been reduced from a volume integral to a surface integral, in which the out-of-plane scattering is represented by filtering of the response by the operator  $\omega^{-1/2} e^{i\pi/4}$ , and inclusion of the term  $(\tau_{,22})^{-1/2}$  in the integral kernel.

Finally, combining (2.48) with (2.45), one can express the 2½-dimensional ray-Born scattering integral for an arbitrary parameterization as:

$$U_{mn}^{\Omega}(\mathbf{x}, \mathbf{y}, \omega) \approx \omega^{3/2} e^{i\pi/4} \bar{g}_m(\mathbf{s}) \hat{g}_n(\mathbf{r}) \int_A [s_p L_{pq} \Delta m_q] (\tau_{,22})^{-1/2} A e^{i\omega \tau} dx \quad . \quad (2.49)$$

For discrete problems, this expression may be written symbolically as

$$\mathbf{U} = \mathbf{B} \Delta \mathbf{m} \quad , \quad (2.50)$$

to emphasize the linear relationship between data and model parameters implied by equation (2.49).

## 2.5 Least-squares inversion

Although a linearized framework for forward modeling has been presented, the large dimensions of  $\mathbf{B}$  (typically  $\sim 10^5 \times 10^4$ ) preclude the use of standard matrix methods for solving the inverse problem. Moreover, uncertainties in the data (e.g., noise) and constraints on the model should be accounted for. These features can be incorporated using a generalized least-squares formalism (Tarantola and Valette, 1982; Tarantola, 1987). To this end, a generalized least-squares objective function can be defined as

$$E = \frac{1}{2}(\Delta\mathbf{u} * \mathbf{W}_u \Delta\mathbf{u} + \Delta\mathbf{m} * \mathbf{W}_m \Delta\mathbf{m}) \quad , \quad (2.51)$$

where  $\mathbf{W}_u^{-1}$  and  $\mathbf{W}_m^{-1}$  are covariance operators associated with the data and model, respectively,  $\Delta\mathbf{u} = \mathbf{u}_{\text{obs}} - \mathbf{U}$ , and the \* superscript denotes the conjugate transpose operator. The strategy for inversion is to determine an estimates for earth parameters such that  $E$  is minimized. Following Beydoun and Mendes (1989), an iterative conditioned-gradient technique is employed that makes use of the first and second derivatives of  $E$  with respect to the model parameters. Assuming that the initial model is a close approximation to the actual earth, minimization is performed by requiring that the gradient function,  $\mathbf{g} \equiv \nabla E$ , go to zero. Using equation (2.50),  $\mathbf{g}$  may be written:

$$\mathbf{g} = -\mathbf{B} * \mathbf{W}_u \Delta\mathbf{u} + \mathbf{W}_m \Delta\mathbf{m} \quad . \quad (2.52)$$

In the Gauss-Newton approximation (Adby and Dempster, 1974), the Hessian operator ( $\mathbf{H} \equiv \nabla\mathbf{g}$ ) is approximated by

$$\mathbf{H} = \mathbf{B}^* \mathbf{W}_u \mathbf{B} + \mathbf{W}_m \quad , \quad (2.53)$$

and the model update is given by

$$\Delta \mathbf{m} \approx -\mathbf{H}^{-1} \mathbf{g} \quad . \quad (2.54)$$

The full Hessian operator and its inverse are difficult to compute. Various strategies have been employed to estimate  $\mathbf{H}^{-1}$  for acoustic problems in an iterative fashion (Lebras and Clayton, 1988). Using a different approach, Beydoun and Mendes (1989) give an analytic form for an approximate Hessian operator that neglects the off-diagonal terms, but is easily inverted. The same form for the approximate Hessian is used here, adapted to the TI elastic case. Details of this operator are given in chapter 5. The function of the approximate Hessian is to condition the gradient estimate by partially removing parameter coupling effects (Beydoun and Mendes, 1989).

In equation (2.50), the matrix  $\mathbf{B}$  incorporates the effects of both forward wave-propagation and scattering. Conversely,  $\mathbf{B}^*$  filters the data residual, and maps each point into the model image (filtered backprojection). Thus, as pointed out by Tarantola (1984), the first step in the linearized inversion scheme is functionally equivalent to seismic migration. Viewing migration as the calculation of a model gradient with respect to a least-squares objective function is significantly different from the conventional perception of migration as a downward continuation of the wavefield from sources and receivers until an imaging principle is satisfied (see Claerbout, 1985).

## 2.6 Summary

In this chapter, the principles of elastic wave propagation, anisotropy, the ray and Born approximations and a specific least-squares inversion technique have been

reviewed. These form the mathematical foundation for the elastic migration/inversion algorithm, as well as other techniques employed in this study. A common element in the discussion of the forward problem is the use of asymptotic techniques for studying the behaviour of seismic wavefields at high frequencies and in the far field. This has led to a description of suitable asymptotic form of the elastodynamic Green's tensors that comprises a set of discrete arrivals, corresponding to the different elastic wave types. Each arrival has a characteristic amplitude, traveltime and polarization vector.

In the ray-Born scattering approximation, no multiple scattering events are considered, and perturbations to each of the model parameters from the set  $\{\alpha, \beta, \gamma, \delta, \epsilon, \rho\}$  leads to a unique scattering radiation pattern.

Inverse scattering is posed here as a least-squares optimization problem. Provided that the initial model satisfies the ray validity conditions and is a close approximation to the true earth, and that the observations cover a sufficiently wide aperture range, this method is capable, in principle, of producing high-resolution images of the individual parameter variations in the subsurface.

# Chapter 3

## Converted-wave binning techniques

### 3.1 Introduction

Effective data-preprocessing techniques are often critical to the success of seismic migration and inversion (M/I). The choice of the processing algorithms that are applied prior to M/I is guided by several considerations. For example, it is essential to ensure that coherent energy not accounted for by ray-Born scattering (e.g., multiples, direct arrivals or surface waves) is removed from the data in a manner that preserves the relative amplitudes of primary-scattered events. Moreover, rapid methods for obtaining unmigrated images of the subsurface facilitate correlation of events between different wave types (e.g., Geis et al., 1990), estimation of background velocities, and verification of M/I results. Preprocessing algorithms are also frequently required to handle much larger volumes of data than can be practically accommodated using fully elastic prestack imaging techniques.

A number of these issues have been previously examined in the context of elastic migration and inversion (Mora, 1988; Beydoun et al., 1990; Pratt and Gouly, 1991). In many cases, conventional seismic processing techniques can be adapted without difficulty to process elastic-wavefield (multicomponent) data. However, special attention must be given to mode-converted events, which can convey considerable information about the elastic properties of scattering bodies (see Figs. 2.5 to 2.8). In particular, the standard industry practice of common-midpoint (CMP) data stacking is not valid for converted waves. A number of alternative methods for binning and stacking mode-converted

reflections have been suggested recently (Tessmer and Behle, 1988; Tessmer et al., 1990; Stewart, 1991). These methods provide a means of generating images using converted waves that are approximately equivalent to unmigrated CMP- or VSPCDP-stacked data.

This chapter begins with a discussion of the raypath geometry for converted reflections in vertically inhomogeneous media. Several existing methods for performing isotropic, common-conversion point (CCP) binning in this type of medium are then reviewed. The main emphasis is on surface, rather than borehole, measurements, reflecting the more important role of unmigrated, stacked displays for the low signal-to-noise ratio, surface-recording environment. In order to analyze the inherent periodicity of CCP binning, a method for constructing *P-SV* surface stacking charts is discussed. Finally, several new methods for CCP binning are discussed, for both isotropic and anisotropic media.

### 3.2 Raypath geometry for converted waves: Isotropic case

Reflection (and transmission) of elastic waves at an interface between different elastic layers can be reconciled with ray-Born theory by viewing the reflected energy as an integrated point-scattering response over the entire boundary. The region on the interface that contributes most to this integration is known as the Fresnel zone (Sheriff, 1980). For converted waves in an isotropic medium, the radius of the Fresnel zone is given by

$$R_F \approx \frac{c_m (t_0 T)^{1/2}}{2} \quad , \quad (3.1)$$

where  $c_m$  is the migration velocity necessary to collapse a converted-diffraction into a point,  $t_0$  is the zero-offset traveltime and  $T$  is the dominant period of the seismic wavelet (Eaton et al., 1991). The reflection or conversion "point" ( $P$ ) is then defined to be at the

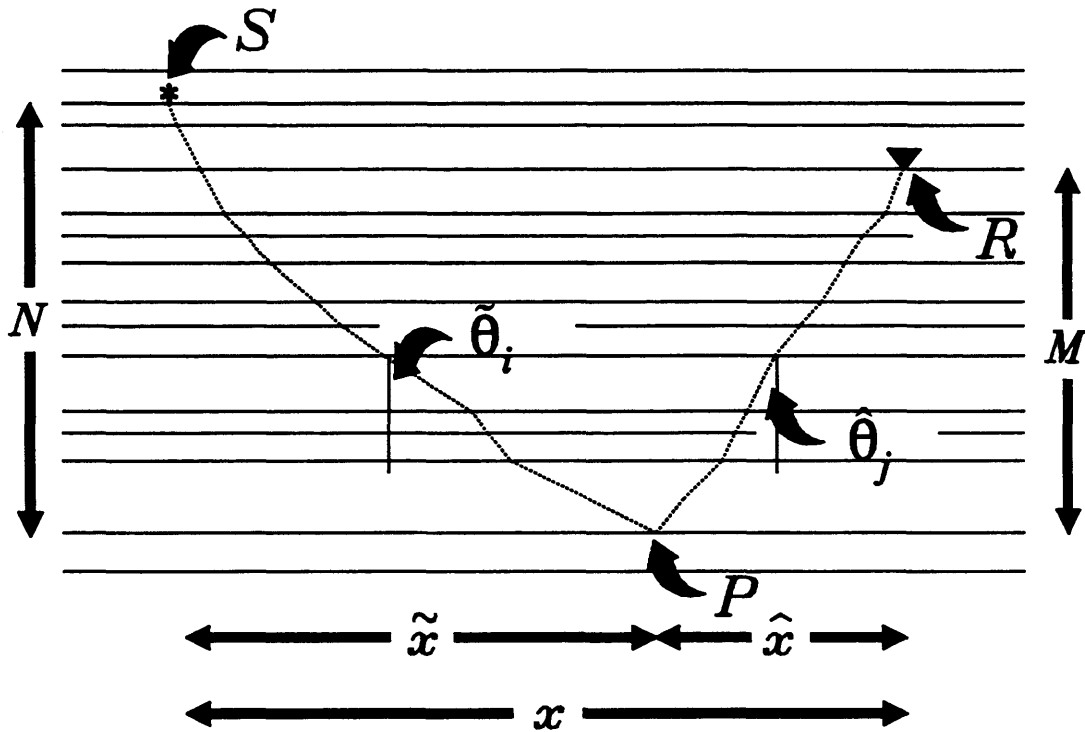


Fig. 3.1. Converted-wave raypath geometry in a horizontally stratified medium.

centre of this zone, such that the reflection raypath  $S$ - $P$ - $R$  (Fig. 3.1) satisfies Fermat's principle (Aki and Richards, 1980).

Consider a layered medium, where the parameters depend only on depth,  $z$ . In this type of medium, Snell's Law implies that the ray parameter, or the horizontal component of the slowness ( $p_1$ ), is conserved along the raypath, for both the isotropic and anisotropic cases (Gajewski and Psenčik, 1987). For a reflected ray passing through  $N$  layers prior to reflection/conversion, and  $M$  layers subsequently, the total horizontal distance travelled can be expressed as the sum of the downgoing and upgoing parts,

$$x = \bar{x} + \hat{x} = \sum_{i=1}^N h_i \tan(\tilde{\theta}_i) + \sum_{i=1}^M h_i \tan(\hat{\theta}_i) \quad . \quad (3.2)$$

In equation (3.2),  $h_i$  is the thickness and  $\theta_i$  is the ray angle with respect to the  $z$  axis for the  $i$ th layer. As in the previous chapter, quantities with the ( $\sim$ ) and ( $\hat{\phantom{a}}$ ) superscripts are associated with the incident and reflected rays, respectively. By symmetry, the ray angles in each layer for the upgoing and downgoing ray segments are the same for unconverted primary events ( $qP$ - $qP$ ,  $qSV$ - $qSV$ ,  $SH$ - $SH$ ), provided that the symmetry axis is horizontal or vertical, or the medium is isotropic. Hence, for a source and receiver at the same elevation, the lateral position of the reflection point always occurs at the midpoint. This is not the case for converted reflections ( $qP$ - $qSV$  and  $qSV$ - $qP$ ); in general, the ray angle is different in each layer, for the downgoing and upgoing segments of the ray.

If each layer is isotropic, then

$$\tan(\theta_i) = \frac{v_i p_1}{(1 - v_i^2 p_1^2)^{1/2}} \quad , \quad (3.3)$$

where  $v_i$  is the velocity of the  $i$ th layer, and equation (3.2) may be written

$$x = \sum_{i=1}^N \frac{h_i \tilde{v}_i p_1}{(1 - \tilde{v}_i^2 p_1^2)^{1/2}} + \sum_{i=1}^M \frac{h_i \hat{v}_i p_1}{(1 - \hat{v}_i^2 p_1^2)^{1/2}} \quad . \quad (3.4)$$

The horizontal distance from the source to the conversion point,  $\bar{x}$ , is given by the first sum in equation (3.4). I will consider first the asymptotic behaviour of  $\bar{x}$  as  $x \rightarrow 0$  and as  $x \rightarrow \infty$ . In the first limiting case, the raypath approaches vertical incidence and the horizontal slowness vanishes, implying that

$$\bar{x} \approx p_1 \sum_{i=1}^N h_i \bar{v}_i \quad , \quad (3.5)$$

and

$$\hat{x} \approx p_1 \sum_{i=1}^M h_i \hat{v}_i \approx \left( \frac{\sum_{i=1}^M h_i \hat{v}_i}{\sum_{i=1}^N h_i \bar{v}_i} \right) \bar{x} \quad . \quad (3.6)$$

If the source and receiver are at the same level (i.e.,  $M = N$ ) then for  $P$ - $SV$  events,

$$x \approx \bar{x}(1 + \bar{\beta}/\bar{\alpha}) \quad , \quad (3.7)$$

or

$$\bar{x} \approx \frac{x}{1 + \bar{\beta}/\bar{\alpha}} \quad , \quad (3.8)$$

where  $\bar{\alpha}$  and  $\bar{\beta}$  are the average  $P$ - and  $S$ -wave velocities along the raypath. Similarly,

$$\bar{x} \approx \frac{x}{1 + \bar{\alpha}/\bar{\beta}} \quad , \quad (3.9)$$

for  $SV$ - $P$  events. Equations (3.8) and (3.9) are referred to here as *asymptotic* conversion-point approximations.

Conversely, for very long offsets, the horizontal slowness becomes progressively larger. As it approaches the  $P$ -wave slowness of the first layer,  $\bar{x}/\hat{x} \rightarrow \infty$  (i.e., conversion at the receiver) for the  $P$ - $SV$  case, and  $\bar{x}/\hat{x} \rightarrow 0$  (i.e., conversion at the source) for the  $SV$ - $P$  case. This result also represents the raypath with the minimum traveltime, in agreement with Fermat's Principle.

For the single-layer case ( $M = N = 1$ ), equation (3.4) may be written:

$$x \approx \bar{x} + \frac{\hat{z}\hat{v}p_1}{(1-\hat{v}^2p_1^2)^{1/2}} \quad , \quad (3.10)$$

where  $\hat{z}$  is the depth of the reflector below the receiver. Analytic solutions to equation (3.10) have been obtained by several authors (Tessmer and Behle, 1988; Taylor, 1989). The derivation is outlined below. Substituting

$$p_1 = \frac{\bar{x}}{\bar{v}(\bar{x}^2 + \bar{z}^2)^{1/2}} \quad , \quad (3.11)$$

into (3.10) leads to the expression

$$x = \bar{x} + \frac{\hat{z}\bar{x}}{[G^2(\bar{x}^2 + \bar{z}^2) - \bar{x}^2]^{1/2}} \quad . \quad (3.12)$$

where  $\bar{z}$  is the depth of the reflector below the source and

$$G = \frac{\bar{v}}{\hat{v}} \quad , \quad (3.13)$$

for the single layer velocities  $\bar{v}$  and  $\hat{v}$ . Equation (3.12) can be rearranged to give the quartic polynomial

$$\eta_j \bar{x}^j = 0 \quad , \quad j=0, \dots, 4 \quad , \quad (3.14)$$

where:

$$\begin{aligned}
\eta_0 &= -(Gx\bar{z})^2 \quad , \\
\eta_1 &= 2G^2x\bar{z}^2 \quad , \\
\eta_2 &= \hat{z}^2 - G^2(x^2 + \bar{z}^2) + x^2 \quad , \\
\eta_3 &= 2x(G^2 - 1) \quad ,
\end{aligned}
\tag{3.15}$$

and

$$\eta_4 = 1 - G^2 \quad .$$

Equation (3.15) can be solved by factorization into two quadratic polynomials (Tessmer and Behle, 1988; Taylor, 1989). Of the four possible solutions to equation (3.15), two are imaginary and one is unphysical, leaving a single solution. This solution is referred to here as the *straight-ray* approximation. Although it has been derived for the single-layer case, this approximation is also useful for multiple layers, bearing in mind that  $G$  is then an average velocity ratio.

The asymptotic and straight-ray approximations are compared in Fig. 3.2. The  $P$ -wave layer velocities were determined using a conventional sonic log from a well at 4-22-53-12W5, in central Alberta (Fig. 3.3). The velocity ratio  $\alpha/\beta$  as a function of  $P$ -wave reflection time has been calculated by correlation of  $P$ - $P$  and  $P$ - $SV$  reflections observed on a nearby 3-component seismic line (Harrison, 1989). This function was used to compute the  $S$ -wave velocities shown in Fig. 3.2a. The zone of interest in this case is the Cardium Zone (CZ), at a depth of about 1.5 km. The average value of  $\alpha/\beta$  to this depth is 1.95 (Harrison, 1989). Using this ratio, the straight-ray method gives a good approximation to the ray-traced conversion point locations for all depths. On the other hand, the error for the asymptotic approximation is  $> 100$  m for depths less than about 1200 m.

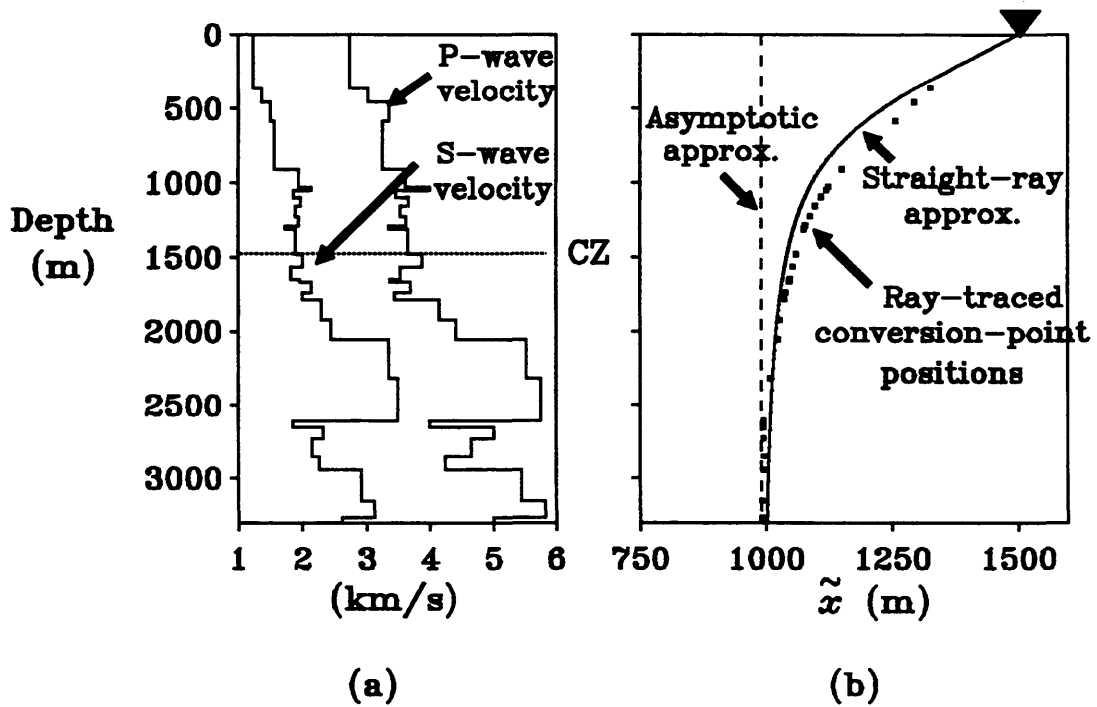


**Fig. 3.2.** a) *P*-wave and estimated *S*-wave layer velocities, for a well at 4-22-53-12 W5. The zone of interest is the Cardium Zone (CZ), at a depth of about 1500 m. b) Conversion point location ( $\tilde{x}$ ) versus depth for a source and receiver offset by 1500 m. Dashed line is asymptotic approximation, solid line is straight-ray approximation, and squares show ray-traced conversion-point locations.

### 3.3 Review of common-conversion-point trace-sorting techniques

In order to position mode-converted reflections close to their actual conversion-point location, some method of common-conversion-point (CCP) binning is essential. CCP trace sorting using the asymptotic and straight-ray approximations has been discussed previously in the literature (Fromm et al., 1985; Tessmer and Behle, 1988; Tessmer et al., 1990). In both cases, seismic traces are gathered and stacked with other

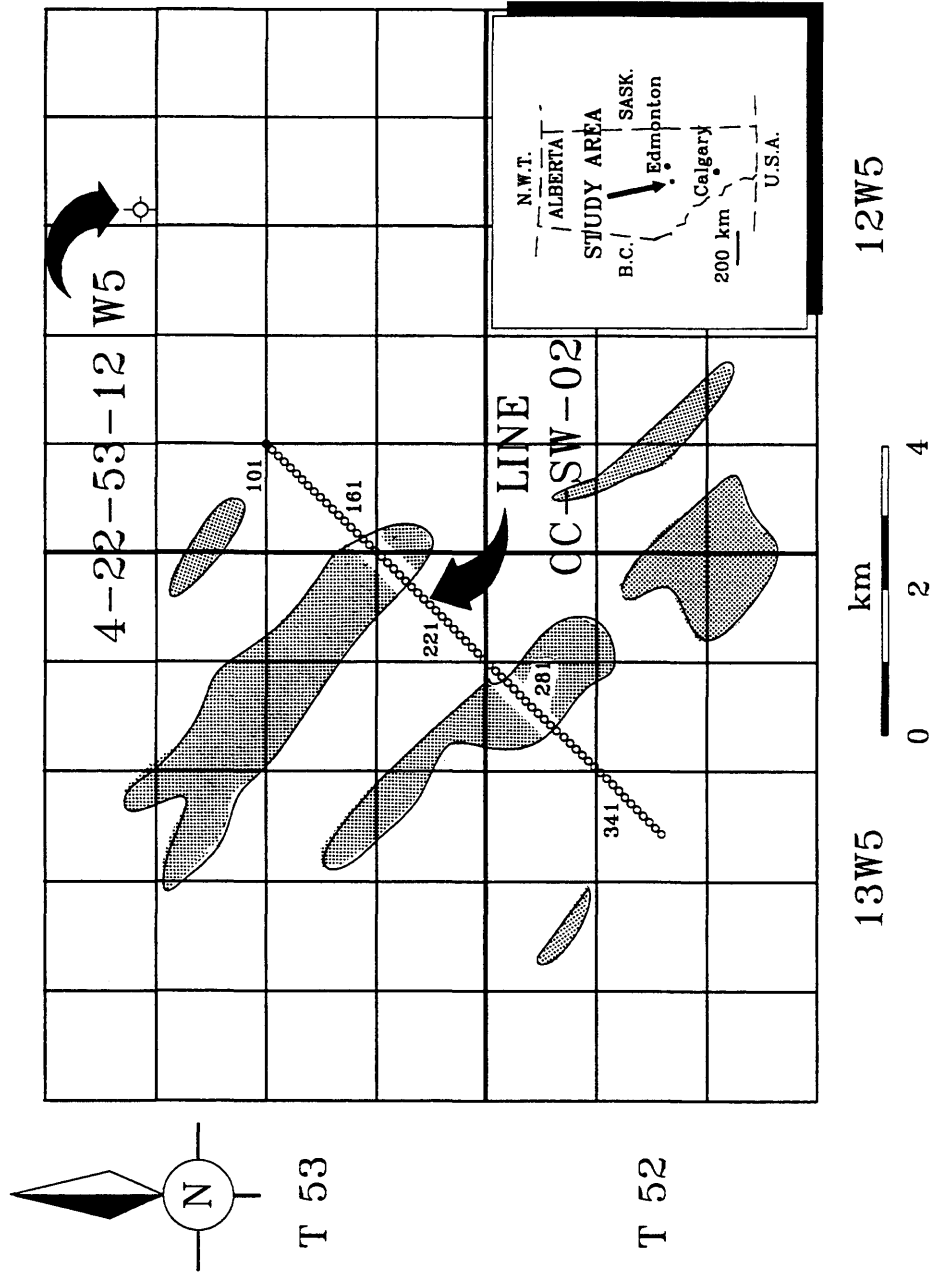


**Fig. 3.3.** Location map showing position of seismic line (CC-SW-02) and well (4-22-53-12W5). Stippled areas are locations of hydrocarbon pools producing from the Cardium Zone (Nazar, 1991).

traces according to an approximate CCP criterion (equations (3.8), (3.9) and (3.14)).

A synthetic dataset was generated in order to compare the results of CCP binning using these two approximations. The dataset consists of 21 end-on shot records, each containing 80 traces. The acquisition geometry is summarized in Table 3.1, and is patterned after line CC-SW-02 (Fig. 3.3). *P-SV* reflections from four horizons have been generated, using a homogeneous background model with  $\alpha = 3000$  m/s and  $\beta = 1500$  m/s. All four horizons are offset by a vertical normal fault with 50 m of throw (Fig. 3.4). The data have been computed by convolving a unit impulse, delayed by the *P-SV* reflection time, with a zero-phase wavelet containing frequencies between 8 and 60 Hz. Phase and amplitude changes with offset, as well as diffractions from the fault, have been neglected. An example shot record from this survey is shown in Fig. 3.5.

After trace sorting, the data were corrected for moveout using a time-shifted hyperbolic formula given by:

$$t = \frac{t_0}{2} + \sqrt{\frac{t_0^2}{4} + \frac{x^2}{2\check{v}^2}}, \quad (3.16)$$

where  $\check{v}$  is the *P-SV* RMS velocity (Tessmer and Behle, 1988). Equation (3.13) provides a better estimate of converted-wave moveout than the standard hyperbolic NMO formula (Slotboom, 1990). A time-shifted hyperbolic moveout formula for converted waves that provides slightly better accuracy than equation (3.13) is derived in Appendix B. To achieve a fair assessment of the CCP binning as it applies to real data, the dataset was muted after NMO. The mute profile consisted of a straight line defined by the  $(x,t)$  pairs  $(0, 0)$  and  $(2550, 1800)$ , where  $x$  is in m and  $t$  is in ms.

Different versions of the stacked data are shown in Figs. 3.6 to 3.8. Fig. 3.6 shows the results of applying the asymptotic method of binning (with  $\alpha/\beta = 2$ ). In

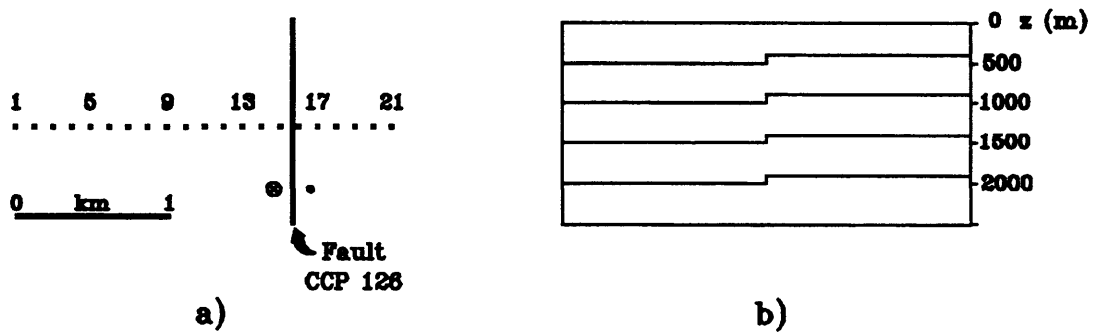


Fig. 3.4. a) Map view of synthetic survey, showing shot numbers. b) Cross-section view of synthetic survey. Throw on vertical fault is 50 m.

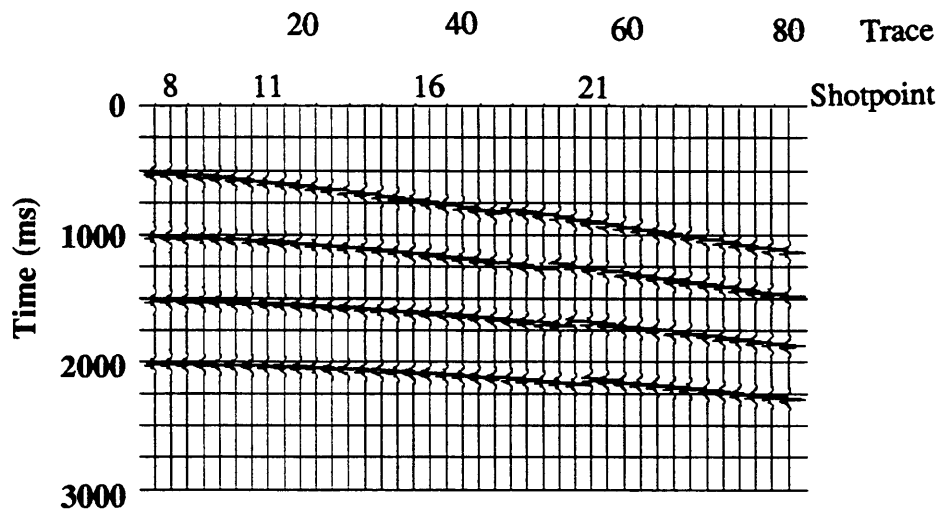
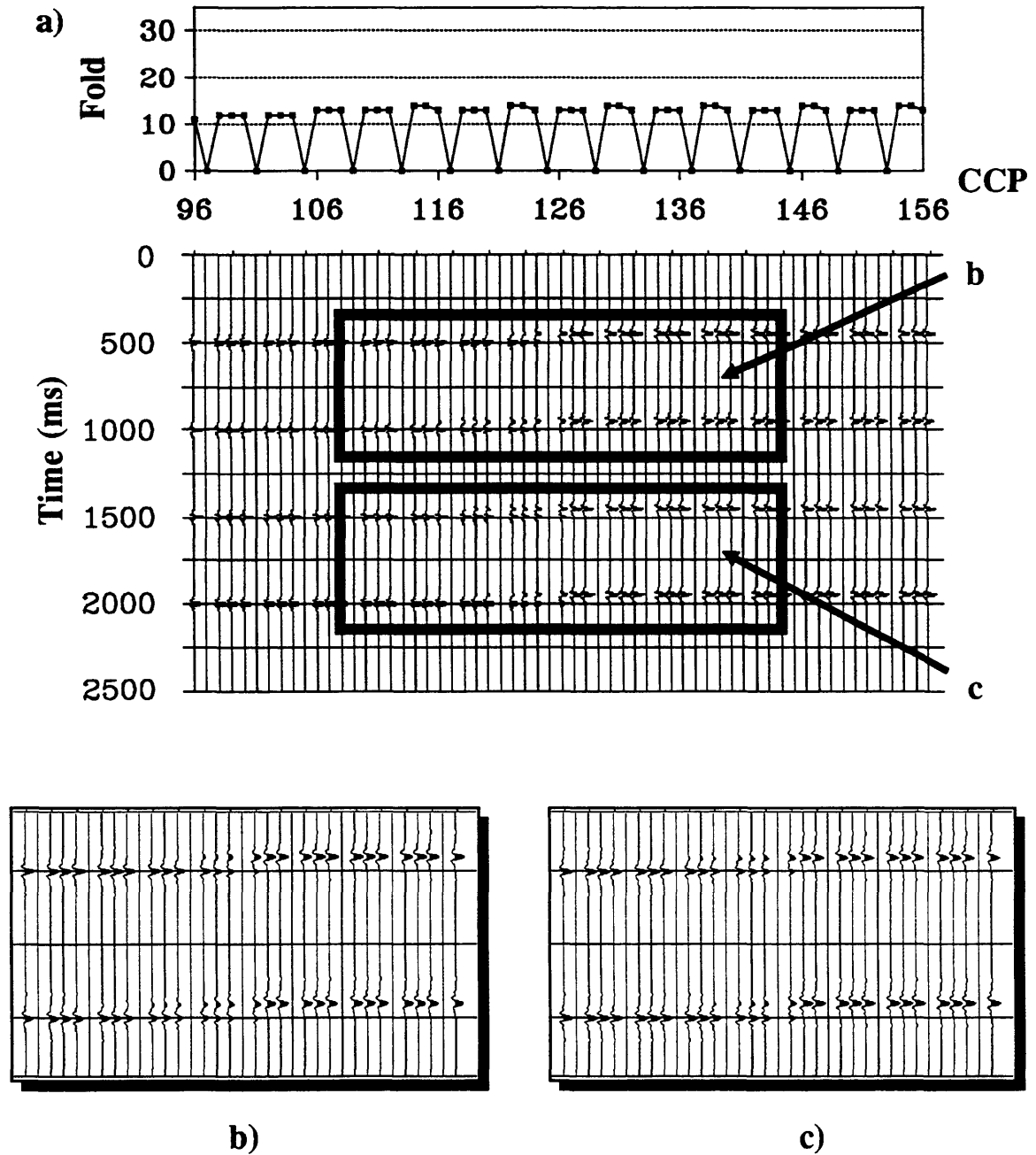


Fig. 3.5. Shot record 6 from the synthetic dataset (every second trace shown). Note that the apparent position of the fault shifts to the right for deeper events.

Spread type	Number of channels ( $n$ )	Near offset	Far offset	Group interval ( $\Delta r$ )	Source interval ( $\Delta s$ )
end on	80	180 m	2550 m	30 m	120 m

Table 3.1. Acquisition geometry for synthetic dataset.



**Fig. 3.6.** a) Stacked data gathered using the asymptotic approximation. Data window is 900 m across. Note that there is an empty CCP bin every fourth trace. b) Enlarged view of two shallow events near the fault. c) Enlarged view of two deep events near the fault.

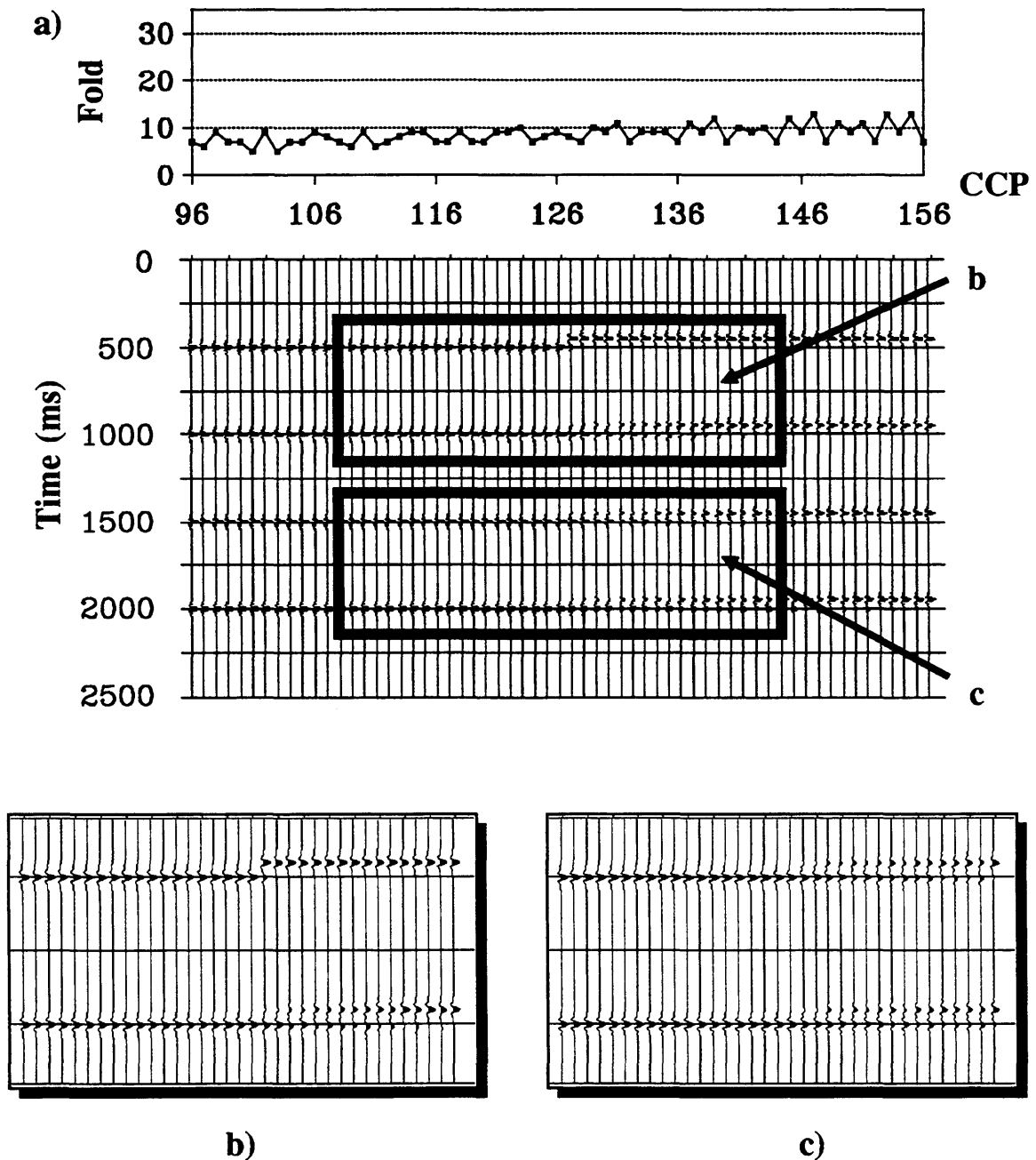


**Fig. 3.7.** a) Stacked data gathered using the straight-ray approximation, for a target depth of 500 m. Data window is 900 m across. b) Enlarged view of two shallow events near the fault. Note that the location of the fault is well resolved for the shallowest event. c) Enlarged view of two deep events near the fault.

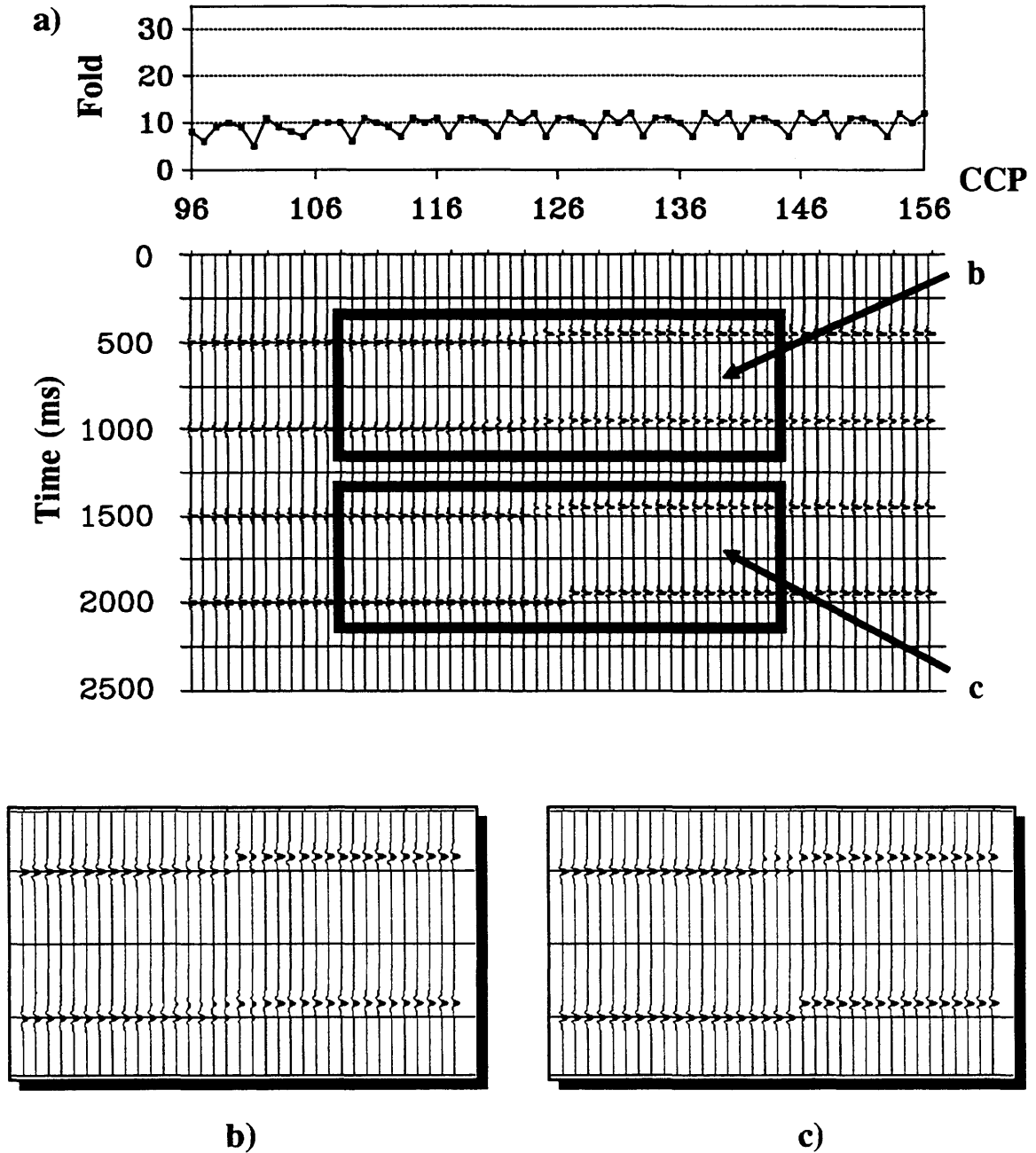


**Fig. 3.8.** a) Stacked data gathered using the straight-ray approximation, for a target depth of 2000 m. Data window is 900 m across. b) Enlarged view of two shallow events near the fault. c) Enlarged view of two deep events near the fault. In this case, note that the location of the fault has been well imaged for the deepest event.

general, resolution of the fault improves with depth, as expected. Surprisingly, however, the location of the fault appears to be well reconstructed for the shallowest depth. The reason for this is that the application of the mute has removed incorrectly binned data that would otherwise have corrupted the stack. Binning artifacts are most severe for the intermediate depth zones at 1000 m and 1500 m. Note also that the stacking fold exhibits a strong periodicity, and is zero for every fourth trace. An explanation of this phenomenon is given in the next section.

Converted-wave trace sorting using the straight-ray approximation is illustrated in Figs. 3.7 and 3.8. In Fig. 3.7, CCP gathers have been constructed to create an optimal stack for the shallowest event, by assigning CCP numbers that have been calculated for a depth of 500 m. Fig. 3.8 shows data that have been optimized for the deepest event. In this manner, *P-SV* stacked sections can be generated selectively to enhance specific depth zones (Tessmer and Behle, 1988; Tessmer et al., 1990). However, in order to image correctly multiple depth zones in the same display, it is necessary to combine several different stacked sections. This problem can be avoided by mapping individual data samples to their correct CCP position, rather than sorting entire traces. An implementation of this technique is discussed below, after an analysis of *P-SV* binning periodicity.

### 3.4 *P-SV* stacking charts and binning periodicity

The oscillatory fold pattern observed in Figs. 3.6-3.8 is manifested in the stacked data as a periodic change in event character and amplitude, as well as numerous zero traces. This phenomenon results from spatial resampling that occurs due to CCP binning; i.e., CCP gathers are normally separated by half of a group interval ( $\Delta r/2$ ), but in the

asymptotic approximation, for example, each CCP is separated in the subsurface by the  $\Delta r/(1+\beta/\alpha)$ . The intrinsic fold (and offset) patterns that are imposed by certain choices of acquisition and sorting parameters can be studied using a surface stacking chart overlay technique.

A surface stacking chart (Sheriff and Geldart, 1982; Yilmaz, 1987) is a convenient graphical representation, in source-receiver space, of the trace geometry for a seismic survey. Typically, a horizontal axis is used to denote receiver position and a vertical axis is used to denote source position (Fig. 3.9), so that each seismic trace is specified by a pair of coordinates  $(r, s)$ . Collections of traces corresponding to common-receiver, common-source, common-offset and common-midpoint (CMP) gathers are aligned along vertical, horizontal,  $45^\circ$  and  $135^\circ$  azimuths, respectively. If the source spacing ( $\Delta s$ ) is an integral multiple of the group interval ( $\Delta r$ ) then traces are exactly aligned along these directions (neglecting skids, detours, etc.). The subsurface multiplicity (fold) along lines of constant CMP is then given by the well known expression:

$$f = \frac{n\Delta r}{2\Delta s} \quad , \quad (3.17)$$

where  $\Delta r$  is the group interval,  $\Delta s$  is the source interval and the number of recording channels ( $n$ ) is even.

Here we will consider a  $P$ - $SV$  stacking-chart representation for the asymptotic approximation only (Eaton and Lawton, 1991). Although this approximation has certain shortcomings, this approach provides useful insight that can also be applied to the analysis of more sophisticated binning techniques. Rewriting equation (3.8) in terms of the co-ordinates  $r$  and  $s$ , we have

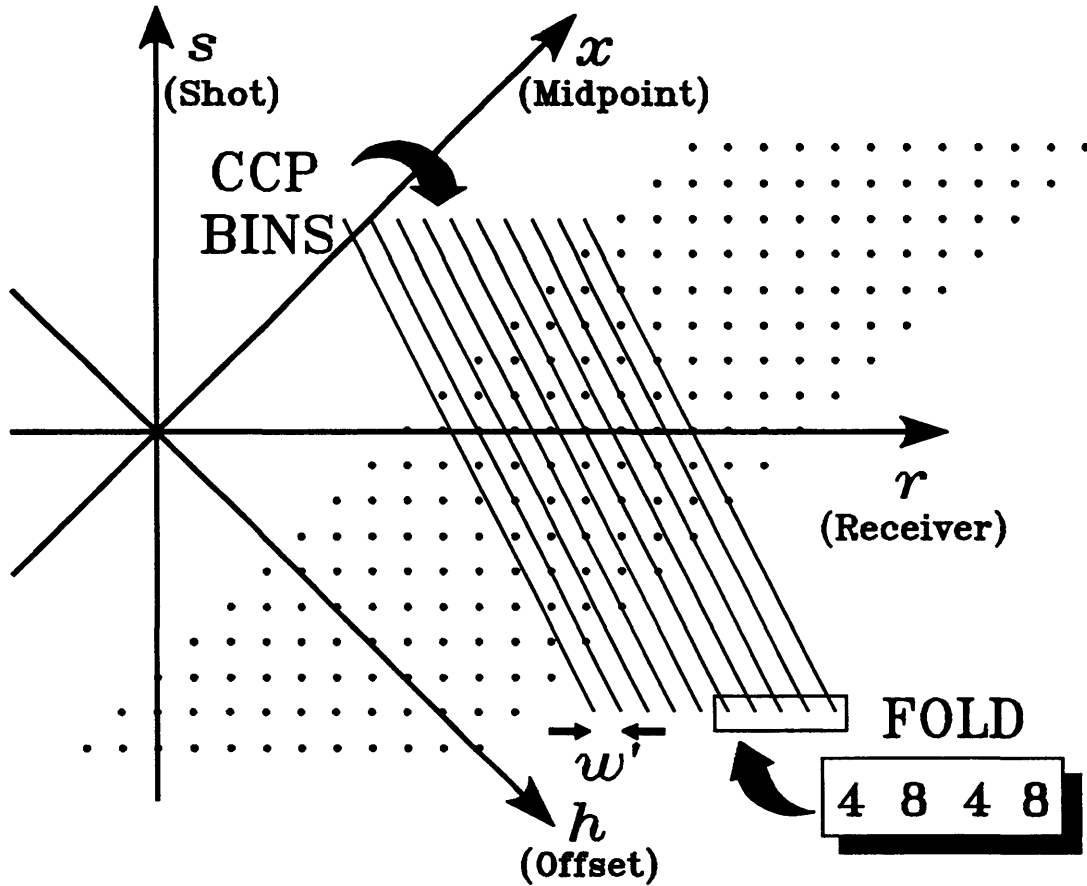


Fig. 3.9. *P-SV* stacking chart, constructed by projecting the boundaries for asymptotic-CCP bins onto a conventional surface-stacking chart (modified from Yilmaz, 1987).

$$\bar{x} = s + \frac{r-s}{1+\bar{\beta}/\bar{\alpha}} \quad (3.18)$$

Therefore,  $s$  and  $r$  are linearly related, in the asymptotic approximation, by the formula

$$s = -(\bar{\alpha}/\bar{\beta})r + (1+\bar{\alpha}/\bar{\beta})\bar{x} \quad (3.19)$$

Lines of constant CCP position, thus, have slopes equal to  $-\alpha/\beta$  in  $(r,s)$  space, as noted

by Frasier and Winterstein (1990). However, traces are aligned exactly along lines given by equation (3.19) only if  $\bar{\alpha}$  is an integral multiple of  $\bar{\beta}$ . For the more general case, lines of equal CCP position will not necessarily pass through the trace locations on a stacking chart. It then becomes necessary to sort traces into bins of finite width, similar in principle to processing 3-D or crooked-line 2-D conventional (*P-P*) data.

This gathering procedure can be represented graphically by projecting lines corresponding to the boundaries of a given CCP bin onto the stacking chart, and collecting traces that fall within the two lines (Fig. 3.9). For bins of width  $w$  in the  $s$ -direction, the equations of the boundary lines for a bin centred at  $x_b$  are

$$s = -(\bar{\alpha}/\bar{\beta})r + (1 + \bar{\alpha}/\bar{\beta})(x_b \pm w/2) \quad . \quad (3.20)$$

The corresponding bin width in the  $r$ -direction is given by

$$w' = (1 + \bar{\beta}/\bar{\alpha})w \quad . \quad (3.21)$$

Fig. 3.9 illustrates CCP bin overlays for a 12-trace spread, with a source point at every station. A velocity ratio of  $\bar{\alpha}/\bar{\beta} = 2.0$  and the normal convention of  $w = \Delta r/2$  have been employed. Note that the fold oscillates between 4 and 8, giving a mean fold of 6, as predicted by equation (3.17). This periodicity in fold becomes more problematic if  $\Delta s = 2\Delta r$ , in which case every 4th bin contains no live traces (for  $\bar{\alpha}/\bar{\beta} = 2.0$ ). In general, empty CCP bins will occur whenever  $\Delta s/\Delta r$  is an integral multiple of  $\bar{\alpha}/\bar{\beta}$  (Eaton and Lawton, 1991).

A number of methods can be used to achieve a more equitable distribution of traces into CCP bins. If  $\bar{\alpha}$  is an integer multiple of  $\bar{\beta}$ , then it is sometimes possible to choose a natural bin interval ( $\Delta x_b$ ) such that the fold is constant. For example, if  $\Delta s = \Delta r$  as in Fig. 3.9, a choice of

$$w = \Delta x_b = \frac{\Delta r}{2(1 + \beta/\alpha)} \quad , \quad (3.22)$$

leads to bins having a multiplicity given by:

$$f_{P-SV} = \frac{n}{(1 + \alpha/\beta)} \quad . \quad (3.23)$$

However, this is an inconvenient stacking interval and results in low stacking fold. Furthermore, comparison between stacked  $P$ - $P$  and  $P$ - $SV$  data becomes more difficult because of the different trace spacing.

A more general approach that appears to give satisfactory results is to set  $w = \Delta r$  (i.e., twice the normal bin width) while retaining the normal value for the bin spacing (half of a group interval). This choice of  $w$  results in overlapping bins, and thus leads to a mild trace-mixing effect; however, the loss in spatial resolution is small relative to the  $P$ - $SV$  Fresnel radius. A stacked section produced from the synthetic dataset after gathering by this method is shown in Fig. 3.10. Note that the fold is approximately double the fold shown in Fig. 3.6, and that the problem of empty CCP bins has been eliminated. The character of the events is also much more continuous.

## 3.5 Depth-variant CCP mapping

### 3.5.1 Description of the algorithm

It has already been demonstrated that CCP binning by trace sorting fails to image correctly more than one depth at a time. This limitation hinders interpretation of converted-wave sections, and makes comparison with conventional data somewhat cumbersome. As an alternative to trace sorting, it is preferable to map each data sample from unstacked, NMO-corrected gathers directly into the stacked image. This procedure

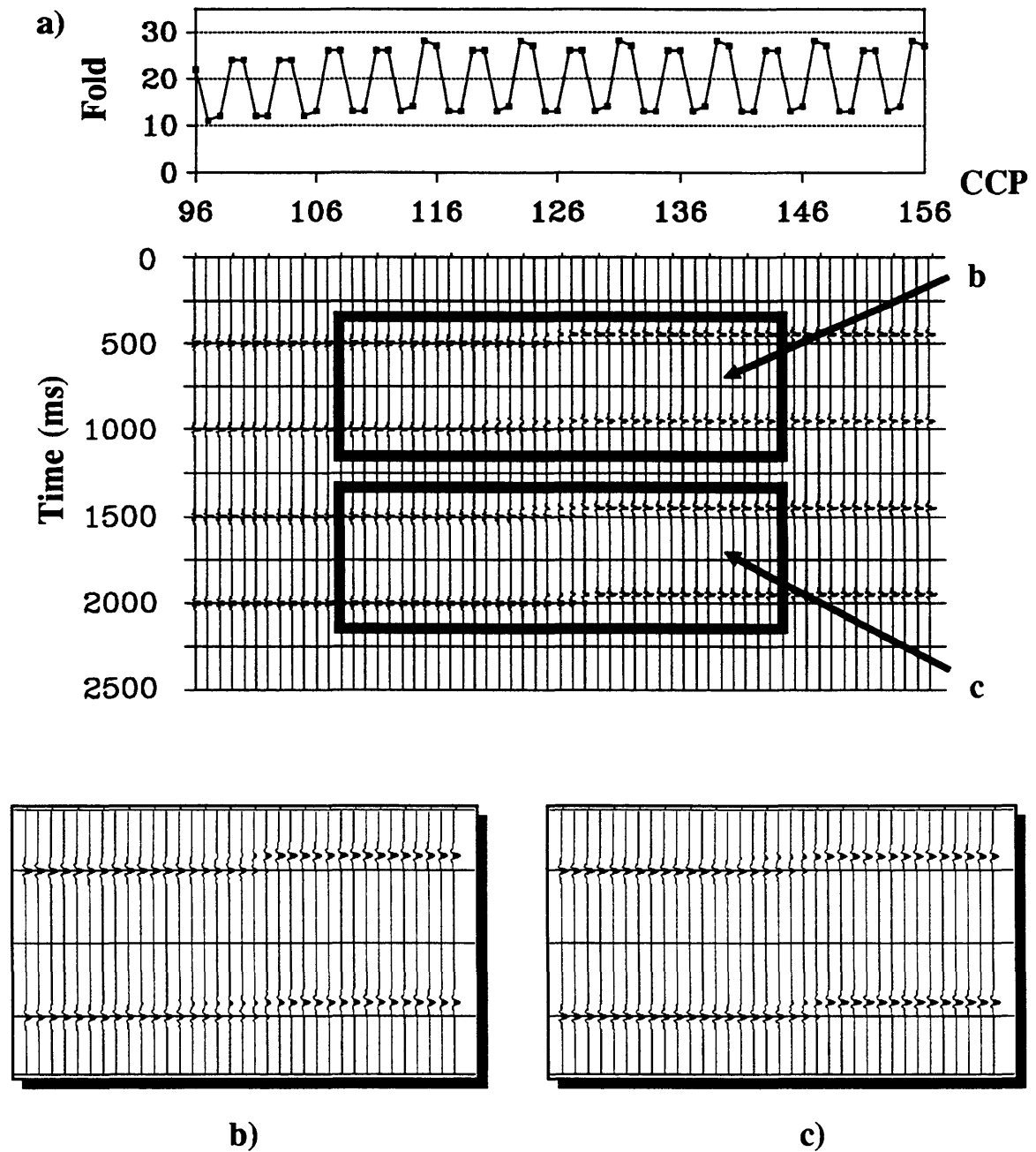


**Fig. 3.10.** a) Stacked data gathered using the asymptotic approximation, using a bin width of  $\Delta r = 30$  m. Note that fold is approximately double that in Fig. 3.6. Data window is 900 m across. b) Enlarged view of two shallow events near the fault. c) Enlarged view of two deep events near the fault.

is analogous to VSPCDP mapping, used to process offset-VSP data (Wyatt and Wyatt, 1984; Dillon and Thompson, 1984), and has been proposed for use with surface data by Chung and Corrigan (1985), Stewart (1988; 1991) and Slotboom and Stewart (1989). The mapped images are directly comparable to conventional, CMP-stacked data.

A  $P$ - $SV$  mapping algorithm for surface data has been implemented using a variable-velocity model.  $P$ - and  $S$ -wave RMS velocity versus depth are used as input, and straight raypaths are assumed. This assumption makes it possible to use the exact single-layer formula for the calculation of  $\bar{x}$  (Tessmer and Behle, 1988; Taylor, 1989) rather than ray tracing. The conversion-point location calculated using straight raypaths is a good approximation to the ray-traced position (Fig. 3.2) and requires a small fraction of the computational effort needed for ray tracing.

The following algorithm is used to process each data sample:

- 1)  $P$ - and  $S$ -wave velocities are found by interpolation between control points.
- 2) The straight-ray conversion-point location is determined for each time (depth).
- 3) The data sample is weighted and summed into the two nearest CCP bins.

Weighting is inversely proportional to distance from the bin centre.

- 4) A corresponding normalization (fold) array is updated with the correct weights.

Once all of the traces have been mapped, the final image is produced by dividing each mapped/stacked data value by the corresponding normalization factor.

This technique has the disadvantage that the rebinned data are not available for subsequent prestack processing. It therefore should be reserved for later stages of the preprocessing flow, after velocity analysis, residual-statics estimation, etc.

### 3.5.2 Examples

As a first example, the  $P$ - $SV$  mapping technique has been applied to the previously described synthetic dataset (see Fig. 3.4 and Table 3.1). The results are shown

in Fig. 3.11. This method has simultaneously imaged the fault at all four depth levels. The corresponding normalization values vary between 10 and 40 (Fig. 3.12). These values reflect the density of mapped points, and provide a useful quality-control tool. The fold exhibits some spatial oscillation near the surface, but remains relatively constant at greater depths. Generally speaking, the fold increases downwards and in the upline direction, or the direction of the end-on spread.

Data from line CC-SW-02 (Fig. 3.3) are used in the second example. These data were acquired using Vibroseis sources with the same spread parameters given in Table 3.2, except that the source interval is 2 groups rather than 4, and some split-spread records are present. The prestack processing included trace reversals for the trailing part of the spread, application of *P*-wave source statics, hand receiver statics, spiking deconvolution, gain, velocity analysis, surface-consistent residual statics, NMO, mute and CCP binning. The target zone here is the Cardium Formation (Fig. 3.2).

Fig. 3.13 shows a portion of the stacked data where the seismic line is known to cross a Cardium bar. A pronounced increase in the amplitude of the *P*-*SV* reflection is associated with the presence of an increase in the thickness of a porous Cardium conglomerate interval (Nazar, 1991). The data that were binned using the mapping technique (Fig. 3.13b) exhibit a more consistent amplitude and character across the Cardium anomaly than the same data binned using the asymptotic approximation (Fig. 3.13a), permitting the edge of this feature to be delineated with greater confidence. The wavelet-character variation in Fig. 3.13a has a period of 4 traces, and most likely correlates with the stacking fold.

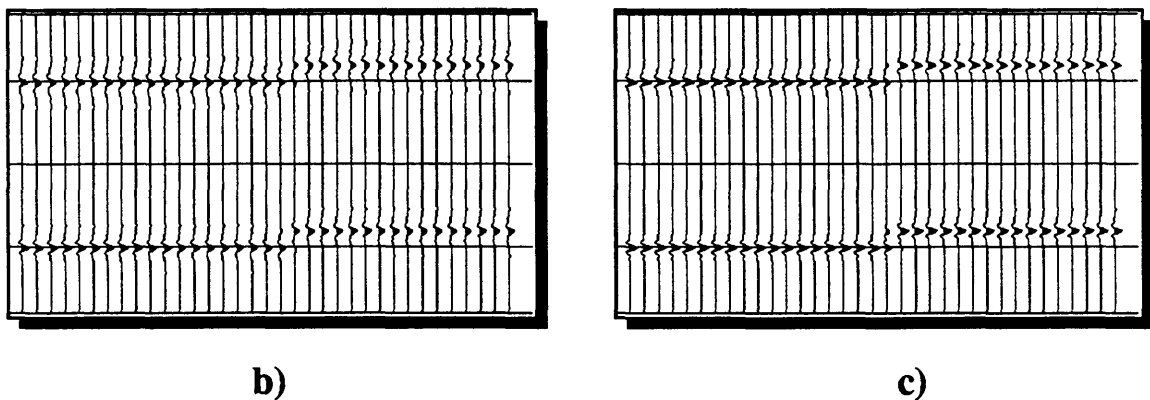
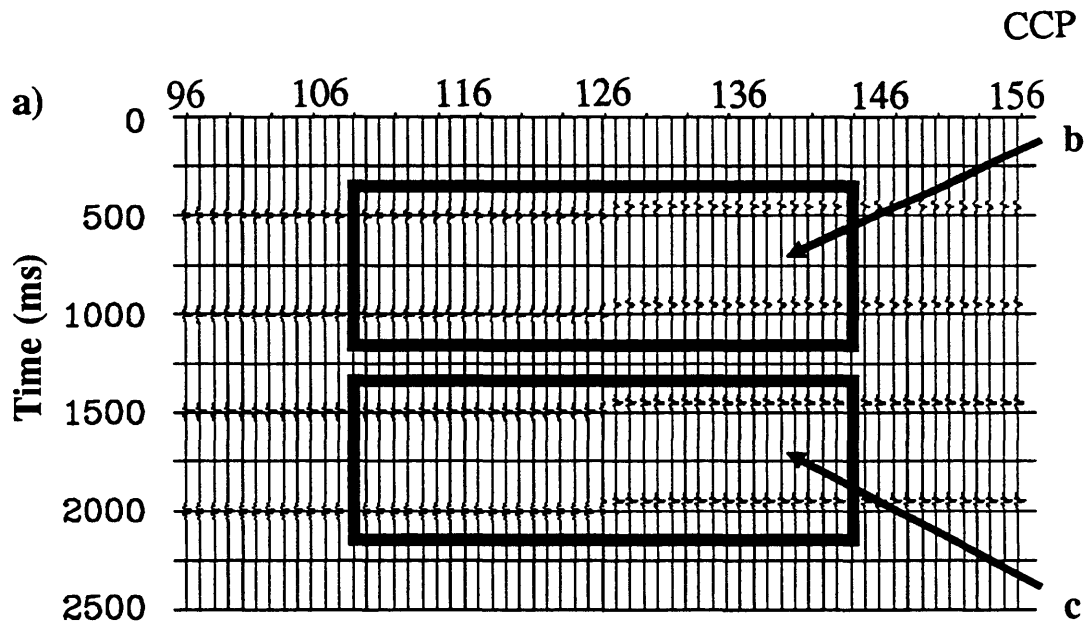


**Fig. 3.11.** a) Stacked data generated using the *P-SV* mapping technique. Data window is 900 m across. b) Enlarged view of two shallow events near the fault. c) Enlarged view of two deep events near the fault. Note that the fault location is now well imaged for all events, simultaneously.

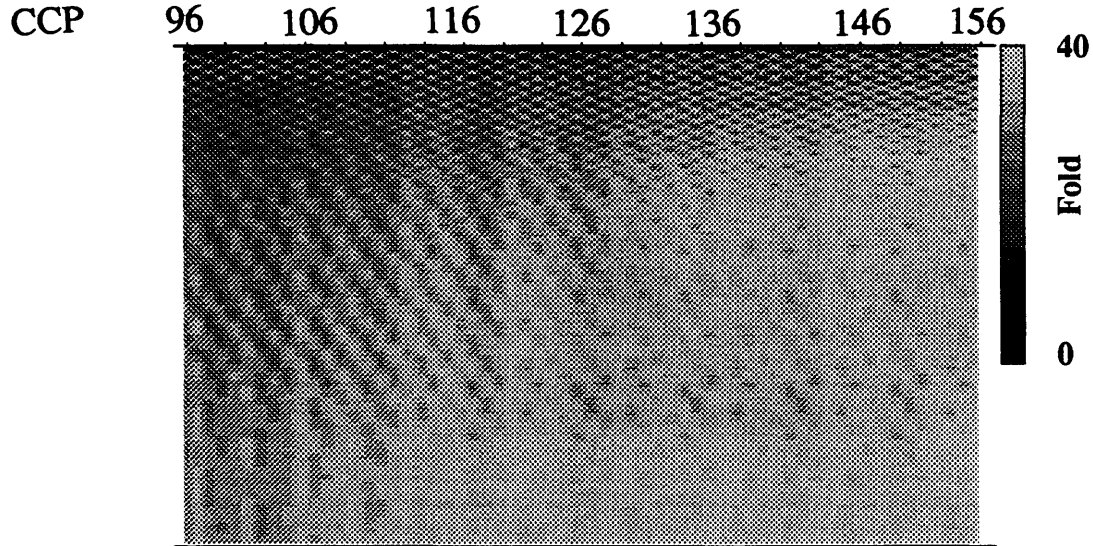


Fig. 3.12. Normalization array corresponding to mapped data shown in Fig. 3.11.

### 3.7 Anisotropic CCP trace sorting

All of the methods discussed thus far have been restricted to isotropic media. The ramifications of transverse isotropy for converted-wave binning will now be briefly considered. The goal is to evaluate the potential significance of anisotropy, as it applies to this approach to unmigrated converted-wave imaging. As for the isotropic case, the straight-ray approximation is employed. For an incident plane wave at a welded interface separating two homogeneous, anisotropic media, the reflection/transmission angles are governed by the generalized form of Snell's Law (e.g., Thomsen, 1988),

$$\frac{\sin\tilde{\phi}}{\tilde{v}_p} = \frac{\sin\hat{\phi}}{\hat{v}_p} = p_1 \quad , \quad (3.23)$$

where  $v_p$  is phase velocity, and  $\phi$  is the phase angle with respect to the normal to the interface. Thus, for a vertically inhomogeneous medium, equation (3.20) is simply a

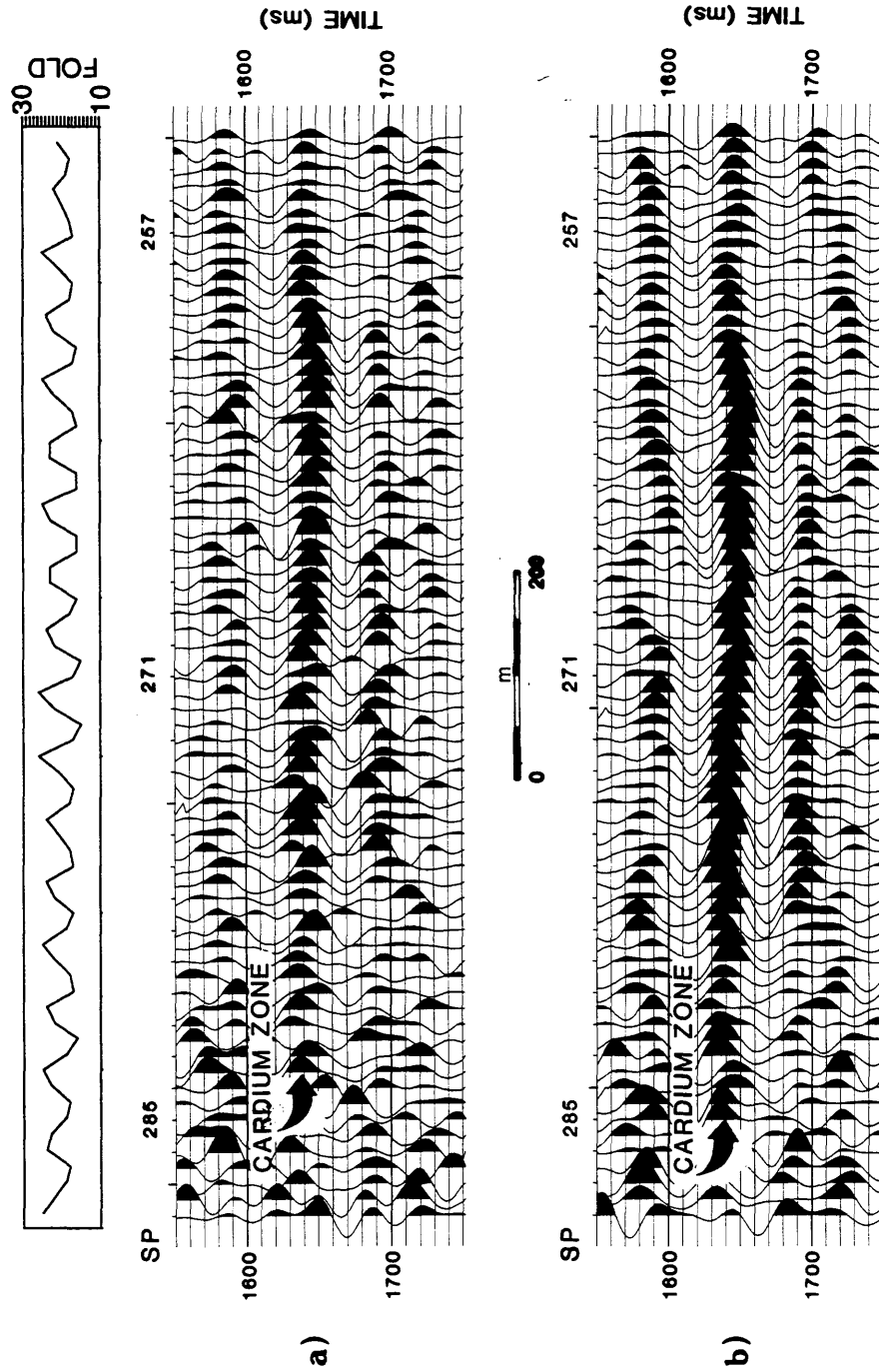


**Fig. 3.13.** Portion of stacked P-SV data from line CC-SW-02, where the line crosses a known bar deposit. a) Binned using the asymptotic method, with  $\alpha/\beta = 1.95$ . The fold is plotted above the seismic display. b) Binned using the P-SV mapping technique.

restatement of the conservation of horizontal slowness. This condition stems from the requirement that displacement and stress be continuous across the interface.

For an isotropic medium, the phase angle,  $\phi$ , and the ray angle (energy flux direction),  $\theta$ , are equivalent. This is not the case for an anisotropic medium, where it is necessary to first match horizontal slowness components for the incident and reflected rays, and then solve for the reflected ray angle (Gajewski and Psenčik, 1987). Matching the horizontal components of slowness leads to a sixth-order polynomial equation (see Appendix C), which can be solved numerically. As an illustrative example for significant anisotropy, the conversion point has been calculated for a layer of Greenhorn shale of thickness  $z = 1000$  m, for a series of offsets ranging from 0 to 2500 m. The axis of symmetry was taken to be vertical.

A graph of  $\bar{x}$  versus  $x$  for this scenario is plotted in Fig. 3.14a. The conversion-point position for the isotropic case is also shown, using the vertical  $P$ - and  $S$ -wave velocities (3377 and 1490 m/s). Observe that, for the anisotropic case, the conversion point occurs *closer* to the source than the receiver for  $x/z < 2$ . This situation is not possible for isotropic media. The explanation for this unusual behaviour lies in the geometry of the  $qP$  and  $qSV$  wave sheets (Fig. 2.2b). Recall that the slowness vector is always normal to the wave surface, and note from Fig. 2.2b that the curvature of the  $qP$  wave sheet is much greater than the curvature of the  $qSV$  wave sheet for near-vertical propagation. In order to match the horizontal component of the two slownesses, the  $qSV$  ray angle must be further from vertical than the  $qP$  ray angle, although the magnitude of the  $qSV$  slowness vector is greater. Because the  $qSV$  ray angle is larger, the conversion point moves closer to the source. Note that multiple mode-converted arrivals are not possible for this example, because the horizontal component of slowness on two of the branches of the  $qSV$  triplication zone is greater than the maximum magnitude of the  $qP$

slowness.

The traveltime curve for this experiment is shown in Fig. 3.14b, along with the traveltime for the isotropic case. The hyperbolic stacking velocity for the anisotropic curve is  $\approx 3050$  m/s. This compares to a vertical  $P$ - $SV$  RMS velocity of 2243 m/s, and is a clear indication of the anisotropic nature of the medium.

As a test of anisotropic converted-wave binning, a second synthetic dataset has been generated, using the same acquisition geometry as in the first example (Fig. 3.4, Table 3.1). In this case, however, the stiffnesses and density for the Greenhorn shale were used to represent the background medium. Again, angle-dependent reflectivity and diffractions from the fault have been neglected. An example shot record (shot 6) from the anisotropic dataset is shown in Fig. 3.15. Comparing this to the same shot record from the first dataset (Fig. 3.5), we see that the fault appears on relatively farther offset traces, as a consequence of the conversion-point shift toward the source.

It was found that constant-velocity NMO using either of the hyperbolic or shifted-hyperbolic formulas produced unsatisfactory results. Therefore, a (hyperbolic) velocity analysis was undertaken. The velocities that were picked are given in Table 3.2. The traces were then sorted into anisotropic CCP bins with a bin width equal to  $\Delta r$  and a target depth of 1000 m, NMO corrected, muted and stacked. The resulting section is shown in Fig. 3.16. As in the isotropic case, additional stack sections must be created to achieve optimal binning for other depths.

The same dataset was also binned using the (isotropic) asymptotic formula, with  $\alpha/\beta = 3377/1490 = 2.27$ . The stacked results are shown in Fig. 3.17. Observe that the apparent position of the fault has been shifted by approximately 300 m from its true location, indicative of the magnitude of the binning error possible if strong anisotropic

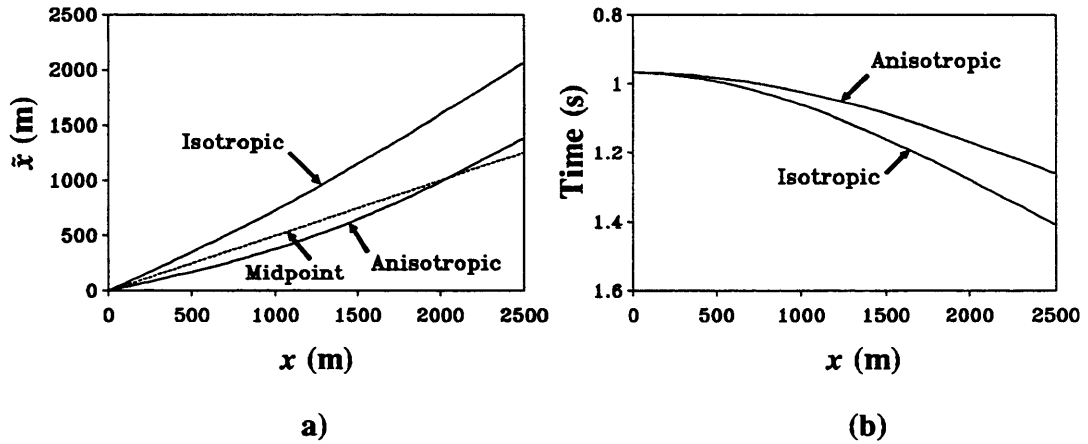


**Fig. 3.14.** a) Graph of conversion-point offset ( $\tilde{x}$ ) versus source-receiver offset ( $x$ ) for a 1000 m thick layer of Greenhorn shale. The isotropic conversion-point curve was computed using  $\alpha/\beta = 2.27$ . b) Traveltime curves for the example shown in a).

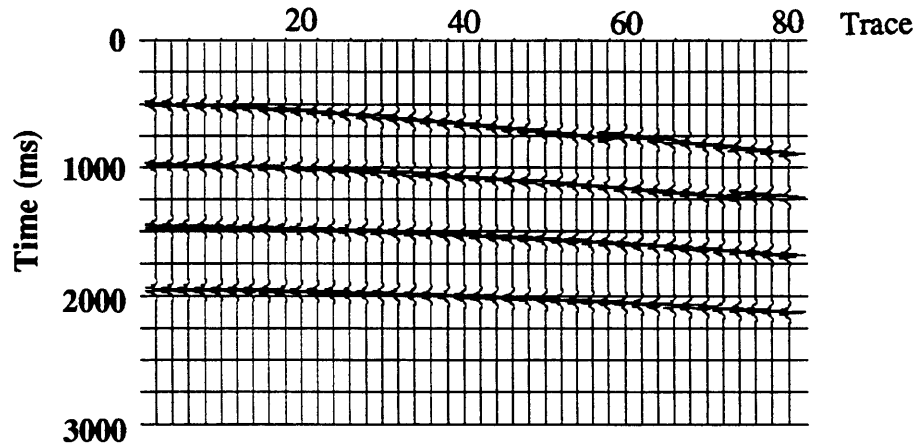


**Fig. 3.15.** Shot record 6 from the anisotropic dataset (every second trace shown).

<b>Time (ms)</b>	<b>0</b>	<b>970</b>	<b>2000</b>
<b>Velocity (m/s)</b>	<b>3450</b>	<b>3050</b>	<b>2990</b>

**Table 3.2.** Empirical velocity function used to NMO correct the anisotropic dataset.

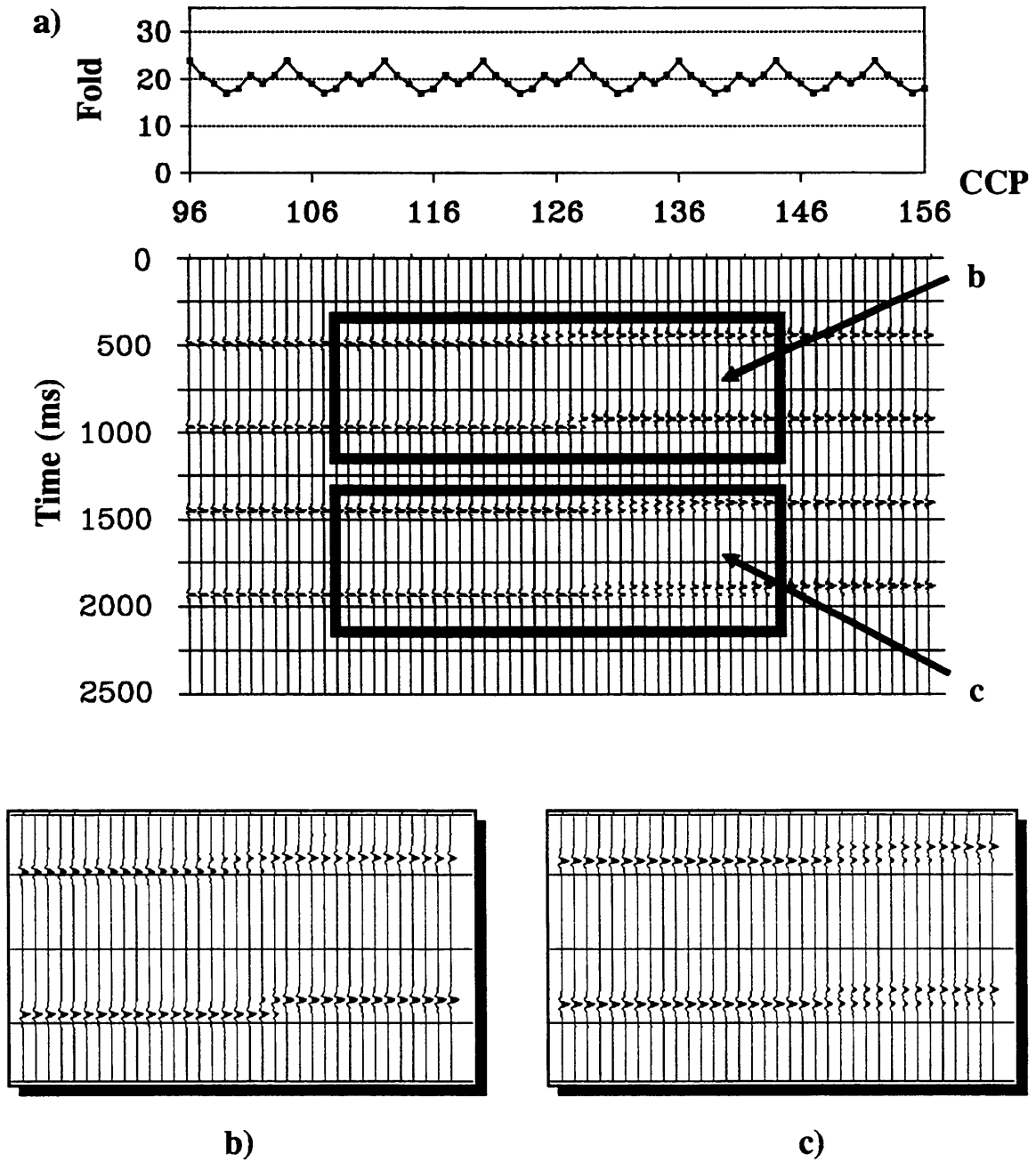


**Fig. 3.16.** a) Anisotropic data gathered for a target depth of 1000 m. Data window is 900 m across. b) Enlarged view of two shallow events near the fault. The fault has been correctly imaged at the target depth. c) Enlarged view of two deep events near the fault.

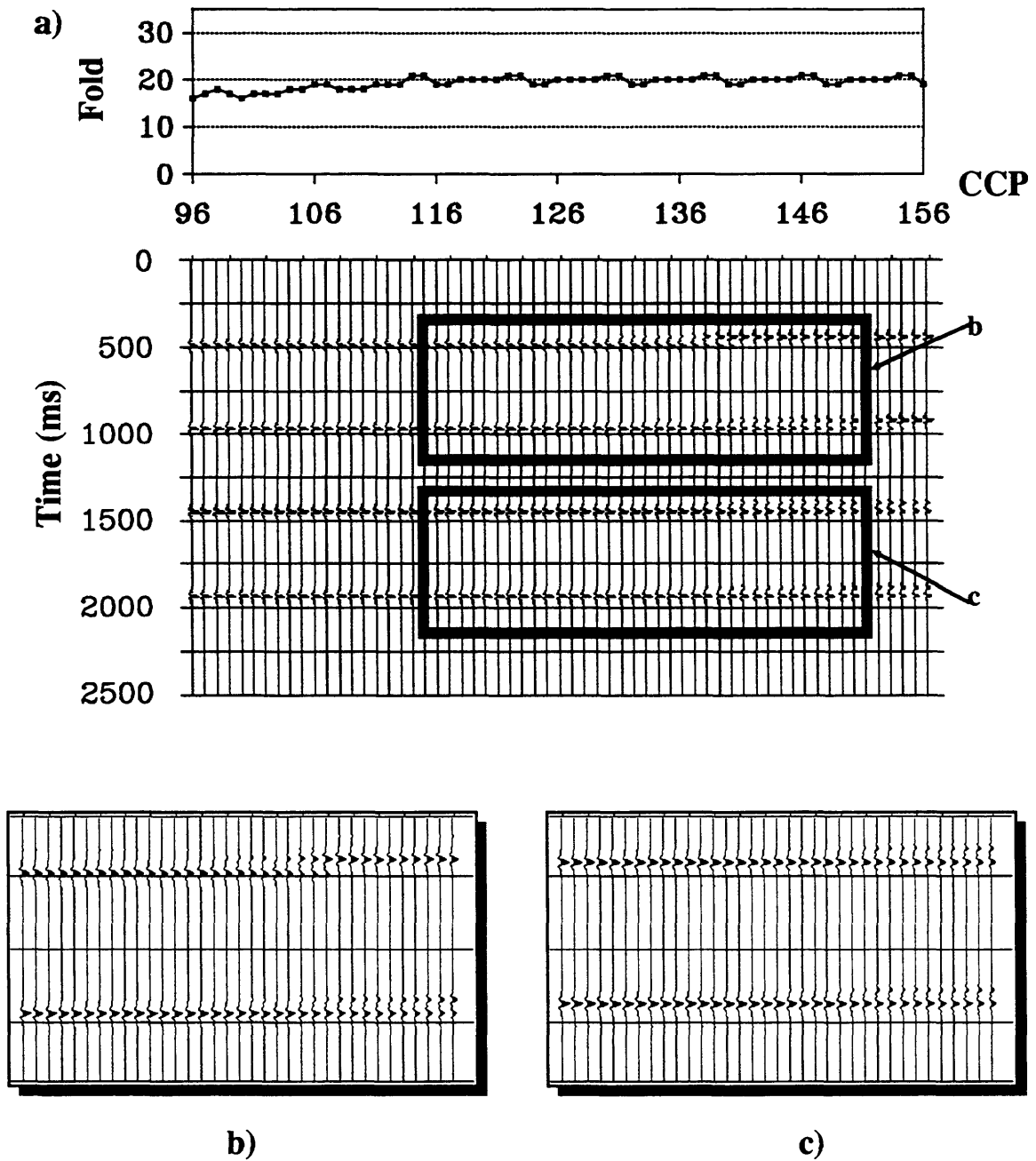


**Fig. 3.17.** a) Stacked data generated by applying the (isotropic) asymptotic gathering technique ( $\alpha/\beta = 2.27$ ) to the anisotropic dataset. The fault has been badly misplaced, because of the failure to account for anisotropic effects. b) Enlarged image of the two shallow events. c) Enlarged image of the two deep events.

effects are not accounted for.

### 3.8 Summary

Methods for obtaining unmigrated, stacked images of the subsurface are extremely valuable prior to migration/inversion. In order to stack mode-converted reflections properly, a common-conversion point technique must be employed. Here, only vertically inhomogeneous media have been considered. The asymptotic and straight-ray methods for trace sorting have been reviewed and compared. The inherent problem of binning periodicity due to spatial resampling has been analyzed by means of a stacking-chart overlay technique. When asymptotic binning is used and the source interval/group interval ratio is an integer multiple of  $\alpha/\beta$ , a larger bin width should be used to avoid empty bins.

A new *P-SV* mapping technique has also been described. The algorithm is analogous to VSPCDP mapping techniques used to process offset-VSP dataset. By stacking converted-wave data in this manner, all depth zones are correctly binned in a single stacked image.

For anisotropic media, the determination of the conversion-point position is more complex, and depends critically on the precise shape of the *qP* and *qSV* wave sheets. It has been demonstrated by means of an example that for anisotropic media the conversion point can be shifted closer to the source than the receiver for *qP-qSV* events. A synthetic-data example has been used to show that, for a strongly anisotropic medium, the effects of anisotropy are sufficiently large that they must be accounted for in the CCP binning procedure.

## Chapter 4

# Finite-difference calculation of ray-Green's functions

### 4.1 Introduction

In the ray-Born formalism, the incident and scattered wavefields are propagated independently through a background medium. Born-scattering, in this approximation, is most accurate when perturbations to the background medium are small. However, elastic parameters in the earth often exhibit strong, systematic changes. Thus, to satisfy the small-perturbation condition, a practical requirement for the migration/inversion algorithm considered here is the ability to compute high-frequency (ray) Green's functions corresponding to a relatively general class of inhomogeneous, transversely isotropic elastic media. Specifically, at each point in the model space, the traveltime, particle-motion vector, initial slowness, out-of-plane spreading factor ( $\tau_{,22}$ ) and geometrical spreading function must be known. This information is required for all wave types and source/receiver locations. Collectively, these quantities are referred to here as the ray-Green's parameters. Experience has shown that calculation of these parameters constitutes a major computational bottleneck, particularly for an inhomogeneous, anisotropic reference model.

The traveltime and geometrical-spreading functions are governed by the eikonal and transport equations (2.27 and 2.29), respectively. Typically, these are solved numerically along rays (characteristics), thereby reducing the partial differential equations to systems of ordinary differential equations (Červený et al., 1977; Bleistein, 1986). For

imaging applications, subsequent interpolation of the computed ray-Green's parameters is necessary, e.g., by the paraxial ray method (Beydoun and Mendes, 1989). Alternatively, numerical solutions can be obtained using a finite-difference approach (Smith, 1985). The ray-Green's parameters are then directly available on a grid, in a form that is well suited to migration/inversion. Previous implementations of this technique for isotropic traveltime and amplitude calculations (Vidale, 1988; 1990; Vidale and Houston, 1990; Van Trier and Symes, 1991) have demonstrated that this method is potentially much faster than ray tracing, or finite-difference methods based directly on the equations of motion.

In this chapter, techniques for computing the ray-Green's parameters for 2½-dimensional transversely isotropic elastic media are presented. The first step in the procedure is the calculation of traveltimes by solving the eikonal equation using an explicit, second-order finite-difference method. The traveltimes are differentiated to yield the vector components of slowness, which are then used to compute the corresponding eigenvectors. The initial slowness at the source is determined using an adaptation of a method suggested by Vidale and Houston (1990). Next, ray tracing is used to determine the out-of-plane spreading factor,  $\tau_{22}$ . Finally, amplitudes are computed using a ray-Jacobian technique. Each component of the algorithm is considered in sequence, below.

Five models, summarized in Table 4.1, are employed to illustrate the advantages and limitations of this methodology. The first model is a homogeneous isotropic solid, and has been included to demonstrate that anisotropic artifacts of the algorithm used here are relatively minor. The second example is a homogeneous, strongly anisotropic material (the Greenhorn shale). This example is used for quantitative assessment of the accuracy of these techniques in the presence of strong anisotropy, relative to analytic, far-field high-frequency Green's functions (see equation 2.18). The first two examples are

Model	Description	See also
4.1	Homogeneous, isotropic $\alpha = 3000$ m/s, $\beta = 1500$ m/s $\rho = 2400$ kg/m <sup>3</sup>	
4.2	Strongly anisotropic, homogeneous (Greenhorn shale)	p. 23
4.3	Linear velocity gradient, fractured	Table 4.2
4.4	Anisotropic block	Fig. 4.1
4.5	Anticline model	Fig. 4.2

**Table 4.1.** Summary of models used to test the finite-difference algorithms.

---

included for illustrative purposes; in practice, the analytic form of the asymptotic Green's function would be used in the migration/inversion procedure.

The third model represents a medium characterized by vertical fracturing, coupled with a linear velocity gradient versus depth. For this model, finite-difference traveltimes are compared to ray-traced traveltimes. The final two models are used for a more qualitative assessment of the procedure. The fourth example (Fig. 4.1) contains a block of anisotropic material in one quadrant, and is used to determine how well the algorithm handles sharp corners in the model, as well as head-waves traveling along an anisotropic/isotropic interface. Finally, a complex model containing an anticline structure is considered (Fig. 4.2). This model illustrates the numerical stability of the algorithm in the presence of caustics, and demonstrates the feasibility of these techniques for a complex scenario.

$\alpha_0$	$\beta_0$	$k_\alpha$	$k_\beta$	$\nu a^3$
3000 m/s	1500 m/s	1.0 s <sup>-1</sup>	0.5 s <sup>-1</sup>	0.05

**Table 4.2.** Parameters for model 4.3, representing an initially isotropic medium with a vertical velocity gradient, that has subsequently been fractured. The velocity gradient (prior to fracturing) is given by  $\alpha = \alpha_0 + k_\alpha z$  and  $\beta = \beta_0 + k_\beta z$ , where  $z$  is depth in metres. The effects of thin, fluid-filled vertical fractures have been computed using formulae from Hudson (1981), where  $a$  is the fracture radius and  $\nu$  is the crack density.

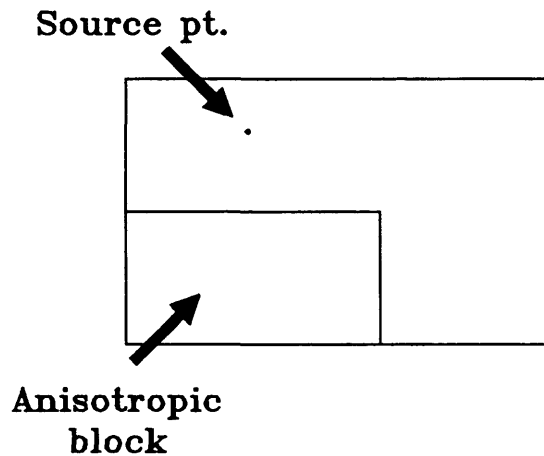


**Fig. 4.1.** Configuration for model 4.4. The source is located in an isotropic layer with  $\alpha = 2887$  m/s and  $\beta = 1443$  m/s. The anisotropic block has the same parameters as the Greenhorn shale. Dimensions of the model are 1330 m in width by 831 m in height.

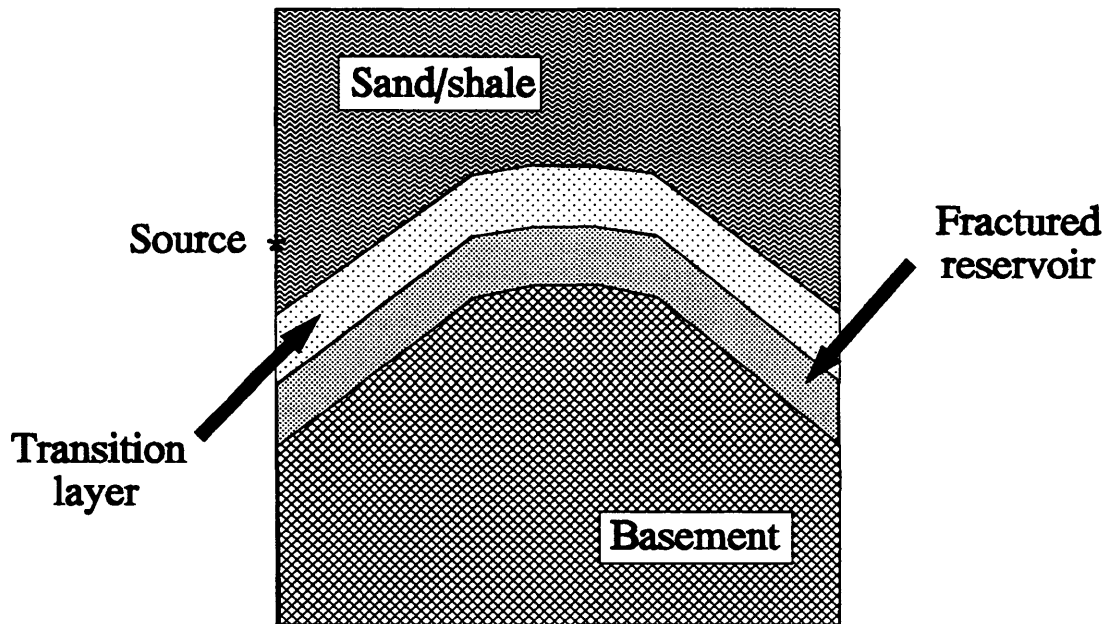


**Fig. 4.2.** Layer configuration for model 4.5. The first layer is a TI composite material consisting of thin sand and shale layers in equal proportion (Levin, 1979). The anisotropic symmetry axis is everywhere normal to the layer boundary. The second and third layers are partially anisotropic, but with a symmetry axis parallel to the layer boundary (to represent fracturing). Both layers are nearly isotropic at the sides of the model, but become progressively more anisotropic toward the core of the anticline. In addition, the transition layer is isotropic at the top, with a gradual increase in anisotropy toward the base of the unit. The underlying basement unit is isotropic, but with a linear velocity gradient normal to the layer boundary. The area shown is 1275 m across and 1000 m deep. Smoothed elastic parameters used for the calculation of Green's functions are displayed in Fig. 4.3.

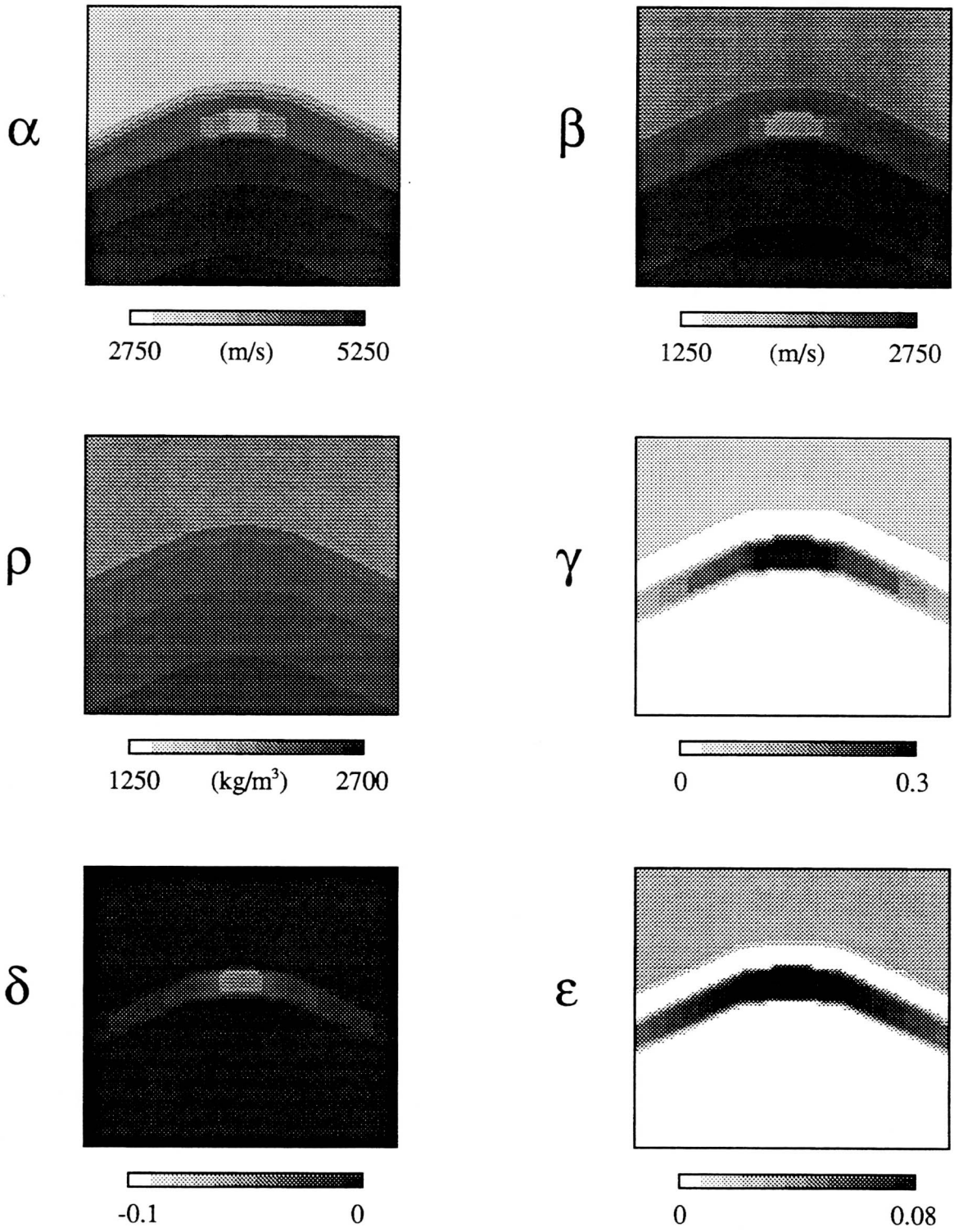


Fig. 4.3. Grey-scale plots of the medium parameters for model 4.5.

## 4.2 Traveltime calculation

The traveltime function,  $\tau$ , is the most fundamental component of the ray-Green's parameter set. From a forward-modeling perspective, calculation of traveltimes simulates the propagation of wavefronts throughout a medium. The migration/inversion viewpoint is complementary; the traveltime information is used to "focus" diffracted energy into the spatial position where the scattering originated. In both cases, errors in the traveltime function are critical; they lead to incorrect focusing of scattered energy during M/I, and adversely affect all subsequent forward-modeled ray-Green's parameters.

### 4.2.1 Description of the algorithm

Traveltime calculation by finite-difference solution of the eikonal equation was introduced by Vidale (1988), who demonstrated that this approach correctly treats head waves and shadow zones, and is also computationally efficient compared to ray tracing. However, in his algorithm the traveltime function is constrained to be single-valued; thus, this technique is primarily suited to modeling first arrival traveltimes. Modifications to Vidale's method are discussed by Qin et al. (1990) and Van Trier and Symes (1991). In particular, Qin et al. (1990) showed that in the presence of moderate to strong parameter contrasts, Vidale's algorithm fails to honour the principle of causality. Qin et al. proposed an expanding wavefront methodology to deal with this problem. Here, the basic philosophies underlying the Vidale (1988) and Qin et al. (1990) algorithms have been used to design a technique for solving the anisotropic eikonal equation.

Rather than a conventional Cartesian grid, a hexagonal mesh of points is used (Fig. 4.4), similar to grids employed in modeling studies involving cellular automata (Rothman, 1988). One reason for this choice is that  $qSV$  wavefronts in many anisotropic solids (with a vertical or horizontal axis of symmetry) tend to possess triplication zones along  $45^\circ$  azimuths (Musgrave, 1970). These directions coincide with corners of the

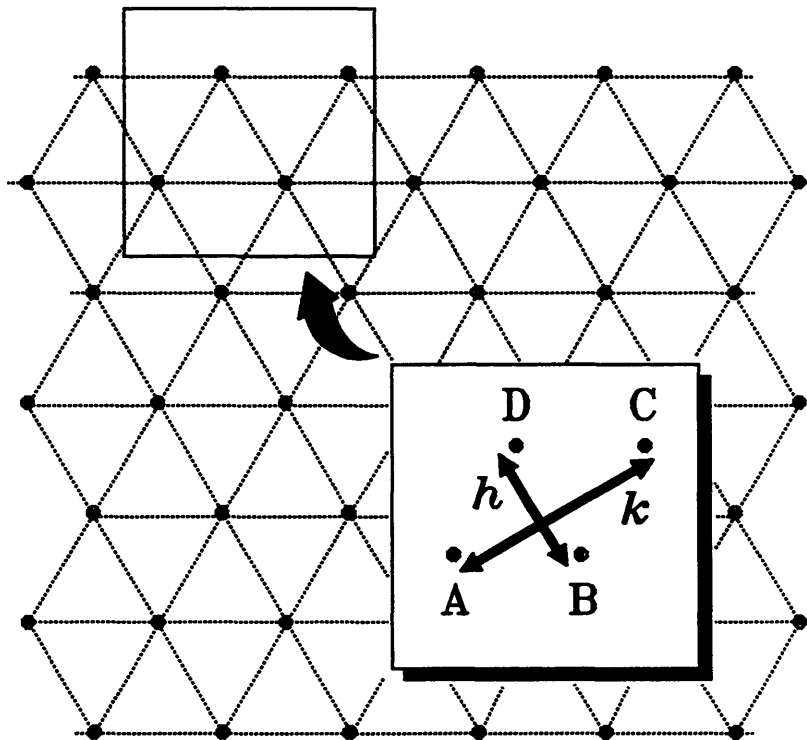


**Fig. 4.4.** Hexagonal mesh used for finite-difference calculations. Inset: Example of a four-point finite-difference stencil.

---

computational front used in Vidale's (1988) Cartesian implementation, where the errors are largest. In addition, the hexagonal grid permits the use of finite-difference stencils with a denser angular coverage than the Cartesian grid. This feature is particularly important when phase velocity varies rapidly with direction.

For the general three-dimensional, anisotropic case, solving the eikonal equation requires the solution of a sixth-order polynomial (Appendix C). In essence, the strategy is to use estimates of two components of the slowness vector,  $\mathbf{p}$ , to deduce the value of the third component. The problem is simplified for  $2\frac{1}{2}$ -dimensional propagation in the

plane of symmetry, since  $p_2$  (the component of slowness normal to the symmetry plane) vanishes. Suppose, then, that for a given four-point stencil, the traveltimes are known at points A, B and D (Fig. 4.4). This stencil defines a local co-ordinate system, with the  $x_3$ -axis pointing from A to C. Because this direction may not coincide with the anisotropic symmetry axis, it is generally necessary to rotate the stiffness tensor into the correct orientation. Using the approximation

$$p_1 \approx \frac{\tau_D - \tau_B}{h} \quad , \quad (4.1)$$

the traveltimes at point C is approximated by

$$\tau_C = \tau_A + p_3 k \quad . \quad (4.2)$$

In equation (4.2),  $p_3$  is chosen to satisfy the eikonal equation,

$$\det |c_{ijkl} p_j p_l - \rho \delta_{ik}| = 0 \quad , \quad (4.3)$$

at the centre of the stencil. Substituting equation (4.1) into (4.3) leads to a sixth-order polynomial equation for  $p_3$ ,

$$\xi_j p_3^j = 0 \quad , \quad j=0, \dots, 6 \quad . \quad (4.4)$$

The coefficients of equation (4.4) are given in Appendix C.

Fixing  $p_1$  and  $p_2$  in equation (4.4) leads to six possible solutions for  $p_3$ , corresponding to three different wave types, propagating either away from or toward the source. Degeneracies occur for the following cases:

1) at a shear-wave singularity (or if the medium is isotropic), in which case the two shear-wave solutions have the same value;

2) if  $p_1$  is zero, in which case the function  $f(p_3) = \xi_j p_3^j$  reduces to a cubic

polynomial in  $p_3^2$ .

With the exception of these special cases, all seven of the coefficients are nonzero. Graphs of  $f(p_3)$  are shown in Fig. 4.5, calculated using stiffness parameters for the Greenhorn shale. Fig. 4.5a shows  $f(p_3)$  with the local  $x_3$ -axis orientated at an angle of  $5^\circ$  with respect to the symmetry axis. Because this is very close to a shear-wave singularity, the  $qSV$  and  $SH$  solutions are nearly the same, and become equal for propagation in the direction of the singularity. Fig. 4.5b shows  $f(p_3)$  with the local  $x_3$ -axis normal to the symmetry axis. The two shear-wave solutions are now easily distinguished.

In this thesis, an iterative technique is used to solve  $f(p_3)$ . First, the direction of propagation with respect to the local axis of symmetry is estimated. Using this, along with knowledge of the wave type (i.e.,  $qP$ ,  $qSV$  or  $SH$ ), an initial guess of the phase velocity can be obtained using equation (2.12), which in turn can be used to give an estimate of  $p_3$ , knowing  $p_1$ . Starting with this initial guess, Newton's method is employed to refine the solution. For most cases, this approach converges rapidly (in approximately 1 to 8 iterations, depending on the degree of anisotropy). The algorithm has the most difficulty near a shear-wave singularity because of the locally nonlinear nature of  $f(p_3)$  (Fig. 4.5a).

Following Vidale (1988), the initial step in the overall procedure is to time the points in the immediate vicinity of the source point (the source is given a travelttime of zero). For the type of grid considered here, there are six grid nodes that neighbour the source point (Fig. 4.6a), forming a hexagon. The travelttime to each neighbouring point is simply

$$\tau = \Delta x/v \quad , \quad (4.5)$$

where  $\Delta x$  is the distance between each node on the grid and  $v$  is the group velocity given

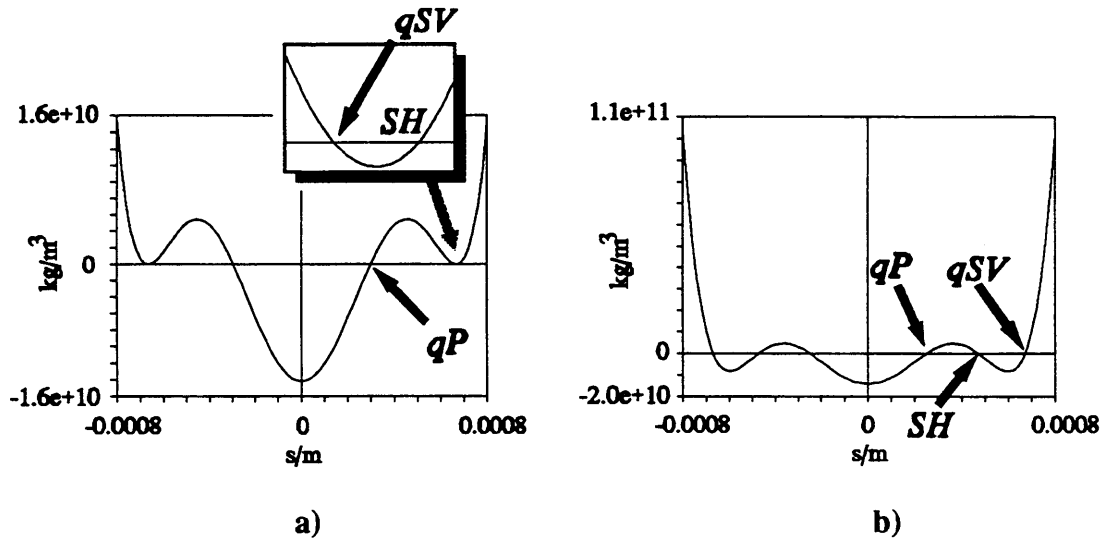


**Fig. 4.5.** a) Plot of  $f(p_3) = \xi_j p_3^j$  for the Greenhorn shale ( $p_1 = p_2 = 0$ ), with the  $x_3$ -axis of the finite-difference stencil oriented  $5^\circ$  from the axis of symmetry. Because this is close to a shear-wave singularity, the  $qSV$  and  $SH$  solutions are nearly the same (see inset). b) Plot of  $f(p_3)$  when the local  $x_3$ -axis is normal to the axis of symmetry.

by equation (2.15). This set of six points comprises the initial computational front. After each subsequent iteration, the new computational front is taken to be the set of points that have been timed, but are not completely surrounded by a timed point (circles in Fig. 4.6). This set of points will roughly approximate the true wavefront at each iteration. The algorithm proceeds by determining the node that has the minimum traveltime on the computational front. The traveltime to all nodes bordering the minimum are then computed by solving equation (4.4) as described above. By rigorously working away from traveltime minima, this method honours the principle of causality, even in the presence of large parameter contrasts (Qin et al., 1990). The procedure is repeated until all points on the grid within some prespecified zone of interest have been timed.

In many cases, ambiguities can still exist. That is, there may be several ways to

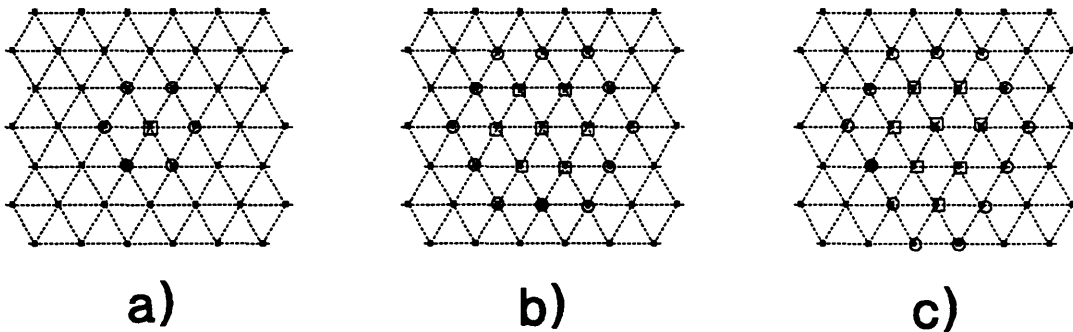


**Fig. 4.6.** a) The first step in the algorithm is the calculation of times for the six neighbouring points around the source point (square). The current wavefront is represented by circles. The solid circle indicates the point with the minimum  $\tau$  on the current wavefront. b) Timed points after several more iterations. Squares represent points that are timed, but not on the current wavefront. c) Timed points one iteration after b).

---

construct a finite-difference stencil connecting an untimed node to three neighbouring timed points, each giving a slightly different answer. Vidale (1988) handled this case by choosing the configuration that produces the minimum traveltime. However, applying this strategy to anisotropic media produces incorrect results. The criterion used here to select the correct stencil configuration, where ambiguities exist, is to minimize the tangential slowness term. This is equivalent to finding the stencil that extrapolates the traveltime most nearly normal to the wavefront. Note that this approach implicitly minimizes the traveltime for the isotropic case.

#### 4.2.2 Examples

The first example represents a homogeneous isotropic medium. The source is located in the centre of the grid, which spans an area of 1000 m by 623 m. A grid

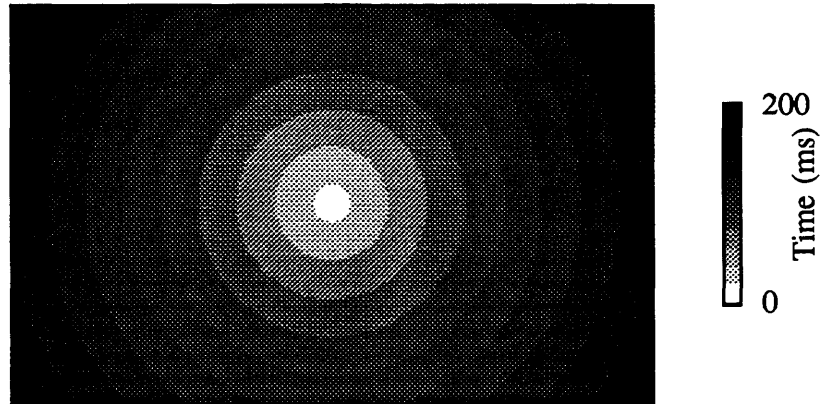


**Fig. 4.7.** Finite-difference  $P$ -wave traveltimes for model 4.1.

interval of 10 m was used, giving approximately 7200 grid nodes. Fig. 4.7 shows the computed  $P$ -wave traveltimes for this model. In the grey-scale scheme used to display these data, the light areas represent small traveltimes (close to the source) and the dark areas represent large traveltimes. Since a wavefront is a surface of constant traveltime (Aki and Richards, 1980), the shapes of the wavefronts are defined by the boundary between different shades of grey. In this case, the wavefronts do not exhibit any visible anisotropic artifacts, and the maximum traveltime error on the grid is 0.8 ms (0.7%).

The second example illustrates the behaviour of the algorithm for a homogeneous, strongly anisotropic medium. Fig. 4.8 shows the traveltime field computed in the Greenhorn shale for all three wave types. Overall, the wavefronts have the correct geometry for this material (see Fig. 2.2). However, since the traveltime field computed using this method is single-valued, the behaviour of the  $qSV$  wavefront in the triplication zone cannot be replicated. Instead, the calculated wavefronts possess an abrupt corner in this region, approximating the first arrival.

The traveltime error ( $\tau_{\text{finite-difference}} - \tau_{\text{analytic}}$ ) is displayed in Fig. 4.9. For the  $qSV$

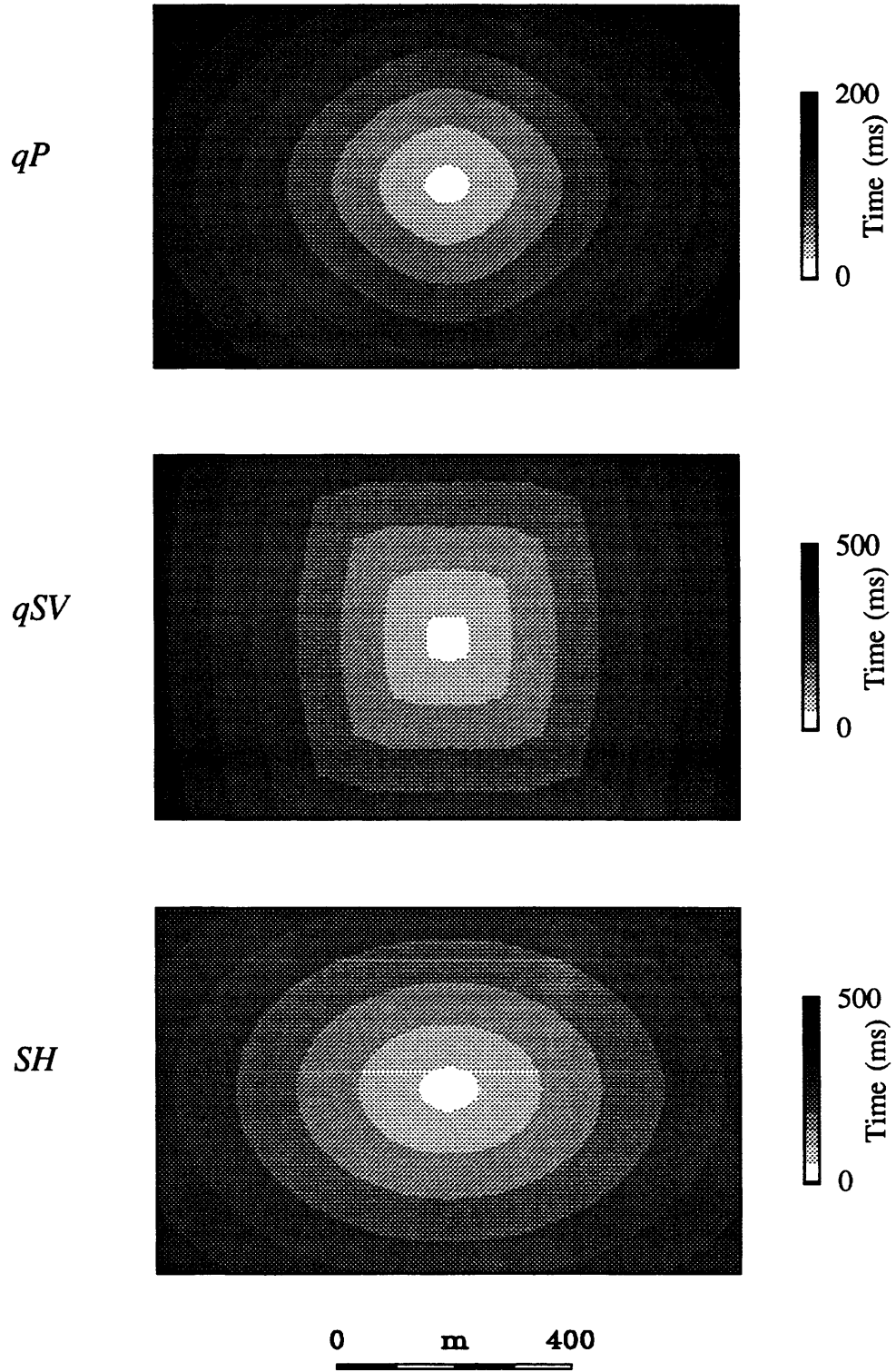


Fig. 4.8. Finite-difference traveltimes computed for model 4.2.

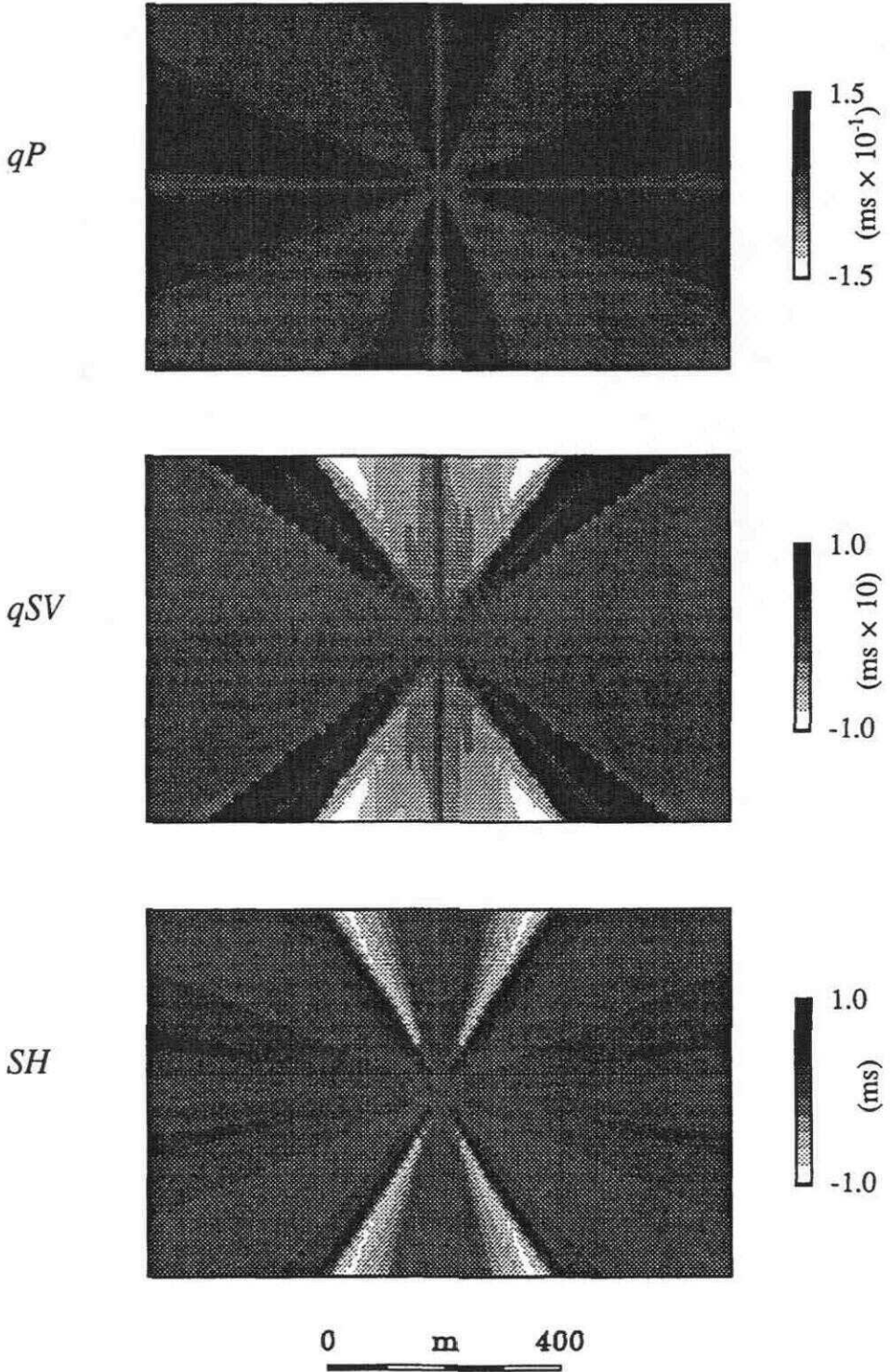


Fig. 4.9. Finite-difference traveltime error for model 4.2.

wavefront, the "analytic" traveltime in the triplication zone is taken to be the first arriving branch. For  $qP$  waves, the error is less than 0.15 ms, or 0.1% error at the edge of the grid. The magnitude of the error is similar for  $SH$  waves, except near singularities. The maximum error in this case is about 1 ms, or 0.25% error at the edge of the grid. The error is significantly larger for  $qSV$  waves, particularly within the triplication zone and close to the symmetry axis. In the latter case, the large errors are due to numerical difficulties associated with solving the eikonal equation near a shear-wave singularity.

The third example represents a medium characterized by an increase in velocity with depth, coupled with vertical fracturing. In the absence of fracturing, raypaths for this type of medium fall along the arcs of circles. Computed traveltimes for a source located at a depth of 744 m are shown in Fig. 4.10. Note again the unusual shape of the  $qSV$  wavefronts. For this model, ray-traced traveltimes have also been calculated in order to verify the accuracy of the finite-difference results. Kinematic ray tracing calculations were performed by solution of the anisotropic ray-tracing system (Červený, 1972)

$$\begin{aligned}\frac{\partial x_i}{\partial \tau} &= a_{ijkl} p_j g_k g_l \\ \frac{\partial p_i}{\partial \tau} &= -1/2 (a_{mjkl})_{,i} p_m p_j g_k g_l \quad , \\ a_{ijkl} &= c_{ijkl} / \rho\end{aligned}\tag{4.6}$$

using a fourth-order Runge-Kutta technique (Press et al., 1990). A complete discussion of the numerical implementation of anisotropic ray tracing is given by Gajewski and Psenčík (1987). Fig. 4.11 shows a comparison between ray-traced and finite-difference traveltimes at the top of the model. The agreement between the two techniques in this case is excellent.

The fourth example tests the algorithm in the presence of a boundary separating

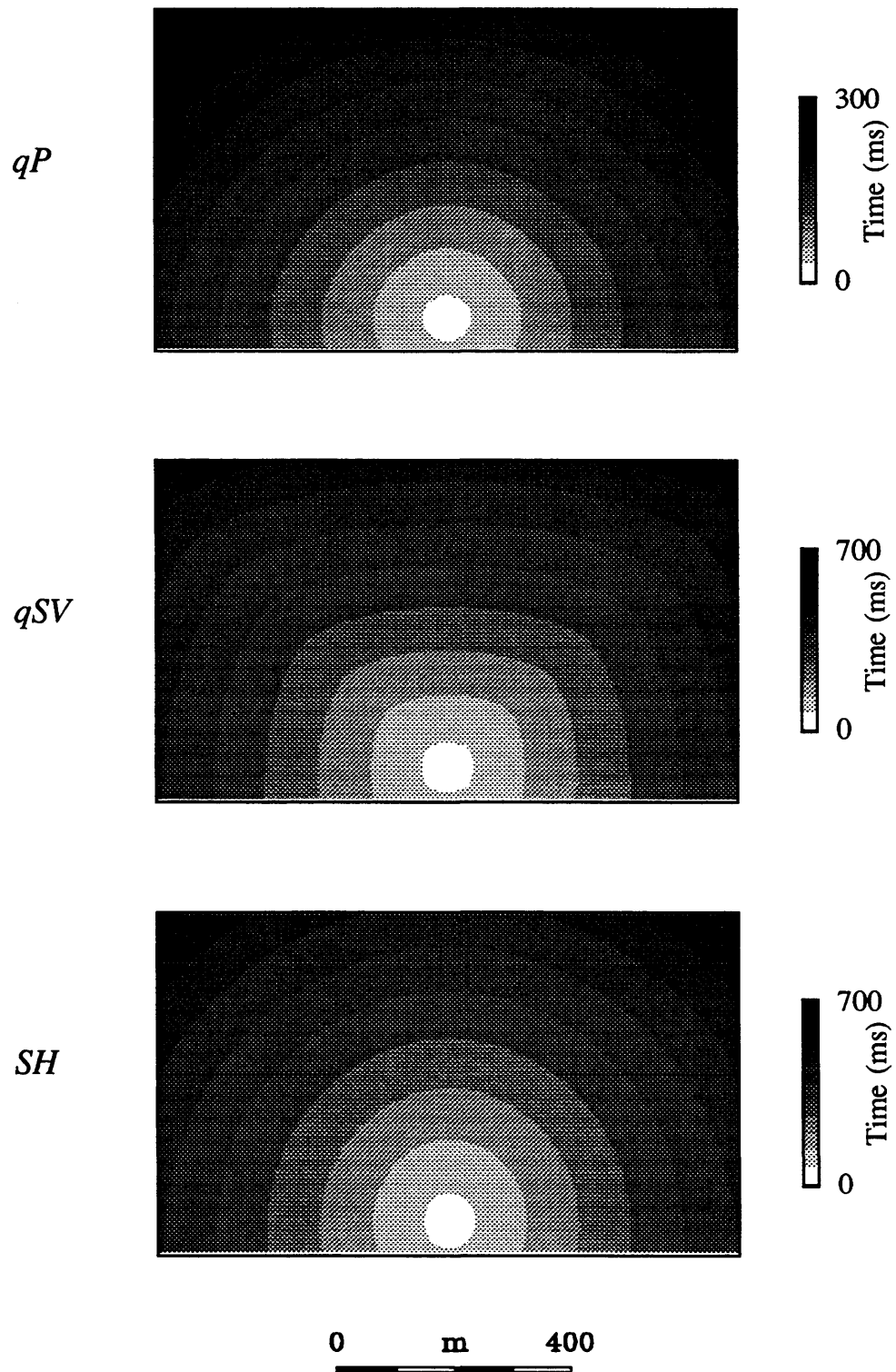


Fig. 4.10. Finite-difference traveltimes for model 4.3.

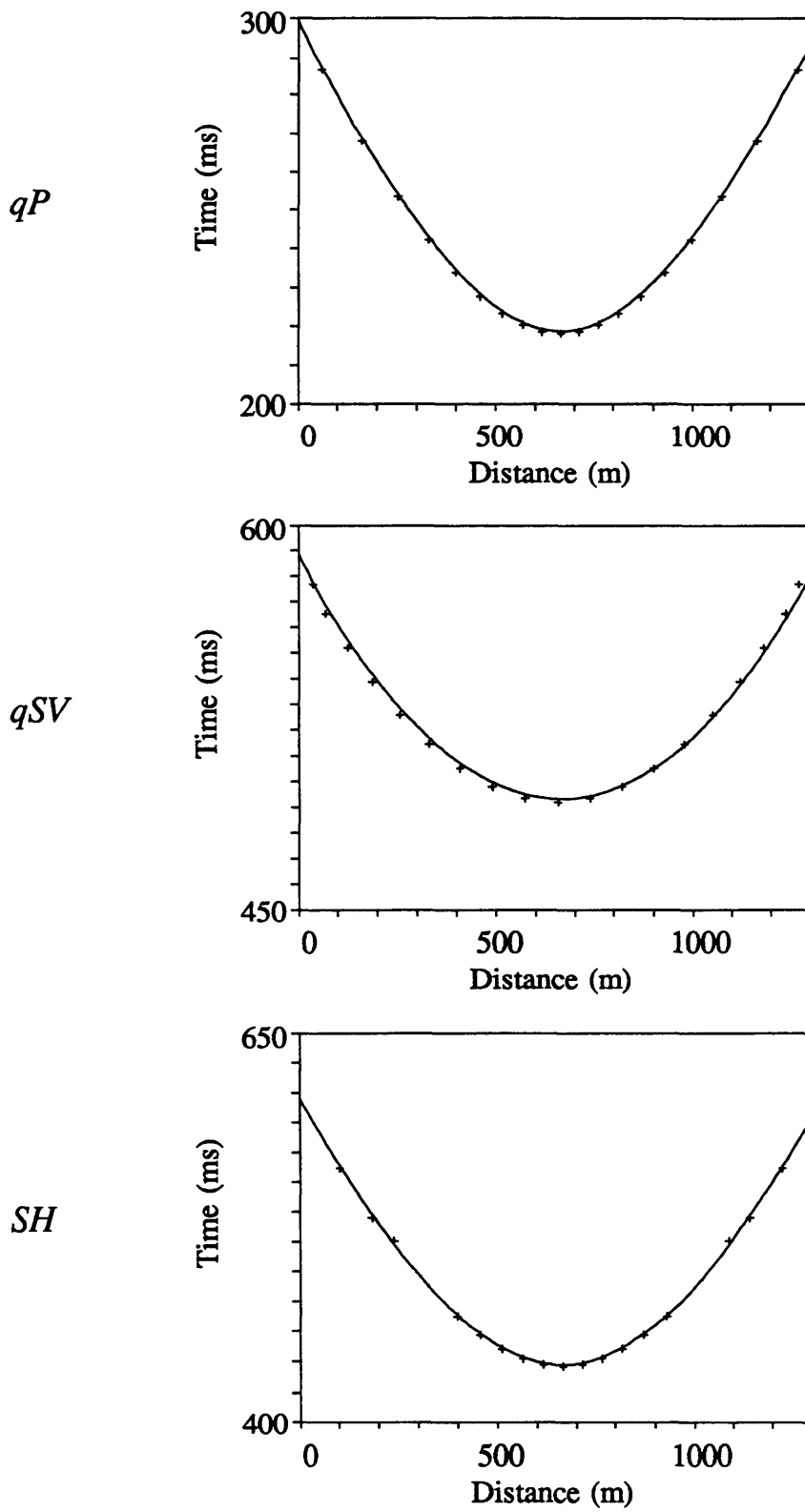
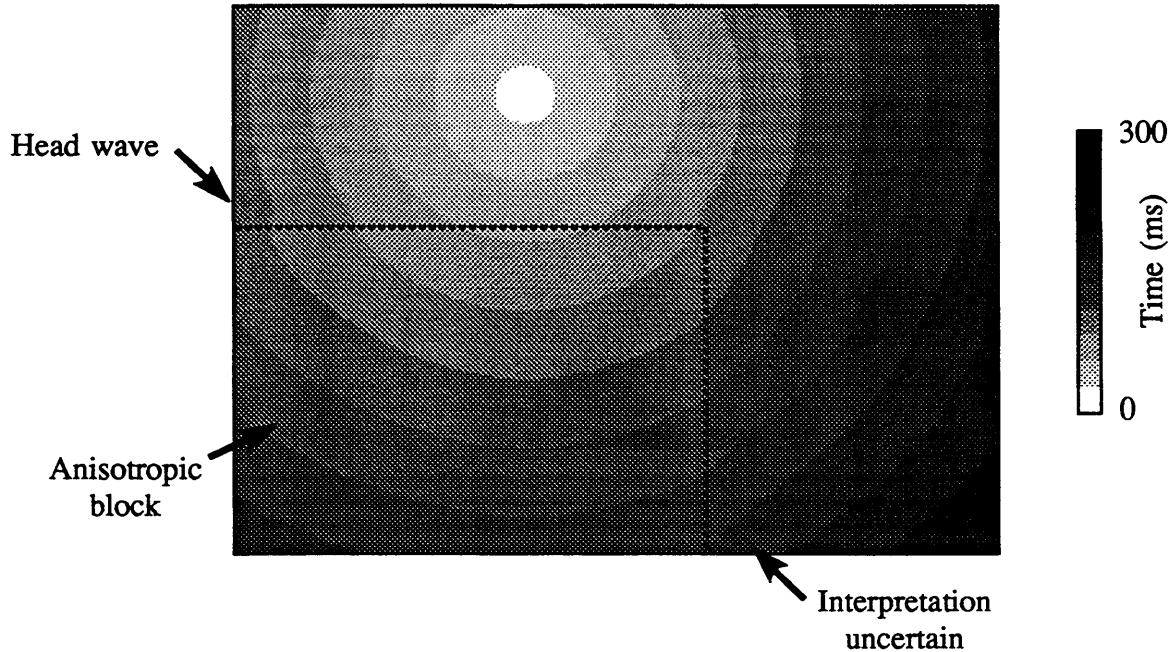


Fig 4.11. Ray-traced (+'s) and finite-difference (lines) traveltimes at top of model 4.3.



**Fig. 4.12.** Finite-difference  $qP$  traveltimes for model 4.4.

an anisotropic region from an isotropic region. At the interface, the wavefronts exhibit noticeable change in shape (Fig. 4.12). A refracted head wave travelling along the top of the isotropic/anisotropic boundary is also evident. However, interpretation of the wavefield immediately to the right of the anisotropic block (within the isotropic material) is uncertain. Possible interpretations are:

- 1) diffraction from the corner of the anisotropic block;
- 2) diffracted head wave along the vertical boundary;
- 3) a refracted wave through the anisotropic material.

It is most likely that the computed wavefield, ideally representing the first arrival, contains elements of more than one of these possibilities. Note that the critical angle and velocity of propagation for head waves along this type of boundary are functions of the angle between the interface and the anisotropic symmetry axis.

The final example considered in this chapter is intended to illustrate the behaviour of these algorithms for a complex background model, representing an anticline structure. The shallowest layer is modeled using a transversely isotropic medium composed of alternating thin layers of sandstone and shale (Levin, 1979). The two layers beneath this zone are also anisotropic, with the intensity of anisotropy increasing toward the core of the anticline (see Fig. 4.3), where structural deformation is the greatest. Beneath this is a basement unit, characterized by a linear velocity gradient, with the largest velocities in the core of the anticline. The source is positioned on one side of the anticline, to simulate the scenario of a downhole source in a well that missed the crest of the structure. The computed  $qP$  traveltimes are illustrated in Fig. 4.13. The traveltime fields for shear waves are not shown, but are very similar in appearance. The wavefield distortion due to anisotropy in the core of the anticline is easily visible, as are larger scale effects attributable to the overall velocity increase toward the core of the structure.

### 4.3 Calculation of eigenvectors

In a transversely isotropic medium, the particle motion associated with  $qP$  and  $qSV$  waves can deviate from the purely longitudinal and transverse directions which characterize an isotropic medium. Thus, it is necessary to determine the direction of particle motion by computing normalized eigenvectors of the matrix  $\Gamma_{ik} = c_{ijkl} p_j p_l$ . In principle, this task is relatively straightforward since the slowness  $\mathbf{p}$  is readily computed by differentiating the known traveltimes. In practice, some care must be exercised since the computed slownesses are approximate, so that  $\Gamma_{ik}$  is generally nonsingular. Also, at a shear-wave singularity the  $qSV$  eigenvector possesses, in theory, an additional degree of freedom. The added constraint is that  $qSV$  waves are polarized in the acquisition plane.

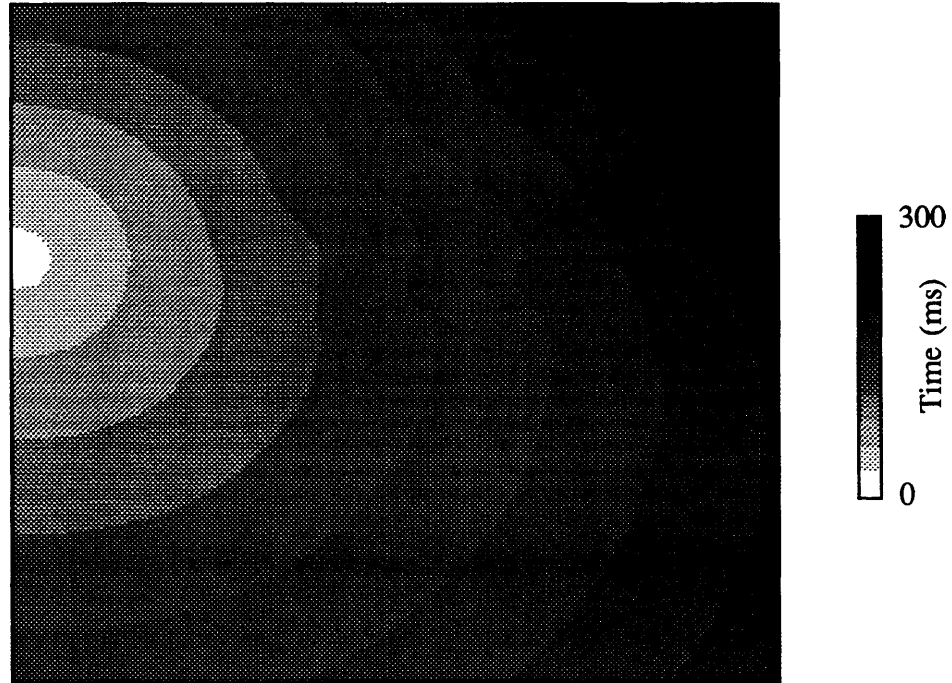


**Fig. 4.13.** Finite-difference  $qP$  traveltimes for model 4.5.

---

### 4.3.1 Description of the algorithm

The program for computing eigenvectors is split into two parts. The first sub-routine attempts to extract two rows from  $\Gamma$  that represent independent equations. Two empirical criteria are used to reject a row:

1) if the power (sum of squares of each coefficient) of the row is less than the threshold value of  $\rho v^2/6$ ;

2) if, after normalization to unit power, the row vector makes an angle of less than  $5^\circ$  with a preceding row.

Once two independent rows have been determined, the eigenvector is found by simply solving the system of two equations. Geometrically, each row is the equation of a plane

in which particle motion is permitted, and the eigenvector lies along the intersection of these two planes.

### 4.3.2 Examples

Only two of the five examples are considered in this section. Fig. 4.14 shows the angular difference between the particle motion vector computed from the finite-difference traveltimes (Fig. 4.8) and the analytic solution. For  $qP$  waves, the computed eigenvalues are very accurate, with errors less than  $\sim 0.01$  radians, except in the near field. For  $qSV$  waves, small irregularities in the computed traveltimes result in large errors in the calculated polarization directions, since the latter depend on derivatives of  $\tau$ . The computed eigenvectors are most accurate for directions of propagation that make a large angle with respect to the axis of symmetry. Within the triplication zones and near singularities, the errors are very large ( $> 0.25$  radians).

The absolute eigenvector directions (with respect to the positive  $x_3$ -axis) for model 4.5 are shown in Fig. 4.15. For the most part, the particle-motion direction appears to fan out parallel to the raypaths emanating from the source point, since the anisotropy is weak at the sides of the model. However, significant distortion is visible in the centre of the structure.

## 4.4 Initial-slowness calculation

Two initial ray parameters, denoted  $\gamma_1$  and  $\gamma_2$ , are required in general to uniquely specify (in three dimensions) a ray at the source.  $\gamma_1$  and  $\gamma_2$  can be computed from the initial slowness, and may be, for example, initial phase angle with respect to the  $x_2$  and  $x_3$  axes ( $\theta$  and  $\phi$ ). Knowledge of the initial ray parameters is required to compute the source amplitude radiation pattern, and can also be used to estimate the geometrical-

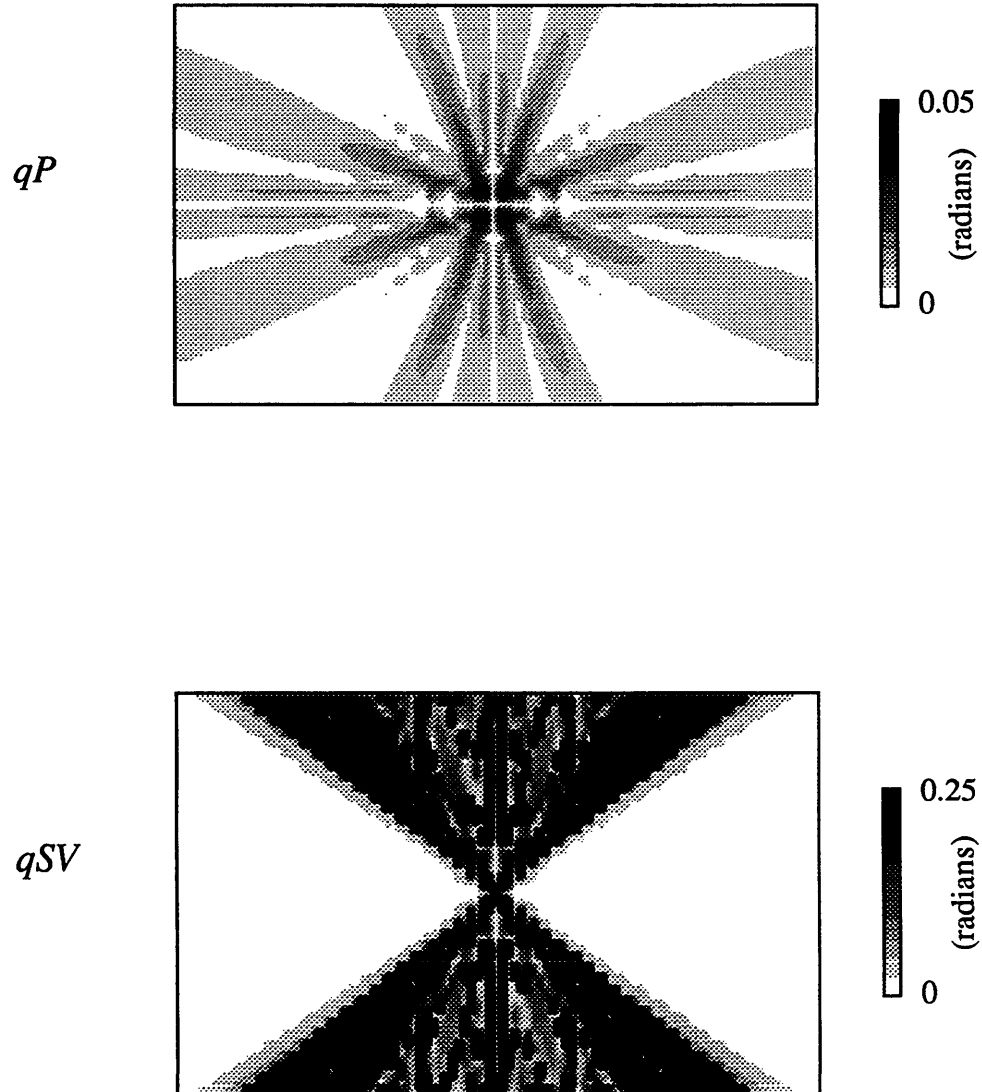


**Fig. 4.14.** Angular difference between the eigenvector (polarization vector) computed using the finite-difference traveltimes and the analytic solution, for model 4.2.  $SH$  waves are not shown, since the corresponding particle motion is always in the  $x_2$ -direction.

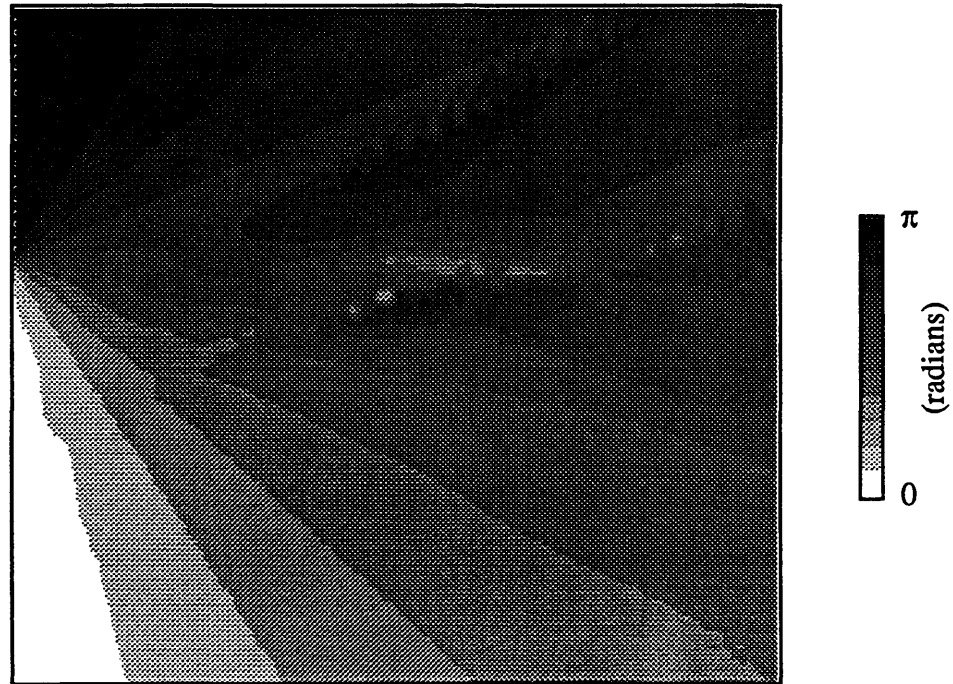


Fig. 4.15.  $qP$  polarization direction with respect to the  $x_3$ -axis for model 4.5.

---

spreading function. In conventional ray tracing, the initial parameters are readily available (they must be, in order to trace rays). However, determination of these parameters is less straightforward using a finite-difference approach, since in a general  $2\frac{1}{2}$ -dimensional medium both the  $p_1$  and  $p_3$  components of slowness can vary along a ray. Recently, Vidale and Houston (1990) suggested a method for computing the initial slowness, that exploits the finite-difference approach for travelttime calculation. Their technique was cast in terms of an isotropic model and a Cartesian coordinate system, but is equally valid for anisotropic media, and is easily adapted to the hexagonal grid system employed here.

#### 4.4.1 Description of the algorithm

The method of Vidale and Houston (1990) derives from the principle of reci-

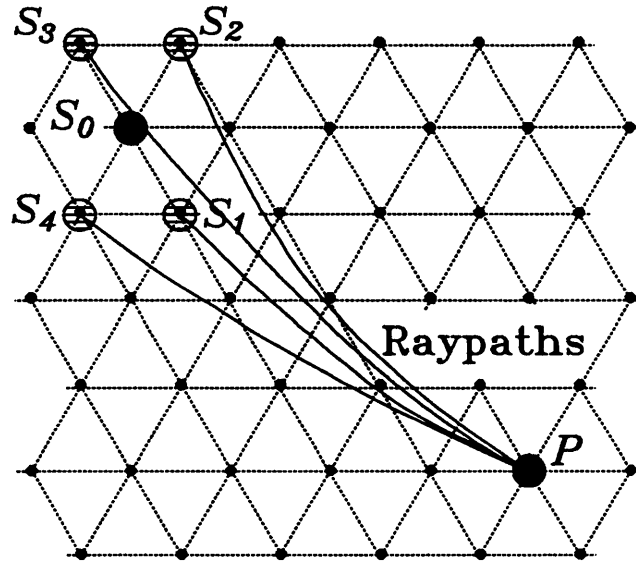


**Fig. 4.16.** Sketch of the raypaths joining four closely spaced source points ( $S_1$ ,  $S_2$ ,  $S_3$  and  $S_4$ ) to a point  $P$  on the grid (modified from Vidale and Houston, 1990). Differentiating the traveltimes computed from the four neighbouring source points yields the initial slowness for the ray from  $S_0$  to  $P$ .

---

procuity (Aki and Richards, 1980), which implies that the source and receiver can be interchanged with no effect on the total traveltime. In their approach, the traveltime is recomputed using four perturbed source positions, arranged around the actual source position,  $S_0$ . Fig. 4.16 shows the configuration for the four perturbed source positions,  $S_1, \dots, S_4$  on the hexagonal grid. By reciprocity, the perturbed traveltimes are the same as those that would have been received at  $S_1, \dots, S_4$  using point  $P$  as the source. Based on this observation, it is easily shown that final value of the slowness vector on the ray from  $P$  to  $S_0$  and the initial slowness on the ray from  $S_0$  to  $P$  have the same magnitude, but are in the opposite direction. Hence, the initial slowness at  $S_0$  is given approximately by

$$\begin{aligned}
 p_1^0 &= \frac{-\tau_1 - \tau_2 + \tau_3 + \tau_4}{2\Delta x} \\
 p_3^0 &= \frac{-\tau_1 + \tau_2 + \tau_3 - \tau_4}{2\sqrt{3}\Delta x}
 \end{aligned}
 \tag{4.7}$$

where  $\tau_j$  is the travelt ime from  $S_j$  to  $P$ , and  $\Delta x$  is the spacing between grid points. Instead of storing the initial slowness components, it is more efficient to store in memory the initial phase angle,

$$\theta_0 = \tan^{-1}(p_1^0/p_3^0) \quad . \tag{4.8}$$

It is often necessary to smooth the computed values of  $\theta_0$  to remove erroneous fine-scale variations. This is accomplished here by low-pass filtering the data, with a cutoff wavenumber equal to one quarter of the Nyquist. Note also that for the isotropic case,  $\theta_0$  is equivalent to the ray takeoff angle, but for the anisotropic case the two are not exactly equivalent.

#### 4.4.2 Example

Fig. 4.17 illustrates the  $qP$  initial phase angle calculated for model 4.5. The regular pattern of rays fanning out near the source becomes disrupted due to inhomogeneity/ anisotropy in the centre of the model. Note the rapid change in phase angle roughly along the arc  $SA$ . This behaviour is indicative of a caustic, and will be discussed in the section on amplitude calculation, below.

### 4.5 Out-of-plane spreading function

The matrix of partial derivatives of the travelt ime field,  $\mathbf{N}$ , has the structure

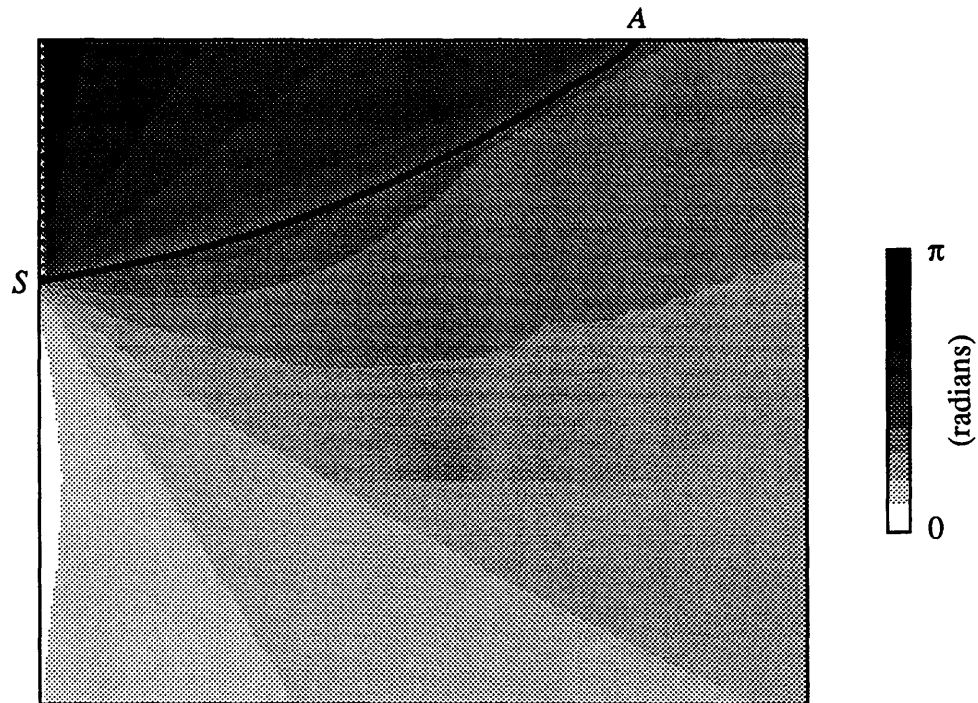


**Fig. 4.17.**  $qP$  initial phase angle ( $\theta_0$ ) for model 4.5.  $\theta_0$  changes rapidly along the arc  $SA$ , indicating the likely presence of a caustic.

---


$$\mathbf{N} = \begin{bmatrix} \tau_{,11} & 0 & \tau_{,13} \\ 0 & \tau_{,22} & 0 \\ \tau_{,31} & 0 & \tau_{,33} \end{bmatrix}, \quad (4.9)$$

for the assumed  $2\frac{1}{2}$ -dimensional symmetry of this study. This matrix expresses the curvature of the wavefront. Here, the "out-of-plane spreading function" is understood to be  $\tau_{,22}$ , since it is the only wavefront-curvature parameter that cannot be estimated directly from the in-plane traveltime values.  $\tau_{,22}$  also distinguishes two-dimensional spreading from  $2\frac{1}{2}$ -dimensional spreading, and is required in the inversion procedure to account for out-of-plane scattering effects.

### 4.5.1 Description of the algorithm

The value of  $\tau_{,22}$  for each point on the grid is estimated as follows. First, a suite of rays are traced away from the source in  $1^\circ$  increments of  $\theta_0$ . The initial slowness of each ray is given a small positive  $p_2$  component that remains constant as the ray propagates. At every point  $P$  along a ray, let  $P'$  be its projection onto the plane  $x_2 = 0$ . At the point  $P'$ , using the fact that  $p_2 = 0$  and has mirror symmetry across the acquisition plane, we have

$$\tau_{,22} \approx \frac{p_2}{y} \quad , \quad (4.10)$$

where  $y$  is the  $x_2$ -component at  $P$ . The parameters  $y(\theta_0, \tau)$  and  $p_2(\theta_0)$  are also required for later use during the calculation of seismic amplitudes. The values of  $\tau_{,22}$  are then extrapolated from each ray to neighbouring points on the grid. This set of 360 rays is usually sufficient to give  $\tau_{,22}$  for most points on the grid. Holes in the coverage are filled by tracing additional rays, using the computed initial slowness values from the previous step as a guide.

A potential shortcoming of this approach, when used in conjunction with the finite-difference traveltimes method, is the possibility that the raypaths determined by raytracing will not match the first-arriving wavefronts propagated by the in-plane traveltimes calculation (e.g., for head waves, diffractions, etc.). At present, no automatic method has been devised to ensure that this scenario does not occur. However, experience has indicated that  $\tau_{,22}$  tends to be very smooth and continuous. Thus, errors introduced in the amplitude calculations and in the inversion procedure by using a value for  $\tau_{,22}$  corresponding to a later arrival are likely to be relatively small.

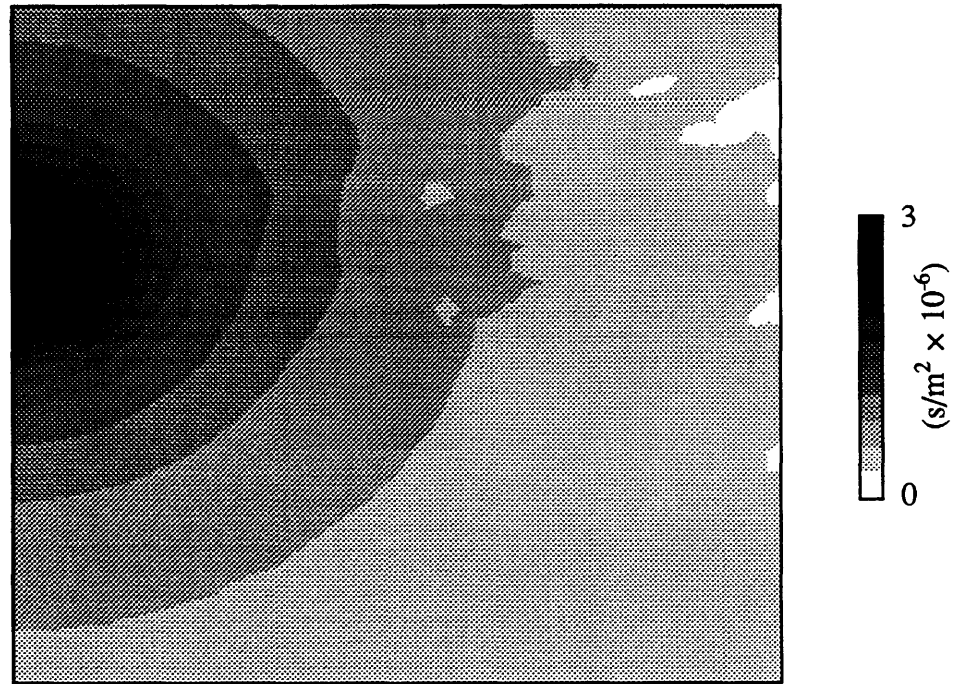


**Fig. 4.18.**  $qP$  out-of-plane spreading factor ( $\tau_{22}$ ) for model 4.5.

#### 4.5.2 Example

Fig. 4.18 illustrates  $\tau_{22}$  for  $qP$  waves in model 4.5. The out-of-plane spreading function in this (and other) model(s) is generally quite smooth, and decays approximately as  $r^{-1}$ , where  $r$  is distance from the source. The grey shading is opposite to the traveltime plot (Fig. 4.13), in the sense that the maximum values of  $\tau_{22}$  (dark regions) occur close to the source rather than in the far field.

#### 4.6 Estimation of seismic amplitudes

Knowledge of the initial-ray parameters at all points on the grid can be employed to obtain a useful estimate of the geometrical-spreading function. The ray-Jacobian,  $J$ , is related to a differential surface element on the wavefront via the relation  $d\sigma = J d\gamma_1 d\gamma_2$ ;

i.e., the ratio  $J_0/J$  ( $J \neq 0$ ) is equivalent to the surface-element ratio,  $L = d\sigma_0/d\sigma$ , contained within a ray tube (section 2.3). Thus, expansion and contraction of the ray tube, or an increase or decrease in the value of  $L^{-1}$ , corresponds to a geometrical amplitude decrease or increase, respectively.

#### 4.6.1 Description of the algorithm

Vidale and Houston (1990) have presented a method for approximate amplitude calculation based on these geometrical concepts. Here again, their basic technique is modified to suit the present algorithm. The initial assumption is that the length of intersection of the wavefront at a point  $P$  with the circular region containing the six points surrounding  $P$  (Fig. 4.19) is constant (roughly equal to  $2\Delta x$ ). The accuracy of this assumption depends on the in-plane radius of curvature of the wavefront, which should be large. The change in the first ray parameter,  $\theta_0$ , corresponding to this arc length,  $ds$ , is approximated by

$$\Delta\gamma_1 = \Delta\theta_0 \approx \max\{\theta_0\} - \min\{\theta_0\} \quad , \quad (4.11)$$

where  $\max\{\theta_0\}$  and  $\min\{\theta_0\}$  are the maximum and minimum initial phase angle from the set of six points surrounding  $P$ . Since  $ds$  is taken to be constant, the total area of the far-field surface element,  $d\sigma$ , is then proportional to the quantity  $y(\theta_0, \tau)$ . The corresponding near-field surface element,  $d\sigma_0$ , belonging to the respective ray tube can be estimated numerically for some arbitrary small traveltime, given  $\theta_0$ ,  $\Delta\gamma_1$ ,  $p_2(\theta_0)$  and knowledge of the geometry of the wavefront in a homogeneous region in the vicinity of the source. The amplitude function is then computed to within a scale factor that is independent of wave type and source position using the formula:

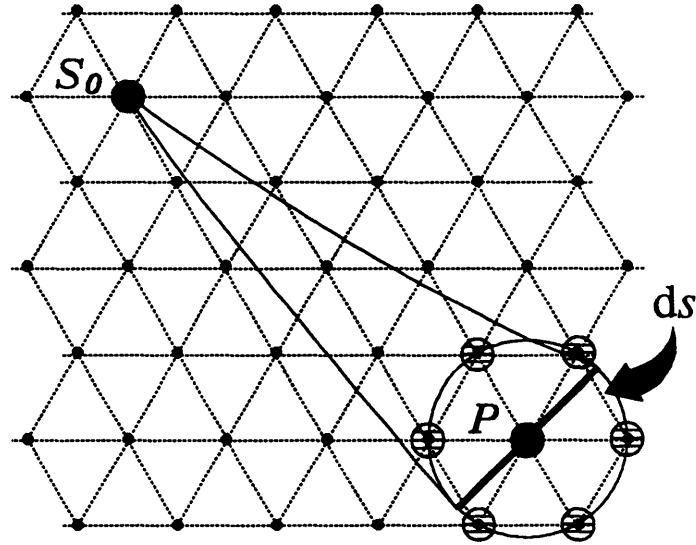


**Fig. 4.19.** Method for calculating  $\Delta\gamma_1$ . The total change in the initial phase angle corresponding to the line element  $ds$  on the wavefront is approximated by the difference  $\max\{\theta_0\} - \min\{\theta_0\}$  from the set of six points neighbouring  $P$ .

---


$$\hat{A} = \left[ \frac{\rho_0 V_0 d\sigma_0}{\rho V d\sigma} \right]^{1/2} A_0(\mathbf{p}^0) \quad , \quad (4.12)$$

where  $A_0$  is determined using equation (2.21).

The amplitude function obtained in this manner usually contains artifacts, due to the approximations made here, and small errors in the quantities computed from previous steps. As a general rule, a mild low-pass filter is applied to remove some of these artifacts. Another general limitation of this treatment of seismic amplitudes is the use of geometrical spreading only; amplitude variations related to reflection/ transmission at interfaces, attenuation, etc., are not accounted for.

### 4.6.2 Examples

Fig. 4.20a shows the relative amplitude function computed for model 4.1. The data have been scaled by an empirical constant, in order to bring a significant portion into the range 0.1 to 1.0 for display purposes. Overall, the computed values are a reasonable approximation to the theoretical  $1/r$  amplitude decay. However, certain undesirable artifacts are also clearly visible. These artifacts are caused by erroneous estimates of  $\Delta\gamma_1$  arising from the method described above. The computed amplitudes are somewhat higher for rays that make an angle with the vertical that is an integral multiple of  $30^\circ$ . A similar phenomenon was reported by Vidale and Houston, except that on a Cartesian grid the amplitudes are higher for rays every  $45^\circ$ . Fig. 4.20b shows a plot of the computed amplitudes along two horizontal cross-sections through the data in Fig. 4.20a, at  $z = 312$  m (the depth of the source) and  $z = 35$  m. The profile at  $z = 312$  m matches almost exactly the (scaled)  $1/r$  function (the two can barely be distinguished in Fig. 4.20b), whereas in the second case the fit is not as good, with a maximum error of about 7%. This degree of error does not seem as bad, however, when one considers that the amplitude function varies over nearly two orders of magnitude.

Figs. 4.21 and 4.22 show the computed and theoretical amplitude functions for the Greenhorn shale (model 4.2). Comparison of the two sets of plots reveals the presence of the aforementioned grid-related artifacts. In addition, certain artifacts visible in the shear wave plots can be correlated with errors in the traveltime field (Fig. 4.9). Nonetheless, the distinctive overall shapes of the amplitude contours are approximately represented for all three wave types, as is the ratio of about 4:1 between the shear wave amplitudes and the  $qP$  amplitude. The  $qSV$  amplitude plot also exhibits apparent caustics along the  $45^\circ$  directions with respect to the vertical. These are due to the presence of corners in the computed wavefronts (Fig. 4.8).

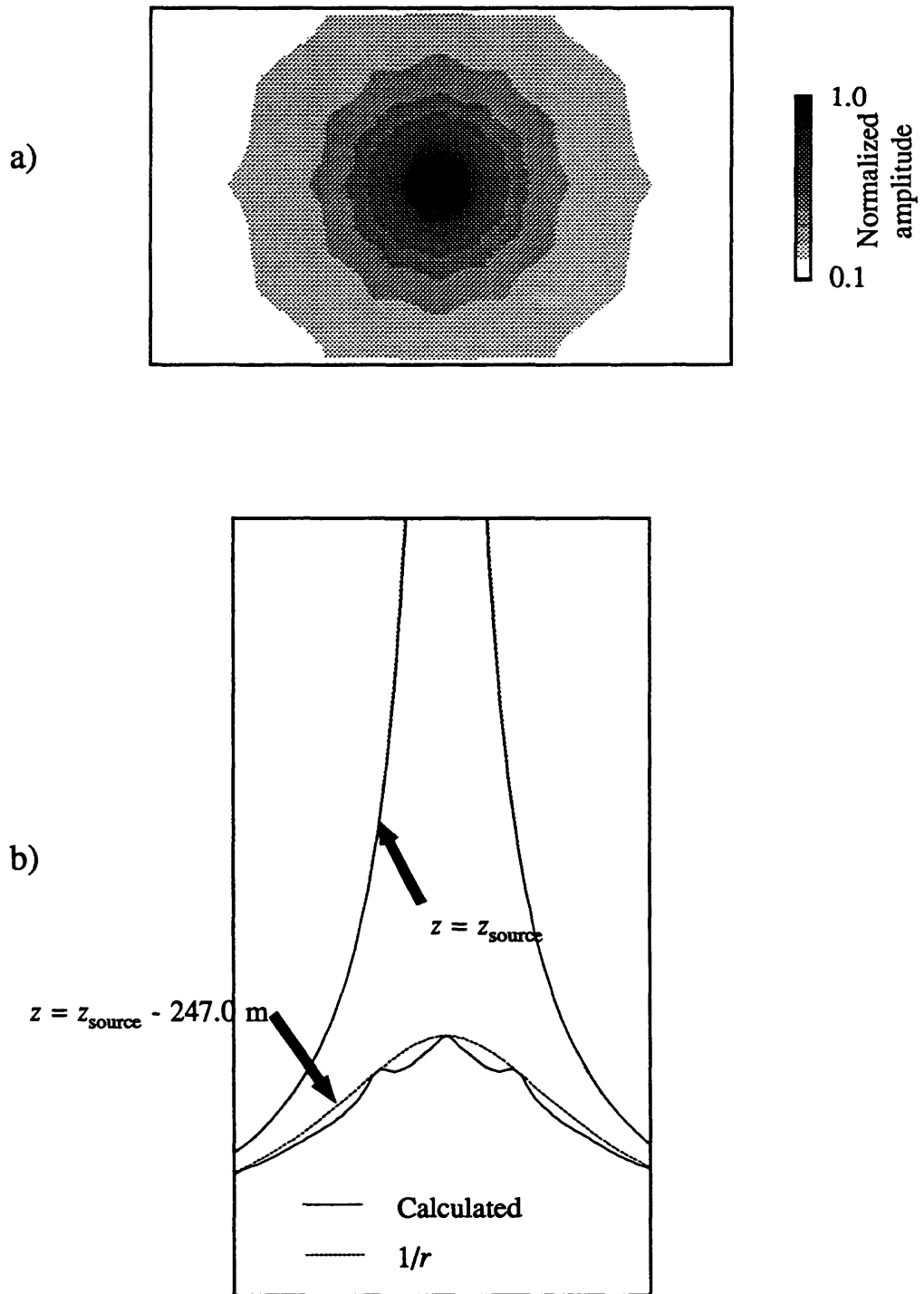


Fig. 4.20. a) Normalized amplitude values computed for model 4.1. b) Plot of normalized amplitudes near the top of the grid, and at the same depth as the source.

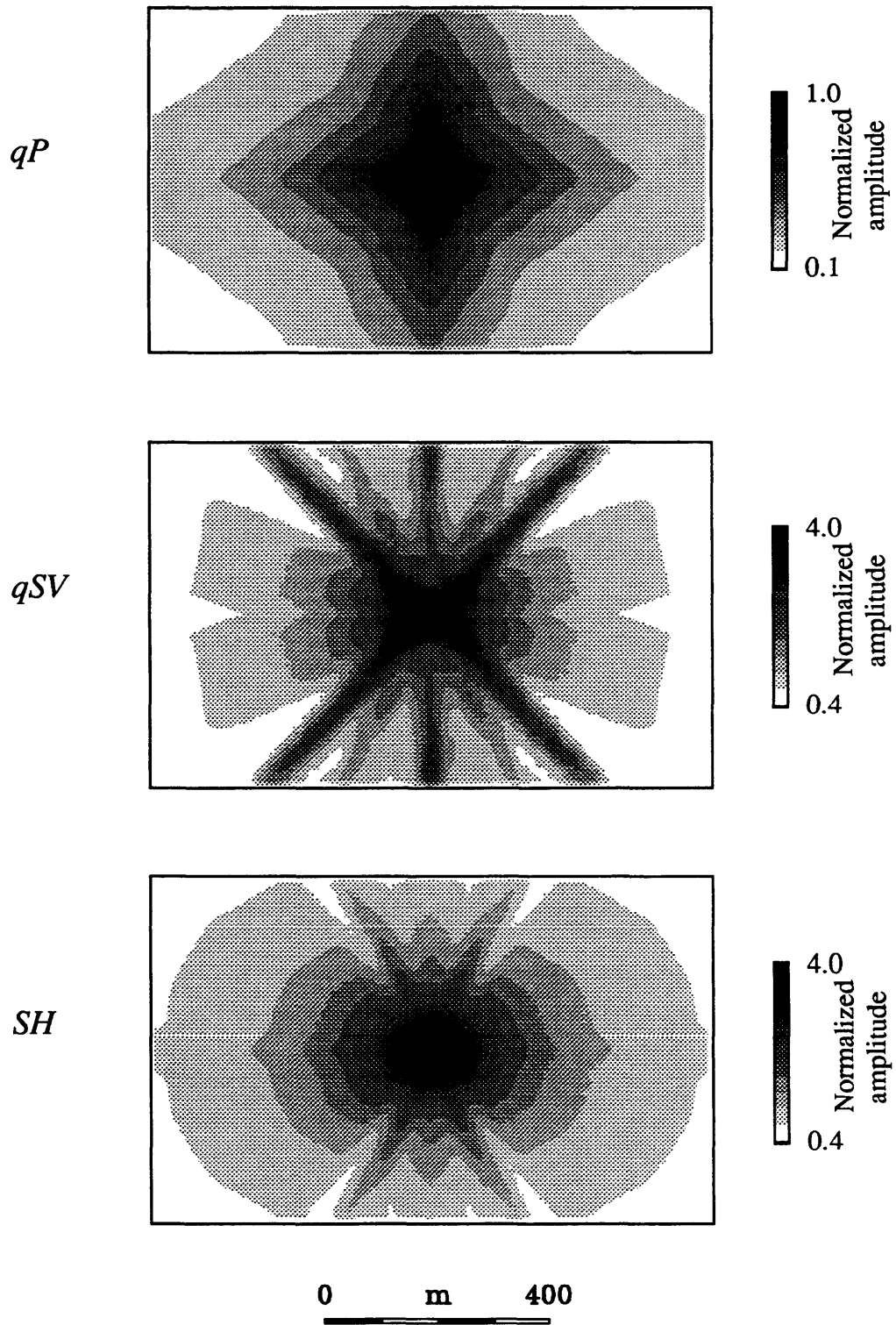


Fig. 4.21. Normalized amplitudes computed for model 4.2.

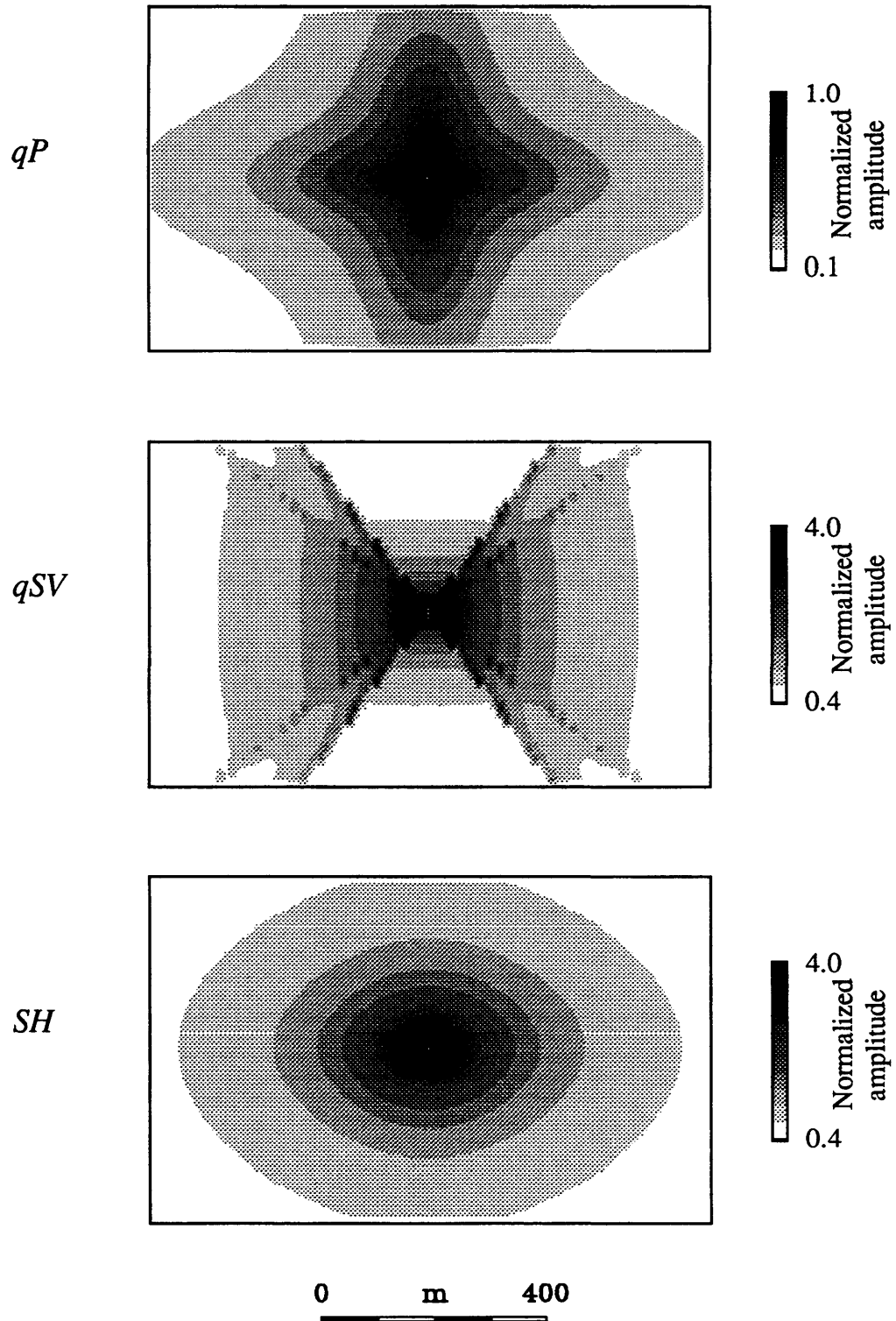


Fig. 4.22. Theoretical amplitude function (normalized) for model 4.2.

Figs. 4.23 and 4.24 show the calculated  $qP$  amplitudes for models 4.3 and 4.5. Fig. 4.24, in particular, is interesting because it clearly shows the presence of two caustics, one of which was apparent from the plot of initial phase angle (Fig. 4.17). These caustics are produced by focusing of rays in the velocity gradient zones. It is significant that the procedures used here for seismic modeling are tolerant of this type of anomalous feature, and behave in a numerically stable manner.

## 4.7 Concluding remarks

A new methodology has been presented for computing approximate ray-Green's tensors for  $2\frac{1}{2}$ -dimensional, transversely isotropic, elastic media. The procedure is based primarily on finite-difference solution of the anisotropic eikonal equation, and a ray-Jacobian approach for computing seismic amplitudes from a point source. All of the ray-Green's parameters are directly available on a grid, in a form that is well suited to imaging applications. Although the particular implementation described here is restricted to transversely isotropic media, the numerical methods used are easily generalizable to any anisotropic symmetry system. Due to the inability of these techniques to model triplication zones and other pathologic features of wavefronts in strongly anisotropic solids correctly, this method is ultimately restricted to use with moderately or weakly anisotropic media.

Another practical consideration here is program execution time. Running on a Sun Sparcstation 2, computation of the full Green's functions required about 20 minutes of CPU (on average) for the models described in this chapter. The traveltimes component of the calculation represented about 2 to 3 minutes. The bulk of the execution time was shared between the computation of initial slowness and the out-of-plane spreading factor. For each trace in a multicomponent dataset, three or more ray-Green's functions must

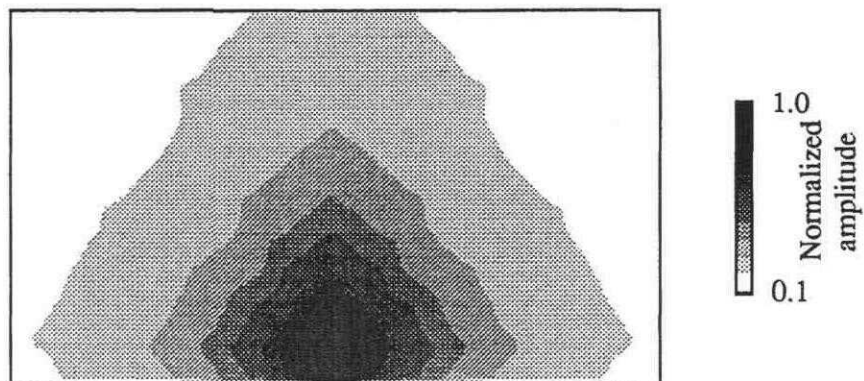


Fig. 4.23. Normalized amplitudes computed for model 4.3.

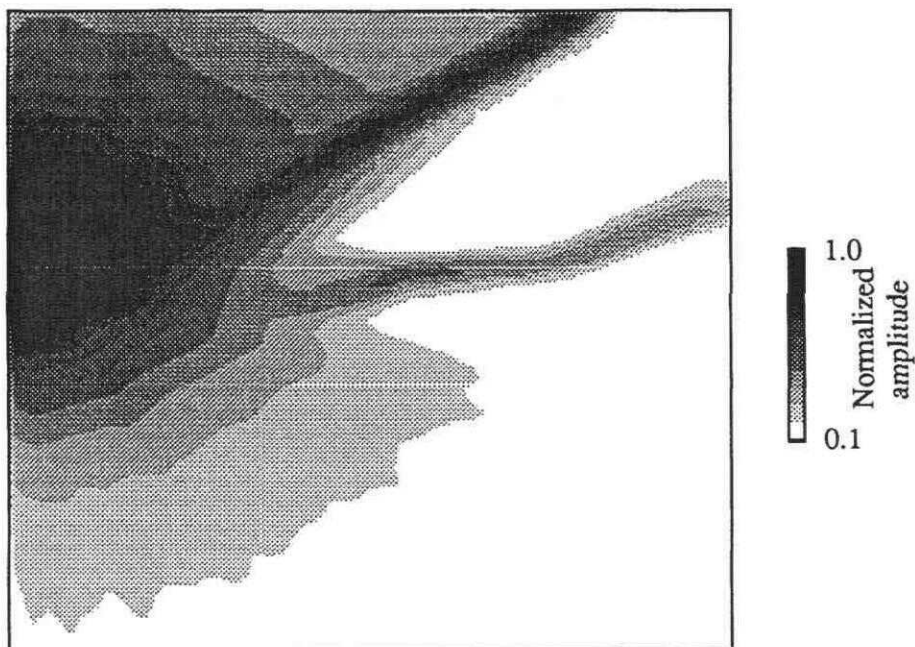


Fig. 4.24. Normalized amplitudes computed for model 4.5. The linear amplitude anomalies represent caustics.

be determined. Without a much faster computer, this effectively limits these techniques to small datasets, or to models with a homogeneous background.

# Chapter 5

## Least-squares migration/inversion

### 5.1 Introduction

In this chapter, the techniques developed in previous chapters will be brought to bear on the problem of seismic migration/inversion, using a linearized least-squares approach. The  $l_2$ -objective (cost) function (equation 2.47) incorporates data and model parameter information in the form of covariance operators, and is minimized using an iterative three-step conditioned-gradient procedure. The first step of each iteration resembles prestack Kirchhoff depth migration, and comprises filtered backprojection of the data residual to yield a set of gradient subimages. An approximate inverse-Hessian operator is then applied to these images, giving new parameter perturbation estimates throughout the model. The effect of this operator is to scale the gradient images, and also to compensate somewhat for parameter-coupling effects. Following this, the predicted wavefield is generated by scattering from the current model, and is used to compute a new data-residual vector. Iterations continue (ideally) until convergence is achieved.

This methodology possesses certain inherent advantages over many other seismic imaging and inversion techniques. Unlike seismic migration, the close association between forward and inverse modeling can be exploited to permit some simple posterior analysis of the inversion results. Furthermore, this approach is intended to image intrinsic properties of a medium, rather than its angle-dependent reflectivity (which is also a function of the geometry and aperture of the acquisition experiment). The use of approximate ray-Green's tensors allows almost arbitrary configuration of the sources and

receivers, as well as a very general form for the background model. The least-squares inversion method is flexible enough to accommodate prior information, in addition to insufficient (e.g., single- component) and inaccurate (noisy) observations. Finally, linearization of the problem guarantees that the Green's functions, governing propagation of the wavefield through the background medium, need to be computed only once. More general nonlinear techniques (e.g., Tarantola, 1986; Mora, 1987) require very time-consuming repropagation of the wavefield for each iteration.

The geophysical literature contains numerous examples of similar ray-Born imaging techniques applied to seismic data, predicated upon various assumptions about the nature of the background medium. In order of increasing complexity (and ill-posedness of the inverse problem), these assumptions range from constant-density acoustic media (e.g., Cohen and Bleistein, 1979; Beylkin, 1985; Miller et al., 1987) and variable-density acoustic media (e.g., Raz, 1981; Clayton and Stolt, 1981; Weglein et al., 1986; Lebras and Clayton, 1988) to isotropic-elastic media (Beydoun and Mendes, 1989; Beydoun et al., 1989, 1990; Beylkin and Burridge, 1990) and fractured media (Tura, 1990). The methodology employed here is based primarily on an elastic ray-Born migration/inversion technique introduced by Beydoun and Mendes (1989). However, Beydoun and Mendes (1989) considered 2-D isotropic-elastic media, whereas here the problem is assumed to be  $2\frac{1}{2}$ -dimensional and the medium to be transversely isotropic.

The principle aim of this chapter is to employ ray-Born imaging to explore the short-wavelength resolving power of seismic data for each of the six medium parameters ( $\alpha$ ,  $\beta$ ,  $\gamma$ ,  $\delta$ ,  $\epsilon$ ,  $\rho$ ) used in this study. The influences of surface versus crosswell acquisition geometries, horizontal versus vertical direction of the anisotropic symmetry axis, and the presence of background anisotropy are also investigated by means of a series of simple synthetic-data examples generated within the Born approximation. An inversion example

based on a structurally deformed geological model will illustrate the feasibility of these techniques for a complex imaging problem. Finally, a ray-traced synthetic-data example computed using the reflection properties of plane waves at a welded interface (rather than the Born approximation) is used to test the properties of this algorithm for a non-Born dataset. To facilitate a description of the computer algorithm, the mathematical theory for the continuous case outlined in chapter 2 will be recast in discrete form.

## 5.2 Description of the algorithm

### 5.2.1 Overview

A flow chart summarizing the FORTRAN program MITI (migration/inversion for transversely isotropic media) is given in Fig. 5.1. The program utilizes two primary inputs: the observed seismic dataset(s), and a description of the background model in terms of the parameters  $(\alpha, \beta, \gamma, \delta, \epsilon, \rho)$ . In principle, a better first input to the program would be an initial estimate of the data residual (i.e., the difference between the observed data and modeled data obtained by some other means). However, the inversion results in this case are often dominated by artifacts arising from the modeling procedure (Pratt and Goulety, 1991).

The migration/inversion algorithm attempts to minimize the  $l_2$ -objective function (Tarantola and Valette, 1982)

$$E = \frac{1}{2} (\Delta \mathbf{u} * \mathbf{W}_u \Delta \mathbf{u} + \Delta \mathbf{m} * \mathbf{W}_m \Delta \mathbf{m}) \quad , \quad (5.1)$$

where  $\Delta \mathbf{u} = \mathbf{u}_{\text{obs}} - \mathbf{B} \Delta \mathbf{m}$  is the data residual,  $\Delta \mathbf{m}$  are the model-parameter perturbations and  $\mathbf{B}$  is the Born operator defined by equation (2.45). For simplicity, the covariance operators  $\mathbf{W}_u^{-1}$  and  $\mathbf{W}_m^{-1}$  are assumed to be equal to a constant ( $w_u^{-1}$  and  $w_m^{-1}$ , respect-

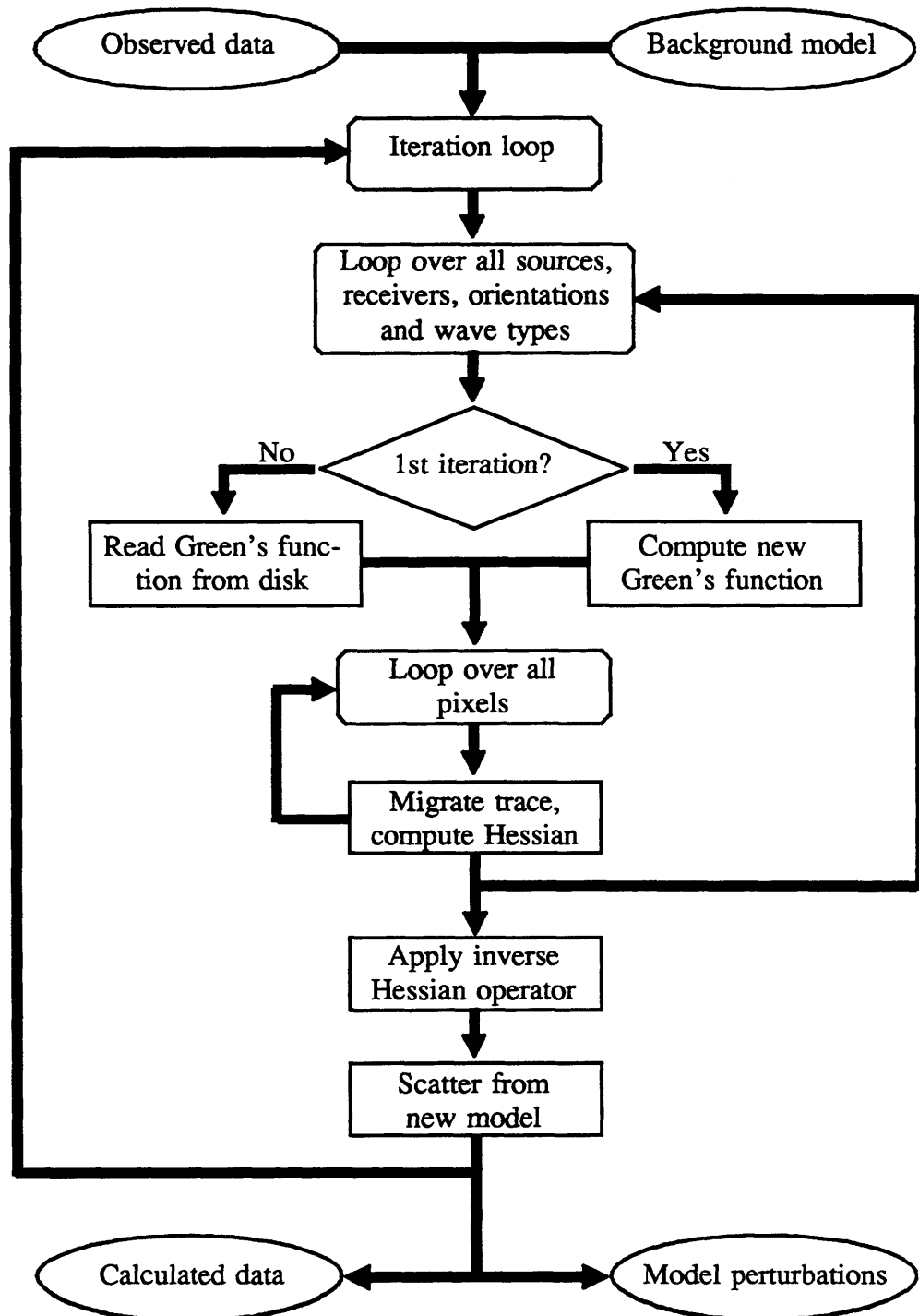


**Fig. 5.1.** Flow chart for MITI program (migration/inversion for transversely isotropic media).

ively) times an identity matrix. Each iteration of the algorithm consists of an inversion step followed by a forward-modeling procedure. Linearization of the problem decouples the background (propagation) model from the perturbation (scattering) model. Therefore, the Green's functions do not need to be recomputed after the first migration pass. This feature is potentially of great significance for an inhomogeneous model, for which calculation of the Green's functions requires a much greater amount of computational effort than the other steps.

The output from the program includes the calculated wavefield, scattered from the current model, in addition to the inversion results. This information can be compared directly to the input seismic dataset to evaluate the success of the migration/inversion process.

### 5.2.2 Filtered backprojection of the data residual

In symbolic notation, the gradient function  $g_k = \partial E / \partial m_k$  (not to be confused with the unit eigenvectors  $\tilde{\mathbf{g}}$  and  $\hat{\mathbf{g}}$ ) may be written (Beydoun and Mendes, 1989)

$$\mathbf{g} = -\mathbf{B}^* \mathbf{W}_u \Delta \mathbf{u} + \mathbf{W}_m \Delta \mathbf{m} \quad . \quad (5.2)$$

In the algorithm used here, the gradient is computed in the  $t$ - $x$ , rather than the  $\omega$ - $x$ , domain, for computational efficiency. Assuming, for sake of illustration, that the source wavelet is a delta function, this transformation collapses a summation (for each data sample) over the entire image zone to a weighted backprojection along the corresponding path of constant traveltime. This procedure closely resembles prestack Kirchhoff depth migration, but with a weighting function derived from the Born approximation rather than the Kirchhoff integral equation (Schneider, 1978; Kuo and Dai, 1984). Prior to backprojection, the data-residual traces are filtered by the  $\omega^{3/2}\pi/4$  factor (see equation

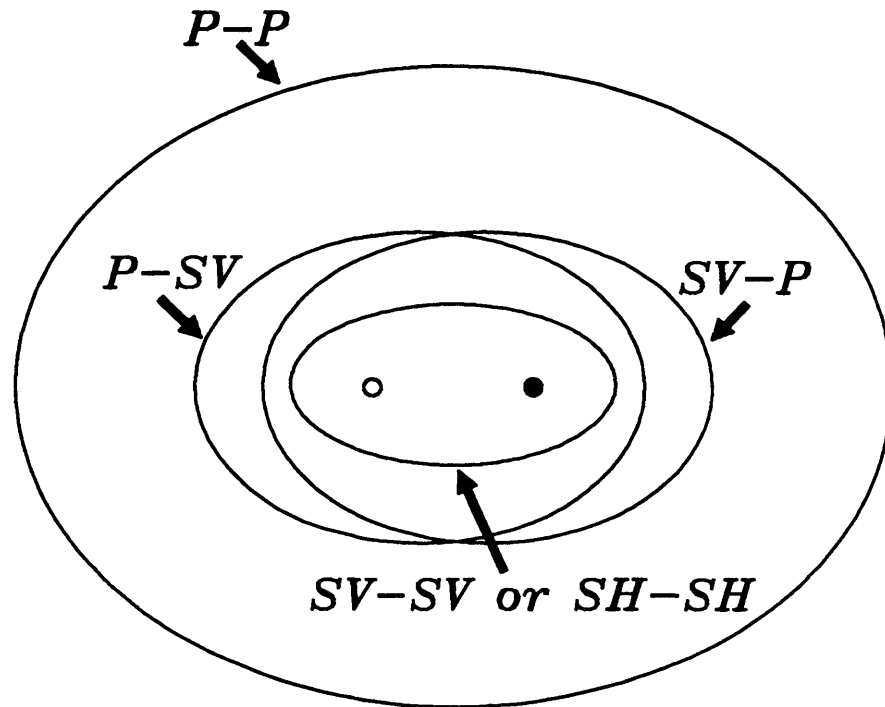
2.44), corrected for the phase function of the source (if known), and operated on by the data-covariance operator. Written explicitly, the  $k$ th component of  $\mathbf{g}$  for the  $j$ th iteration may be expressed in terms of the filtered data residual,  $\Delta \mathbf{u}_{sr mn}^{(j)}(t)$ , via the summation

$$g_k^{(j)}(\mathbf{x}) = \sum_{s,r} \sum_{m,n} \sum_u \bar{g}_{su}(\mathbf{x}) \sum_v \hat{g}_{rv}(\mathbf{x}) \sum_t \{ \Delta u_{sr mn}^{(j)}(t) S_{kstruv}(\mathbf{x}) (\tau_{,22}^{(struv)}(\mathbf{x}))^{-1/2} A_{struv}(\mathbf{x}) \delta(t - \tau_{struv}(\mathbf{x})) \} - \Delta m_k^{(j)}(\mathbf{x}) \quad , \quad (5.3)$$

where  $s$  and  $r$  are the set of all sources and receivers,  $m$  and  $n$  are the set of source and receiver orientations,  $u$  and  $v$  are the source and receiver ray codes ( $qP$ ,  $qSV$  and  $SH$ ),  $S_{kstruv}(\mathbf{x})$  is the scattering amplitude radiation pattern (see equations (2.39) - (2.42) and Figs. 2.4 - 2.7) and  $\Delta \mathbf{m}^{(j)}(\mathbf{x})$  is the model-perturbation vector (after application of the model covariance operator) for the  $j$ th iteration. Symbols for the ray-Green's parameters correspond to those used in chapter 4.

Conventional Kirchhoff migration and acoustic ray-Born imaging techniques map individual data points to traveltime isochrons in the model coordinates (Schneider, 1978; Miller et al., 1987). Elastic migration/inversion is fundamentally different: data points are mapped to several isochrons (Fig. 5.2), corresponding to the relevant subset from the set of ray codes  $\{ qP-qP, qP-qSV, qSV-qP, qSV-qSV, SH-SH \}$ . For unconverted scattered events in a homogeneous-isotropic medium, these curves are elliptical, with foci at the source and receiver. The radius of curvature of the isochron is the largest for  $qP-qP$  scattering, because of the generally higher velocity of  $qP$  waves. For the same reason, isochron curves for converted events are normally shifted away from the source/geophone that is radiating/receiving  $qP$  waves.

Valuable insight into the nature of the elastic-migration procedure implied by equation (5.3) can be gained by studying its impulse response. Figs. 5.3 to 5.6 show plots



- Source
- Receiver

**Fig. 5.2.** Sketch of traveltime isochrons in a homogeneous isotropic medium. Typically, the target zone will include only a portion of the isochrons shown here.

of the impulse-response function for various source and receiver orientations. A single trace containing a band-limited zero-phase pulse at a time of 500 ms was used to generate these plots, which show the steepest-descent direction for the objective function,  $E$ , with respect to the individual model parameters. The source and receiver are assumed to be located within an infinite, isotropic-homogeneous medium with parameters  $\alpha = 3000$  m/s,  $\beta = 1500$  m/s and  $\rho = 2400$  kg/m<sup>3</sup>. Note that, by including the source and receiver in the image zone, these examples violate the far-field assumption. In practice, a target zone would include only portions of the impulse-response functions illustrated here.

Observe that the number of imaged parameters depends on the wave types radiated from the source, and received at the geophone. In Fig. 5.6, where both the source and receiver are oriented in the  $x_2$  (transverse) direction, only  $SH$  waves are scattered, and three of the six possible parameters are imaged ( $\beta$ ,  $\gamma$ , and  $\rho$ ). The other three plots involve  $P$ - $SV$  scattering, and image five of the six parameters. The number of parameters imaged remains the same even in the presence of background anisotropy (although the impulse response can be much different), provided that the symmetry axis lies in the plane of acquisition. Hence, in order to resolve all six of the parameters, a complete nine-component (i.e., 3-component sources and receivers) experiment is a practical requirement (otherwise sources and receivers would have to be oriented out of the plane such that all three wave types are radiated). However, it may be possible to invoke a statistical relationship between  $\gamma$  and  $\epsilon$ , as noted in chapter 1 (Fig. 1.3), to reduce the number of parameters and thus avoid this complication.

Variation in amplitude along a single isochron in Figs. 5.3 to 5.6 can be attributed to both the elastic radiation patterns at the source and receiver, and the scattering radiation patterns for individual parameters (Figs. 2.4-2.7). Larger variations in the

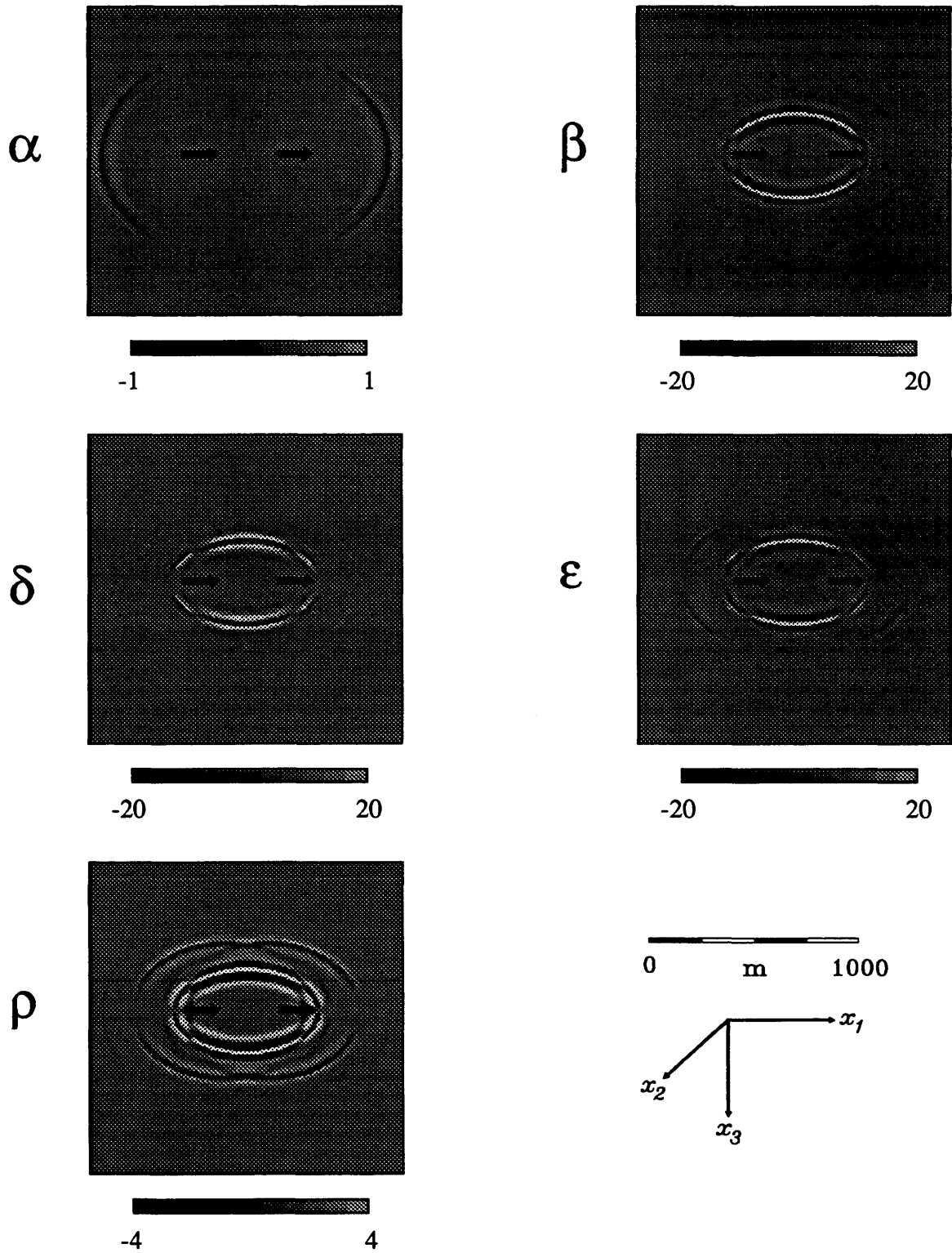


**Fig. 5.3.** Impulse response of the elastic-migration operator, for source (rightmost arrow) and receiver (leftmost arrow) in the  $x_1$ -direction. Note relative plot amplitudes.

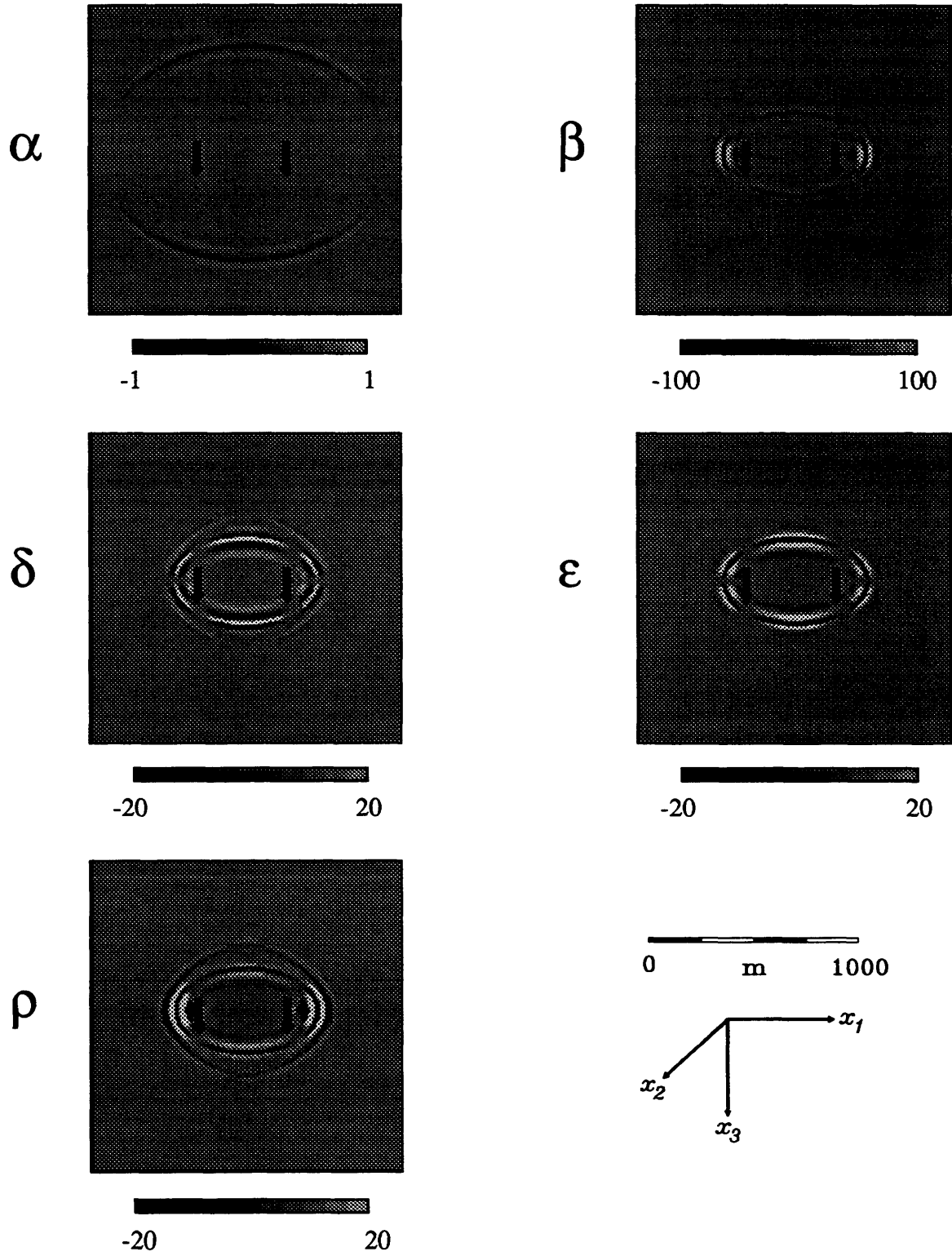


**Fig. 5.4.** Impulse response of the elastic-migration operator for vertical source (right-most arrow) and vertical receiver (leftmost arrow). Note relative plot amplitudes.

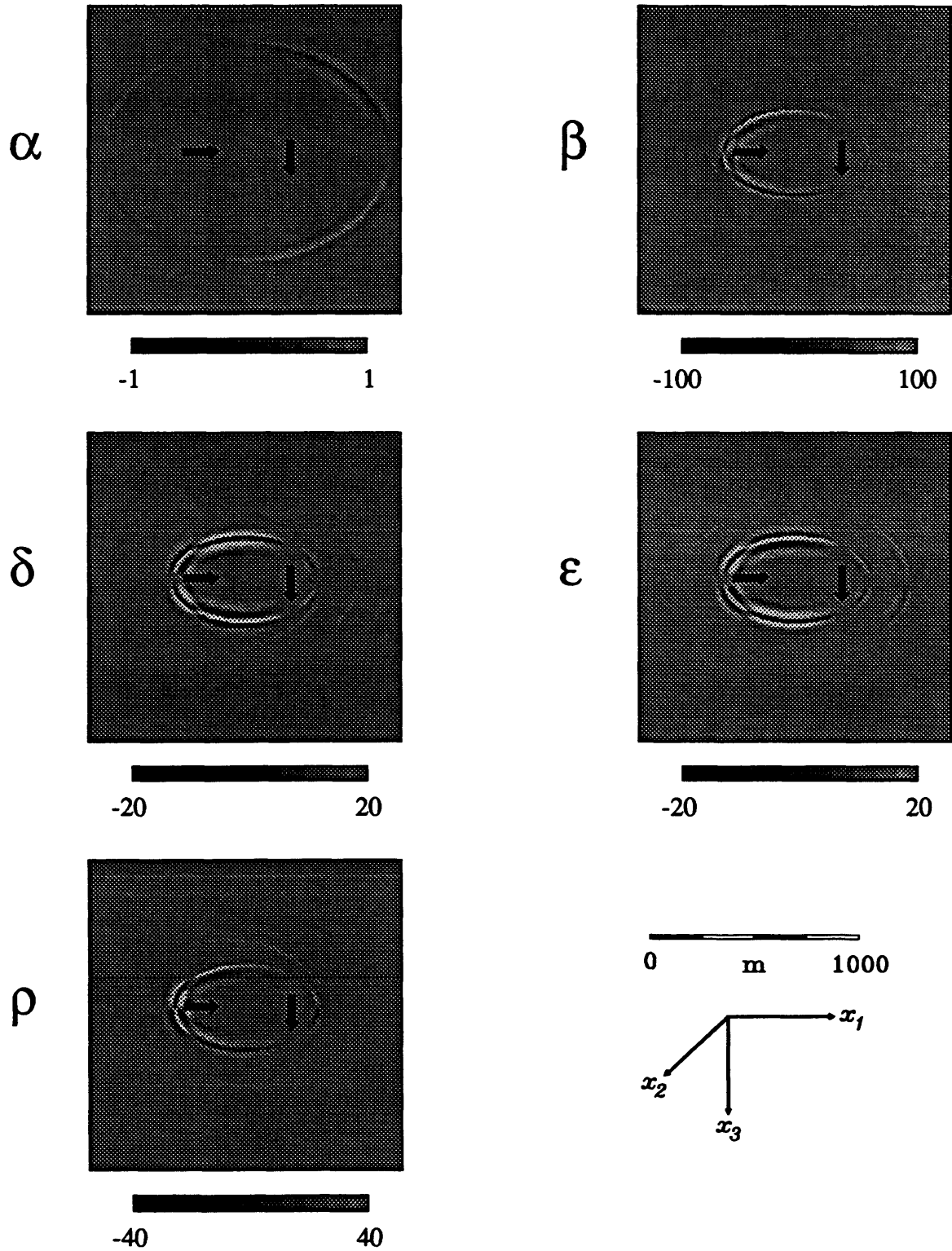


Fig. 5.5. Impulse response of the elastic-migration operator for a source (right-most arrow) and receiver (leftmost arrow) oriented as shown. Note relative plot amplitudes.

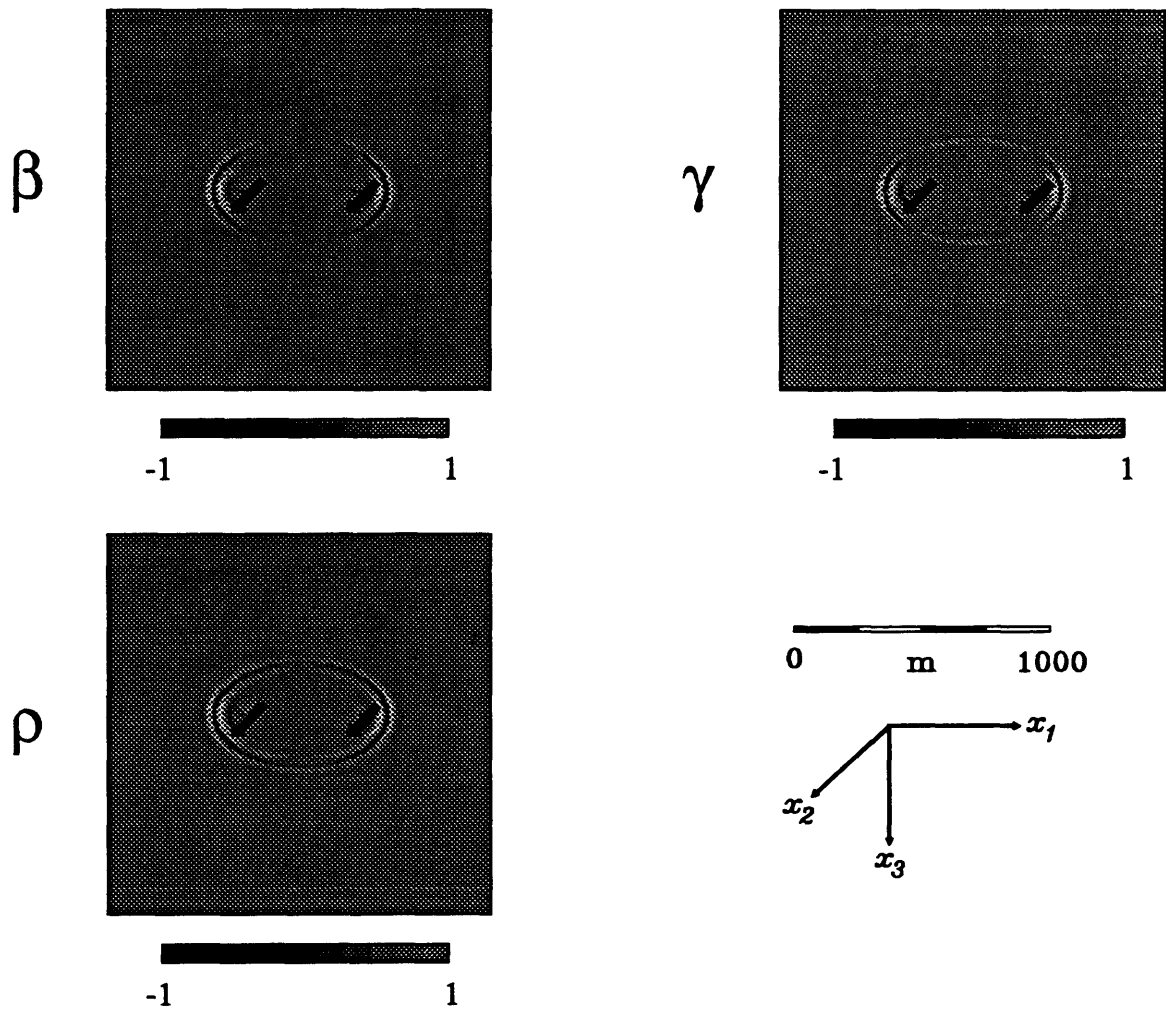


Fig. 5.6. Impulse response of the elastic-migration operator for source and receiver oriented in the  $x_2$ -direction. Only  $SH$  waves are radiated.

magnitude of the gradient function between different isochrons (note the relative plot scales used) are mainly due to differences in the geometrical spreading ( $A$ ) and out-of-plane spreading ( $\tau_{,22}$ ) factors for different wave types. For example, at a given travelttime in a homogeneous-isotropic medium, the geometrical spreading factor is inversely proportional to the cube of velocity (Aki and Richards, 1980), and  $\tau_{,22}$  is inversely proportional to the square of velocity. Considering that the amplitude term  $A_{,sr\mu\nu}$  and the out-of-plane spreading term  $\tau_{,22}^{(sr\mu\nu)}$  in equation (5.3) are the product and sum of two such quantities, respectively, the gradient for  $P$ - $P$  events is, on average, smaller than the gradient for  $SV$ - $SV$  or  $SH$ - $SH$  scattering by a factor of  $(\beta/\alpha)^5$ , or approximately 1/32.

### 5.2.3 The approximate Hessian

The negative gradient function,  $-\mathbf{g}$ , establishes a steepest-descent direction in the model space, with respect to the cost function,  $E$ . Rather than performing an incremental search in this direction, faster convergence can usually be achieved using the second-order model update

$$\Delta \mathbf{m}^{(j)} = -\hat{\mathbf{H}}^{-1} \mathbf{g}^{(j)} \quad , \quad (5.4)$$

provided that an estimate of  $\hat{\mathbf{H}}^{-1}$  is available. Beydoun and Mendes (1989) introduced an approximate elastic Hessian operator, based on the Gauss-Newton approximation as well as the assumption that the Hessian matrix is diagonal. Because the neglected off-diagonal elements of the Hessian operator represent interaction between spatially separated points, the second assumption is similar to the single-scatter assumption implicit in the Born approximation. These simplifications lead to a small (up to 6×6) matrix for each model pixel, that can be inverted analytically. In the notation used here, this matrix may be written:

$$\hat{H}_{lq}(\mathbf{x}) = w_u \sum_{s,r} \sum_{m,n} \sum_u \bar{g}_{su}^2(\mathbf{x}) \sum_v \hat{g}_{rv}^2(\mathbf{x}) \sum_t \quad (5.5)$$

$$S_{lsruv}(\mathbf{x}) S_{qsr uv}(\mathbf{x}) (\tau_{,22}(\mathbf{x}))^{-1} A_{sr uv}^2(\mathbf{x}) + w_l(\mathbf{x}) \delta_{lq} \quad .$$

The matrix  $\hat{\mathbf{H}}(\mathbf{x})$  can be computed during the first pass of migration, at the same time as the gradient is computed. However, since  $\hat{\mathbf{H}}$  is independent of the data, it only needs to be computed once, like the Green's functions. Furthermore, since  $\hat{\mathbf{H}}$  is symmetric, only half of the matrix needs to be retained in memory.

The parameter variance,  $w_l^{-1}$ , has the role of a "prewhitening" term on the diagonal of the approximate Hessian matrix. Experience has shown that  $\hat{\mathbf{H}}$  is often almost singular (i.e., the problem is ill-posed) unless this term is included. However, in practice, it is difficult to estimate the magnitude that the  $w_l$  terms should have. In this implementation, relative weights are used as input. After the first migration pass, the program MITI computes the average value on the diagonal of the Hessian for each parameter, in order to convert the relative weights to absolute numbers. Small relative values (e.g., 10% of the average or less) have been found, empirically, as sufficient to guarantee the stability of the matrix inversion.

#### 5.2.4 Computing the step size

Once the migration step has been completed and the approximate Hessian is known, the model update is then given approximately by equation (5.4), and can be used to compute a new scattered wavefield. The explicit formula for forward modeling in the ray-Born approximation is very similar to equation (5.3). However, the magnitude of the parameter change implied by  $\hat{\mathbf{H}}^{-1}$  is typically too large, because of the neglected off-

diagonal terms. Therefore, the approximate model update given by equation (5.4) should be treated as a conditioned gradient estimate, rather than an absolute model update.

An optimal model-update step size can easily be computed by exploiting the linear nature of the Born approximation. I begin by defining the total model perturbation after  $J$  iterations as the sum of incremental model perturbations,

$$\Delta \mathbf{m}_k^J(\mathbf{x}) = \sum_{j=1}^J \delta \mathbf{m}_k^{(j)}(\mathbf{x}) \quad , \quad (5.6)$$

where the incremental model-parameter perturbation vector for the  $j$ th iteration is

$$\delta \mathbf{m}^{(j)} = \lambda^{(j)} \hat{\mathbf{H}}^{-1} \mathbf{g}^{(j)} \quad , \quad (5.7)$$

and  $\lambda^{(j)}$  is a damping factor applied to the update given in (5.4). Defining  $\mathbf{u}_{sc}^{(j)}$  as

$$\mathbf{u}_{sc}^{(j)} = \mathbf{B} \cdot (-\hat{\mathbf{H}}^{-1} \mathbf{g}^{(j)}) \quad , \quad (5.8)$$

it can be easily demonstrated that the data residual after the  $j$ th iteration may be written

$$\Delta \mathbf{u}^{(j)} = \Delta \mathbf{u}^{(j-1)} - \lambda^{(j)} \mathbf{u}_{sc}^{(j)} \quad . \quad (5.9)$$

$\lambda^{(j)}$  can then be chosen to minimize

$$E_\lambda^{(j)} = \sum_d \sum_t [\Delta \mathbf{u}^{(j-1)}(t) - \lambda^{(j)} \mathbf{u}_{sc}^{(j)}(t)]^2 \quad , \quad (5.10)$$

by setting

$$\lambda^{(j)} = \frac{\sum_d \sum_t \Delta \mathbf{u}^{(j-1)}(t) \Delta \mathbf{u}_{sc}^{(j)}(t)}{\sum_d \sum_t (\Delta \mathbf{u}_{sc}^{(j)}(t))^2} \quad . \quad (5.11)$$

The secondary cost function,  $E_\lambda$ , expresses the  $l_2$ -norm of the misfit between the previous data residual vector, and the current scattered wavefield. In equations (5.10) and (5.11), the sum over  $d$  represents the sum over all of the data traces (i.e., the first four summations in (5.3)), to reduce the number of subscripts used. Equation (5.11) simply states that  $\lambda^{(j)}$  is taken to be the zeroth lag of the cross-correlation of the scattered

wavefield,  $\mathbf{u}_{sc}^{(j)}$ , with the previous data residual,  $\Delta\mathbf{u}^{(j-1)}$ , divided by the zeroth lag of the autocorrelation of  $\mathbf{u}_{sc}^{(j)}$ , taken over all traces.

## 5.3 Examples

### 5.3.1 Surface-data examples

The first series of synthetic-data examples have been computed using the model geometry shown in Fig. 5.7. The parameters of the background medium for the examples that follow are the same as those used previously for the impulse-response calculation (see Table 5.1). Six of the scatterers shown in Fig. 5.7 represent small positive perturbations to the individual parameters. The isotropic parameters ( $\alpha$ ,  $\beta$  and  $\rho$ ) are perturbed by 10% relative to the background medium. The anisotropic perturbations ( $\gamma$ ,  $\delta$ , and  $\epsilon$ ) have a magnitude of 0.1. The central point represents a 10% perturbation to all parameters. In this section, I will consider the migration/inversion of three Born-synthetic surface shot records generated by scattering from these 7 points, using a 12-trace end-on spread geometry, with a group interval and near-offset of 50 m. These records have been modeled as pure-mode synthetics using a  $P$ -wave source. That is,  $P$ - $P$  events and  $P$ - $SV$  events are treated separately, and the source and receiver radiation patterns have been neglected. This simplification is valid in the presence of a low-velocity near-surface layer, which, coupled with the effect of the free surface, tends effectively to separate  $P$  and  $SV$  waves onto the vertical and radial recording channels, respectively (Eaton, 1989).

Fig. 5.8a shows the scattered  $P$ - $P$  and  $P$ - $SV$  events calculated for model 5.1a, where the anisotropic symmetry axis is taken to be vertical. The source function is zero phase, with a 5-15-55-90 Hz trapezoidal amplitude spectrum. These are the best possible

Model	Background medium	Acquisition geometry	Notes
5.1	Homogeneous, isotropic $\alpha = 3000$ m/s, $\beta = 1500$ m/s $\rho = 2400$ kg/m <sup>3</sup>	Surface (see Fig. 5.7)	5.1a: vertical axis of symmetry 5.1b: horizontal axis of symmetry
5.2	Same as model 5.1	Crosswell (see Fig. 5.7)	5.2a: vertical axis of symmetry 5.2b: horizontal axis of symmetry 5.2c: vertical axis of symmetry, <i>SH-SH</i> scattering only
5.3	Strongly anisotropic, homogeneous (Greenhorn shale - see p. 23)	Crosswell	<i>SH-SH</i> scattering only
5.4	Anticline model - see Figs. 4.2,4.3	Crosswell/VSP (see Fig. 5.16)	
5.5	Dipping reflector - see Fig. 5.19	Crosswell/VSP (see Fig. 5.19)	

Table 5.1. Summary of models used to test the migration/inversion algorithm.

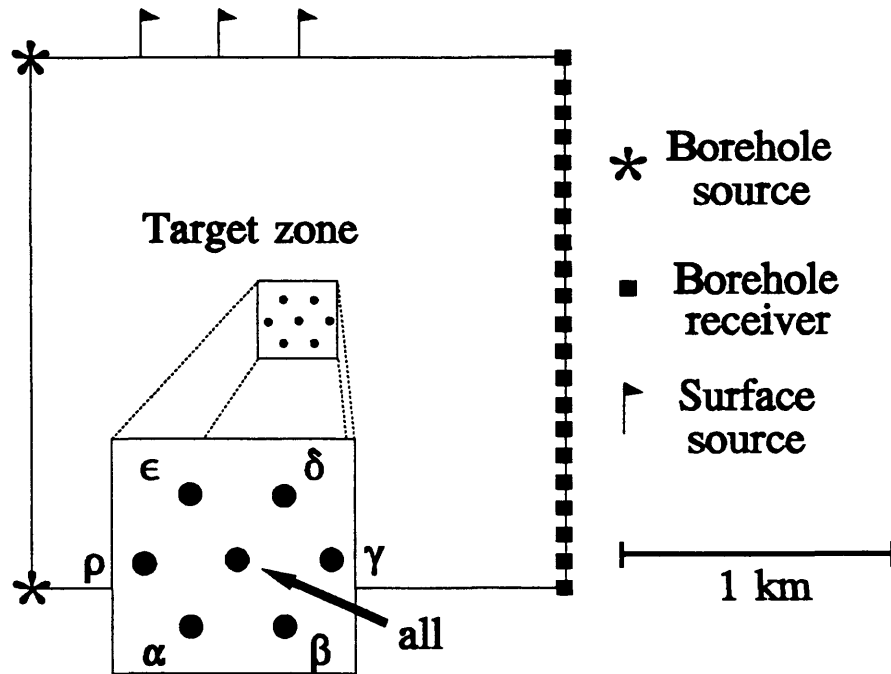


**Fig. 5.7.** Model geometry used for the first three examples. Inset shows the distribution and type of scatterers, each representing a line segment extending into and out of the page.

data for the migration/inversion algorithm, because they are noise-free, satisfy all of the assumptions (e.g., far-field), and have been computed using the ray-Born approximation. The migration/inversion results for this input dataset after three iterations are shown in Fig. 5.9.

The limited aperture of the recording geometry used for this example severely restricts the range of scattering angles. Artifacts that result from this restriction include smearing of the images, and parameter cross-coupling. Nevertheless, some of the essential features of the input model have been recovered within the bandwidth of the source function. In particular, the isotropic parameters appear to be much better resolved than the anisotropic parameters in this example. Some leakage of the  $\rho$  scattering point

onto the  $\alpha$  and  $\beta$  images suggests that perhaps  $P$ - and  $S$ -wave impedance would be a better parameterization for surface reflection data than  $\alpha$  and  $\beta$ , as suggested by Tarantola (1986). No leakage of the anisotropic parameters onto the  $\alpha$ ,  $\beta$  and  $\rho$  images is apparent. Note that the anisotropic perturbations are not imaged as points, but as a criss-crossing linear feature. This artifact is interpreted as preferential alignment of gradient maxima due to the anisotropic nature of the scattering radiation patterns (see Figs. 2.5 to 2.7).

Fig. 5.8b shows seismograms computed by scattering from the perturbation models shown in 5.9. The frequency content of the output traces appears to be slightly lower than the frequency content of the input traces, due to the spatial smearing of the scattering points. The data residual, found by taking the difference between the traces in Fig. 5.8a and 5.8b, is about 19% of the energy of the input traces. At first glance, the magnitude of the inversion results, expressed here as a percentage of the actual scattering strength, appears to be too small. However, in the Born approximation each point scatters energy independently. Thus, scattering from a collection of closely spaced, weak scatterers can produce results nearly identical to scattering from a single, large perturbation. Integrating the scattering response over a rectangular area of 40 m by 20 m, centred over the true position of the  $\alpha$  perturbation, for example, gives a net scattering strength of 109% of the true perturbation. Prior to application of the damping factor,  $\lambda$ , the maximum scattering strength computed using equation (5.4) at the true position of the  $\alpha$  perturbation was about 50%, very similar to results reported by Beydoun and Mendes (1989). A summary of the integrated scattering strengths for this model over 40 m by 20 m rectangles appropriately positioned for each parameter is given in Table 5.2.

Fig. 5.10 shows the migration/inversion results for the case in which the

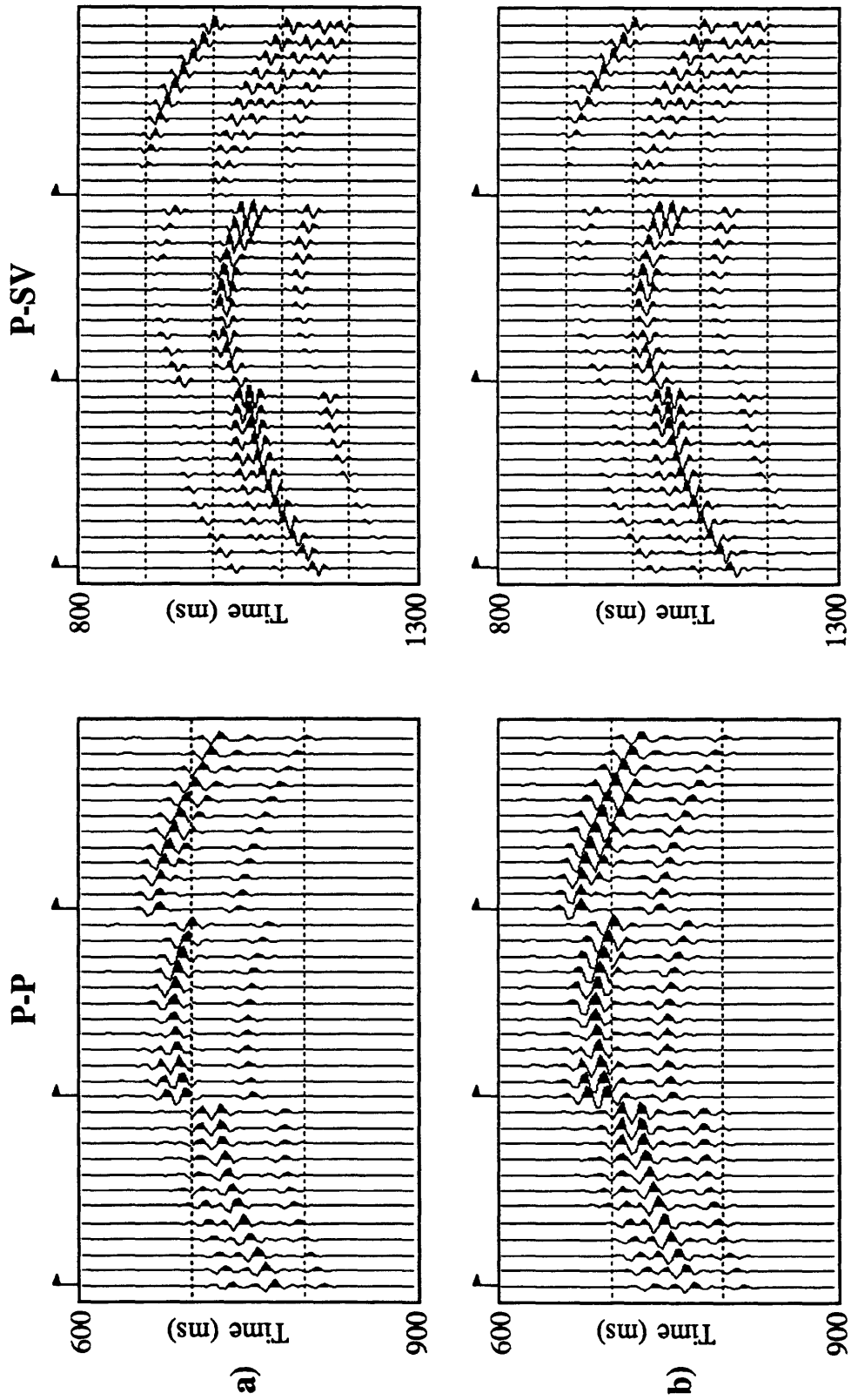


Fig. 5.8. a) Ray-Born synthetic data for model 5.1a, used as input to the M/I algorithm. Flags indicate the first trace for each shot record. b) Seismograms computed by scattering from the perturbation models shown in Fig. 5.9.

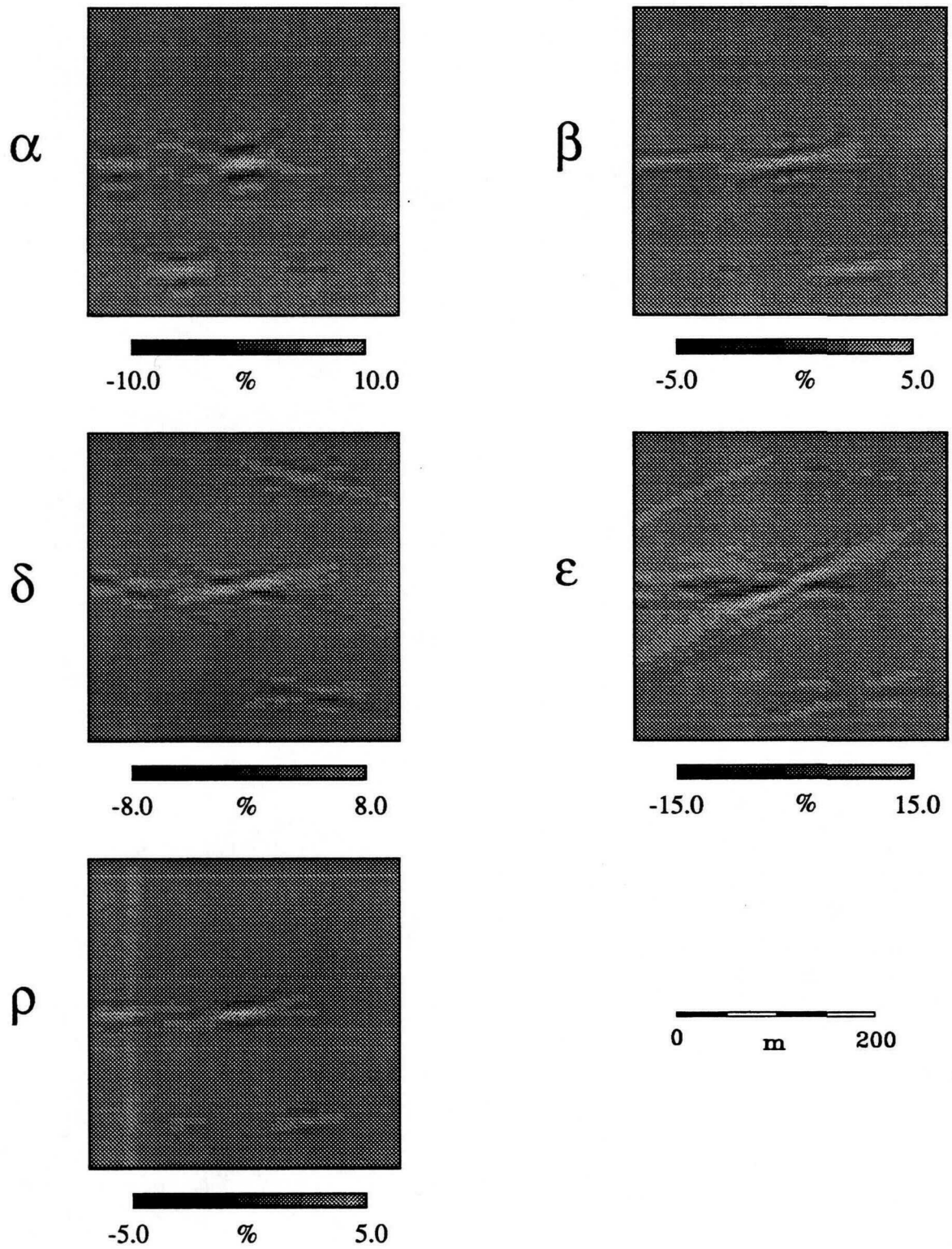


Fig. 5.9. Results of three iterations of migration/inversion for model 5.1a.

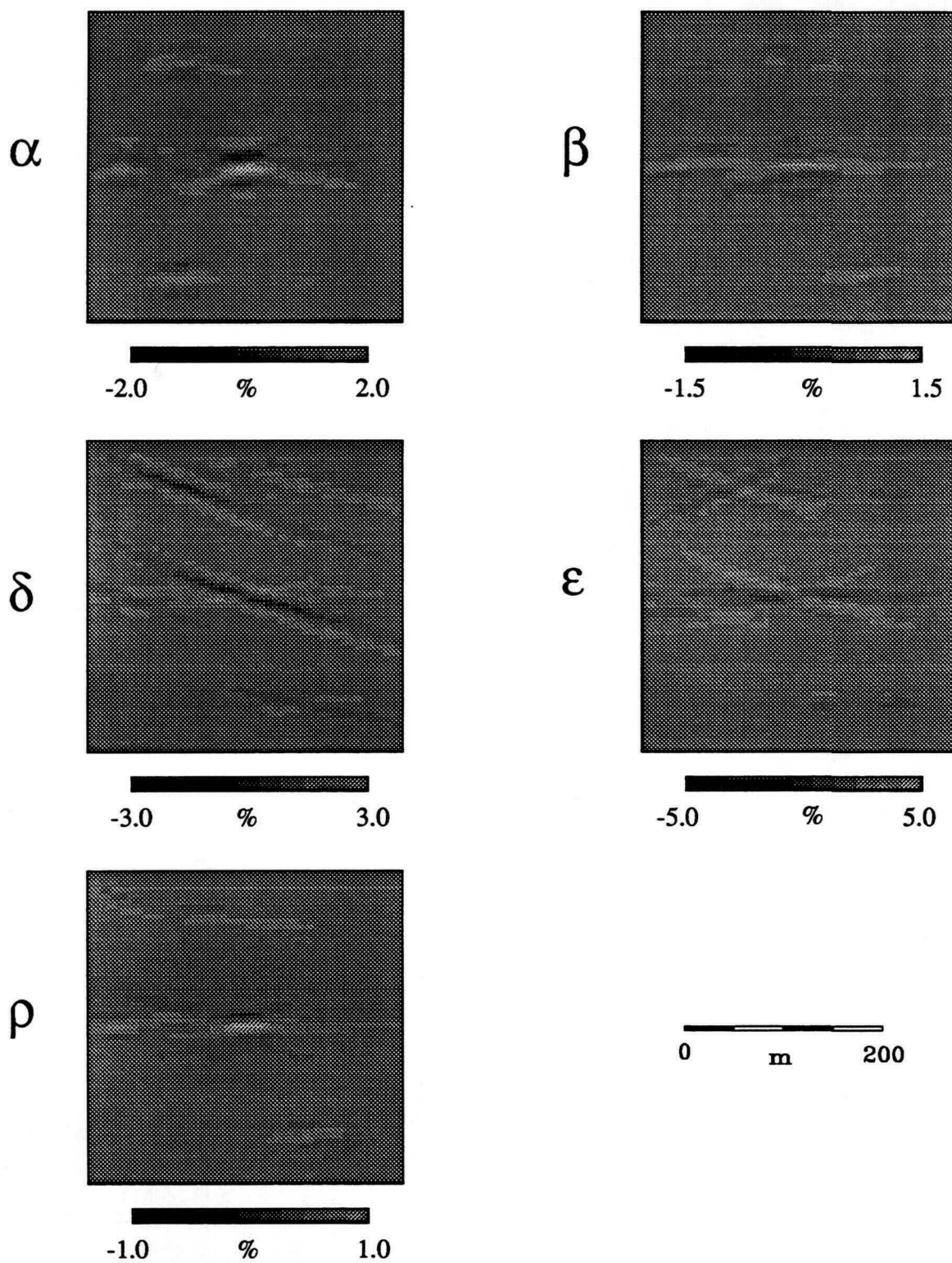


Fig. 5.10. Results of three iterations of migration/inversion for model 5.1b.

anisotropic symmetry axis is horizontal (model 5.1b). The results are similar to the previous case, except that some leakage of the  $\epsilon$  parameter onto the other images is now visible. The total energy in the data-residual traces in this case was 77% of the energy of the input traces. The parameter recovery statistics, found by integrating the inversion results over a 40 m by 20 m area, are also given in Table 5.2. The smaller integrated values for model 5.1b relative to model 5.1a (ideally, the values should be close to 100%) suggest that for the surface recording geometry used here parameter cross-coupling is a more serious problem when the anisotropic symmetry axis is horizontal, rather than vertical.

Parameter	$\alpha$	$\beta$	$\delta$	$\epsilon$	$\rho$
<b>Model 5.1a</b>					
Individual parameter	109 %	45 %	58 %	40 %	48 %
Centre of target zone	175 %	79 %	134 %	202 %	87 %
<b>Model 5.1b</b>					
Individual parameter	18 %	9 %	18 %	16 %	7 %
Centre of target zone	44 %	17 %	38 %	35 %	17 %

**Table 5.2.** Summary of integrated M/I perturbation values for models 5.1a and 5.1b, over a rectangular area 40 m by 20 m in size. A value of 100% would signify that the true perturbation amplitude has been estimated, but the perturbations have been smeared over a finite area, rather than concentrated in a point.

### 5.3.2 Crosswell examples for an isotropic background model

Numerical experiments similar to the previous example have been conducted for a crosswell acquisition geometry, using the same isotropic background model and set of scattering points. The model includes two boreholes that are equidistant from the target zone, and separated by 2000 m. Two sources were modeled, at depths of 0 m and 2000 m, with 21 receivers in the opposite well. Each source consisted of a single impulse in the  $x_1$ -direction. However, both the  $x_1$ - and  $x_3$ -components of particle motion were calculated at each receiver position. The calculated  $x_1$ -component traces are displayed in Fig. 5.11a, for the case of a vertical axis of symmetry (model 5.2a). The (trapezoidal) source amplitude spectrum in this case is 10-40-80-200 Hz.

The results after three iterations of migration/inversion are shown in Fig. 5.12. The images of perturbations to  $\alpha$ ,  $\beta$  and  $\epsilon$  are the most satisfactory. Arguably, the best inversion image for this example is  $\epsilon$ , rather than any of the isotropic parameters. The re-scattered results are displayed in Fig. 5.11b, for comparison with the input data. The residual energy in this case was only 8%. The algorithm seems to have the most difficulty matching the converted-wave response (middle panel in Fig. 5.11).

Two other models were conducted using this acquisition geometry. Model 5.2b used a horizontal axis of symmetry, but was otherwise the same as model 5.2a. Migration/inversion results are plotted in Fig. 5.13, and tabulated in Table 5.3. The change from a vertical to a horizontal axis of symmetry seems to have had much less effect on parameter resolution for the crosswell geometry than the surface geometry considered in model 5.1.

The final example from this set used sources and receivers in the  $x_2$ -direction, generating only  $SH$ -waves. The migration/inversion results for this case (model 5.2c) are plotted in Fig. 5.14, and summarized in Table 5.3. The  $\gamma$  parameter, which can only be

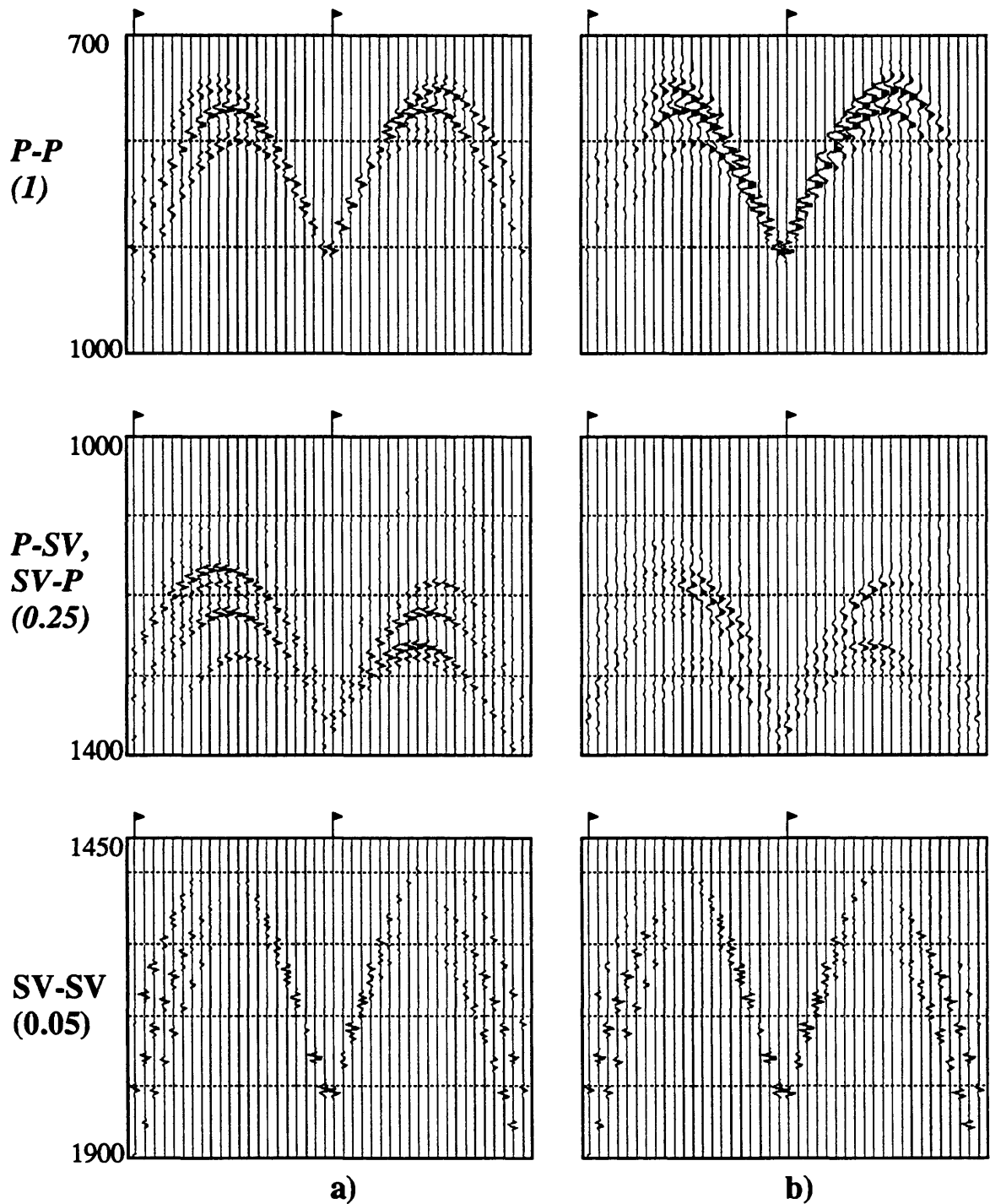


**Fig. 5.11.** a) Ray-Born synthetic data for model 5.2a ( $x_1$ -component). Flags indicate the first trace in a shot record. Time is in ms, and bracketed number is the plot amplitude (lower plot amplitude implies larger amplitude for trace data). b) Seismograms computed by scattering from the perturbation models shown in Fig. 5.12.

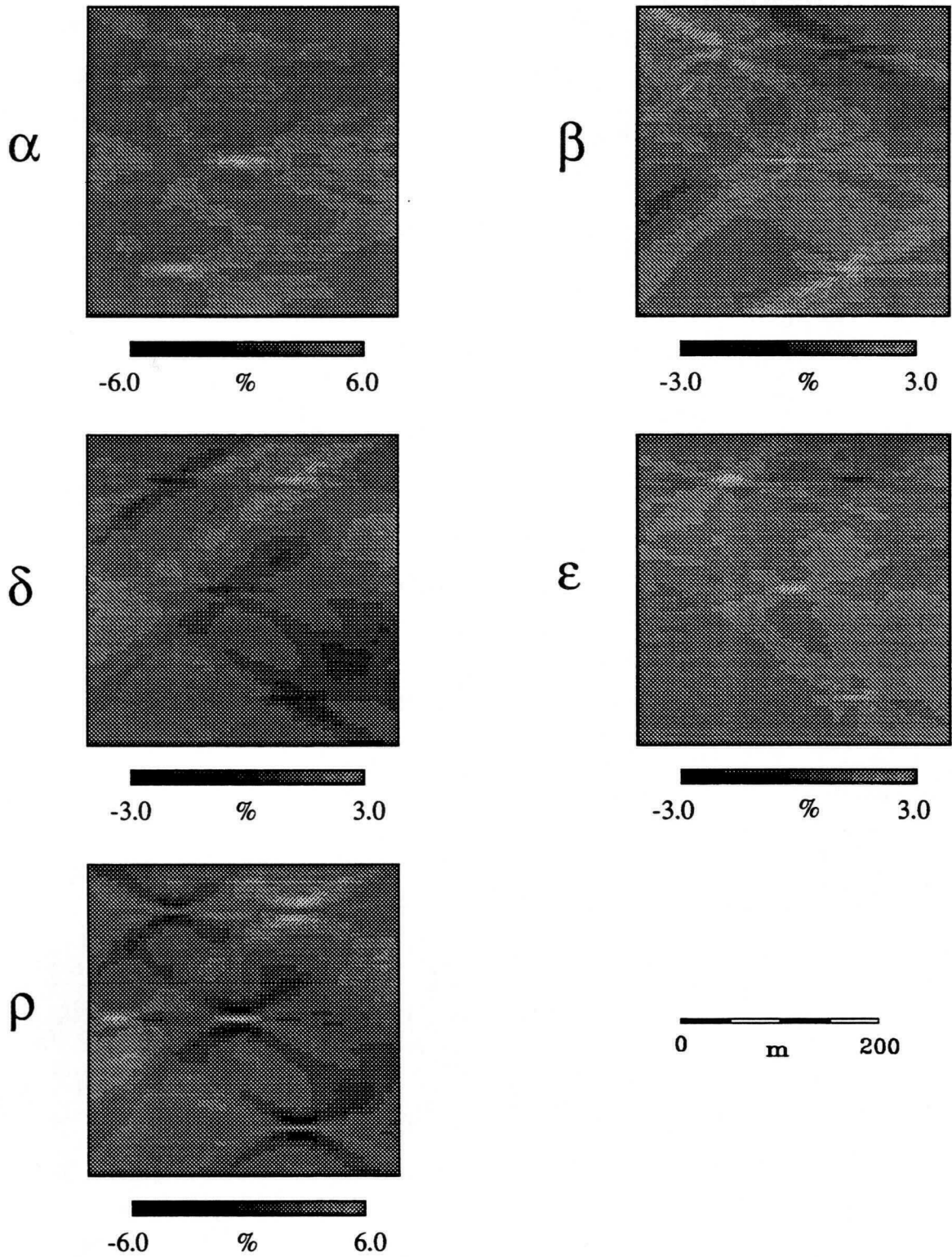


Fig. 5.12. Results of three iterations of migration/inversion for model 5.2a.

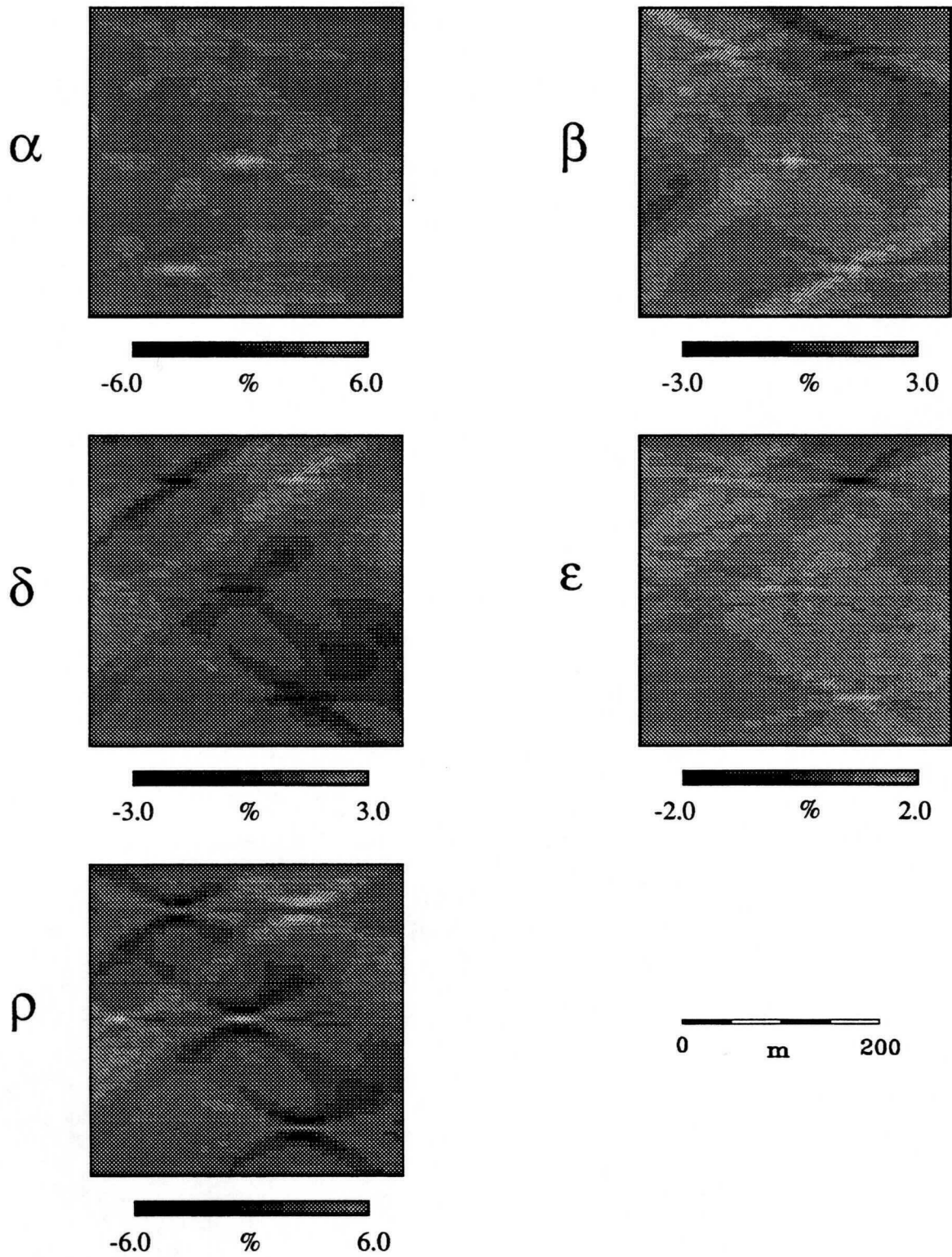


Fig. 5.13. Results of three iterations of migration/inversion for model 5.2b.

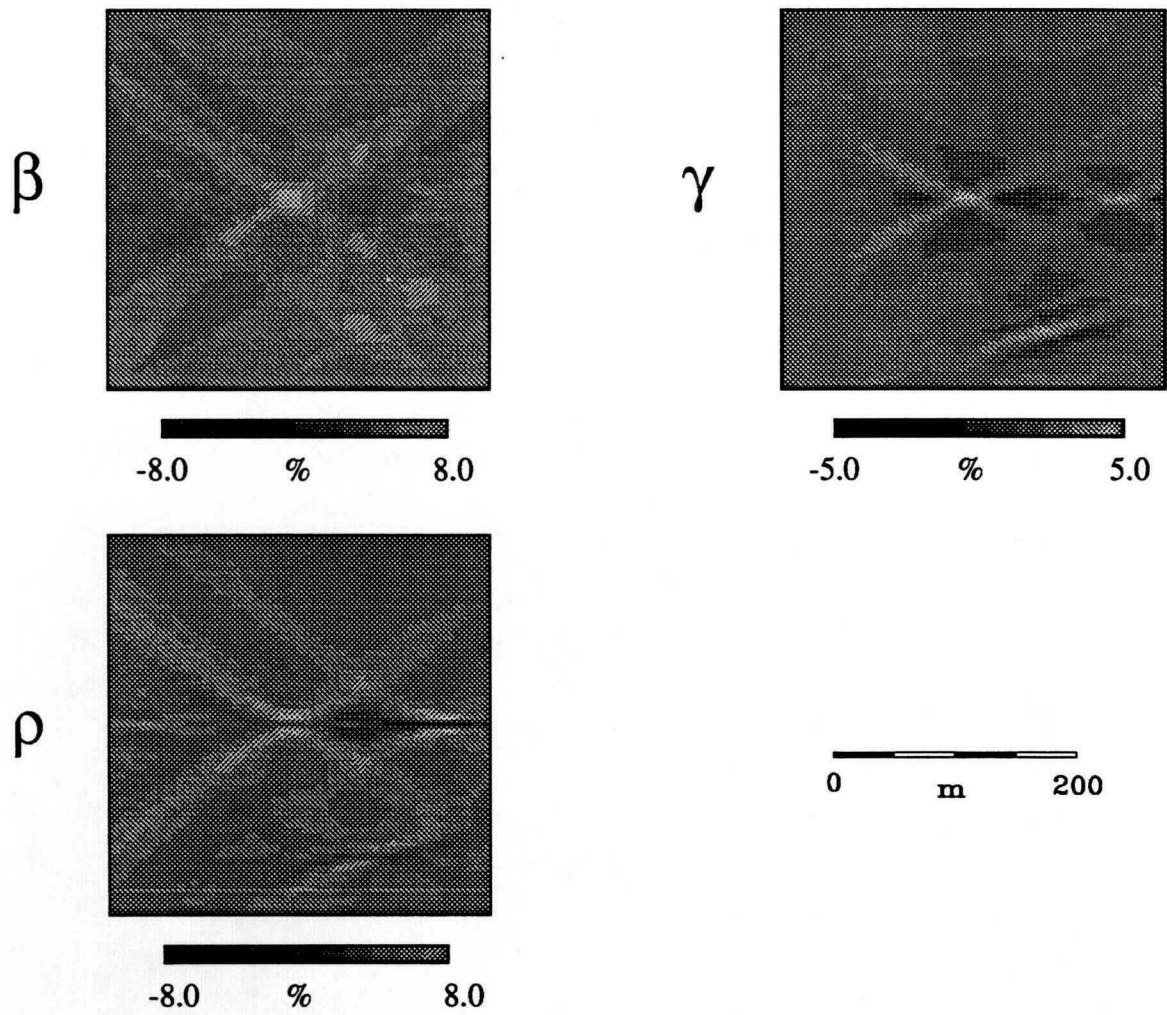


Fig. 5.14. Results after three iterations of migration/inversion for model 5.2c.

Parameter	$\alpha$	$\beta$	$\delta$ ( $\gamma^\dagger$ )	$\epsilon$	$\rho$
<b>Model 5.2a</b>					
Individual parameter	81 %	54 %	55 %	29 %	62 %
Centre of target zone	90 %	41 %	50 %	39 %	152 %
<b>Model 5.2b</b>					
Individual parameter	76 %	56 %	57 %	15 %	65 %
Centre of target zone	87 %	51 %	61 %	21 %	160 %
<b>Model 5.2c</b>					
Individual parameter	-	170 %	48 %	-	71 %
Centre of target zone	-	209 %	55 %	-	173 %
<b>Model 5.3</b>					
Individual parameter	-	8.3 %	5.5 %	-	2.8 %
Centre of target zone	-	7.9 %	5.7 %	-	3.8 %

<sup>†</sup> This parameter is taken to be  $\delta$  for models 5.2a and 5.2b, and  $\gamma$  for models 5.2c and 5.3.

**Table 5.3.** Summary of integrated M/I perturbation values for models 5.2 and 5.3, over a rectangular area 40 m by 20 m in size.

resolved by the  $SH$ - $SH$  mode of scattering, is moderately well resolved in Fig. 5.14 but exhibits some cross-coupling with the  $\beta$  parameter.

### 5.3.3 Crosswell example for an anisotropic background

An example similar to model 5.2c was computed using a homogeneous, anisotropic background medium having the same parameters as the Greenhorn shale. Experimentation with  $qP$ - $qSV$  datasets (not shown) revealed that all perturbations except  $\gamma$  were sensitive to  $qSV$  converted and unconverted scattering. Thus, inversion results for sources and receivers oriented in the  $x_1$ - or  $x_3$ -directions were dominated by artifacts related to the anomalous seismic amplitudes on the cusps of the  $qSV$  wavefront (see Fig. 2.3).

The results of migration/inversion applied to the  $SH$ - $SH$  response of the anisotropic model (model 5.3) are shown in Fig. 5.15. The results are essentially the same as for model 5.2c, except the inversion images exhibit a noticeable bulk shift toward negative values, and are characterized by much smaller magnitudes, for reasons that are as yet uncertain.

### 5.3.4 Crosswell example for a complex geological model

The preceding examples have all featured a homogeneous background model. In practice it is unlikely that a homogeneous model will be a sufficiently good approximation to the true earth. The next example makes use of the anticline model from the previous chapter (see Figs. 4.2 and 4.3). Green's functions for the source and receivers were computed using the finite-difference technique described in the previous chapter. In this case, a crosswell-recording geometry, similar to a VSP, is employed (Fig. 5.16), consisting of 14 receivers at an interval of 50 m. However, there are no receivers within the transition layer because of severe amplitude anomalies associated with the strong heterogeneity in this zone. Three scattering points, each representing a 10% perturbation to  $\alpha$ ,  $\beta$  and  $\rho$  were used to generate the input ray-Born dataset (Fig. 5.17a). The target

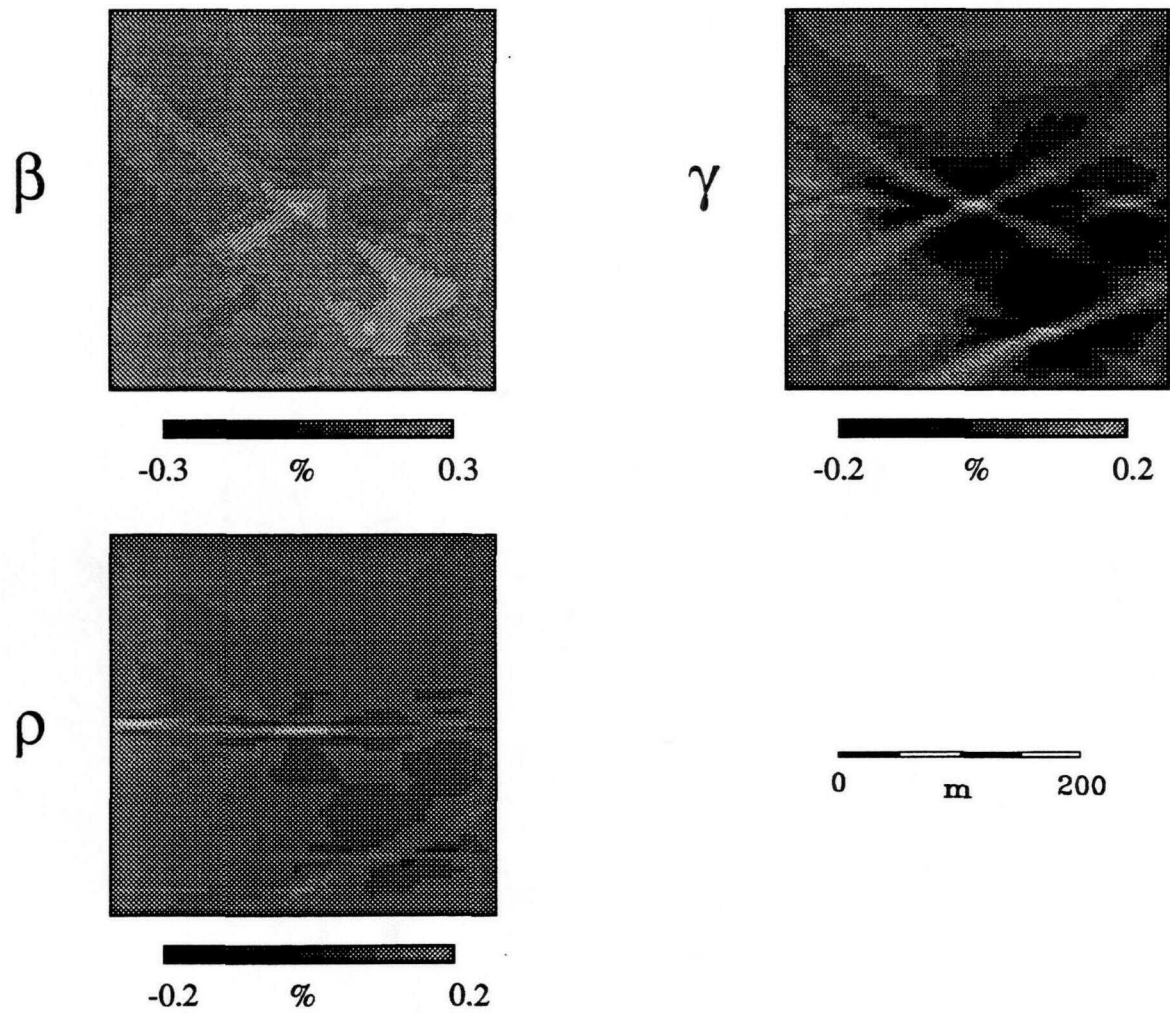
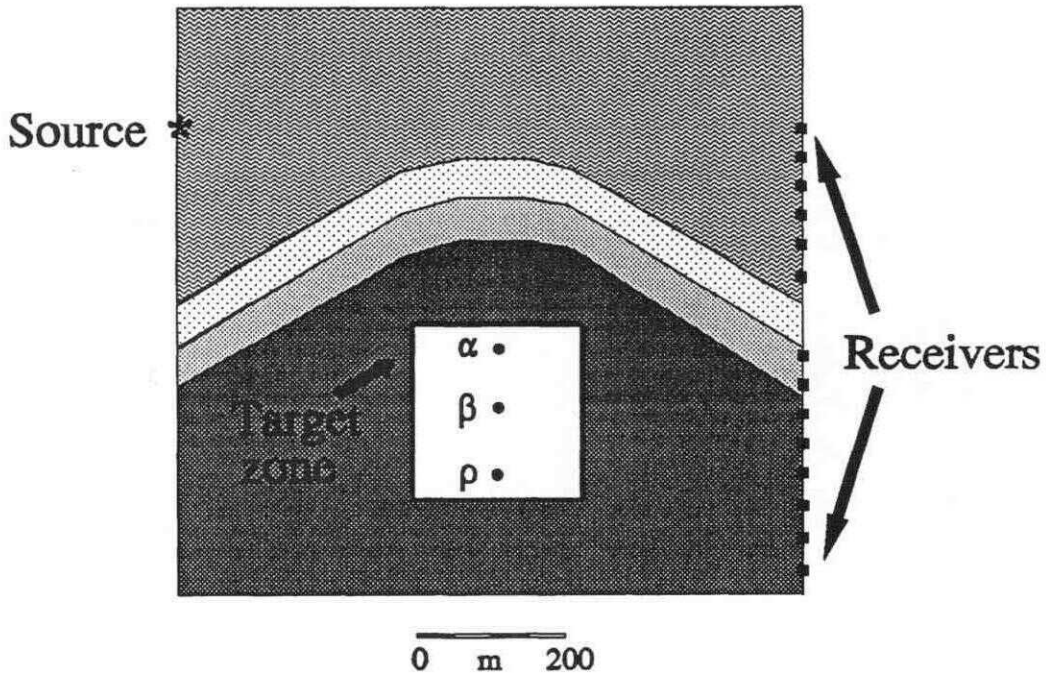


Fig. 5.15. Results after three iterations of migration/inversion for model 5.3.



**Fig. 5.16.** Acquisition geometry used for model 5.4. See Figs. 4.2 and 4.3 for a more complete description of the background model.

zone was not positioned around the fractured reservoir to avoid complications associated with the caustics near the zone.

M/I results for model 5.4 after ten iterations are shown in Fig. 5.18. Only the isotropic parameters are shown; the anisotropic parameters were effectively decoupled from the inversion procedure by assigning very large values for the corresponding inverse variances. Thus, propagation through an anisotropic background medium was modeled, although the scattering itself is modeled as being isotropic. Cross coupling is evident for all three parameters, but is the most problematic for  $\rho$ . The tilted "bow tie" appearance of the M/I images is typical for this type of recording geometry (e.g., Beydoun et al.,

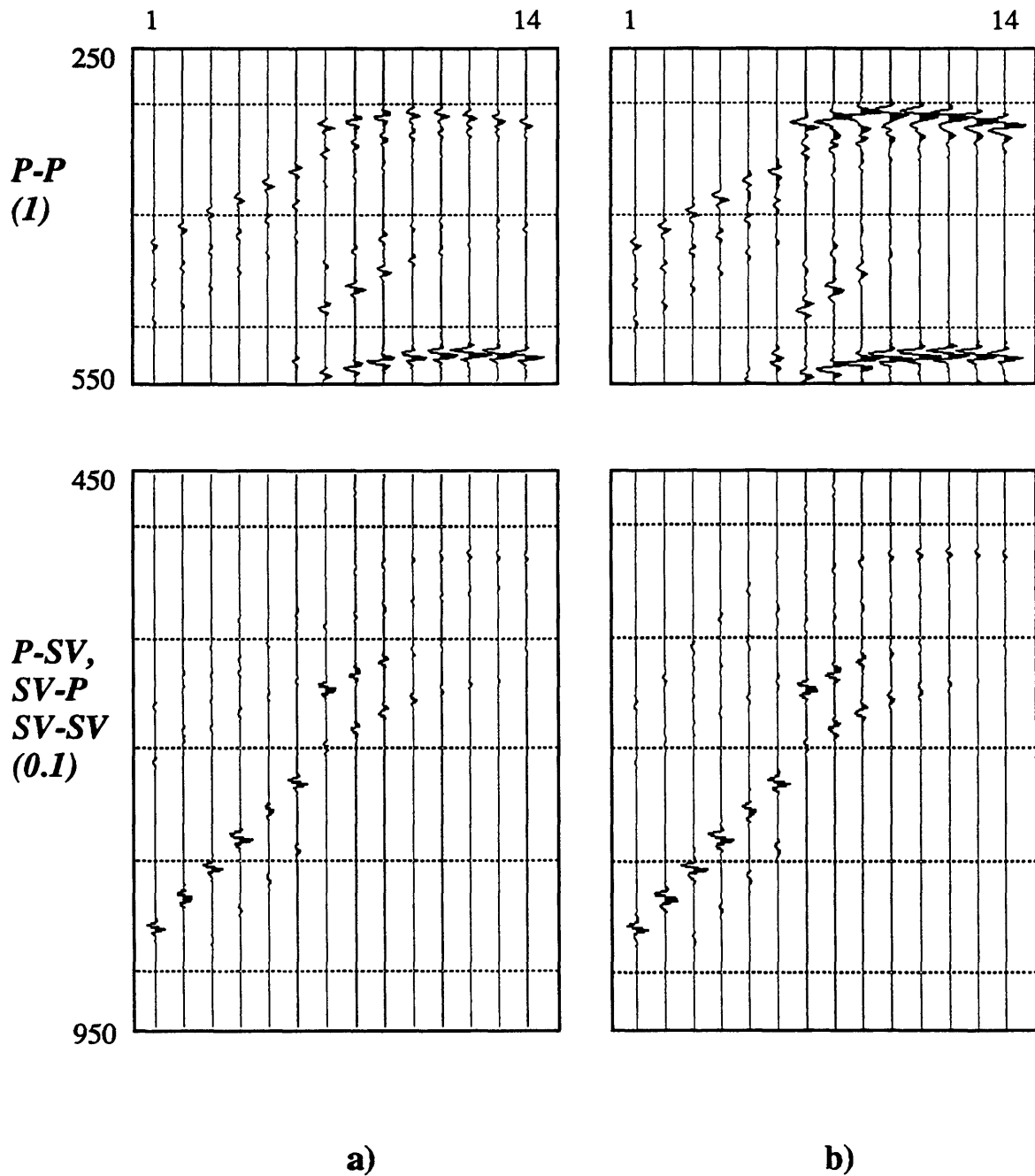


**Fig. 5.17.** a) Input data for model 5.4. Time is in ms, and bracketed number shows plot amplitude (see Fig. 5.11). b) Predicted data, generated by scattering from migration/inversion results (Fig. 5.18).

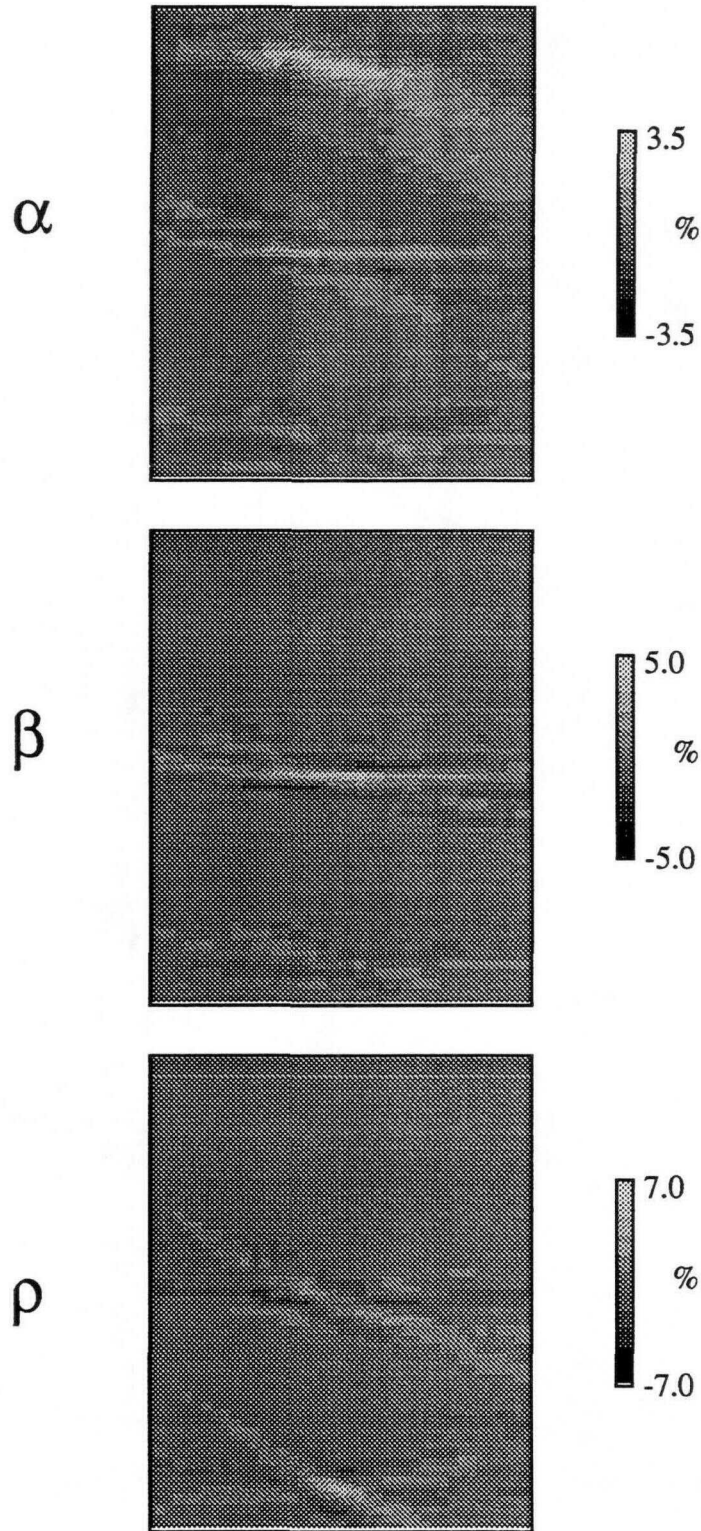


Fig. 5.18. Migration/inversion results (10 iterations) for isotropic parameters, model 5.4.

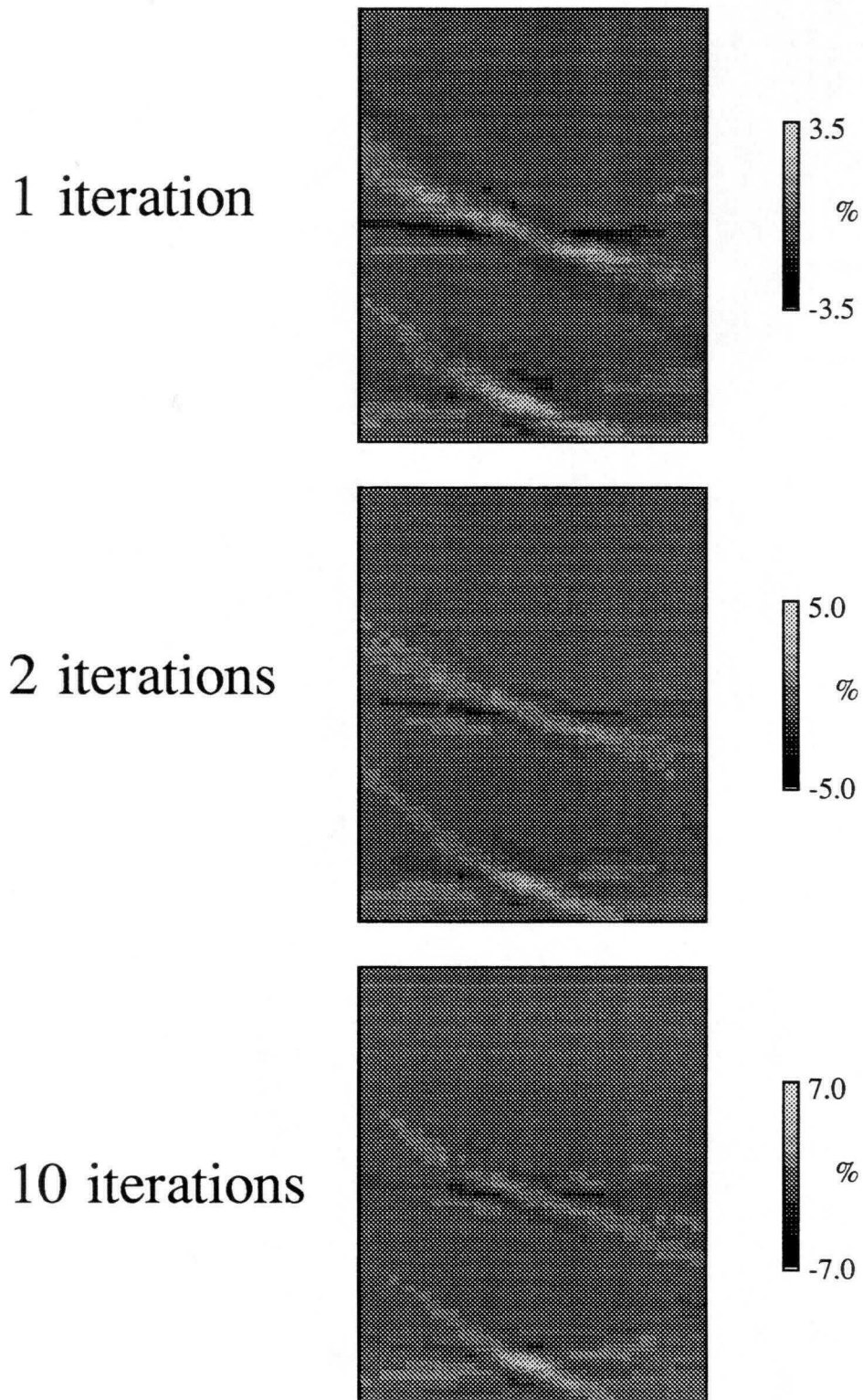
1990). The horizontal component of the re-scattered traces is displayed in Fig. 5.17b for comparison with the input dataset (Fig. 5.17a).

Fig. 5.19 shows the M/I results for  $\rho$  after 1, 2 and 10 iterations. Differences between each of these images are not dramatic, but do illustrate two important features. First, the bow tie smearing artifacts are gradually reduced as the iterations proceed, as the estimated perturbation amplitude becomes more concentrated into a point. Secondly, cross coupling effects, particularly with the  $\beta$  parameter, diminish somewhat from 1 to 10 iterations. In Fig. 5.20 the data-residual energy, as a percentage of the energy in the input dataset, is plotted versus iteration number. The data-residual energy shows a systematic decrease, from about 51% to about 19% over the 10 iterations. Note that the CPU time on a SUN Sparcstation 2 for the first iteration was approximately 4.5 hours, and was devoted mainly to the computation of the background Green's functions. Subsequent iterations required only 20 minutes, because the Green's functions did not need to be recomputed.

### 5.3.5 Migration/inversion using a non-Born dataset

A final example is used here to demonstrate the behaviour of the algorithm using a non-Born input dataset. The input data were generated using the Uniseis raytracing program, and are based on the reflection properties of plane waves at a smooth interface. The source wavelet is the same as in the previous crosswell examples. The background model is shown in Fig. 5.21, and includes a sloping interface that becomes horizontal.

The  $x_1$ -component traces from the ray-traced input dataset, after subtraction of the  $P$ -wave and  $S$ -wave direct arrivals, are shown in Fig. 5.22. This dataset includes  $P$ - $P$ ,  $P$ - $SV$ ,  $SV$ - $P$  and  $SV$ - $SV$  reflections from the interface, but no diffractions. Migration/inversion results are shown in Fig. 5.23. Unfortunately, parameter coupling effects as well as the non-Born nature of the modeled data have resulted in erroneous inversion



**Fig. 5.19.** Migration/inversion images for density after 1, 2 and 10 iterations.

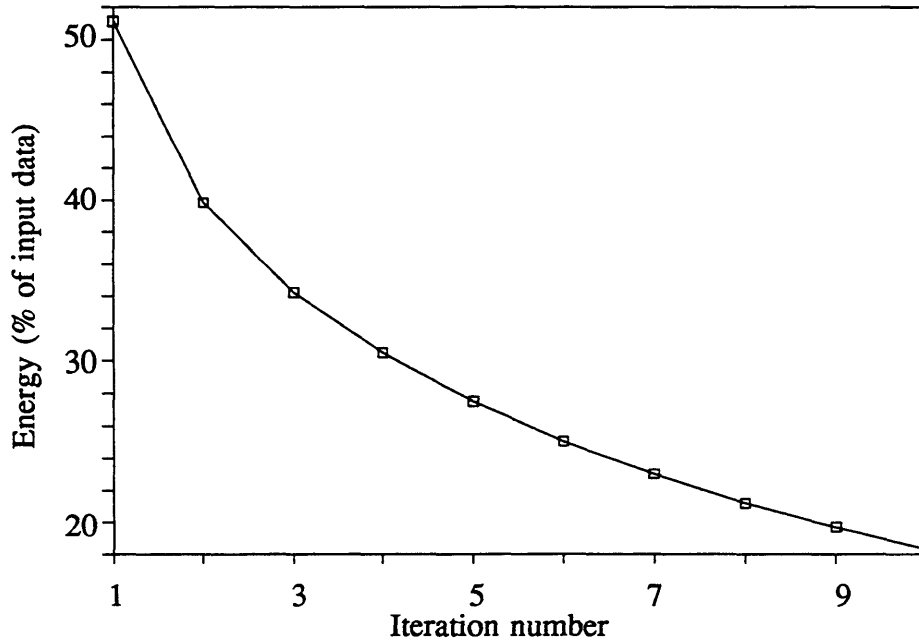


**Fig. 5.20.** Graph of data-residual energy as a function of iteration number for model 5.4.

---

results. For example, no change in  $\delta$ ,  $\epsilon$ , or  $\rho$  exists at the interface, but these are all indicated in the inversion. However, the images do correctly show both the sloping and horizontal parts of the interface.

Note that because only  $P$ - $P$  scattering is used in the inversion, the perturbation image for  $\alpha$  has an appearance that is somewhat different from the other images. The same image, roughly speaking, would be produced by applying conventional depth migration techniques to the  $P$ - $P$  reflection data. The different appearance is partially due

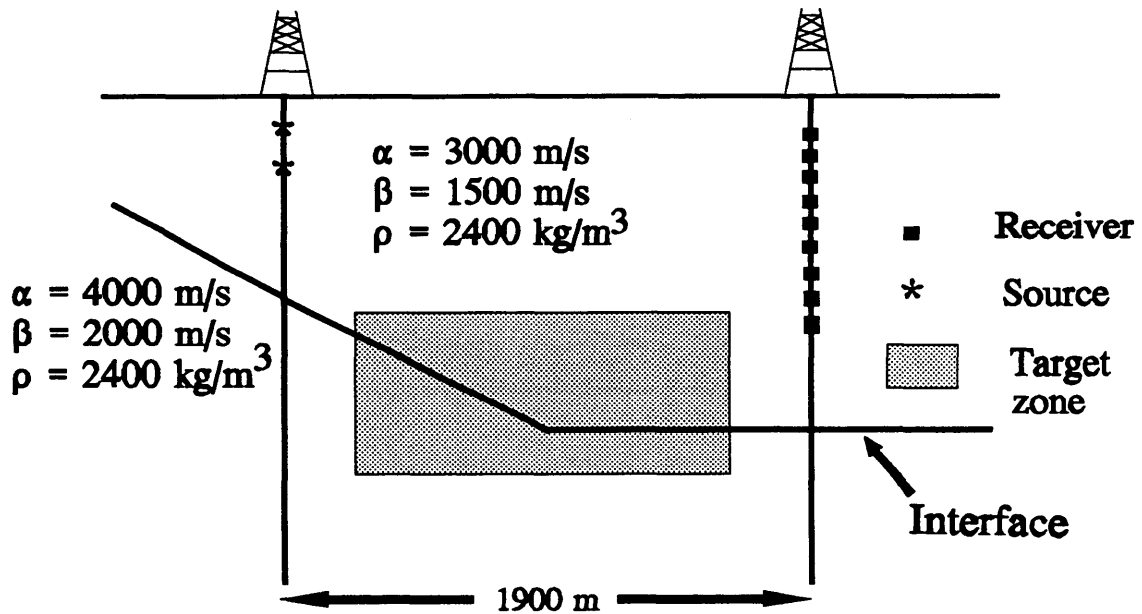


**Fig. 5.21.** Geological model and acquisition geometry used for example 5.5. Every second geophone position is shown in the receiver well.

to the longer wavelength (and thus lower resolution) of  $P$ -waves than  $SV$ -waves, since the bandwidth of the source function is the same in both cases. More significant, however, is the fact that the segments of the interface illuminated by unconverted reflections are shorter than the segments illuminated when both unconverted and converted reflections are considered. Fig. 5.24 illustrates this concept schematically by showing the reflection raypaths connecting one of the sources to the first and last receivers. This result illustrates an important advantage of this migration/inversion approach compared to conventional migration; by using all of the scattered wavetypes

simultaneously, angular coverage of the target zone is improved, thus giving improved resolution of geological features.

## 5.4 Conclusions

In this chapter, a migration/inversion technique has been described, that is suitable for two-dimensional, transversely isotropic elastic media. The technique is based on a ray-Born method introduced by Beydoun and Mendes (1989). Notable differences from the algorithm of Beydoun and Mendes are:

- 1) the incorporation of anisotropy;
- 2) explicit  $2\frac{1}{2}$ -dimensional corrections;
- 3) the use of a finite-difference approach for computing the ray-Green's parameters, instead of the paraxial-ray method (Beydoun and Keho, 1987);
- 4) the use of iteration.

This method attempts to resolve, within some zone of interest, short-wavelength elastic perturbations, relative to a prior background model. High-frequency, far-field, two-dimensional and small-perturbation assumptions are incorporated in the theory. It is also assumed that the direction of the anisotropic symmetry axis lies in the plane of acquisition, and is known. Unlike conventional migration, it is possible to generate a new scattered wavefield from the migration/inversion results, which can be visually compared to the input dataset for quality-control purposes.

The set of synthetic-modeling experiments described here suggest that, given an adequate angular coverage of the target zone and a dataset that satisfies the ray-Born approximation, it is possible to resolve approximately the location and relative magnitude of anisotropic scattering bodies by this technique. In some cases, the anisotropic parameter  $\epsilon$  appears to be resolved as well as, or better than, any of the isotropic

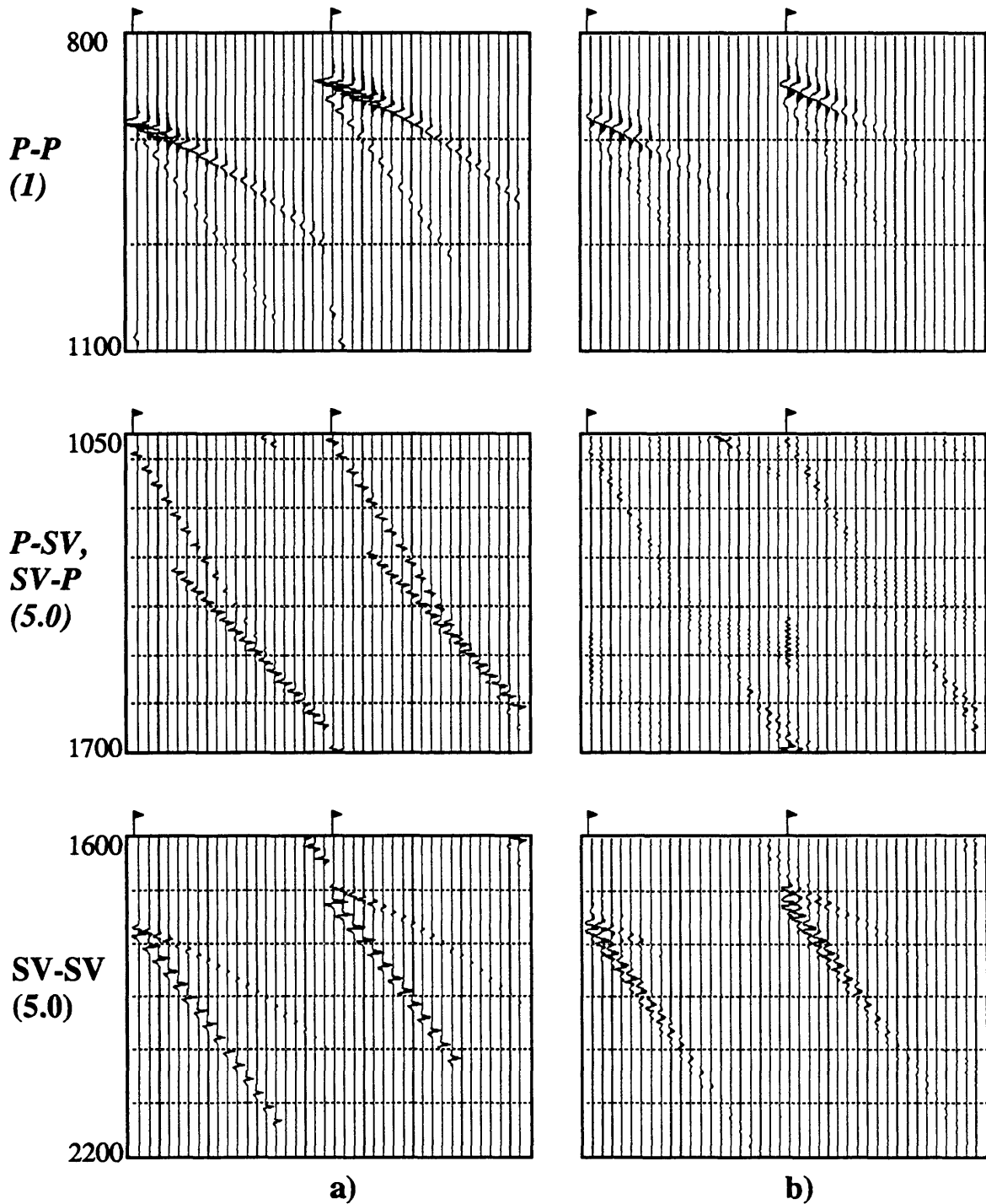


Fig. 5.22. a) Ray-traced input data for model 5.5. Flags indicate the first trace in each shot record. Time is in ms, the bracketed number is the plot amplitude (see Fig. 5.11). b) Seismograms computed by scattering from the perturbation models shown in Fig. 5.23.

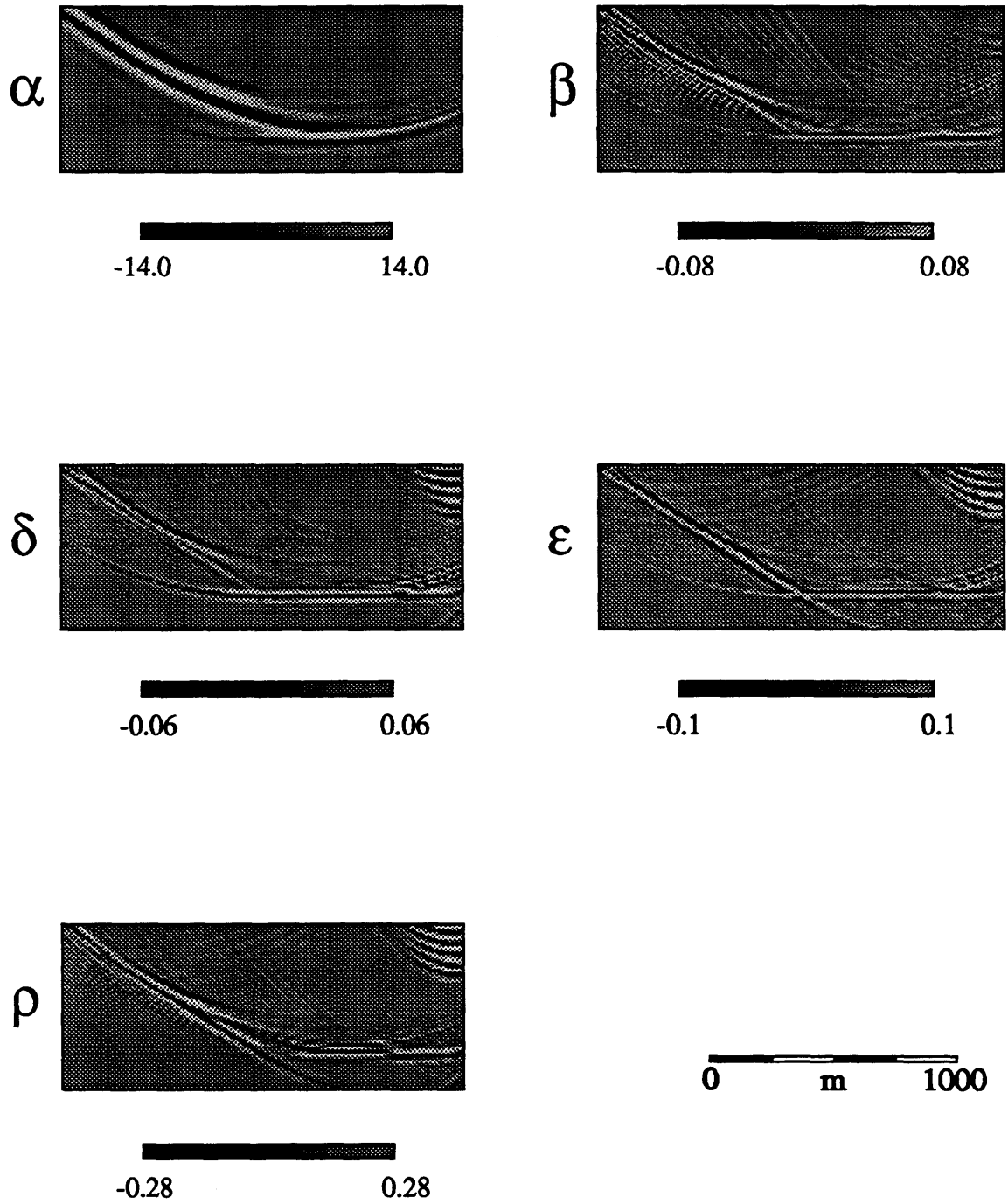
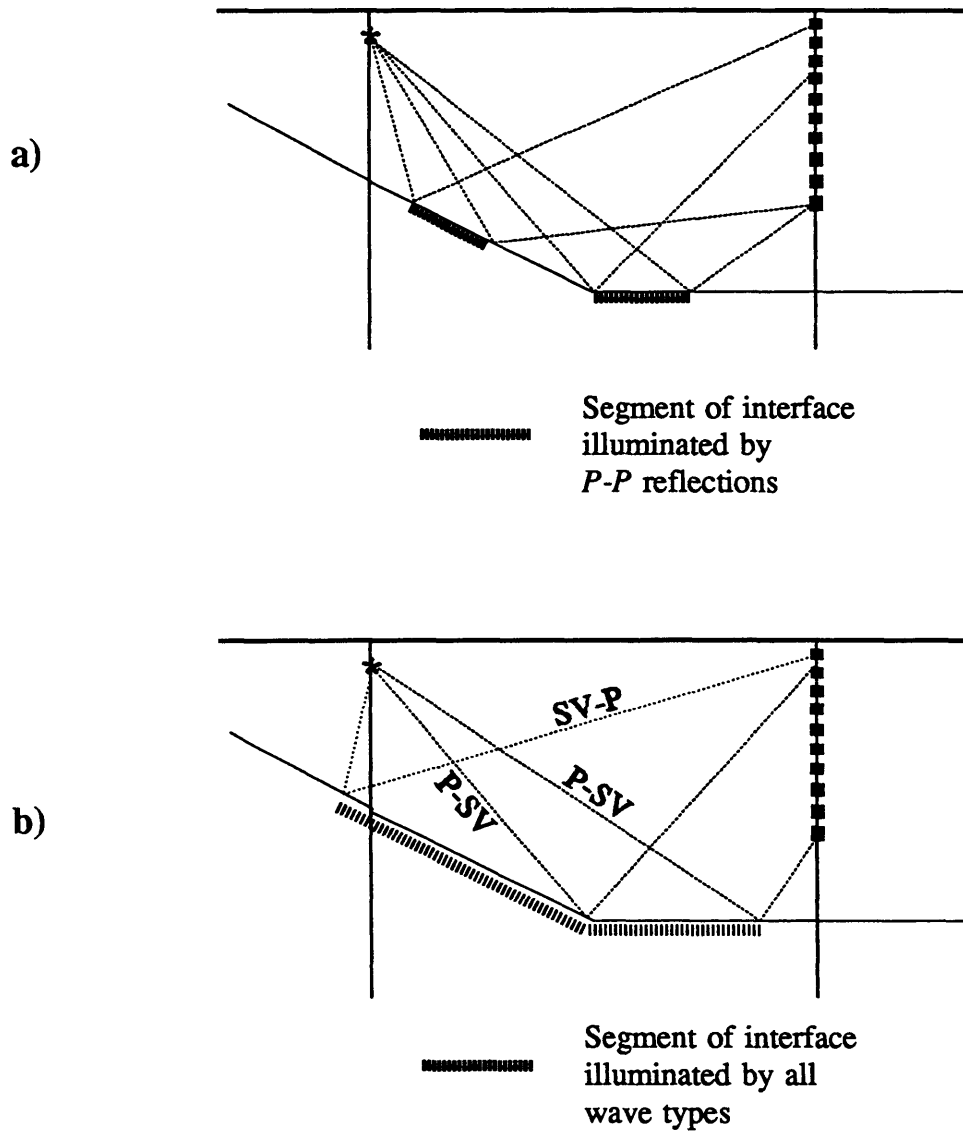


Fig. 5.23. Single-iteration migration/inversion results for model 5.5.



**Fig. 5.24.** Schematic illustration comparing the segments of the interface in model 5.5 illuminated by  $P$ - $P$  reflection (a) with the segments illuminated by all of  $P$ - $P$ ,  $P$ - $SV$ ,  $SV$ - $P$  and  $SV$ - $SV$  reflections (b).

parameters ( $\alpha$ ,  $\beta$  and  $\rho$ ). However, parameter cross-coupling is a more serious problem than for the isotropic case. To achieve the necessary angular coverage, combinations of various acquisition methods may be required (e.g., surface + crosswell). In addition, the resolution of both isotropic and anisotropic parameters, as well as cross-coupling effects, depend on the orientation of the anisotropic symmetry axis.

The simultaneous use of all scattered wave types ( $qP$ - $qP$ ,  $qP$ - $qSV$ ,  $qSV$ - $qP$ ,  $SV$ - $SV$  and  $SH$ - $SH$ ) by this technique has important implications regarding the ability to image accurately slope discontinuities in the subsurface. A ray-traced example has been used to demonstrate the merits of this elastic imaging approach compared to conventional depth migration. The techniques described in this chapter are feasible, at least for small datasets, using present-day workstation technology.

# Chapter 6

## Conclusions

### 6.1 Thesis summary

For each of the topics discussed in this thesis, the underlying theme has been the construction of useful images of the subsurface using multicomponent seismic-reflection data, based on a transversely isotropic, elastic model for wave propagation in the earth. Achieving this objective requires an understanding of the physical basis for anisotropy in sedimentary rocks, basic tools for data preprocessing that correctly handle mode-converted events, and the ability to compute forward models efficiently.

One specific data preprocessing issue, the problem of common-conversion-point data binning, has been considered in some detail. This technique is necessary for the accurate construction of unmigrated, stacked converted-wave images, comparable to the conventional CMP stacked sections that are the workhorse of the seismic industry. Factors that can contribute to undesirable periodic binning behaviour have been analyzed by means of surface stacking charts. A numerical example has been used to illustrate that the presence of anisotropy can potentially have a profound effect on the spatial position of the mode-conversion point.

A new finite-difference methodology has been introduced for the calculation of ray-Green's functions, for TI elastic media. The method stems from a previous finite-difference technique for traveltimes calculation (Vidale, 1988; 1990) and a ray-Jacobian technique for computing geometrical-spreading amplitudes (Vidale and Houston, 1990). This approach permits ray-Green's functions to be computed rapidly for complex

inhomogeneous and weakly anisotropic media. However, amplitudes computed in this manner often exhibit oscillatory spatial artifacts to some degree.

Finally, a least-squares elastic migration/inversion technique introduced by Beydoun and Mendes (1989) has been extended to include the case of a TI background model, and TI perturbations to the background. This is a flexible and relatively cost-efficient technique for generating high-resolution elastic images of the subsurface. Testing of this algorithm using synthetic data indicates that, provided a sufficient angular coverage of the target zone is available using  $qP$  and  $qSV$  wavefields, the anisotropic parameter  $\varepsilon$  may be resolved as well as, or better than, the velocity parameters,  $\alpha$  and  $\beta$ . By performing migration/inversion using all wave types simultaneously, resolution of slope discontinuities in the subsurface can be improved, relative to conventional migration. The method has been developed in a fully iterative form; however, the rate of convergence after the first iteration has been found to be very slow, suggesting that a single iteration is probably sufficient for most cases.

## 6.2 Future work

The depth-variant CCP binning method for  $P$ - $SV$  data is, to date, the only seismic imaging technique developed in this thesis that has been applied to real data. The anisotropic ray-Born imaging techniques have only been tested, so far, using synthetic data. Application of these methods to field observations is an important future goal, but will probably require a dataset with good signal-to-noise characteristics and a broad angular coverage of the target zone.

Beydoun and Mendes (1989) compiled an extensive list of practical and theoretical considerations for this M/I approach. Several of these theoretical considerations

are particularly relevant for studies of anisotropic media, and should be incorporated into future investigations:

1) In practice, it may be difficult to establish prior model covariance operators. This problem is compounded by the general scarcity of independent sources of empirical or statistical information concerning anisotropy. For the simple case of an identity matrix scaled by a constant, the magnitude of model variances appropriate to the problem can be estimated during the computation of the Hessian operator, as described in the last chapter.

2) Data-covariance operators, expressing the relative importance of individual observations, have not been considered here. A potential automated approach for weighting the input data would be to use some local measure of coherence, such as semblance (e.g., Milkereit, 1987).

3) The use of other linearizations of the wave equation (e.g., Rytov, Kirchhoff) and other inversion norms (e.g.,  $l_1$ ,  $l_\infty$ ) may prove to be more suitable for inverting seismic-reflection data.

4) The three anisotropic parameters ( $\gamma$ ,  $\delta$  and  $\epsilon$ ) were originally defined in order to simplify the expressions for phase velocity in weakly anisotropic materials (Thomsen, 1986). These parameters are used here for convenience, and it is unlikely that these particular functions of elastic stiffnesses are optimal for the inversion problem. Thus, some additional testing to determine a better parameterization would be beneficial.

5) The compatibility between the use of effective elastic parameters, arising from the long-wavelength equivalent theories for TI media, and the Born approximation may require additional justification.

6) Investigation of other anisotropic symmetry classes, such as cubic or orthorhombic, may be attempted in the future. While forward modeling of these types of

anisotropic media poses no particular problem using the finite-difference techniques presented here (at least, for wave propagation in symmetry planes), it is uncertain, ultimately, how many independent parameters can be resolved from scattered seismic data. The most general possible anisotropic-elastic inversion scheme would attempt to solve for 24 parameters at each model pixel (i.e., 21 elastic stiffnesses for the triclinic case, density and two direction cosines specifying the orientation of the anisotropic symmetry system). Including anelastic effects would increase the total from 24. It seems highly probable that the actual number of parameters that can be resolved independently is much lower. However, the results from this thesis provide initial evidence that at least one (or more) anisotropic parameters can be obtained from observations of the scattered seismic wavefield. This information should complement velocity and density images, to permit a more complete understanding of geologic structures within the earth.

## References

- Adby, P.R., and Dempster, M.A.H., 1974, Introduction to optimization methods: Chapman and Hall.
- Aki, K. and Richards, P.G., 1980, Quantitative seismology: W.H. Freeman and Company.
- Auld, B.A., 1973, Acoustic fields and waves in solids, Volume 1: Wiley-Interscience.
- Babcock, E.A., 1975, Fracture phenomena in the Waterways and McMurray Formations, Athabasca oil sands region, northeastern Alberta: Bull., Can. Petr. Geol., **23**, 810-826.
- Babcock, E.A., 1978, Measurement of subsurface fractures from dipmeter logs: Bull., Am. Assoc. Petr. Geol., **62**, 1111-1126.
- Backus, G.E., 1962, Long-wave anisotropy produced by horizontal layering: J. Geophys. Res., **66**, 4427-4440.
- Ben-Menahem, A.B., and Beydoun, W.B., 1985, Range of validity of seismic ray and beam methods in general inhomogeneous media - I. General theory: Geophys. J. Roy. Astr. Soc., **82**, 207-234.
- Ben-Menahem, A.B., and Sena, A.G., 1990, Seismic source theory in stratified anisotropic media: J. Geophys. Res., **95**, 15395-15427.
- Bender, C.M. and Orszag, S.A., 1978, Advanced mathematical methods for scientists and engineers: McGraw-Hill.
- Beydoun, W.B., and Kebo, T.H., 1987, The paraxial ray method: Geophysics, **52**, 1639-1653.
- Beydoun, W.B., and Mendes, M., 1989, Elastic ray-Born  $l_2$ -migration/inversion: Geophys. J. Int., **97**, 151-160.

- Beydoun, W.B., Delvaux, J., Mendes, M., Noual, G., and Tarantola, A., 1989, Practical aspects of an elastic migration/inversion of crosshole data for reservoir characterization: A Paris basin example: *Geophysics*, **54**, 1587-1595.
- Beydoun, W.B., Mendes, M., Blanco, J., and Tarantola, A., 1990, North Sea reservoir description: Benefits of an elastic migration/inversion applied to multicomponent vertical seismic profile data: *Geophysics*, **55**, 209-217.
- Beylkin, G., 1985, Imaging of discontinuities in the inverse scattering problem by inversion of a causal generalized Radon transform: *J. Math. Phys.*, **26**, 99-108.
- Beylkin, G., and Burridge, R., 1990, Linearized inverse scattering problems in acoustics and elasticity: *Wave Motion*, **12**, 15-52.
- Bleistein, N., 1984, *Mathematical methods for wave phenomena*: Academic Press.
- Bleistein, N., 1986, Two-and-one-half dimensional in-plane wave propagation: *Geophys. Prosp.*, **34**, 1986.
- Buchwald, V.T., 1959, Elastic waves in anisotropic media: *Proc. Roy. Soc. London, Ser. A*: **253**, 563-580.
- Byun, B.S., Corrigan, D., and Gaiser, J.E., 1989, Anisotropic velocity analysis for lithology discrimination: *Geophysics*, **54**, 1564-1574.
- Byun, B.S., and Corrigan, D., 1990, Seismic traveltime inversion for transverse isotropy: *Geophysics*, **55**, 192-200.
- Carcione, J.M., Kosloff, D. and Behle, A., 1991, Long-wave anisotropy in stratified media: a numerical test: *Geophysics*, **56**, 245-254.
- Castle, R.J., 1988, Shifted hyperbolas and normal moveout: *Soc. Expl. Geophys.*, 58th Ann. Intl. Mtg., Expanded Abstracts, 894-896.
- Červený, V., 1972, Seismic rays and ray intensities in inhomogeneous anisotropic media: *Geophys. J. Roy. Astr. Soc.*, **29**, 1-13.

- Červený, V., Molotkov, I.A., and Psenčík, I., 1977, Ray method in seismology: Univerzita Karlova, Prague.
- Chung, W.Y., and Corrigan, D., 1985, Gathering mode-converted shear waves: A model study: Soc. of Expl. Geophys. Ann. Mtg., Expanded Abstracts, 602-604.
- Claerbout, J.F., 1985, Imaging the Earth's interior: Blackwell Sci. Publ.
- Clayton, R.W., and Stolt, R.H., 1981: A Born-WKBJ inversion method for acoustic reflection data: Geophysics, 1559-1567.
- Cohen, J.K., and Bleistein, N., 1979, Velocity inversion procedure for acoustic waves: Geophysics, **44**, 1077-1087.
- Crampin, S., 1981, A review of wave motion in anisotropic and cracked elastic-media: Wave Motion, **3**, 343-391.
- Crampin, S., 1985, Evaluation of anisotropy by shear-wave splitting: Geophysics, **50**, 142-152.
- Crampin, S., 1986, Anisotropy and transverse isotropy: Geophys. Prosp., **34**, 94-99.
- Crampin, S., 1987, The geological and industrial implications of extensive dilatancy anisotropy: Nature, **328**, 491-496.
- Crampin, S., Chesnokov, E.M. and Hipkin, R.A., 1984, Seismic anisotropy: The state of the art: Geophys. J. Roy. Astr. Soc., **76**, 1-16.
- Dillon, P.B., and Thompson, R.C., 1984, Offset source VSP surveys and their image reconstruction: Geophys. Prosp., **35**, 803-814.
- Duff, G.F.D., 1960, The Cauchy problem for elastic waves in an anisotropic medium: Phil. Trans. Roy. Soc. London, Ser. A: **252**, 249-273.
- Eaton, D.W.S., 1989, The free surface effect: Implications for amplitude-versus-offset inversion: J. Can. Soc. Expl. Geophys., **25**, 97-103.

- Eaton, D.W.S., and Lawton, D.C., 1991, *P-SV stacking charts and binning periodicity: Geophysics*, in press.
- Eaton, D.W.S., Stewart, R.R., and Harrison, M.P., 1991, The Fresnel zone for P-SV waves: *Geophysics*, **56**, 360-364.
- Frasier, C., and Winterstein, D., 1990, Analysis of conventional and converted mode reflections at Putah Sink, California using three-component data: *Geophysics*, **55**, 646-659.
- Fromm, G., Krey, T., and Wiest, B., 1985, Static and dynamic corrections: *In* Dohr, G., Ed., *Seismic shear waves: Handbook of Geophysical Exploration*, **15a**, Geophysical Press, 191-225.
- Gajewski, D., and Psenčik, T., 1987, Computation of high frequency seismic wavefields in 3-D laterally inhomogeneous anisotropic media: *Geophys. J. Roy. Astr. Soc.*, **91**, 383-411.
- Garbin, H.D., and Knopoff, L., 1975, Elastic moduli of a medium with liquid-filled cracks: *Quart. Appl. Math.*, **33**, 301-303.
- Gardner, G.H.F., Gardner, L.W., and Gregory, A.R., 1974, Formation velocity and density - the diagnostic basics for stratigraphic traps: *Geophysics*, **39**, 770-780.
- Geis, W.T., Stewart, R.R., Jones, M.J., and Katopodis, P.E., 1990, Processing, correlating, and interpreting converted shear waves from borehole data in southern Alberta: *Geophysics*, **55**, 660-669.
- Geoltrain, S., and Cohen, J.K., 1989, Asymptotic solutions to direct and inverse scattering in anisotropic elastic media: *SEG 1989 Intl. Mtg., Expanded Abstracts*, 938-942.
- Gibson, R.L., and Toksöz, M.N., 1990, Permeability estimation from velocity anisotropy in fractured rock: *J. Geophys. Res.*, **95**, 15643-15655.

- Graustein, W.C., 1962, Differential geometry: Dover Publications, Inc.
- Harrison, M.P., 1989, Three-component seismic data processing: Carrot Creek, Alberta: *In Consortium for Research in Elastic Wave Exploration Seismology, Research Report, The University of Calgary, 1, 6-26.*
- Helbig, 1981, Systematic classification of layer-induced transverse isotropy: *Geophys. Prosp.*, **29**, 550-577.
- Helbig, 1983, Elliptical anisotropy - Its significance and meaning: *Geophysics*, **48**, 825-832.
- Helbig, 1984, Anisotropy and dispersion in periodically layered media: *Geophysics*, **49**, 364-373.
- Hudson, J.A., 1981, Wave speeds and attenuation of elastic waves in material containing cracks: *Geophys. J. Roy. Astr. Soc.*, **64**, 133-150.
- Iwuagwu, C.J., and Lerbekmo, J.F., 1982, The petrology of the basal Belly River sandstone reservoir, Pembina Field, Alberta: *Bull., Can. Petr. Geol.*, **30**, 187-207.
- Jannane, M., Beydoun, W., Crase, E., Cao, D., Korn, Z., Landa, E., Mendes, M., Pica, A., Noble, M., Roeth, G., Singh, S., Snieder, R., Tarantola, A., Trezeguet, D., and Zie, M., 1989, Wavelengths of earth structures that can be resolved from seismic reflection data: *Geophysics*, **54**, 906-910.
- Jones, E.A., and Wang, H.F., 1981, Ultrasonic velocities in Cretaceous shales from the Williston basin: *Geophysics*, **46**, 288-297.
- Kendall, J-M., and Thomson, C.J., 1989, A comment on the form of the geometrical spreading equations, with some numerical examples of seismic ray tracing in inhomogeneous, anisotropic media: *Geophys. J. Int.*, **99**, 401-413.
- Krey, T., and Helbig, K., 1956, A theorem concerning anisotropy of stratified media and its significance for reflection seismics: *Geophys. Prosp.*, **4**, 294-302.

- Kuo, J.T., and Dai, T., 1984, Kirchhoff elastic wave migration for the case of non-coincident source and receiver: *Geophysics*, **49**, 1223-1238.
- Lebras, R., and Clayton, R.W., 1988, An iterative inversion of back-scattered acoustic waves: *Geophysics*, **53**, 501-508.
- Levin, F.K., 1979, Seismic velocities in transversely isotropic media: *Geophysics*, **44**, 918-936.
- Lynn, H.B. and Thomsen, L.A., 1990, Reflection shear-wave data collected near the principal axes of aximuthal anisotropy: *Geophysics*, **55**, 147-156.
- Meadows, M., 1985, Exact and approximate inversion of plane-layered isotropic and anisotropic media by layer stripping: *Soc. Expl. Geophys., 55th Ann. Int. Mtg., Expanded Abstracts*, 336-339.
- Melia, P.J. and Carlson, R.L., 1984, An experimental test of P-wave anisotropy in stratified media: *Geophysics*, **49**, 374-378.
- Milkereit, B., 1987, Migration of noisy seismic data: *J. Geophys. Res.*, **92**, 7916-7930.
- Miller, D., Oristaglio, M., and Beylkin, G., 1987, A new slant on seismic imaging: Migration and integral geometry: *Geophysics*, **52**, 943-964.
- Mora, P.R., 1987, Nonlinear two-dimensional elastic inversion of seismic data: *Geophysics*, **52**, 1211-1228.
- Mora, P.R., 1988, Elastic wavefield inversion of reflection and transmission data: *Geophysics*, **53**, 750-759.
- Musgrave, 1970, *Crystal acoustics: Introduction to the study of elastic waves and vibrations in crystals*: Holden-Day.
- Nazar, B., 1991, An interpretive study of multicomponent seismic data from the Carrot Creek Field, West Central Alberta: M.Sc. thesis, The University of Calgary.
- Newton, R.G., 1966: *Scattering theory of waves and particles*: McGraw-Hill.

- Postma, G.W., 1955, Wave propagation in a stratified medium: *Geophysics*, **20**, 780-806.
- Pratt, R.G., and Gouly, N.R., 1991, Combining wave-equation imaging with travelttime tomogrphy to form high-resolution images from crosshole data: *Geophysics*, **56**, 208-224.
- Press, W.H., Flannery, B.P., Teukolsky, S.A., and Vetterling, W.T., 1990, *Numerical Recipes: The art of scientific computing*: Cambridge University Press.
- Qin, F., Olsen, K.B., Luo, Y., and Schuster, G.T., 1990, Solution of the eikonal equation by a finite-difference method: *Soc. Expl. Geophys. Ann. Mtg., Expanded Abstracts*, 1004-1007.
- Raz, S., 1981, Direct reconstruction of velocity and density profiles from scattered field data: *Geophysics*, **46**, 832-836.
- Robertson, J.D. and Corrigan, D., 1983, Radiation studies on a shear-wave vibrator in near-surface shale: *Geophysics*, **48**, 19-26.
- Rothman, D.H., 1988, Cellular-automaton fluids: A model for flow in porous media: *Geophysics*, **53**, 509-518.
- Schneider, W.A., 1978, Integral formulation for migration in two and three dimensions: *Geophysics*, **43**, 49-76.
- Sheriff, R.E., 1980, Nomogram for Fresnel-zone calculation: *Geophysics*, **45**, 968-972.
- Sheriff, R.E., and Geldart, L.P., 1982, *Exploration seismology, volume 1: History, theory and acquisition*: Cambridge University Press.
- Singh, S.C., and Chapman, C.H., 1988, WKBJ seismogram theory in anisotropic media: *J. Acoust. Soc. Am.*, **84**, 732-741.
- Slotboom, R.T., 1990, Converted wave (P-SV) moveout estimation: *Soc. Expl. Geophys. Ann. Mtg., Expanded Abstracts*, 1104-1106.

- Slotboom, R.T., and Stewart, R.R., 1989, Depth-variant gathering of P-SV seismic data: Presented at the 16th Ann. Mtg., Can. Soc. Expl. Geophys.
- Smith, G.D., 1985, Numerical solution of partial differential equations: Finite difference methods: Clarendon Press.
- Stewart, R.R., 1991, Rapid map and inversion of *P-SV* waves: *Geophysics*, **56**, 859-862.
- Stolt, R.H., and Weglein, A.B., 1985, Migration and inversion of seismic data, *Geophysics*, **50**, 2458-2472.
- Stolt, R.H. and Benson, A.K., 1986, Seismic migration: Theory and practice: Geophysical Press.
- Synge, J.L., 1957, Elastic waves in anisotropic media: *J. Math. and Phys.*, **35**, 323,334.
- Tarantola, A., 1984, Linearized inversion of seismic reflection data: *Geophys. Prosp.*, **32**, 998-1015.
- Tarantola, A., 1986, A strategy for nonlinear inversion of seismic reflection data: *Geophysics*, **51**, 1893-1903.
- Tarantola, A., 1987, Inverse problem theory: Methods of data fitting and model parameter estimation: Elsevier.
- Tarantola, A., and Valette, B., 1982, Generalized nonlinear inverse problems solved using the least squares criterion: *Rev. Geophys. and Space Phys.*, **20**, 219-232.
- Taylor, G., 1989, The point of P-S mode-converted reflection: An exact determination: *Geophysics*, **54**, 1060-1063.
- Tessmer, G., and Behle, A., 1988, Common reflection point data-stacking technique for converted waves: *Geophys. Prosp.*, **36**, 671-688.
- Tessmer, G., Krajewski, P., Fertig, J., and Behle, A., 1990, Processing of *PS*-reflection data applying a common conversion-point stacking technique: *Geophys. Prosp.*, **38**, 267-286.

- Thomsen, L., 1986, Weak elastic anisotropy: *Geophysics*, **51**, 1954-1966.
- Thomsen, L., 1988, Reflection seismology over azimuthally anisotropic media: *Geophysics*, **53**, 304-313.
- Tura, M.A.C., 1990, Acoustic and elastic diffraction tomography and its application to fracture detection, Ph.D. thesis, University of California at Berkeley, 182 pp.
- Uren, N.F., Gardner, G.H.F., and McDonald, J.A., 1990, The migrator's equation for anisotropic media: *Geophysics*, **55**, 1429-1434.
- Van Trier, J., and Symes, W.W., 1991, Upwind finite-difference calculation of traveltimes: *Geophysics*, **56**, 812-821.
- Vidale, J.E., 1988, Finite-difference calculation of travel times: *Bull. Seis. Soc. Am.*, **78**, 2062-2076.
- Vidale, J.E., 1990, Finite-difference calculation of traveltimes in three dimensions: *Geophysics*, **55**, 523-528.
- Vidale, J.E., and Houston, H., 1990, Rapid calculation of seismic amplitudes: *Geophysics*, **55**, 1504-1507.
- Weglein, A.B., Violette, P.B., and Kebo, T.H., 1986, Using multiparameter Born theory to obtain certain exact multiparameter inversion goals: *Geophysics*, **51**, 1069-1074.
- Winterstein, D.F., 1986, Anisotropy effects in P-wave and SH-wave stacking velocities contain information on lithology: *Geophysics*, **51**, 661-672.
- Winterstein, D.F., 1990, Velocity anisotropy terminology for geophysicists, *Geophysics*, **55**, 1070-1088.
- Winterstein, D.F. and Paulsson, B.N.P., 1990, Velocity anisotropy in shale determined from crosshole seismic and vertical seismic profile data: *Geophysics*, **55**, 470-479.

- Winterstein, D.F. and Meadows, M.A., 1990, Changes in shear-wave polarization azimuth with depth in Cymric and Railroad Gap oil fields: 60th Ann. Internat. Mtg., Soc. Explor. Geophys., Expanded Abstracts, 1435-1438.
- Wu, R.S., and Aki, K., 1985, Scattering characteristics of elastic waves by an elastic heterogeneity: *Geophysics*, **50**, 582-595.
- Wyatt, K.D., and Wyatt, S.B., 1984, Determining subsurface structure using the vertical seismic profile, *In* Toksöz, M.N., and Stewart, R.R., Eds., Vertical seismic profiling, Part B: Advanced concepts: Geophysical Press.
- Yilmaz, Ö., 1987, Seismic data processing: Society of Exploration Geophysicists.
- Zamora, M., and Poirier, J.P., 1990, Experimental study of acoustic anisotropy and birefringence in dry and saturated Fontainebleau sandstone: *Geophysics*, **55**, 1455-1465.

# Appendix A

## Elastic-scattering radiation patterns

### A.1 Stiffness components and vector constraints

Scattering radiation patterns due to small perturbations to the elastic stiffnesses (Rayleigh scattering) are considered here, for a transversely isotropic medium. With no loss of generality, the elastic stiffnesses, the slowness vectors and eigenvectors are referred to a coordinate system with the  $x_3$ -axis aligned with the anisotropic symmetry axis, and the  $x_1$ -axis in the acquisition plane. Perturbation to the stiffness matrix elements,  $C_{11}$ ,  $C_{33}$ ,  $C_{13}$ ,  $C_{44}$  and  $C_{66}$  affect the following tensor components (see Table 2.1):

$$\begin{aligned}
 C_{11}: & c_{1111}; \\
 C_{33}: & c_{3333}; \\
 C_{13}: & c_{1133}, c_{3311}; \\
 C_{44}: & c_{3232}, c_{3223}, c_{2332}, c_{2323}, c_{3131}, c_{3113}, c_{1331}, c_{1313}; \\
 C_{66}: & c_{2121}, c_{2112}, c_{1221}, c_{1212}.
 \end{aligned} \tag{A.1}$$

Because the source, receivers and anisotropic symmetry axis are assumed to be coplanar (section 1.1.2),

$$\tilde{p}_2 = \hat{p}_2 = 0 \quad . \tag{A.2}$$

As before, all quantities with the  $\sim$  and  $\wedge$  superscripts are associated with the source and receiver Green's functions, respectively. For  $qP$  and  $qSV$  waves, we also have

$$\bar{g}_2 = \hat{g}_2 = 0 \quad , \quad (\text{A.3})$$

whereas for *SH* waves,

$$\begin{aligned} \bar{g}_1 = \bar{g}_3 = \hat{g}_1 = \hat{g}_3 = 0 \\ \bar{g}_2 = \hat{g}_2 = 1 \quad . \end{aligned} \quad (\text{A.4})$$

## A.2 The scattering vector

Rayleigh scattering for general anisotropic elastic media may be written as the dot product between a scattering vector,  $\mathbf{s}$ , and a model perturbation vector,  $\Delta\mathbf{m}^0 = (C_{11}, C_{33}, C_{13}, C_{44}, C_{66}, \rho)$  via the relation (see Beylkin and Burridge, 1990, equation 2.12)

$$\mathbf{s} \cdot \Delta\mathbf{m}^0 = [\Delta\rho\delta_{ik} + \Delta c_{ijkl}\bar{p}_l\hat{p}_j]\bar{g}_k\hat{g}_i \quad . \quad (\text{A.5})$$

Using (A.1), (A.2) and (A.3), the scattering vector,  $\mathbf{s}$ , for *qP* and *qSV* waves may be written

$$\begin{aligned} \mathbf{s} = (\hat{p}_1\bar{p}_1\hat{g}_1\bar{g}_1, \hat{p}_3\bar{p}_3\hat{g}_3\bar{g}_3, \hat{p}_1\bar{p}_3\hat{g}_1\bar{g}_3 + \hat{p}_3\bar{p}_1\hat{g}_3\bar{g}_1, \hat{p}_1\bar{p}_1\hat{g}_3\bar{g}_3 + \hat{p}_3\bar{p}_3\hat{g}_1\bar{g}_1 + \\ \hat{p}_1\bar{p}_3\hat{g}_3\bar{g}_1 + \hat{p}_3\bar{p}_1\hat{g}_1\bar{g}_3, 0, -\hat{g}_q\bar{g}_q)^T \end{aligned} \quad (\text{A.6})$$

For *SH* waves,  $\mathbf{s}$  may be written

$$\mathbf{s} = (0, 0, 0, \hat{p}_3\bar{p}_3, \hat{p}_1\bar{p}_1, -1)^T \quad , \quad (\text{A.7})$$

using (A.1), (A.2) and (A.4).

## Appendix B

### Time-shifted hyperbolic moveout for converted waves

#### B.1 Derivation of the formula

Castle (1988) developed a time-shifted hyperbolic formula for estimating the moveout for  $P$ - $P$  reflections in an isotropic, horizontally layered medium. This formula is exact to the fourth power of offset, and is easily adapted to the case of mode-converted ( $P$ - $SV$ ) reflections. Castle's (1988) NMO formula may be written

$$t(x) \approx \tau_s + \sqrt{\tau_0^2 + \frac{x^2}{v^2}} \quad . \quad (\text{B.1})$$

In equation (B.1),  $x$  is offset,  $t(x)$  is two-way traveltime and  $\mu_j$  is the  $j$ th weighted moment of the velocity distribution, given by

$$\mu_j = \frac{\sum_{k=1}^N \Delta\tau_k V_k^j}{\sum_{i=1}^N \Delta\tau_i} \quad (\text{B.2})$$

where  $\Delta\tau_j$  is the vertical traveltime and  $V_j$  is the velocity ( $P$  or  $S$ ) in the  $j$ th layer.  $S$  is defined as:

$$S \equiv \frac{\mu_4}{\mu_2} \quad . \quad (\text{B.3})$$

In addition,

$$\begin{aligned}
 t_0 &= t(0) \\
 \tau_s &= t_0 \left(1 - \frac{1}{S}\right) \\
 \tau_0 &= \frac{t_0}{S} \\
 v^2 &= S\mu_2 \quad .
 \end{aligned}
 \tag{B.4}$$

For converted waves, Castle's (1988) definitions (equations B.2 - B.4) remain the same, except that the weighted moments of the velocity distributions are summed twice for each layer, once each for  $P$ -wave velocity ( $\alpha$ ) and  $S$ -wave velocity ( $\beta$ ). For the simple case of a single layer with  $\beta/\alpha = G$ ,

$$\begin{aligned}
 \mu_2 &= \alpha^2 G \\
 \mu_4 &= \frac{\alpha^4 G(1+G^3)}{(1+G)} \quad ,
 \end{aligned}
 \tag{B.5}$$

giving

$$S = \frac{(1+G^3)}{G(1+G)} \quad .
 \tag{B.6}$$

Making the assumptions that  $G = 0.5$ , equation (B.6) reduces to

$$t \approx \frac{t_0}{3} + \sqrt{\frac{4t_0^2}{9} + \frac{2x^2}{3V_{\text{rms}}^2}} \quad ,
 \tag{B.7}$$

where  $V_{\text{rms}}^2 \equiv \mu_2$ . Equation (B.7) is a useful approximation for estimating  $P$ - $SV$  moveout.

For other estimates of  $G$ , (B.7) can be modified accordingly.

## B.2 Comparison with other formulas

Tessmer and Behle (1988) and Slotboom (1990) have presented different formulas for estimating  $P$ - $SV$  moveout. Tessmer and Behle (1988) wrote an even-ordered power series expressing the total moveout exactly, and truncated after two terms to give the hyperbolic formula

$$t^2 \approx t_0^2 + \frac{x^2}{V_{rms}^2} \quad . \quad (\text{B.8})$$

Slotboom (1990) used an empirical argument to arrive at the shifted hyperbolic formula,

$$t = \frac{t_0}{2} + \sqrt{\left(\frac{t_0}{2}\right)^2 + \frac{x^2}{2V_{rms}^2}} \quad . \quad (\text{B.9})$$

Observe that (B.9) is equivalent to (B.7) for  $G = 1$  (i.e.  $\alpha = \beta$ ). The relative travelttime error,  $\Delta t = t_{\text{exact}} - t_{\text{formula}}$  versus offset-to-depth ratio,  $x/h$ , is plotted in Fig. B.1 for these three formulas for the single layer case.

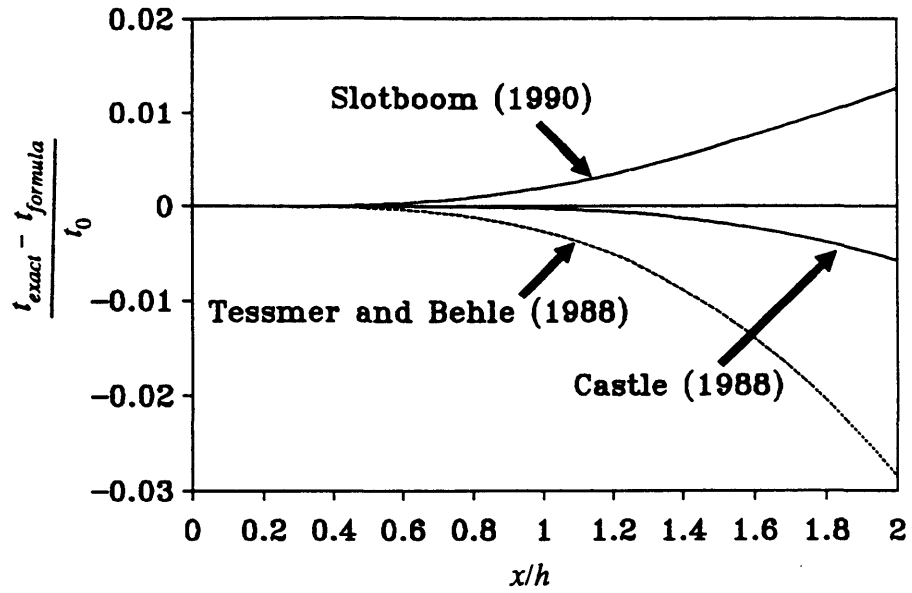


**Fig. B.1.** Comparison of moveout formulas for converted waves, for the single-layer case.

## Appendix C

# The eikonal equation as a sixth-order polynomial

### C.1 Derivation

I begin by writing the eikonal equation for anisotropic media in its determinant form,

$$\det|c_{ijkl}p_j p_l - \rho\delta_{ik}| = 0 \quad . \quad (\text{C.1})$$

For wave propagation in the plane  $x_2 = 0$ , we have  $p_2 = 0$  based on the assumptions given in section 1.1.2. The finite-difference stencils are always chosen so that an estimate of  $p_1$  is available, based on existing knowledge of the travelttime field. Thus, the method of solution here is to substitute known values for  $p_1$  and  $p_2$  into equation (C.1) and solve for  $p_3$ . Substituting  $p_1$  and  $p_2$  into equation (C.1) and collecting equal powers of  $p_3$  leads to a sixth-order polynomial equation. Defining

$$\begin{aligned} A_{ik} &\equiv c_{i3k3} \\ B_{ik} &\equiv (c_{i3k1} + c_{i1k3})p_1 \quad , \\ C_{ik} &\equiv c_{i1k1}p_1^2 - \rho\delta_{ik} \end{aligned} \quad (\text{C.2})$$

equation (C.1) may be rewritten as

$$\xi_j p_3^j = 0 \quad , \quad j=0, \dots, 6 \quad . \quad (\text{C.3})$$

The coefficients,  $\xi_j$ , of equation (C.3) are given by

$$\begin{aligned}
\xi_0 &= |\mathbf{A}| \\
\xi_1 &= |\mathbf{AAB}| + |\mathbf{ABA}| + |\mathbf{BAA}| \\
\xi_2 &= |\mathbf{AAC}| + |\mathbf{ACA}| + |\mathbf{CAA}| + |\mathbf{ABB}| + |\mathbf{BAB}| + |\mathbf{BBA}| \\
\xi_3 &= |\mathbf{ABC}| + |\mathbf{ACB}| + |\mathbf{BAC}| + |\mathbf{BCA}| + |\mathbf{CAB}| + |\mathbf{CBA}| + |\mathbf{B}| \quad , \\
\xi_4 &= |\mathbf{ACC}| + |\mathbf{CAC}| + |\mathbf{CCA}| + |\mathbf{BBC}| + |\mathbf{BCB}| + |\mathbf{CBB}| \\
\xi_5 &= |\mathbf{BCC}| + |\mathbf{CBC}| + |\mathbf{CCB}|
\end{aligned} \tag{C.4}$$

and

$$\xi_6 = |\mathbf{C}| \quad .$$

In equation (C.4), the notation  $[\mathbf{ABC}]$  is used to represent a matrix whose first row comes from  $\mathbf{A}$ , the second from  $\mathbf{B}$  and the third from  $\mathbf{C}$ . Thus, the coefficients of the polynomial equation are found using the determinants of matrices that are row-permutations of the matrices defined in (C.2). The solution of equation (C.3) can also be used for calculating reflection/transmission angles at a welded interface, in agreement with the anisotropic form of Snell's Law (equation 3.20).